University of Huddersfield Repository

Mistry, Dharmit

Mechanistic studies of some chemical and biochemical reactions

Original Citation

Mistry, Dharmit (2014) Mechanistic studies of some chemical and biochemical reactions. Doctoral thesis, University of Huddersfield.

This version is available at http://eprints.hud.ac.uk/id/eprint/23444/

MECHANISTIC STUDIES OF SOME CHEMICAL AND BIOCHEMICAL REACTIONS

DHARMIT MISTRY

A thesis submitted to the University of Huddersfield in partial fulfilment of the requirements for the degree of Doctor of Philosophy

The University of Huddersfield

Submission date: February 2014

Abstract

Three aspects of chemical and biochemical reactions were investigated.

1. The relative reactivities of pyrophosphate (phosphorus(V)) and pyro-di-H-phosphonate (phosphorus(III)) and its derivatives have been analysed at various pHs. The hydrolysis rate of pyro-di-H-phosphonate (PP(III)) was found to be higher than pyrophosphate at all pHs. Using ITC and NMR, pyrophosphate showed metal-ion complexing abilities whereas pyro-di-H-phosphonate showed weak or no complexing to metal-ions, although the rate of hydrolysis at pH 7 slightly increased compared to the spontaneous hydrolysis of PP(III). The enzymatic hydrolysis of pyrophosphate, which is thought to occur via $MgPP(V)^{2-}$, occurs efficiently and is close to being diffusion controlled. Pyro-di-H-phosphonate on the other hand does not act as a substrate or as an inhibitor of pyrophosphatase.

2. Dichloromethane (DCM) is an alkylating agent for pyridine, producing methylene bis-pyridinium dication (MDP) upon refluxing the solution. The kinetics and mechanism of hydrolysis of methylene bis-pyridinium dication have been studied. Below pH 7 MDP is extremely stable and hydrolysis is first-order in hydroxide-ion. Above pH 9 an unusual intermediate is formed on hydrolysis which has a chromophore at 366 nm in water and its formation is second-order in hydroxide-ion. The carbon acidity of the central methylene group was also investigated kinetically using H/D exchange and the pK_a was surprisingly high at 21.2 at 25^oC (I = 1.0 M).

3. Isothermal titration calorimetry (ITC) is a technique mainly used by biochemists to obtain a range of physical and thermodynamic properties of a reaction. Analysing the data can become difficult when investigating complex reactions involving more than one step, for instance metal-ions binding to an enzyme. In this work models have been developed to simulate sequential reactions. These were used to simulate experimental ITC data for metal-ions: Zn^{2+}, Co^{2+} and Cd^{2+} complexing to the active sites of BcII, a metallo β-lactamase responsible for antibiotic resistance, providing additional information on the mechanism by which this enzyme acts to deactivate β-lactam antibiotics. The simulations suggest that BcII has two very similar binding affinities to metal-ions which are filled sequentially.

Acknowledgements

First and foremost I would like to thank my supervisors, Professor Michael I Page and Professor David R Brown. It has been an honour to be your student and I appreciate the time and effort you have taken to supervise and encourage me through this research, it has been of enormous value.

I thank Innovative Physical Organic Solutions (IPOS), for providing the funding for this research and having available top of the range analytical equipment. All the members of IPOS have contributed to my personal and professional time as part of the group. I am especially grateful for the experimental and theoretical help given by Dr Nicholas T Powles and Dr Matthew J Stirling. I also thank the members of the research group especially Professor John H Atherton, Dr Haifeng Sun, Victoria L Sutcliffe and Joseph M Griffin for their useful conversations.

To the members of my research office, past and present, they know who they are. Thank you for always being there, you have made this truly unforgettable.

I thank Professor Robert A Cryan (VC) for taking the time and effort out of his busy schedule to help with the mathematics and solutions to the isothermal titration calorimetry modelling equations.

I would also like to thank Professor Christian Damblon (university of Liege, Belgium) for providing the plasmid containing the gene for the β-lactamase strain we used in this work.

I also thank Dr Neil McLay for his work and help with the NMR.

Table of contents

Abbreviations

A	Adenine
ADP	Adenosine diphosphate
ala	Alanine
AMP	Adenosine monophosphate
Arg	Arginine
Asn	Asparagine
Asp	Aspartate
atm	Atmospheres
ATP	Adenosine triphosphate
β_{lg}	Brønsted leaving group
C or cys	Cytosine
CA	Carbonic anhydrase
cAMP	Cyclic adenosoine monophosphate
CAPS	N-cyclohexyl-3-aminopropanesulfonic acid
CPC	Cetylpyridinium chloride
D_2O	Deuterium oxide
Da	Daltons
DCM	Dichloromethane/methylene chloride
DEPT-135	Distortionless Enhancement by Polarization Transfer 135^o
DMAP	Dimethyl amino pyridine
DMD	Duchenne muscular dystrophy

DMF	Dimethylformamide
DMSO	Dimethylsulfoxide
DNA	Deoxyribonucleic acid
E.coli	*Escherichia coli*
ESI	Electron spray ionisation
FID	Flame ionization detection
G	Guanine
ΔG^o	Standard Gibbs free energy
G-6-Pase	Glucose-6-phosphtase
GC	Gas chromatography
GC-MS	Gas chromatography Mass-spectrometry
Gln	Glutamine
ΔH	Enthalpy
ΔH_{obs}	Observed enthalpy
HCl	Hydrochloric acid
HEPES	4-(2-hydroxyethyl)-1-piperazineethanesulfonic acid
His	Histidine
HSQC	Heteronuclear single quantum coherence
Hz	Hertz
I	Ionic strength
IP	Inositol phosphate
ITC	Isothermal titration calorimetry
J	Joules

K	Kelvin
K_b	Binding constant
k_{cat}	First order rate constant for the breakdown of ES
KCl	Potassium chloride
K_d	Dissociation constant
KIE	kinetic isotope effect
K_m	The Michaelis constant (the substrate concentration at which the reaction rate is half of V_{max})
λ_{max}	Lamda max
Leu	Leucine
m/z	Mass/charge
MBL	Metallo beta-lactamase
MDP	1,1-bispyridinium dication
MHz	Mega Hertz
MOPS	3-(N-morpholino)propanesulfonic acid
MS-QQQ	Triple quadrupole mass spectrometer
NAG	N-acetylglucosamine
NAM	N-acetylmuramic acid
NMR	Nuclear magnetic resonance
NOE	Nuclear Overhauser effect
^{o}C	Degrees Celsius
Pa	Pascals
PCr	Creatine phosphate

pD	Negative logarithm of deuterium ion concentration
phe	Phenylalanine
pK_a	Negative logarithm of acid dissociation constant
pm	Picometers
pNPP	p-nitrophenol phosphate
PP(III)	Pyro-di-H-phosphonate
PP(III.V)	Isohypophosphate
PP(V)	Pyrophosphate
PPase	Pyrophosphatase
ppm	Parts per million
PPM	Phosphoprotein phosphatase M
PPP	Phosphoprotein phosphatase P
psi	Pressure per square inch
PTP	Protein tyrosine phosphatases
Q	Heat
RNA	Ribonucleic acid
S_N(ANRORC)	Addition of nucleophile, ring opening and ring closure
S_N1	Nucleophilic Substitution 1
S_N2	Nucleophilic Substitution 2
SNAr-AE	Nucleophilic aromatic substitution addition-elimination
SNAr-EA	Nucleophilic aromatic substitution elimination-addition
T	Thymine
TSP	Sodium trimethylsilylpropionate

UV-Vis	Ultra violet and visible
V_{max}	Maximal rate of the enzyme catalysed reaction
ZPE	Zero-point energy

Chapter 1 – PHOSPHATES AND H-PHOSPHONATES

1 Introduction

Biological phosphate esters have many roles and underpin most life processes such as the storage and manifestation of genetic information, energy transduction, signalling, regulation, differentiation, compartmentalisation, substrate modification to facilitate chemical reactions and as structural components[1]. These properties are the major reason why phosphates and their derivatives are studied.

1.1 Background

1.1.1 Phosphate esters within DNA

Deoxyribonucleic acid, DNA is present in all life forms, animal and plant. It is the template for the production of proteins via ribonucleic acid (RNA). Genetic information is encoded as a sequence of nucleotides, which contain one of four bases that are derivatives of pyrimidine, thymine (T) and cytosine (C) or purines, adenine (A) and guanine (G). One of these bases is attached to a sugar, either ribose or deoxyribose which also contains phosphate groups (Scheme 1.1)[2].

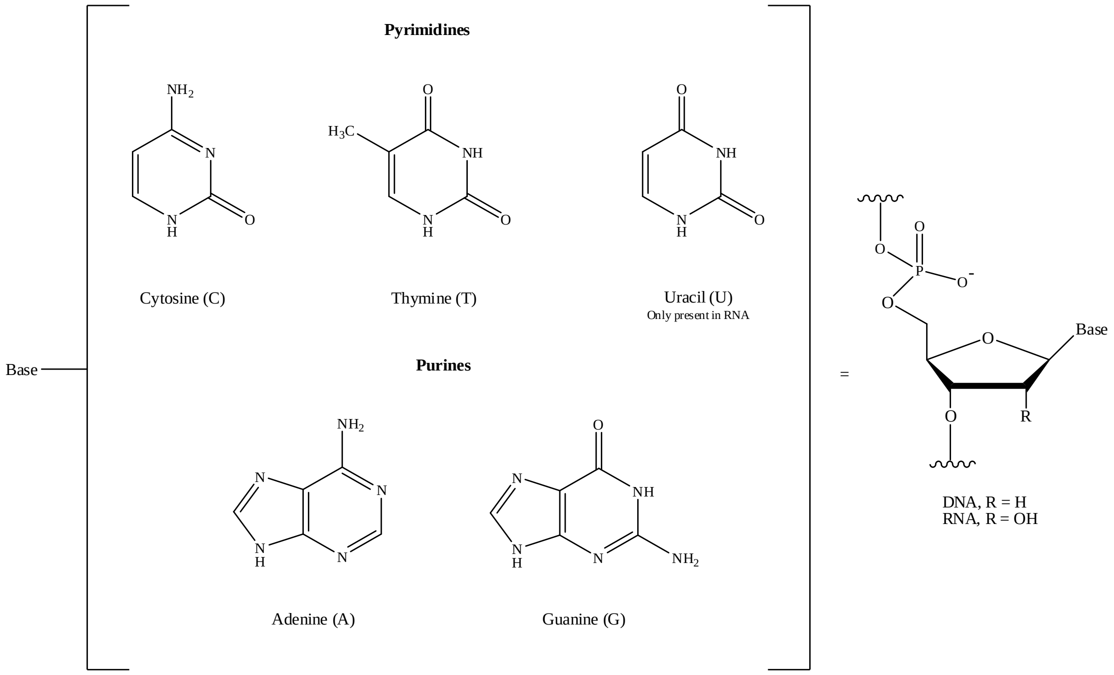

Scheme 1.1 Base, sugar and phosphate group to form a nucleotide which composes DNA and RNA.

The nucleotides are joined by a 3'-5' phosphodiester bond which provides the extremely stable sugar-phosphate backbone of DNA[2]. The phosphate ester backbone has an estimated half-life of 31 million years for its spontaneous water hydrolysis[1] yet RNA which contains a hydroxyl group at position 2 of the ribose unit is significantly less, due to transesterification and hydrolysis which cleaves the phosphate di-ester backbone (Scheme 1.2) i.e. 2'-OH attacks the 3'-P-O bond[3].

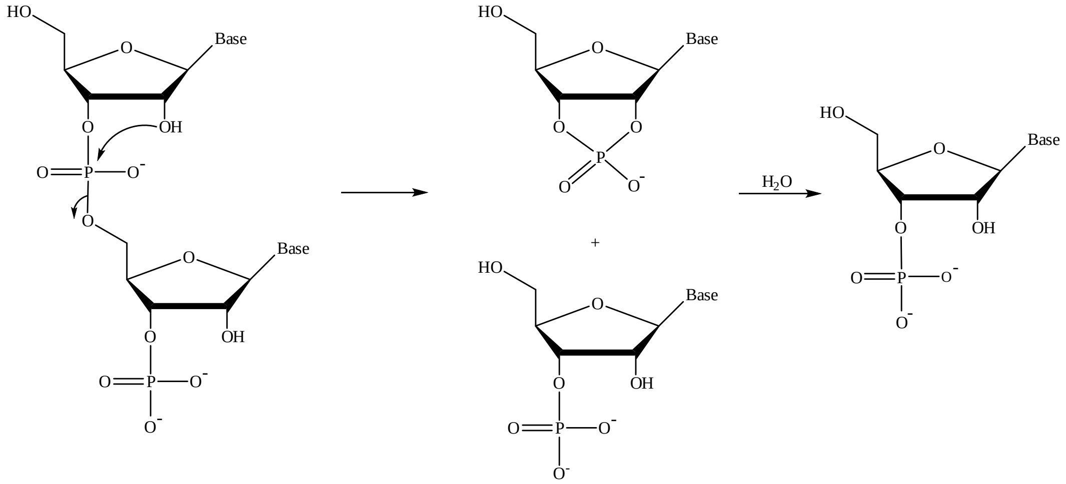

Scheme 1.2 Transesterification of RNA[4].

DNA is a double stranded helix which is stabilised by the opposing strand by hydrogen bond and other intermolecular interactions. In 1953 Watson and Crick proposed the structure for DNA which consisted of two complementary strands which run anti-parallel to each other. Adenine pairs with thymine and guanine pairs with cytosine whereas in RNA, uracil binds to adenine and is usually single stranded[2]. In addition to providing a stable backbone to DNA the phosphate groups provide an area for solvation as the hydrophobic base pairs are contained within the centre of the helix.

Nucleosides (base + sugar) adenosine, thymidine, cytidine and uridine are phosphorylated at the 5'-position of the ribose sugar unit by their respective kinase and additional phosphates can be added to form nucleoside diphosphates and triphosphates such as adenosine triphosphate (ATP)[5].

1.1.2 Phosphorylating agents

Phosphorylation involves the addition of a phosphate group generally to a protein and occurs in many key processes such as signalling and regulation of proteins. In living organisms, phosphorylation is catalysed by enzymes such as kinases and dephosporylation by phosphatases both of which are used widely for the generation, distribution and application of free energy by the manipulation of phosphoric acid anhydrides and its esters. The most common phosphorylating agent is adenosine triphosphate (ATP) (Scheme 1.3) which is the major energy currency in living systems[6].

ATP is an adenine base which is attached to a D-ribose sugar via a N-glycosidic bond, to which phosphate groups are attached at the 5'-position via ester linkages[7]. There are three phosphate groups present in ATP and the closest phosphorus to the ribose ring is referred to as alpha (α), the next beta (β) and finally gamma (γ).

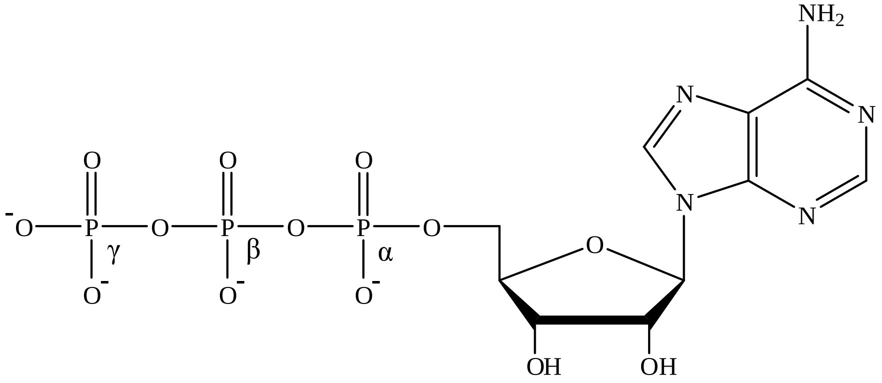

Scheme 1.3 Adenosine triphosphate (ATP)[4].

Phosphate group transfers are also involved in oligonucleotide synthesis which is a useful technique for DNA sequencing and anti-sense therapies to treat diseases such as Alzheimer's, cancer and duchenne muscular dystrophy (DMD). The method for solid-state oligonucleotide synthesis involves a solid support resin and the 3'-hydroxyl group of the first nucleoside base is directly bound to an insoluble support such as silica, glass beads or a polystyrene derivative resin via a succinyl link.

Generally the substrate alcohol (5'-OH) displaces a good leaving group such as chloride, triazolate or diallylphosphate. One method of phosphorylation but not used that often anymore, involves direct reaction with phosphoryl chloride in the presence of a base (Scheme 1.4)[8].

$$\mathrm{ROH + POCl_3 \xrightarrow{-HCl} PO(OR)Cl_2}$$

Scheme 1.4 Alcohol reacting with phosphoryl chloride to produce a phosphate mono-ester[9].

There are several examples of phosphorylating agents such as anhydrides, mono- and di-esters. Tetra-esters of pyrophosphoric acid, mixed anhydrides or a di-ester e.g. phosphorochloridic acid can be used as phosphorylating agents in the presence of a base[10].

Compounds which contain –N=CR-O-P(O)(OR)$_2$ such as imidoyl phosphate (Scheme 1.5) can also be used as phosphorylating agents, once protonated, yield pyrophosphate esters.

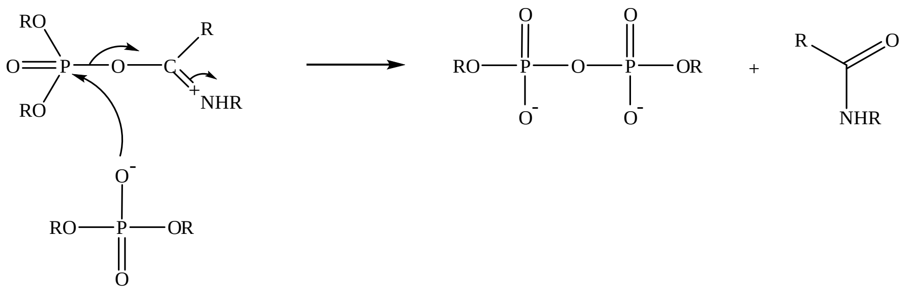

Scheme 1.5 Imidoyl phosphate reacting with a phosphate di-ester to produce a pyrophosphate di-ester[10].

Quinol mono- and di-phosphates which are possible phosphorylating agents are relatively resistant to alkaline hydrolysis in the absence of air, but introduction of an oxidising agent such as bromine in aqueous solution precipitates quinone (Scheme 1.6) and produces the reactive metaphosphate as an intermediate phosphorylating agent[11].

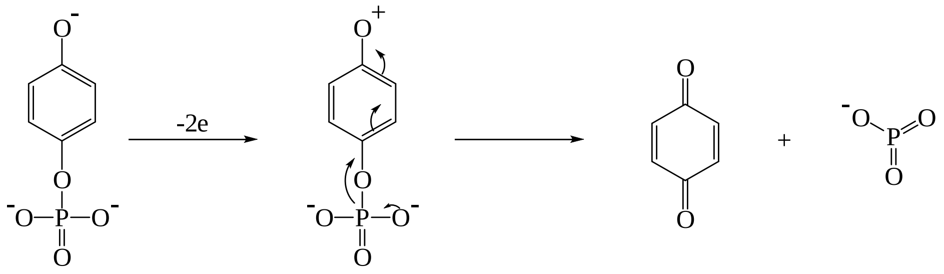

Scheme 1.6 Quinol monophosphate oxidised to produce quinone and metaphosphate[11].

Mono-esters of phosphoramidic acids are possible phosphorylating agents when the nitrogen is protonated it becomes a very good phosphorylating agent for anions (Scheme 1.7)[12].

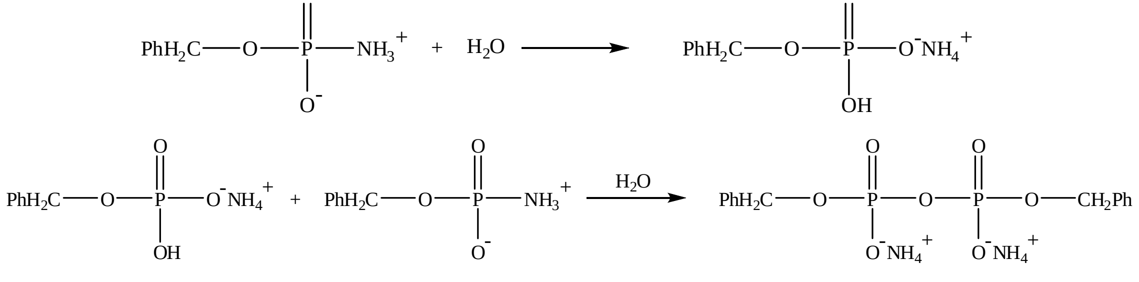

Scheme 1.7 Pyrophosphate di-ester formed from mono-ester phosphoaramidic acids[13].

1.1.3 H-phosphonates

H-phosphonates and their derivatives have many applications in a wide variety of areas such as agriculture, medicine and the pharmaceutical industry. The agricultural industry is the largest consumer of H-phosphonates which uses them as fungicides, herbicides and plant growth regulators[14].

H-phosphonate chemistry involves the parent molecule, phosphorous acid which is also referred to as phosphonic acid (H_3PO_3). Phosphorous acid has two pK_as of 1.07 and 6.58 and is slightly more acidic than phosphoric acid which has pK_as of 2.12, 7.21 and 12.32[15]. There are two tautomeric forms of phosphorous acid and its derivatives in solution, the tetra-coordinated H-phosphonate or the tri-coordinated phosphite which both bear the phosphorus atom in the +3 oxidation state (Scheme 1.8)[16].

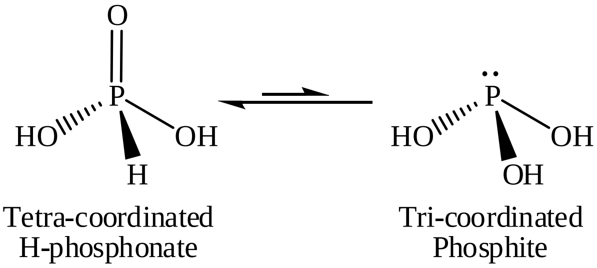

Scheme 1.8 Equilibrium between the tetra-coordinated and tri-coordinated phosphorous species[16].

It has now accepted that H-phosphonates exist predominantly as the tetra-coordinated species and not the tri-coordinated species which was initially believed[16].

Using $^{31}P\{H\}$ NMR as an analytical technique, di-esters of H-phosphonates usually show signals in the region of 0-15 ppm[14] and some phosphorous compounds such as di-esters of pyro-H-phosphonates have negative chemical shift usually between 0 and -10 ppm, characteristic of the tetra-coordinated phosphorus atom[17]. It has been suggested that the tetra-coordinate phosphorous species undergoes tautomerisation as shown in Scheme 1.8 yet there is no evidence within the NMR spectrum that the tri-coordinated species exists (signals usually in the 130 ppm region)[14].

1.1.4 P-H Exchange

Phosphorous acid contains three hydrogens, two oxygen bonded and one directly bonded to phosphorus. The two oxygen bound hydrogens exchange rapidly in D_2O. On the other hand, data supporting the deuterium exchange of the hydrogen directly bonded to the phosphorus for deuterium is inconclusive[18]. The acid catalysed P-H exchange with deuterium and oxidation under acidic conditions with iodine were studied for di-methyl, di-ethyl and di-n-propyl-H-phosphonate[19]. Proton NMR was used to determine the kinetics of P-H/P-D exchange which followed first-order kinetics with respect to H-phosphonate for both exchange and oxidation. The acid catalysed (k_H) and acid-independent rate constants (k_w) for exchange are provided in Table 1.1 for the different H-phosphonates.

Compound	**Exchange**		**Oxidation**	
	k_H / $M^{-1}s^{-1}$	k_w / s^{-1}	k_H / $M^{-1}s^{-1}$	k_w / s^{-1}
Dimethyl H-phosphonate	1.1×10^{-3}	1.3×10^{-4}	5.3×10^{-4}	2.3×10^{-5}
Diethyl H-phosphonate	1.0×10^{-3}	3.3×10^{-5}	4.2×10^{-4}	6.7×10^{-6}
Di-n-propyl H-phosphonate	9.7×10^{-4}	1.2×10^{-4}	4.2×10^{-4}	3.3×10^{-6}

Table 1.1 Rate constants for the deuterium exchange and oxidation of H-phosphonate[19].

The oxidation rate of di-alkyl H-phosphonates with iodine was independent of iodine concentration above a certain ratio of iodine to di-alkyl H-phosphonate. Under acidic conditions the rate law for oxidation (Equation 1.1) was the same as that for the exchange rate for deuterium indicating the rate-determining step is the same for both reactions.

$$\text{Rate of exchange/oxidation} = k_H [H^+] [\text{H-phosphonate}] + k_w [\text{H-phosphonate}]$$

Equation 1.1

The proposed scheme for the acid catalysed exchange and oxidation involves initial protonation of the phosphoryl group followed by formation of a phosphite (tri-coordinated, possessing a lone pair on the phosphorus atom) which is believed to be very reactive. The tri-coordinated phosphite under excess oxidising agent, is oxidised to the phosphate or in the absence of oxidising agent reverts to the D-phosphonate accepting a proton via a suitable donor (Scheme 1.9)[20].

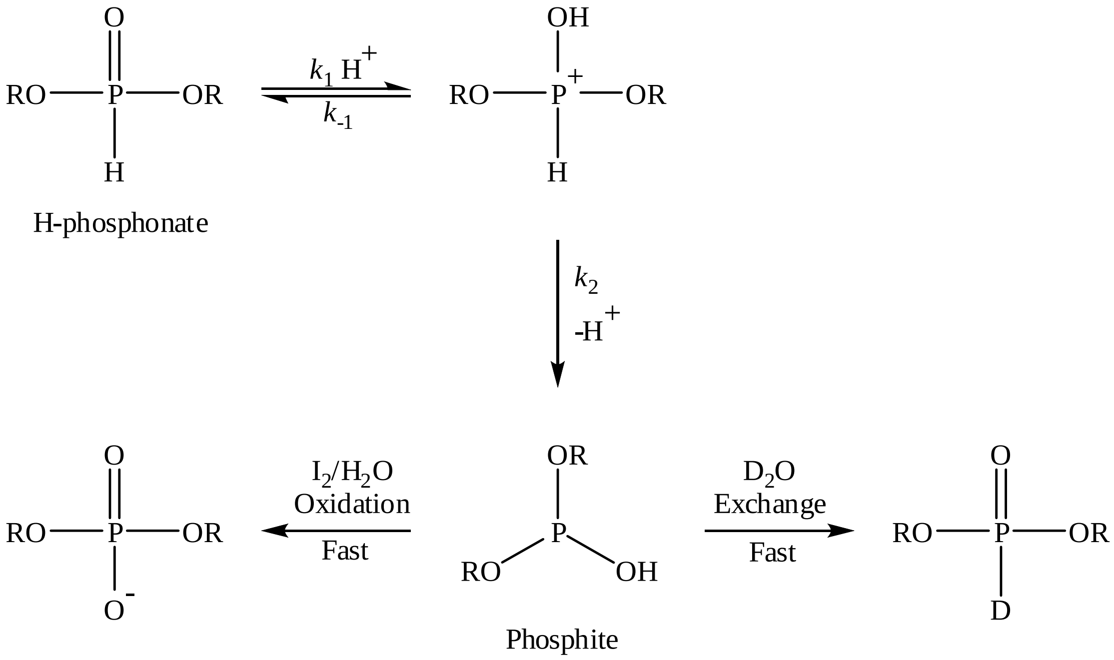

Scheme 1.9 Mechanism of deuterium exchange or oxidation of the directly bound hydrogen of H-phosphonate[20].

Oxidation of H-phosphonates by halogens such as iodine are subject to base catalysis which also produces the phosphite as a reactive intermediate. Increasing the basicity of the base increases the kinetic isotope effect as shown in Table 1.2[21].

Base	pK$_a$	k_H/k_D
CH_3COO^-	4.8	1.01
HPO_4^{2-}	7.2	1.65
NH_3	9.6	1.84
CO_3^{2-}	10.3	2.76

Table 1.2 Kinetic isotope effects for the base catalysed oxidation of diethyl H-phosphonate by iodine[21].

The expected primary kinetic isotope effect for breaking the P-H bond in the rate-limiting step is approximately 5.6 which may be obtained by having a base with a pK$_a$ equal or greater than diethyl-H-phosphonate of 14.6[21, 22]. The presence of a significant kinetic isotope effect by the different buffer bases indicates the rate-determining step is the removal of the P-H proton.

The mechanism associated with the observations must involve slow deprotonation of the P-H bond to produce the phosphite, which would then produce D-phosphonate or phosphate di-ester (Scheme 1.10)[23].

The rate law associated with the base catalysed deuterium exchange and oxidation is equal to the rate of formation of the phosphite where the acid independent rate can be regarded as negligible and therefore rate becomes:

$$\text{Rate of formation of phosphite} = k_1\,[\text{H-phosphonate}]\,[\text{Base}]$$

Equation 1.2

Westheimer observed that a small proportion of diethyl H-phosphonate existed as the tri-coordinated phosphite in alkaline solutions (Scheme 1.10)[22].

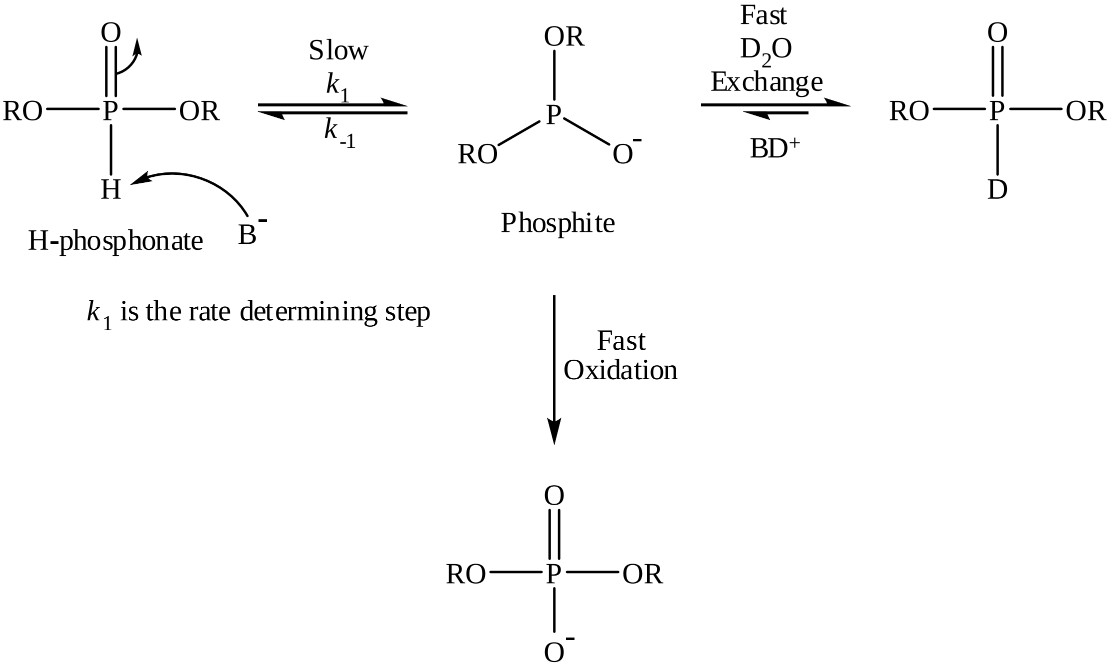

Scheme 1.10 Mechanism of oxidation and P-H/D exchange of dialkyl H-phosphonate by base[23].

1.1.5 pK_a of phosphorus acids

Phosphorus compounds, containing P-OH groups, are capable of losing protons in an aqueous environment. Many phosphorus derivatives used within living systems have at least one pK_a, the most common of which is phosphoric acid which has three dissociable protons with pK_{a1} = 2.12, pK_{a2} = 7.21 and pK_{a3} = 12.32[24] (Scheme 1.11). The two readily dissociable protons of phosphorous acid have pK_as of 1.07 and 6.58[24] (Scheme 1.12). The pK_a of the P-H in H-phosphonate di-anion has been estimated to be approximately 38[25]. Dependent on the pH of the solution the fraction of the various species changes as shown by the speciation plots for phosphoric acid and phosphorous acid (Figure 1.1 and Figure 1.2, respectively).

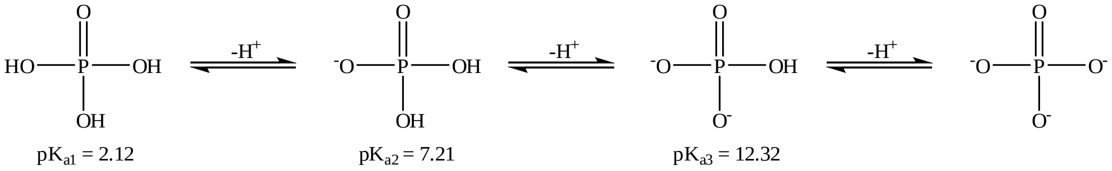

Scheme 1.11 Deprotonation of phosphoric acid.

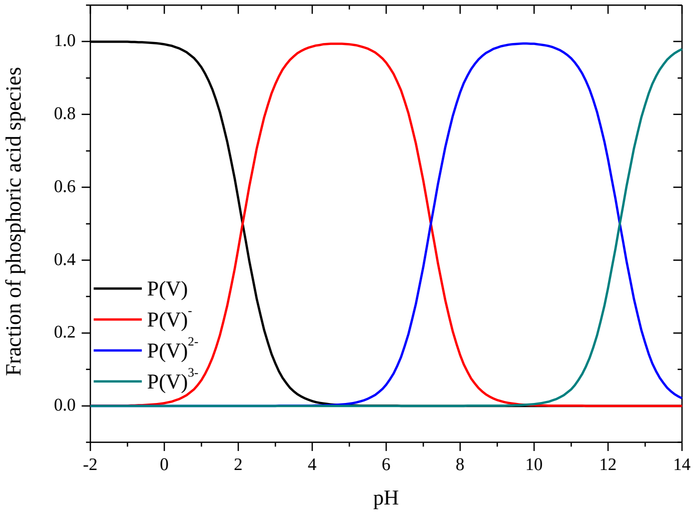

Figure 1.1 Speciation plot of the different anionic species (H_3PO_4 – PO_4^{3-}) of phosphoric acid as a function of pH.

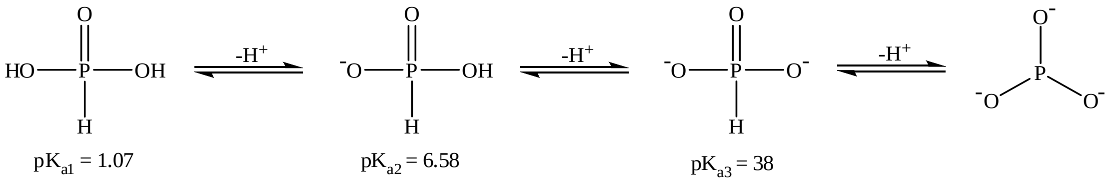

Scheme 1.12 Deprotonation of phosphorous acid.

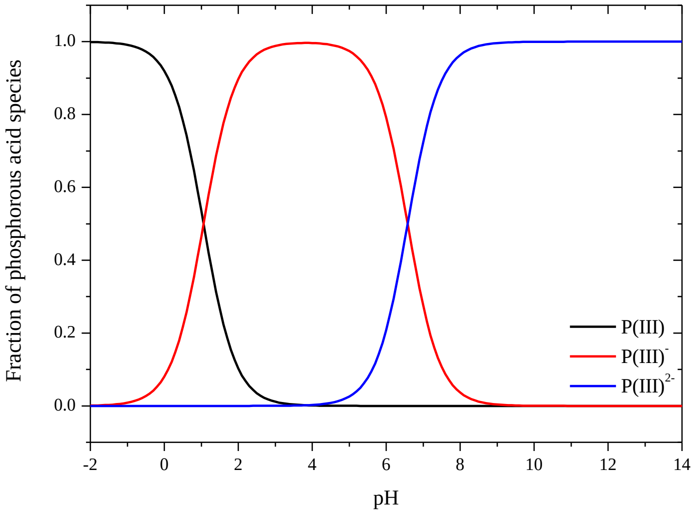

Figure 1.2 Speciation plot of the different species (H_3PO_3 – PO_3^{2-}) of phosphorous acid.

A summary of pK_a values of some phosphoric and phosphorous compounds are shown in Table 1.3.

Phosphates				
Acid	**pK_{a1}**	**pK_{a2}**	**pK_{a3}**	**pK_{a4}**
Phosphoric	2.12	7.21	12.32	
Methyl phosphate	1.54	6.31		
Ethyl phosphate	1.60	6.62		
Pyrophosphoric	0.9	2.0	6.6	9.4
H-phosphonates				
Phosphorous	1.07	6.58		
Ethyl H-Phosphonate	0.81			

Table 1.3 pK_a summary of phosphates and H-phosphonates at 25°C[24].

1.1.6 Mechanism of hydrolysis of phosphate esters

Phosphate ester formation and/or cleavage of the P-O bond are of crucial importance in biological systems, including phosphorylation, control of secondary messengers and protein regulation[26]. The rates of hydrolysis of phosphate esters are complicated by the overall charge on the compound which may be for example, neutral, mono-anionic, di-anionic etc[27, 28]. Phosphate esters may be cleaved by one of three mechanisms which have been extensively studied: associative, dissociative or concerted pathways.

1.1.6.1 Associative mechanism

The associative mechanism for the hydrolysis of phosphate esters involves an addition-elimination designated $A_N + D_N$. The first step involves the nucleophile attacking the phosphorus atom, to generate a penta-coordinate phosphorane intermediate, which expels the leaving group in the second step (Scheme 1.13)[29, 30].

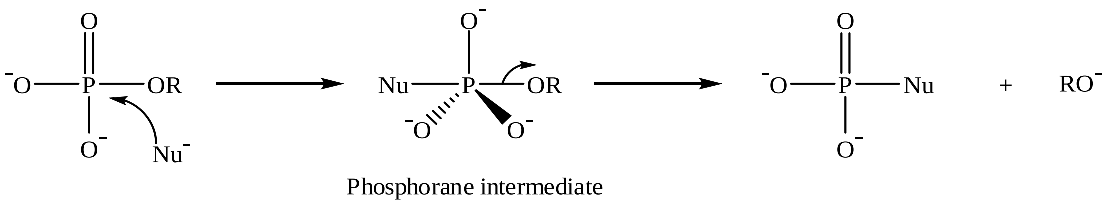

Scheme 1.13 $A_N + D_N$ mechanism which generates a penta-coordinate phosphorane intermediate[30].

1.1.6.2 Dissociative mechanism

The dissociative mechanism ($D_N + A_N$) is similar to a S_N1 mechanism where a planar metaphosphate intermediate is formed (PO_3^-) in the rate-limiting step usually for the hydrolysis of phosphate mono-esters[30]. The highly reactive intermediate is attacked at either side by the nucleophile to form the product (Scheme 1.14)[26, 29, 30].

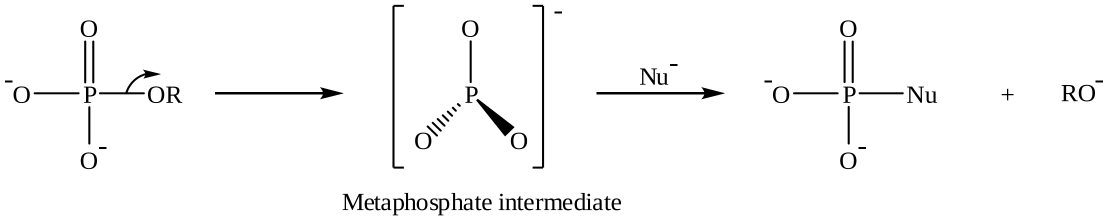

Scheme 1.14 $D_N + A_N$ mechanism which generates metaphosphate intermediate (PO_3^-)[30].

1.1.6.3 Concerted mechanism

The concerted mechanism (A_ND_N or $S_N2(P)$) can be thought of as a combination of the associative and dissociative mechanisms[31]. The A_ND_N mechanism involves nucleophile attack on the phosphorus centre and the leaving group departs in a single step without the formation of an intermediate (Scheme 1.15)[26, 29, 30].

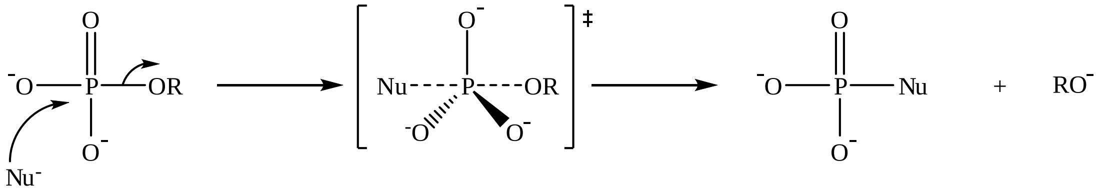

Scheme 1.15 A_ND_N mechanism which is involves concerted bond formation/dissociation[30].

The three mechanisms can be illustrated by a More-O'Ferrell-Jencks scheme (Scheme 1.16). The reactants are depicted in the lower left hand corner and the products in the upper right hand corner[29, 30]. The x-axis represents the extent of bond cleavage of the phosphorus leaving group bond and the y-axis represents the extent of bond formation by the incoming nucleophile.

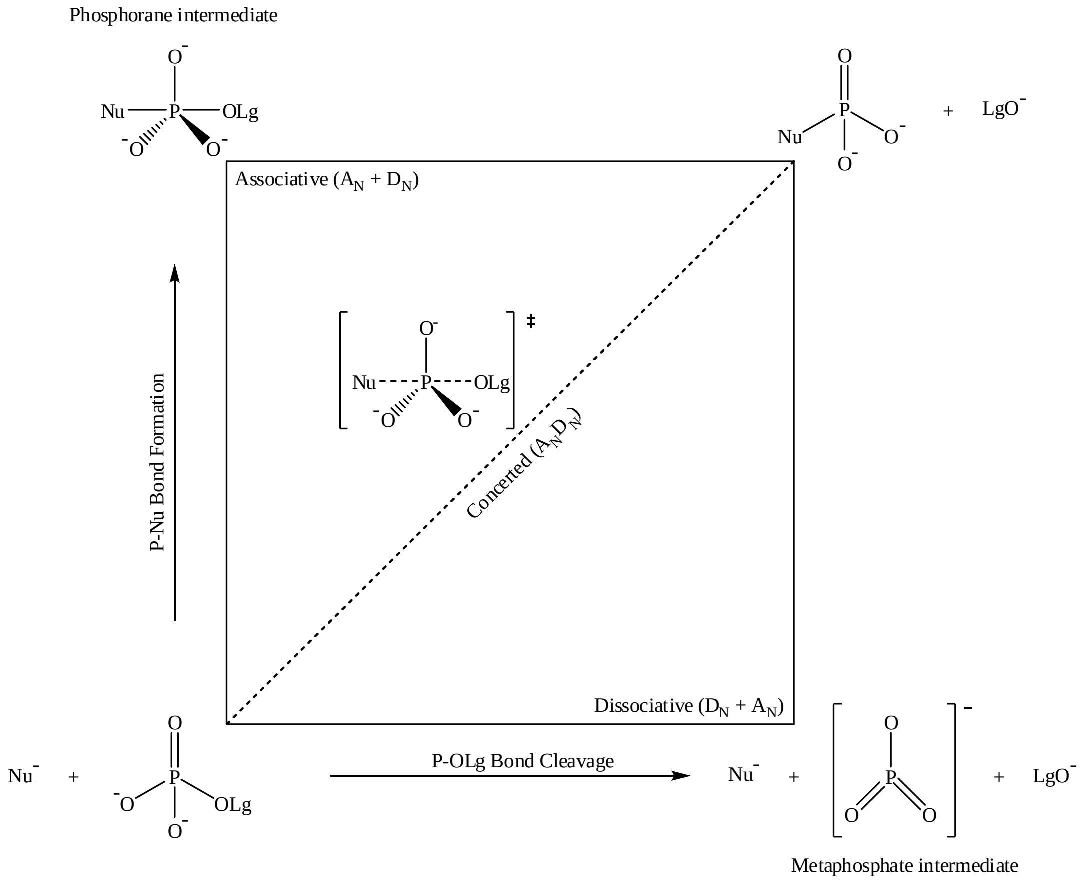

Scheme 1.16 More-O'Ferrell-Jencks plot showing the three different mechanisms involved in phosphate hydrolysis[29, 30].

1.1.7 The mechanisms of hydrolysis and reactivity of phosphate esters

1.1.7.1 Mono-ester Hydrolysis

Phosphate esters are of considerable interest as they are of great biological importance. Mono substituted phosphate esters are capable of losing two protons depending on the dissociation constant and pH; hydrolysis could involve the undissociated acid, mono-anion, di-anion or a mixture of species.

Generally phosphate mono-esters in strongly acidic media, one may expect the major reactive species to be the neutral acid. An acid catalysed hydrolysis may also be observed by the addition of a hydrogen-ion usually to the phosphoryl oxygen and may be more reactive than the neutral acid. At high pH, where the dominant species may be the di-anion and hydroxide-ion attack would be made less favourable due to electrostatic repulsion.

An example of a simple but well studied phosphate mono-ester is methyl phosphate. Hydrolysis of methyl phosphate in acid is very slow - at pH 0 at 100°C it shows an observed first-order rate constant (k_{obs}) = 5.09 x 10^{-6} s^{-1} which increases as the acid concentration increases suggesting an acid catalysed reaction of the neutral species[27, 32]. Using isotopically labelled water (^{18}O) in these acidic conditions shows both C-O and P-O bond fission occurs most likely through an associative mechanism[28]. If protonation of the methyl oxygen occurs and precedes via carbon-oxygen fission the mechanism may be formulated as in Scheme 1.17.

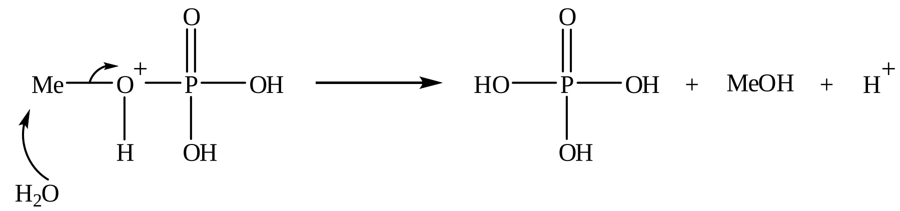

Scheme 1.17 Hydrolysis mechanism of methyl phosphate involving C-O bond cleavage to produce phosphoric acid and methanol[32].

The reaction involving phosphorus-oxygen bond fission involves by nucleophilic attack on the phosphorus atom (Scheme 1.18):

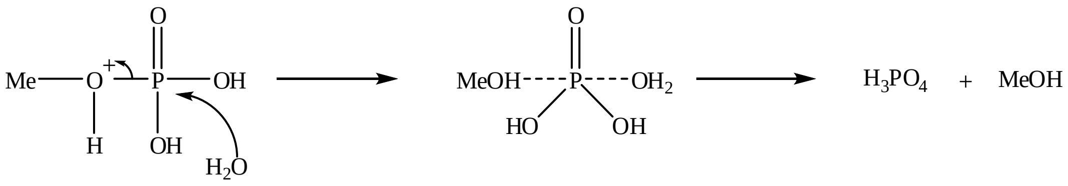

Scheme 1.18 Hydrolysis mechanism of methyl phosphate involving P-O bond cleavage to produce phosphoric acid and methanol[27, 32].

Another mechanistic interpretation of the acid catalysed hydrolysis of mono-methyl phosphate involves protonation of the phosphoryl oxygen shown in Scheme 1.19.

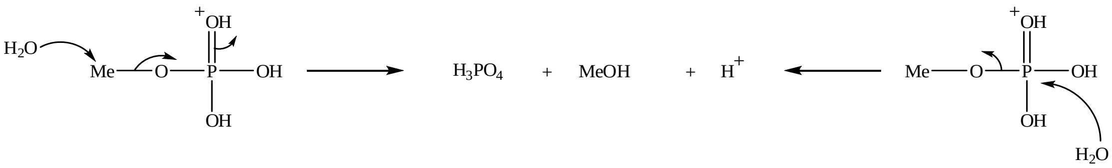

Scheme 1.19 Acid catalysed hydrolysis of methyl phosphate which involves C-O and P-O bond fission[27].

Increasing the pH changes the neutral methyl phosphate species to the mono-anionic species, at pH 1.54 where 50% exists as the mono-anion, but at pH 4, methyl phosphate exists wholly as the mono-anion[32]. The rate of hydrolysis of the mono-anion is unexpectedly fast and one may expect the undissociated acid to be the most reactive species (neutral, mono-anion, di-anion) in solution as additional negative charges would inhibit nucleophilic attack by water. A rate maximum is observed at pH 4.17 at 100°C for methyl phosphate mono-anion[32] (Figure 1.3) and of other simple mono-esters[33]. If the hydroxyl group transfers a proton to the leaving alkoxy group via a metaphosphate intermediate, an alcohol would be formed and dissociation would be a more favourable process than addition-elimination, associative mechanism[27].

Isotopically labelled ^{18}O showed that hydrolysis proceeds via P-O bond fission[32]. A Brønsted plot of log *k* for the mono-anion against pK_a for different leaving groups can indicate the charge distribution in the transition state. A plot for aryl and alkyl phosphates showed a linear response with a slope of -0.3 indicating little negative charge on the alkoxy or aryloxy group in the transition state. If there was a large amount of negative charge on the R-O residue in the transition state a greater slope would be observed and the rate of hydrolysis of the phosphate mono-anion would show a large dependence on the substituent[27].

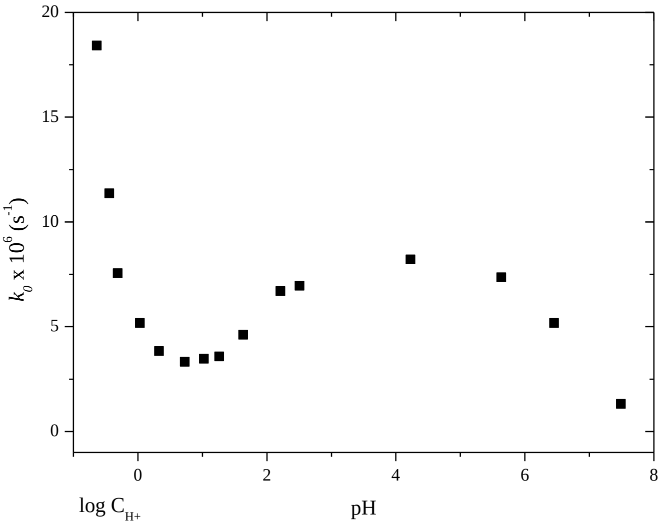

Figure 1.3 pH-rate profile of the hydrolysis of methyl phosphate at 100°C[27].

Two mechanisms have been proposed to account for the hydrolysis of the phosphate ester mono-anion. The proton may be directly transferred (Scheme 1.20) or by way of a six membered cyclic transition state, involving water (Scheme 1.21)[30, 32].

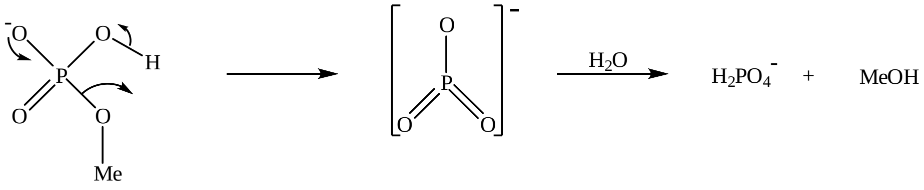

Scheme 1.20 Hydrolysis of methyl phosphate anion which involves proton transfer to generate the metaphosphate intermediate and methanol.

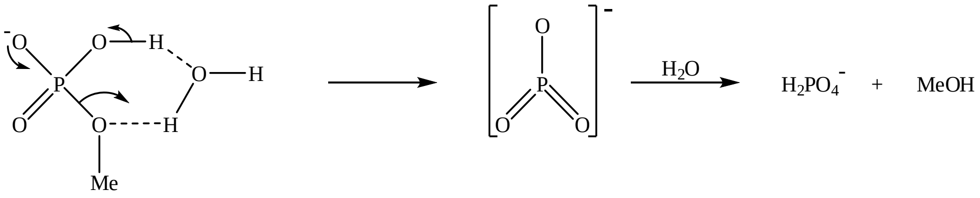

Scheme 1.21 Hydrolysis of methyl phosphate anion which involves a water molecule to generate the metaphosphate intermediate and methanol[30, 32].

As mentioned above the most reactive species of alkyl (CH_3 etc) and aryl (phenyl and p-nitro phenyl)[34] phosphates after the acid catalysed neutral species is the mono-anion which shows a rate maximum at pH 4 (Figure 1.3) and requires proton transfer to the leaving group and is essential for the reaction via a dissociative mechanism[35].

Methyl phosphate di-anion is only slowly hydrolysed at high pH, but if the leaving group contains a strongly electron withdrawing substituent, as in some acyl or nitrophenyl phosphates, the di-anion also be reactive and may be even more reactive than the mono-anion. Hydrolysis of the mono-anion of 2,4-dinitrophenyl phosphate is approximately 30 times slower than the di-anion at 25°C[35]. The phosphate ester di-anion is faster than the mono-anion when the pK_a of the conjugate acid of the leaving group phenol is less than 5; the hydrolysis of 2-chloro-4-nitrophenyl phosphate is almost pH independent (pK_a of phenol = 5.45) as both the mono- and di-anions hydrolyse at the same rate[33].

This high reactivity can be accounted by a dissociative mechanism giving a metaphosphate intermediate (Scheme 1.22) as the rate of hydrolysis of a series of mono-ester di-anions is very sensitive to the pK_a of the leaving group (Brønsted $\beta_{lg} = -1.23$)[33].

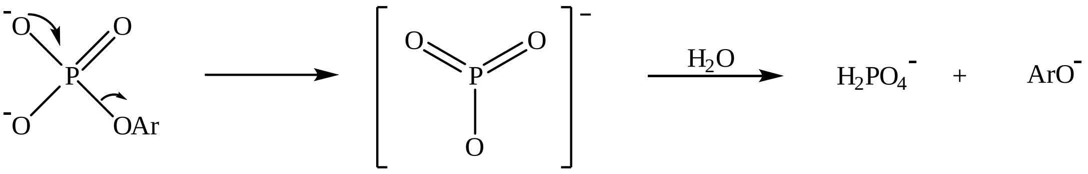

Scheme 1.22 Hydrolysis of an aryl phosphate ester di-anion to form a metaphosphate intermediate[33].

1.1.7.2 Di-ester hydrolysis

Phosphate di-esters are generally very stable towards hydrolysis. The hydrolysis of di-methyl phosphate as a function of pH is significantly different to that of mono-methyl phosphate. Mono-methyl phosphate shows a hydrolysis rate maximum at pH 4.17 where the major reactive species is the mono-anion but the reactivity of the di-methyl mono-anion is low at pH's where the mono-anion concentration also dominates. Decreasing the pH converts the mono-anionic species to the neutral species and in solutions which are not more acidic than pH 0 the only substrate involved in hydrolysis is the neutral species. Hydrolysis using isotopically labelled water (^{18}O) at pH 1.24 where the major reactive species is the neutral dimethyl phosphate as the substrate, the reaction proceeds mainly through C-O bond fission (78%) and a small amount via P-O bond fission in a concerted mechanism. Both processes are shown in Scheme 1.23.

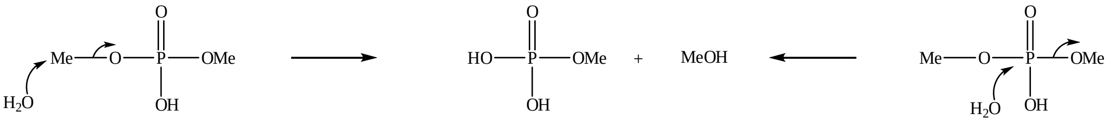

Scheme 1.23 Hydrolysis of undissociated di-methyl phosphate at low pH which involves C-O and P-O bond fission to form methyl phosphate and methanol[36].

The rate of hydrolysis of di-benzyl phosphate was investigated by Westheimer in 1954 who found that the di-ester anion at 75.6°C and an ionic strength of 1.0 M has a very slow hydrolysis rate constant = 4.17 x 10^{-8} s^{-1} and the neutral species = 3.17 x 10^{-5} s^{-1} [37].

The acid catalysed hydrolysis of di-methyl phosphate may involve protonation on either the phosphoryl oxygen or the methoxy oxygen with both C-O and P-O bond cleavage occurring by nucleophilic attack by a water molecule on the carbon or phosphorus atom of the conjugate acid[36] (Scheme 1.24).

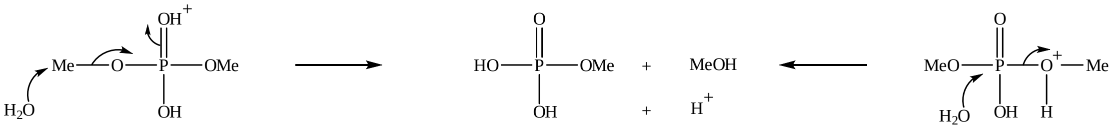

Scheme 1.24 Acid catalysed hydrolysis of di-methyl phosphate which involves C-O and P-O bond fission to form methyl phosphate and methanol[36].

Dialkyl phosphates are not readily hydrolysed under basic conditions. Westheimer *et al.* investigated the hydrolysis of di-methyl phosphate in strongly basic conditions at high temperature. The major mechanism of base-catalysed hydrolysis involved C-O bond fission compared to P-O bond fission as shown by using isotopically labelled solvent[38] (Scheme 1.25).

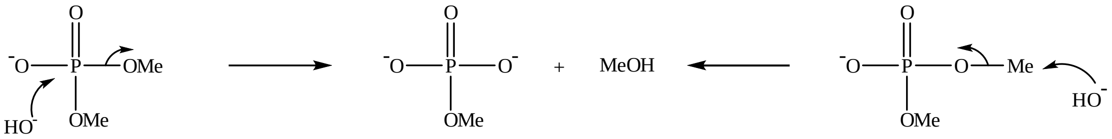

Scheme 1.25 Hydroxide-ion catalysed hydrolysis of di-methyl phosphate which involves both C-O and P-O bond cleavage[38].

Kirby in 1970 investigated the hydrolysis of a series of diaryl phosphate anions; for example diphenyl phosphate at 100°C at pH 10 remained unchanged after 5 hours and the half-life of bis-p-nitrophenyl phosphate at pH 3-4 and at 100°C is unchanged after more than 4 months. The hydrolysis of bis-2,4-dinitrophenyl phosphate, bis-4-nitrophenyl phosphate and bis-3-nitrophenyl phosphate was investigated over a wide pH range and it was found that between pH 2 and 6 the rate of hydrolysis of 2,4-dinitrophenyl phosphate is pH independent and at low and high pH there is an acid and base catalysed reaction of all three compounds[39].

A free-energy relationship plot between the first-order rate constants for a series of diaryl phosphate anions at 100°C and at 1.0 M ionic strength against the pK_a of the leaving group conjugate acid gives a slope of -0.97 which suggests that the leaving group carries significant negative charge in the transition state compatible with almost complete P-O bond fission from the pentacovalent intermediate[39] (Scheme 1.26).

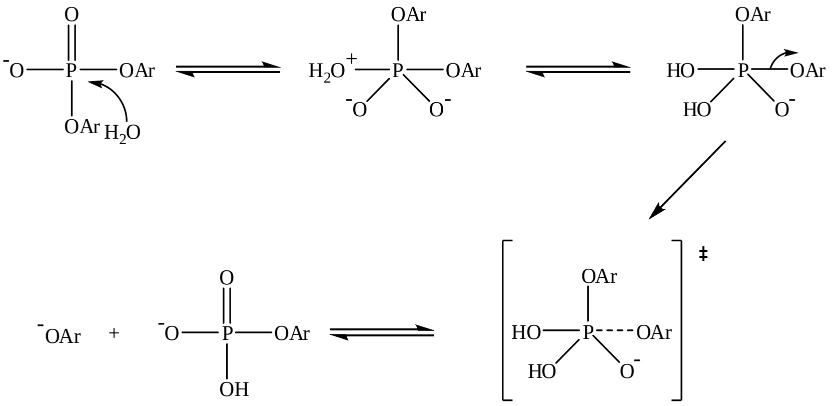

Scheme 1.26 The proposed mechanism of hydrolysis of di-aryl phosphate mono-anion[39].

Phosphate triesters are not naturally occurring substances and therefore not discussed in detail although, they are usually manufactured, for use as insecticides and were used as neurotoxins in World War II[40].

1.1.8 Hydrolysis of the P-O-P bond

Phosphate esters and condensed phosphates (phosphate anhydrides) which contain a P-O-P bond are also subject to hydrolysis. The pH of the solution greatly influences the hydrolytic rate of simple condensed phosphates such as pyrophosphate to give the corresponding phosphate.

The stability of the P-O-P bond of condensed phosphates at neutral pH and at room temperature is in the order of magnitude of years[41]. At higher temperatures e.g. 100°C pyrophosphate hydrolyses in water to give two mole equivalents of phosphoric acid (Scheme 1.27) is near completion within a few hours[42].

Many hydrolytic studies of pyrophosphate have been carried out but traditional analytical methods such as phosphate identification using molybdenum blue are not adequate to measure the stability and hydrolysis of pyrophosphate and polyphosphates [42-45].

$$H_4P_2O_7 \quad + \quad H_2O \longrightarrow 2\,H_3PO_4$$

Scheme 1.27 Hydrolysis of pyrophosphate which produces two moles of phosphoric acid.

Pyrophosphoric acid has four dissociable protons and the anionic state is sensitive to pH. In highly acidic (1-2 M HCl) conditions the majority of pyrophosphate exits as the undissociated form ($H_4P_2O_7$) but increasing the pH changes the species through four anionic states from $H_4P_2O_7$ to $P_2O_7^{4-}$ and in alkaline solutions pyrophosphate tetra-anion is very stable due to electrostatic repulsion of the hydroxide-ion.

Unsymmetrical pyrophosphate di-esters are difficult to isolate probably because they are very unstable and hydrolyse rapidly in water. The hydrolysis of P_1,P_1-diethyl pyrophosphate is pH dependent and above pH 6 diethyl pyrophosphate exists as the di-anion (Scheme 1.28, ii) and hydrolyses rapidly with a first-order rate constant = 1.15×10^{-3} s^{-1},whereas the mono-anion below pH 6 hydrolyses (Scheme 1.28, i) more slowly with a first-order rate constant = 3.0×10^{-5} s^{-1}[46]. The mechanism of hydrolysis resembles that of phosphate mono-esters where a metaphosphate intermediate is formed which is shown in Scheme 1.28.

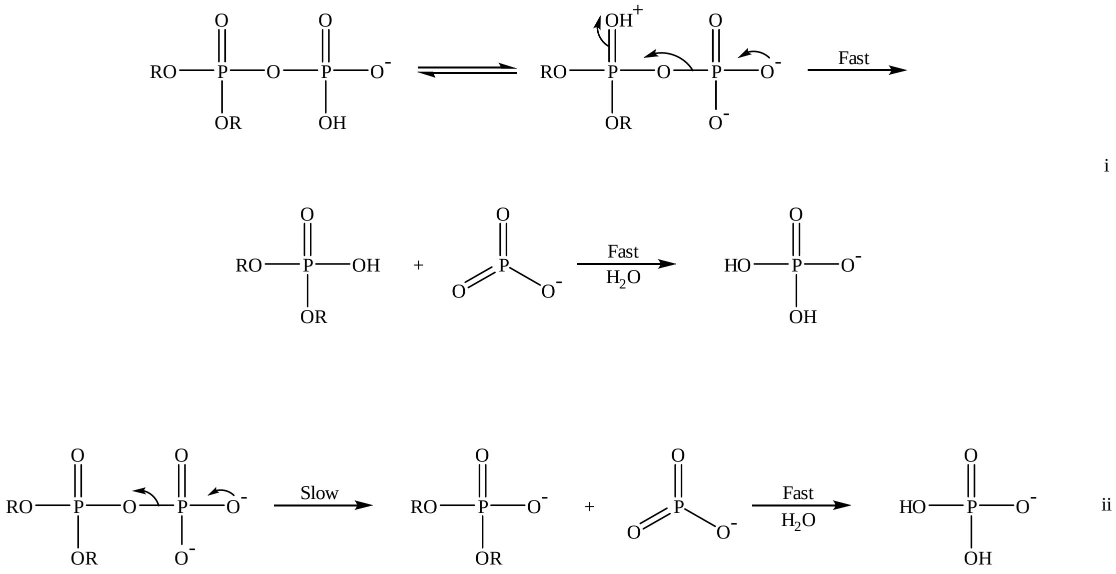

Scheme 1.28 Hydrolysis of an unsymmetrical pyrophosphate (P_1,P_1-diethyl pyrophosphate) mono-anion and di-anion via a metaphosphate intermediate[46].

It is interesting to note that the di-anion hydrolyses faster than the mono-anion, which is the opposite of what is observed for alkyl phosphates and pyrophosphate mono-esters. This rate reversal is dependent on the pK_a of the leaving group and a strong acid such as di-ethyl phosphate is a good leaving group[46].

1.1.9 Metal coordinated hydrolysis

Phosphates undergo a variety of reactions associated with proteins and metals. Metal-ions are assumed to increase hydrolysis by neutralising charge on the substrate, transition state or both[47]. Divalent metal-ions catalyse the hydrolysis of acyl phosphates, Briggs, Satchell and White studied the hydrolysis of acetyl phosphate catalysed by four divalent metal-ions Mg^{2+}, Ca^{2+}, Sr^{2+} and Ba^{2+} which had some catalytic effect on the rates of hydrolysis at pH 8.45, I = 0.6 M at 25^{o}C[48]. The rate of hydrolysis at the same pH, ionic strength and temperature without the divalent metal (k_0) was 1.1 x 10^{-5} s^{-1} but the addition of Mg^{2+}, Ca^{2+}, Sr^{2+} and Ba^{2+} provided second-order rate constants ($k_{metal}{}^{2+}$) = 9.6 x 10^{-4}, 7.3 x 10^{-4}, 2.4 x 10^{-4} and 7.0 x 10^{-5} M^{-1} s^{-1} respectively[48] and the intercepts show background hydrolysis without metal ions (Figure 1.4).

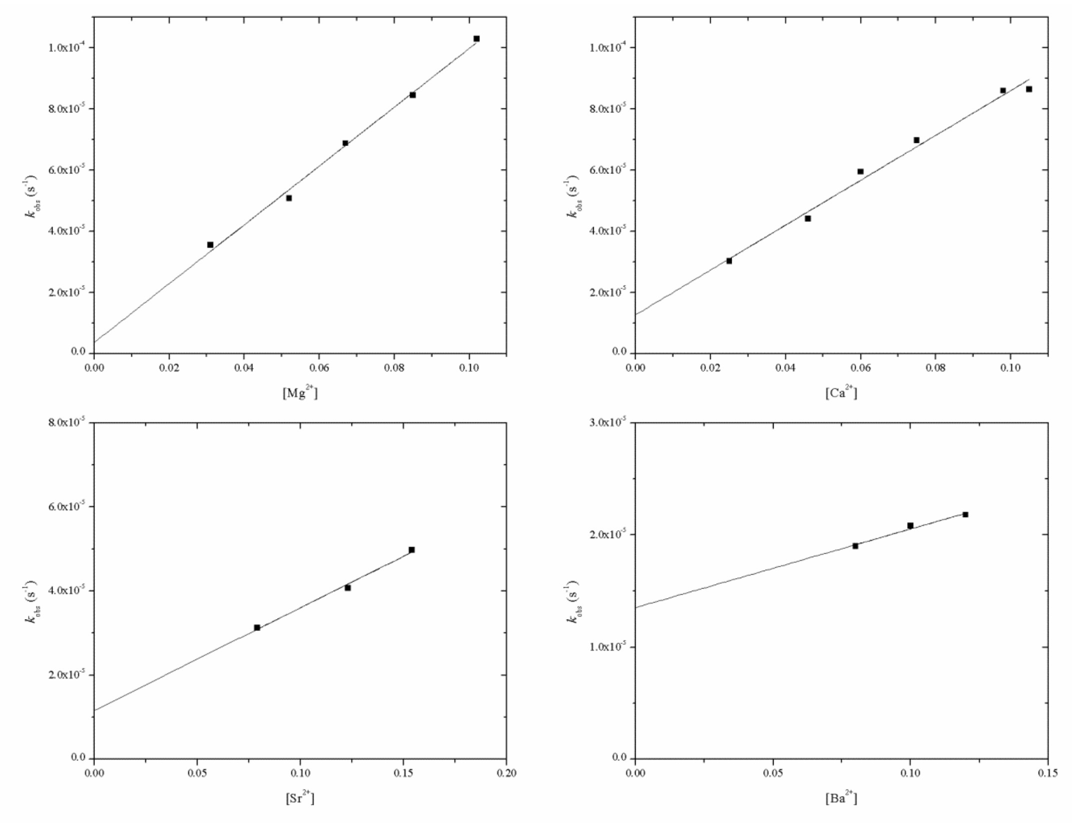

Figure 1.4 Plot of k_{obs} against metal concentration for Mg^{2+}, Ca^{2+}, Sr^{2+} and Br^{2+}, the solid line represent a linear fit to the data providing a second-order rate constant[48].

The pH independent hydrolysis of acetyl phosphate without metal-ions above pH 6 where the di-anion dominates involves P-O bond cleavage (via a dissociative mechanism) but at higher pH involves C-O bond fission as the hydroxide-ion preferentially attacks the carbonyl atom. In the presence of metal-ions such as Mg^{2+} the hydrolysis of acetyl phosphate is much more sensitive to pH and attack of water (Scheme 1.29, i) and hydroxide-ion (Scheme 1.29, ii) occurring via the cleavage of the C-O bond to form acetate and phosphate ions.

The metal-ion coordinates to the phosphate oxygens presumably convert it into a better leaving group[48].

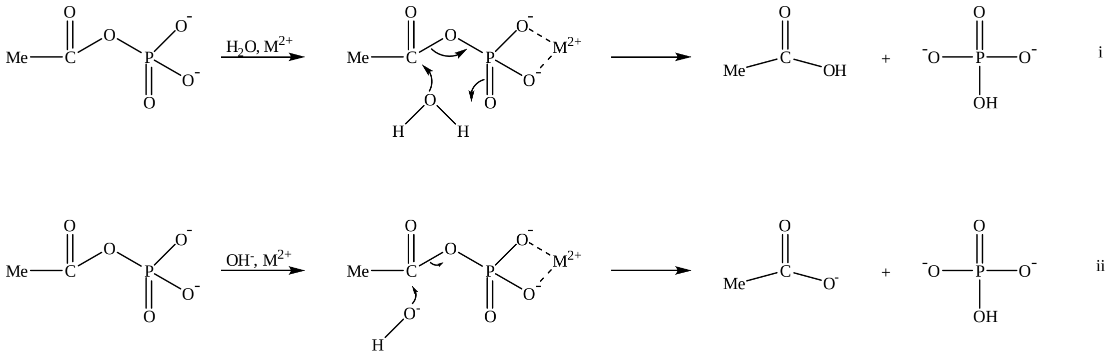

Scheme 1.29 Spontaneous hydrolysis of acetyl phosphate (i) and hydrolysis involving hydroxide-ion (ii) both aided by a metal di-cation[48].

Another example of metal-ions promoting hydrolysis of phosphates is when phosphate esters (Scheme 1.30) which are bound to di-nuclear metal complexes such as Co(III) which may be similar in structure to some enzyme catalytic sites[49, 50].

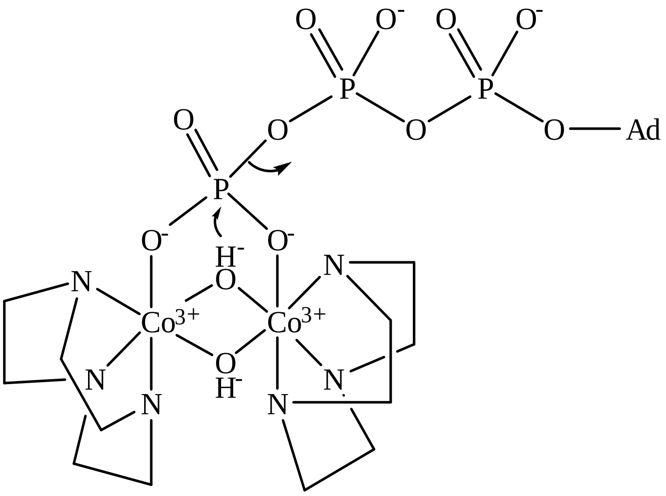

Scheme 1.30 A cobalt bi-nuclear complex providing charge neutralisation of the phosphate oxygens and an internal nucleophile[50].

In aqueous solution, hydrolysis occurs by cleaving the P-O bond forming ADP and a phosphate bridging the two Co(III) centres[50]. A specific base catalysed reaction was observed in basic solution with a second-order rate constant = 0.027 $M^{-1}\ s^{-1}$ at 25°C and at 1.0 M ionic strength (KCl). Using ^{31}P NMR, a solution of the phosphate bound complex (Scheme 1.30) at pH 8 and at ambient temperature remained unchanged for a month[50].

Between pH 8.1 and 10 and maintaining the ionic strength at 1.0 M, magnesium complexes to the ATP moiety (Scheme 1.31) which increases the hydroxide catalysed hydrolysis giving a second-order rate constant = 80 M^{-1} s^{-1} which is 3 x 10^3 times faster than the magnesium uncomplexed hydrolysis.[50]

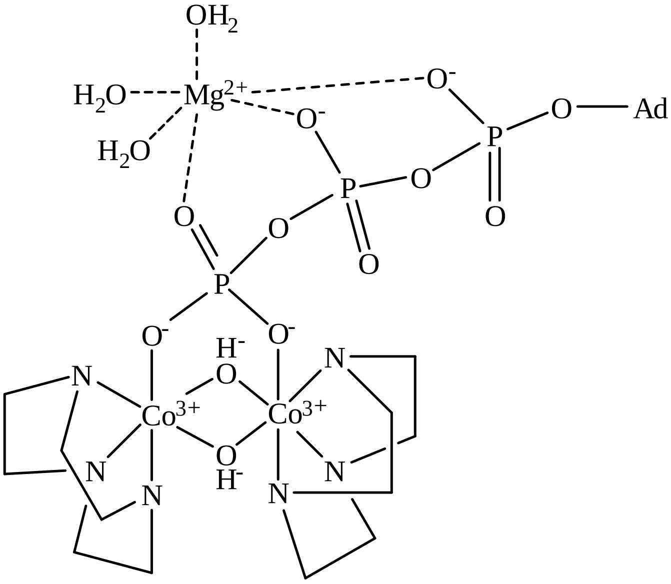

Scheme 1.31 The binuclear complex of ATP coordinated to a magnesium-ion which promotes hydrolysis via an associative mechanism[50].

The mechanism for biological phosphoryl transfer involving metal-ion cofactors are usually based on the metal-ions being able to stabilise the transition state. However ATP hydrolysis involves a dissociative mechanism where the bond to the ADP leaving group is broken before the attacking water molecule and interaction of the magnesium would have a larger catalytic effect if it interacted with the leaving group of the α and β phosphates and not the β and γ phosphates as observed (although in Scheme 1.31 it is shown that the magnesium-ion is interacting with the α-phosphate too)[50].

The coordination of magnesium to ATP does not affect the mechanism of hydrolysis as a β_{lg} of -1.1 indicates a large negative charge has developed in the transition state and therefore the P-O bond is largely broken. It was initially proposed that the coordination of magnesium may change the hydrolysis mechanism from dissociative to associative[51].

There have been several proposals to explain the role of metal-ions in aiding hydrolysis:

The first emphasises the formation of a cyclic intermediate by the metal-ion and the phosphate di-anion which presumably neutralises some of the negative charge which may facilitate nucleophilic attack on phosphorus[52] (Scheme 1.32).

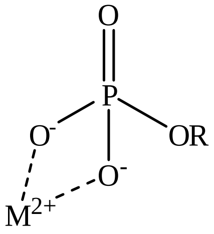

Scheme 1.32 Metal-ion coordinating to a phosphate mono-ester di-anion which may aid hydrolysis by ring strain or charge neutralisation.

The second is making phosphate a better leaving group[52] (Scheme 1.33).

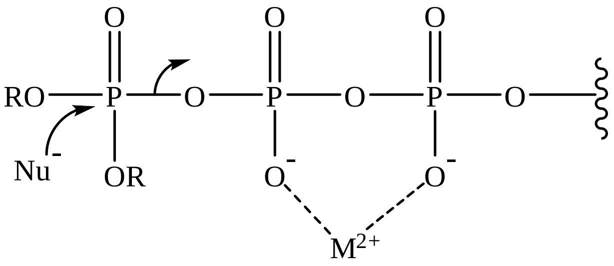

Scheme 1.33 Metal-ion neutralising negative charges on phosphate which makes it a better leaving group.

1.1.10 Enzymatic Hydrolysis of phosphate esters

Phosphate esters have a variety of biological uses. Phosphate mono-esters can occur as alkyl phosphates and sugar phosphates whereas phosphate di-esters occur in the backbone of DNA and RNA and form phospholipid membranes of cells.

Phosphoryl transfer is of great importance in biochemistry and allows many reactions which are too slow or thermodynamically unfavourable to occur. These reactions are needed for energy balance and cellular control.

Many reactions involve cleavage of phosphoric mono-esters/anhydrides which give rise to large free chemical energy driving a reaction to completion.

Enzymatic cleavage of phosphate esters is carried out by a family of phosphatases which have been classified by William P Taylor and Theodore S Widlanski[53]. There are three major groups (Figure 1.5) of phosphatases which are based on substrate preference. The first class comprises of non-specific substrates which are subdivided dependent on pH, i.e. the most suitable/optimum operating conditions such as alkaline and acid phosphatases. The second class known as phosphoprotein phosphatases cleave phosphorylated proteins, this group includes phosphoserine, phosphoserine/threonine phosphatases, phosphotyrosine phosphatases and duel specificity phosphatases.

The final class includes enzymes which hydrolyse specific substrates or structurally similar substrates such as glucose-6-phosphate[53, 54].

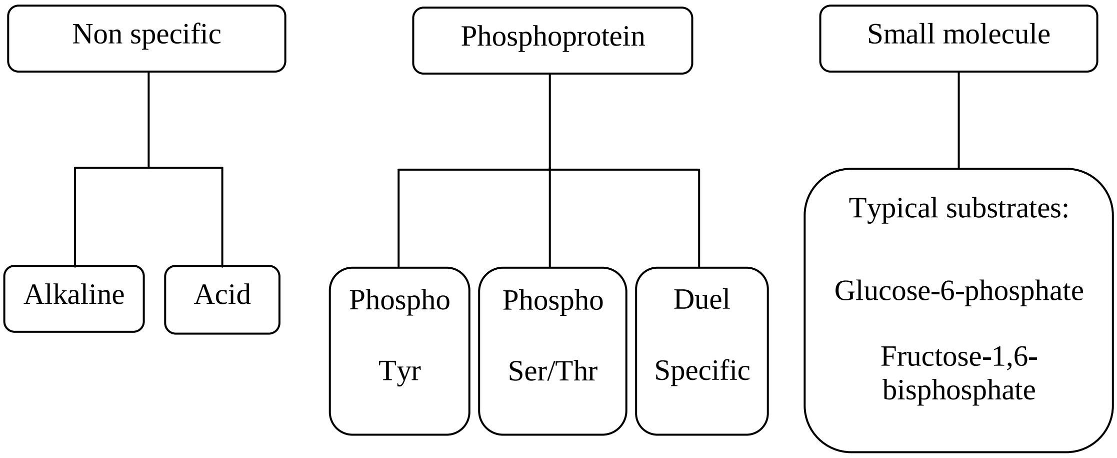

Figure 1.5 The three groups of phosphatases dependent on substrate specificity.

1.1.10.1 Non-specific phosphatase – Alkaline phosphatase

E.coli phosphatase is the most studied alkaline phosphatase and preferentially catalyses phosphate mono-esters although some members of the alkaline phosphatase superfamily hydrolyse phosphate di-esters[55, 56]. Previous studies have shown that at low pH the enzyme dissociates into subunits followed by conformational change which can be reverted dependent on pH, temperature and metal concentration[57, 58]. The active site of *E.coli* alkaline phosphatase contains two Zn^{2+} ions and an Mg^{2+} ion which are required for enzyme activity with normal pH operating conditions around pH 8[55]. The active site transition state for the hydrolysis of a phosphate monoester is shown in Scheme 1.34, where the charge is stabilised by the metal-ions.

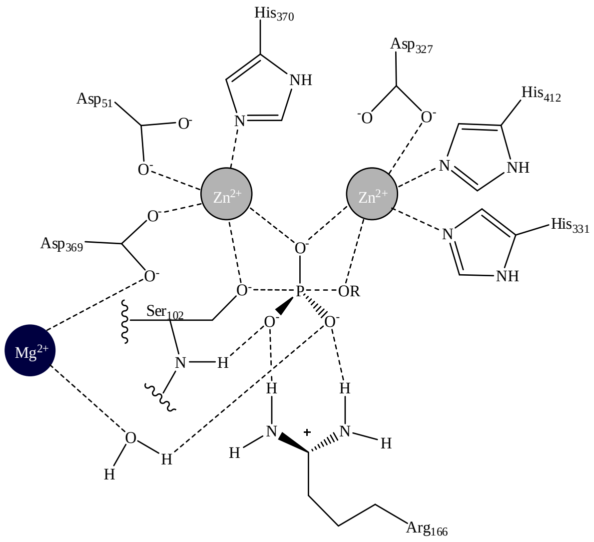

Scheme 1.34 *E.coli* Pase active site transition state when catalysing the hydrolysis of phosphate mono-esters[56].

1.1.10.2 Alkaline pyrophosphatase

Yeast pyrophosphatase from *Saccharomyces cerevisiae* and pyrophosphatase from *Escherichia coli* belong to the family of alkaline phosphatases which require three or four metal-ions to catalyse the non-specific hydrolysis of phosphate mono-esters.

Alkaline pyrophosphatases catalyses the hydrolysis of pyrophosphate tetra-anion to two equivalents of phosphate generally in the pH region of 6-10[59] (Scheme 1.35).

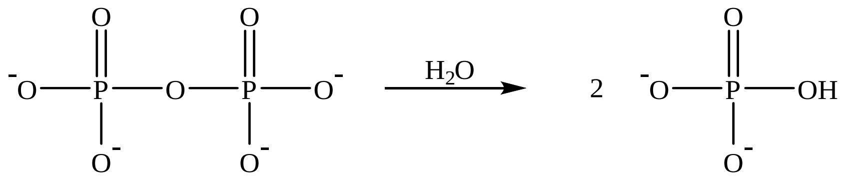

$$^{-}O-P(=O)(O^{-})-O-P(=O)(O^{-})-O^{-} \xrightarrow{H_2O} 2\ ^{-}O-P(=O)(O^{-})-OH$$

Scheme 1.35 Pyrophosphate terta-anion hydrolysing to two equivalents of phosphoric acid.

E.coli PPase is the most studied pyrophosphatase (PPase) and is similar to yeast PPase both essentially are near perfect catalysts, with a $k_{cat}/K_m = 3 \text{ x } 10^7\ M^{-1}\ s^{-1}$ [60]. The active site contains four magnesium-ions termed Mg1-Mg4 which are required for catalytic hydrolysis of pyrophosphate. Two magnesium-ions fill site Mg1 and Mg2, of higher and lower affinity respectively, before the substrate complexes and Mg3 and Mg4 sites are filled in the enzyme substrate complex[61, 62]. There are 13 polar residues within the active site which interact directly or via a water molecule with the four magnesium-ions and two of the phosphorus oxygen atoms of pyrophosphate[63].

The major coordination residues are Mg1 and Mg2 bridged by a water molecule (Figure 1.6, magenta), Asp$_{70}$ and pyrophosphate while Mg3 is coordinated to pyrophosphatase Asp$_{97}$ and Asp$_{120}$ and Mg4 is coordinated Glu$_{31}$ as well as the pyrophosphate moiety. In addition to the amino acid residues which coordinate the magnesium-ions, 9 water residues also coordinate to complete the octahedral coordination of the magnesium-ions. Also Lys$_{29}$, Lys$_{142}$ and Arg$_{43}$ are coordinated to the substrate via electrostatic interaction and an important amino acid residue Asp$_{67}$ acts as a general base to deprotonate the bridging water molecule which would predominantly act as a nucleophile[64, 65] (Scheme 1.36).

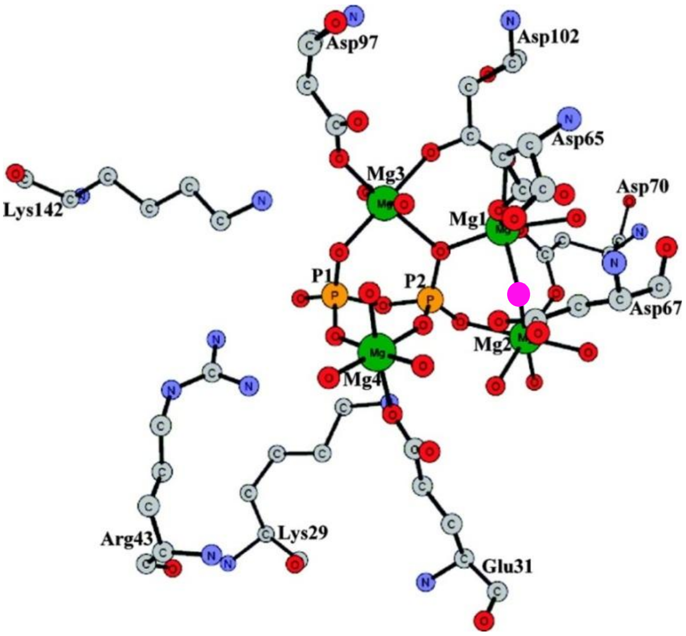

Figure 1.6 X-ray crystal structure of the active site of *E.coli* PPase with the bridging water molecule shown in magenta[64].

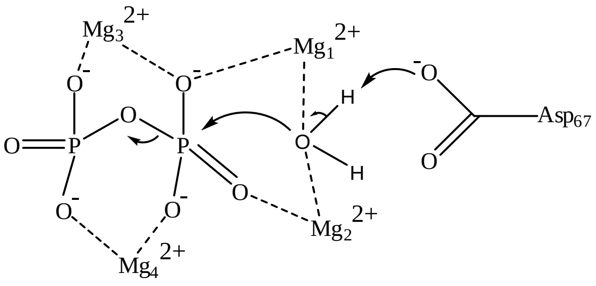

Scheme 1.36 Possible mechanism of pyrophosphate hydrolysis by *E.coli* PPase initially involving deprotonation of water by a general base[64].

1.1.10.3 Acid phosphatases

Acid phosphatases are enzymes which hydrolase small phosphate monoesters under acidic conditions[66]. Purple acid phosphatases are an example which fit into this category although they may overlap into others and are able to catalyse the hydrolysis of phosphoric esters and anhydrides such as ATP in the pH region of 4 to 7. Purple acid phosphatases usually contain two metal-ions one of which is Fe(III) and the second could be Zn(II), Mn(II) or even another iron-ion[67].

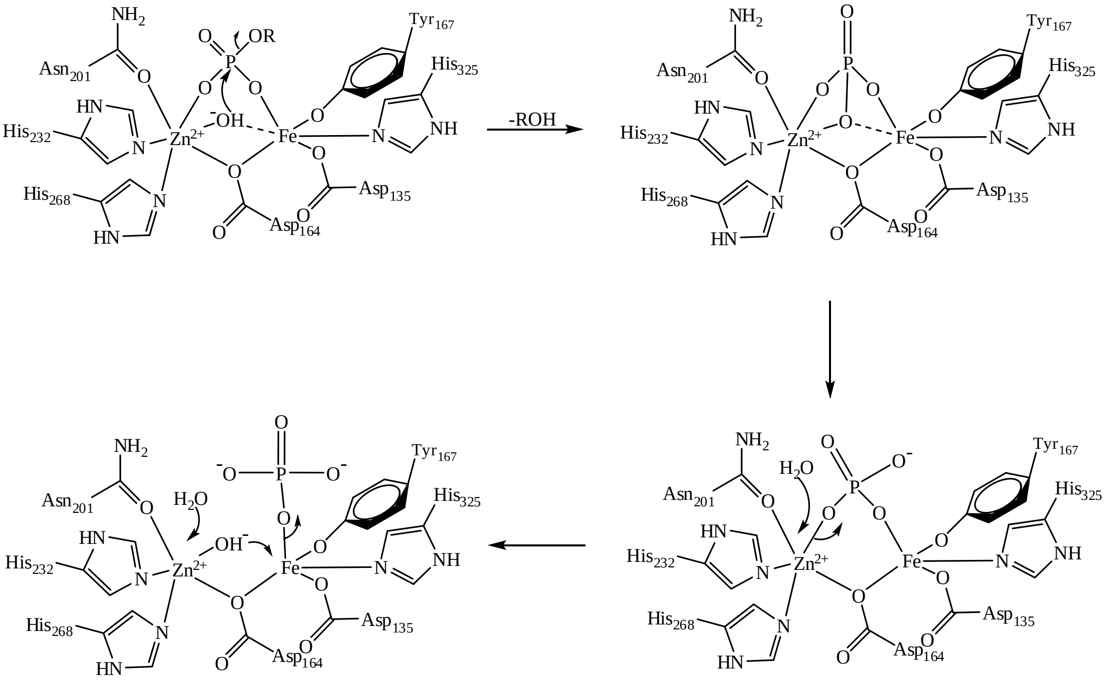

Scheme 1.37 Proposed mechanism of purple acid phosphatases (PAP), where a hydroxide-ion bridging the two metal-ions attacks the phosphorus centre or a non-coordinated hydroxide-ion attacks initially then the phosphate is release on exchange with two water molecules which also reform the bridging hydroxide-ion[68].

1.1.10.4 Phosphoprotein phosphatases

Protein phosphatases are represented by three distinct gene families. Two of these families, phosphoprotein phosphatase P (PPP) and phosphoprotein phosphatase M (PPM) dephosphorylate phosphoserine and phosphothreonine residues, whilst protein tyrosine phosphatases (PTP) dephosphorylate phosphotyrosine residues. The largest family which dephosphorylate serine/threonine amino acid residues are metallo enzymes and hydrolysis uses a metal activated nucleophilic water molecule[69].

The major protein serine/threonine phosphatase activity *in vivo* is accounted for by PP1, PP2A and PP2B which are part of the PPP family together with PP2C of the PPM family. The three members of the PPP family share a common catalytic domain of 280 amino acid residues and therefore highly conserved[70]. The catalytic subunit of PP1 (Figure 1.7) adopts an α/β fold with a β sandwich wedged between two α domains[71]. Conserved amino acid residues (three histidines, two aspartic acids and an asparagine) coordinate two metal-ions. The two metal-ions Fe^{2+} (or Fe^{3+}) and Mn^{2+} are present in protein which has been expressed in *E.coli* but other metal-ions such as two Mn^{2+} ions can occupy both sites[71].

One water molecule is bridged by the two metal-ions which contribute to the octahedral hexacoordinate geometry. The mechanism of phosphate ester hydrolysis involves direct nucleophilic attack on the phosphorus atom by metal-bound hydroxide-ion and the leaving group is protonated by the imidazolium side chain of His_{125}[72] (Figure 1.7).

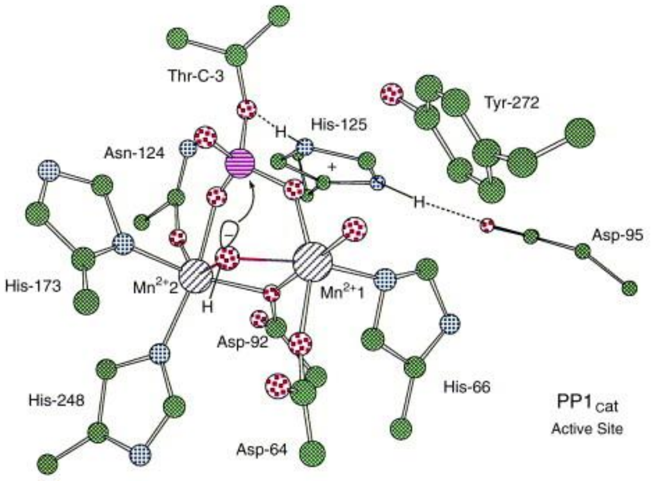

Figure 1.7 Active site of *E.coli* PP1phosphatase[72].

1.1.10.5 Substrate specific/similar phosphatases

One of the most important enzymes in metabolism is glucose-6-phosphatase (G-6-Pase), which is mainly found in the kidneys and liver. Excess glucose is stored as glycogen. Gluconeogenesis and glycogenolysis produce glucose-6-phosphate which can be released into the bloodstream once the phosphate group has been cleaved by glucose-6-phosphatase thus playing a major role in blood glucose homoeostasis[73]. The active site of G-6-Pase is on the lumen side of the endoplasmic reticulum and is highly conserved in mammalian cells[74]. It contains many histidine residues, His_{9}, His_{52}, His_{179}, His_{197}, His_{252}, His_{307} and His_{353}[75]. It was discovered, by point mutations at those positions, that the majority of the histidine residues do not play an essential role in the hydrolysis of glucose-6-phosphate but altering His_{179} abolished enzyme activity. Other key residues within the active site including G-6-Pase Lys_{76}, Arg_{83}, Arg_{170} and His_{119} take part in catalysis and point mutation of these residues also abolishes enzyme activity[76].

The mechanism of action on G-6-P (Scheme 1.38) is initiated by His_{176} providing nucleophilic attack on the phosphorus centre forming a phospho-histidine enzyme intermediate. $His_{119}H^+$ acts as a general acid enabling the cleavage of the P-O bond to produce free glucose. Water then attacks the phospho-intermediate which is stabilised by hydrogen bonding to Arg_{83} and Arg_{170}, proton transfer via His_{119} dissociates the phosphate leaving group from the active site[75].

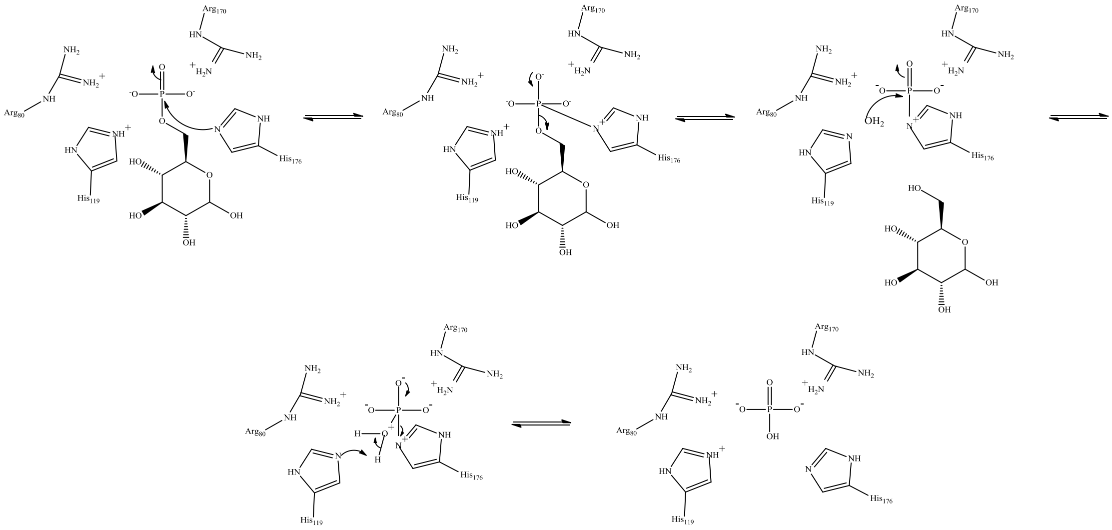

Scheme 1.38 Mechanism of Glucose-6-Phosphate hydrolysis by glucose-6-phosphatase[75].

1.1.11 Heats of hydrolysis of phosphates

Most chemical or biological reactions are associated with a physical change, generally heat is either taken in from the surroundings or released. The enthalpy change accompanying these reactions is usually measured at 1 bar (1.00×10^5 Pa) and at a specified temperature of 298.15 K. The change in enthalpy (ΔH) can either be exothermic, where heat is given out during the reaction and defined by a negative ΔH or a positive ΔH which corresponds to heat being absorbed from the surroundings and referred to as endothermic. Nature has adopted a way to harness chemical energy by splitting or hydrolysing high energy compounds to provide energy for biological work. The enzymatic cleavages of P-O bonds within phosphate anhydrides are very exothermic under physiological conditions. Examples of high energy phosphate esters are creatine phosphate, phosphoenolpyruvate and 1,3-bisphosphoglycerate (Scheme 1.39) but the most common biological energy currency is ATP[77] (Scheme 1.3).

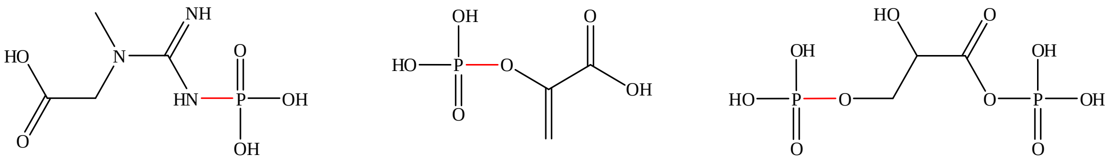

i ii iii

Scheme 1.39 Creatine phosphate (i), phosphoenolpyruvate (ii) and 1,3-bisphosphoglycerate (iii) with the bond which is cleaved in red[77].

ATP and the compounds shown in Scheme 1.39 commonly take part in phosphorylation reactions which drive reactions forward which would be otherwise energetically unfavourable. Typically the free energy change ΔG^o is an indication to whether a reaction would be spontaneous as indicated by a negative ΔG^o or unfavourable by a positive ΔG^o. The standard Gibbs free energies of hydrolysis of ATP, ADP, AMP and pyrophosphate are given in Table 1.4:

Reaction	$\Delta G^o_{\text{hydrolysis}}$ (kJ mol^{-1})
$\mathrm{ATP + H_2O \rightarrow ADP + HPO_4{}^{2-} + H^+}$	-32
$\mathrm{ATP + H_2O \rightarrow AMP + HP_2O_7{}^{3-} + H^+}$	-45
$\mathrm{AMP + H_2O \rightarrow Adenosine + HPO_4{}^{2-}}$	-13
$\mathrm{HP_2O_7{}^{3-} + H_2O \rightarrow 2\ HPO_4{}^{2-}}$	-29

Table 1.4 Gibbs free energies of hydrolysis for phosphate anhydrides[4].

Although the heats of hydrolysis gives no direct indication of the corresponding free energy change, they may provide some indication to whether it could be used as a phosphorylating agent. In approximately 12 M sulphuric acid the heat of hydrolysis of the neutral pyrophosphate is -17.8 kJ mol^{-1} whilst at neutral pH (pH 7.2, catalysed by pyrophosphatase from baker's yeast at 29^{o}C) the heat of hydrolysis of sodium pyrophosphate is -37.4 kJ mol^{-1} which is more than double then that of the neutral species[78, 79]. Ging and obtained a heat of hydrolysis (pH 7.2, 0.1 M ionic strength at 25^{o}C) of -30.6 kJ mol^{-1} for pyrophosphate whilst in phosphate buffer at pH 7.3 ΔH = -24.3 kJ mol^{-1} [78].

An inevitable problem associated with the evolution of the heat of hydrolysis of pyrophosphate is the ionisation states of the reactants and the products, which obviously vary with pH.

An example of P-O bond cleavage which produces a large exothermic heat upon hydrolysis is p-nitrophenyl phosphate (pNPP). Dephosphorylation of p-nitrophenyl phosphate at pH 9.6 and at 29^{o}C produced a ΔH = -19.0 kJ mol^{-1} [79]. A few years later Sturtevant investigated the enthalpy of hydrolysis of pNPP and found it to be -26.3 kJ mol^{-1} over a pH range of 3.6-5.8 using acetate buffers at 25^{o}C[80].

Another example where P-O bond cleavage is of great importance is in the hydrolysis of creatine phosphate which is a key step in muscle contraction. The hydrolysis of creatine phosphate (PCr) occurs in muscle cells and can be represented by Scheme 1.40:

$$\mathrm{PCr^{2-}} \xrightarrow{\mathrm{H_2O}} \mathrm{Cr + HPO_4^{2-}}$$

Scheme 1.40 Creatine phosphate hydrolysing to creatine and phosphoric acid[81].

The hydrolysis of creatine phosphate is catalysed by acid or by alkaline phosphatase and the enthalpy of hydrolysis at 37^{o}C is -41.0 kJ mol^{-1} and -43.2 kJ mol^{-1} respectively[81]. *In vivo* the reaction is accompanied by proton transfer and release/binding of Mg^{2+} from PCr to phosphate and the heat accompanying these factors at pH 7, 1 x 10^{-3} M magnesium is -35 kJ mol^{-1} which is slightly lower than other values of -38 kJ mol^{-1}and -40 kJ mol^{-1} obtained by Woledge and Carlson and Siger respectively[82, 83].

1.1.12 Aim

The aims of this project involve the investigation and comparison of physical and thermodynamic properties of phosphorous(III) and phosphoric(V) acid derivatives. Phosphoric compounds are widely used in chemistry and biochemistry, and phosphoric anhydrides are widely hydrolysed in many biochemical processes. In particular, this work investigates the acidities of dissociable hydrogens in phosphorous(III) and phosphoric(V) compounds and their relative hydrolytic reactivities which are very dependent on the ionic species present in solution. Another aspect of this work involves metal coordination and enzymatic hydrolysis of phosphorus (III and V) derivatives. As phosphorus anhydrides are well known high energy currency compounds, the heats of hydrolysis of P(III) and P(V) were also studied.

1.2 Experimental

1.2.1 Materials

Pyro-di-H-phosphonate (PP(III)) - samples of PP(III) were initially and kindly provided by T. Kee (University of Leeds) and prepared by dissolving phosphorous acid (16.4 g) and sodium hydroxide (8.0 g) in 100 ml water. The water was removed under reduced pressure. The resulting mixture was heated in a tube furnace with N_2 flowing through at 200°C for three days, the analytical details are discussed in the results and discussion (section 1.3). Diethyl pyro-di-H-phosphonate and H-phosphonate monoethyl esters were prepared as previously described and were analytically pure[17]. H-phosphonate di-ethyl ester (>99%), *E. coli* pyrophosphatase (lyophilized powder ≥90%, ≥800 units per mg protein) and tetra sodium pyrophosphate decahydrate were purchased from Sigma.

1.2.2 Kinetics/pK_a

Ionic strength of solutions were maintained using KCl. Reactions monitored by $^{31}P\{H\}$ NMR at 25°C used a 500 MHz Bruker Avance I, and a D_2O insert was used for a lock signal and diphenylphosphate as an internal standard.

Where auto-titration was used to follow reactions these were carried out using a Metrohm 859 instrument. Auto-titration: a jacketed titration vessel aspirated with N_2 was used to maintain a constant temperature. The vessel was charged with 50 ml HCl or NaOH at I = 1.0 M and titrated with an appropriate solution to maintain the pH. The titration was initiated by addition of 1.0 mmole PP(III) to the vessel.

Effect of Mg^{2+} on the hydrolysis of PP(III): samples were run in 0.8 M MOPS buffer at pH 7 and 1.0 M ionic strength containing 10% D_2O for a D_2O lock and 20 mM diphenylphosphate as an internal standard. Magnesium concentrations were varied by the addition of 0.001 M, 0.005 M and 0.01 M magnesium chloride ($MgCl_2$), to 37.6 mM PP(III).

E.coli Pyrophosphatase (PPase) catalysed reactions were followed using VP-ITC: the enzyme (1×10^{-9} M) was prepared in 20 mM HEPES buffer pH 8.40 or 20 mM MOPS buffer at pH 7.55, with 3 mM magnesium chloride. 10 mM PP(V) in the same buffer, excluding PPase and magnesium chloride was used to initiate the reaction to give a final concentration of 0.0411 mM or 0.0211 mM, I = 0.1 M at 25°C. Both solutions were degassed for 15 minutes to prevent bubble formation during the experiment. The same experiment was repeated but with the addition of 1 mM PP(III) as a potential inhibitor.

Using the ITC data, the total heat generated by the reaction can be given be Equation 1.3 where Q is heat and t is time.

$$\int_{0}^{\infty} \frac{\mathrm{dQ}}{\mathrm{dt}}\,\mathrm{dt}$$

Equation 1.3

The velocity (dP/dt) can be given by Equation 1.4.

$$\frac{\mathrm{dP}}{\mathrm{dt}} = \left(\frac{[\mathrm{PP(V)}]_{\mathrm{i}}}{\int_{0}^{\infty} \frac{\mathrm{dQ}}{\mathrm{dt}}\,\mathrm{dt}}\right)\mathrm{dt}$$

Equation 1.4

dQ/dt (which is power) represents the difference between the baseline and the heat released at any time, t, so the concentration of PP(V) at any time, t, ($[\mathrm{PP(V)}]_t$) can be represented by multiplying $[\mathrm{PP(V)}]_i$ by the integrated area for a specific injection at time, t, which is divided by the total integral of the well, Equation 1.5 which was used to obtain a plot of [PP(V)] against time[84, 85].

$$[\mathrm{PP(V)}]_{\mathrm{t}} = [\mathrm{PP(V)}]_{\mathrm{i}}\left(1 - \frac{\int_{0}^{\mathrm{t}} \frac{\mathrm{dQ}}{\mathrm{dt}}\,\mathrm{dt}}{\int_{0}^{\infty} \frac{\mathrm{dQ}}{\mathrm{dt}}\,\mathrm{dt}}\right)$$

Equation 1.5

The $\mathrm{p}K_a$ of PP(III) and ethyl-H-phosphonate was monitored by ^{31}P{H} NMR which contained an insert of diphenylphosphate in MOPS buffer, pH 7, I = 1.0 M as an external standard. PP(III) was analysed at 1.0 M ionic strength at a given pH with concentrations of PP(III) in solution ranging from 2.63 mM – 12.78 mM and ethyl H-phosphonate from 2.90 – 10.50 mM below pH 3. The pH of each solution was taken before the addition of PP(III) or ethyl-H-phosphonate and after to ensure the pH had not changed during analysis.

1.2.2.1 Enzyme kinetics

Michaelis-Menten kinetic constants k_{cat}, K_m and k_{cat}/K_m were obtained by Equation 1.6 and its derivations.

$$\mathrm{E + S} \underset{\substack{k_{-1}\\ \mathrm{K_m}}}{\overset{k_1}{\rightleftharpoons}} \mathrm{ES} \xrightarrow[k_2]{\mathrm{k_{cat}}} \mathrm{E + P}$$

$$\text{rate} = \frac{\mathrm{k_{cat}}\,[\mathrm{E}][\mathrm{S}]}{\mathrm{K_m} + [\mathrm{S}]}$$

Equation 1.6

Below saturation, when $[S] << K_m$ the curve was fitted to a simple first-order rate law to obtain the pseudo first-order rate constants k_{obs}, which were independent of substrate concentration and first-order in enzyme concentration. Above saturation, when $[S] >> K_m$ the profile was fit to a zero-order rate law to provide V_{max} for the reaction, ($= k_{cat}[E]$).

The catalytic efficiency of the enzyme k_{cat}/K_m was obtained by dividing k_{obs} by the initial enzyme concentration; k_{cat} was obtained by dividing V_{max} by the initial enzyme concentration.

1.2.3 Metal-ion complexing

General - metal-ion complexing studies using ITC were performed on a VP-ITC Microcal instrument at 25^{o}C using a cell volume of 1.8 ml (V_0 = active volume 1.4194 ml) and solutions were degassed to prevent bubble formation for 15 minutes. The reference cell was filled with ultra-pure water (18.2 MΩ.cm at 25^{o}C) throughout all experiments.

PP(V):

Magnesium complexing to pyrophosphate was conducted by adding different equivalents of magnesium-ion to a 10 mM solution (1.0×10^{-4} moles in 10 ml water) of sodium pyrophosphate decahydrate. Magnesium equivalents of 0, 0.5, 1 and 2 were added to the 10 ml pyrophosphate solution which all contained diphenyl phosphate as an internal standard and the pH was monitored by adding HCl or NaOH accordingly. 10.12 mg of $MgCl_2.6H_2O$ was added for 0.5 equivalent of Mg^{2+} then an additional 10.16 mg of Mg^{2+} was added to give 1equivalent of metal-ion and 2 equivalents by an additional of 20.71 mg of Mg^{2+}. The complexing at each equivalent was monitored using $^{31}P\ \{H\}$ NMR at 25^{o}C.

Residual metals within the buffer solutions were removed using Chelex 100. Isotherms using ITC were obtained by the titration of 21.0 mM magnesium (syringe, 10 µl injections) into 0.56 mM PP(V) (cell). Both solutions within the syringe and cell were at pH 8.40 buffered by 25 mM HEPES and at I = 0.1 M.

The instrument parameters for the ITC experiments were:

Number of injections: 29, reference power: 10 µcal/sec, initial delay: 300 sec, stirring speed: 307 rpm,volume of injectant: 10 µl, duration: 20 sec, spacing: 180 sec, filter period: 2 sec.

PP(III):

Magnesium complexing to pyrophosphate was conducted by adding different equivalents of magnesium-ion to a 10 mM solution (1.0 x 10^{-4} moles in 10 ml water) of sodium pyro-di-H-phosphonate. Magnesium equivalents of 0, 0.5, 1 and 2 were added to the 10 ml sodium pyro-di-H-phosphonate solution which all contained diphenyl phosphate as an internal standard and the pH was maintained by added HCl or NaOH accordingly. 10.32 mg of $MgCl_2.6H_2O$ was added for 0.5 equivalent of Mg^{2+} then an additional 10.10 mg of Mg^{2+} was added to give 1equivalent of metal-ion and 2 equivalents by an additional of 21.05 mg Mg^{2+}. The complexing at each equivalent was monitored using ^{31}P {H} NMR at 25°C.

Residual metals within the buffer solutions were removed using Chelex 100. Isotherms using ITC were obtained by the addition of 20 mM magnesium- or calcium-ions (syringe, 10 µl injections) titrated into 0.50 mM PP(III). Both solutions within the syringe and cell were buffered using 30 mM MES, 0.1 M Ionic strength at pH 6.00.

The instrument parameters for the ITC experiments were:

Number of injections: 29, reference Power: 10 µcal/sec, initial delay: 200 sec, stirring speed: 307 rpm, volume of injectant: 10 µl, duration: 20 sec, spacing: 250 sec, filter period: 2 sec.

1.2.4 Heats of hydrolysis

Experiments were performed on a VP-ITC Microcal instrument at 25°C using the same general procedures as in 1.2.3. The addition (single injection method) of 10.05 mM PP(III) (syringe, 5µl injections, pH 7) into sodium hydroxide at pH 13 and at pH 13.5 at 25°C, ionic strength 1.0 M. The heat of dilution was subtracted from the hydrolysis of PP(III).

The instrument parameters for the ITC experiments were:

Number of injections: 3, reference power: 30 µcal/sec, initial delay: 300 sec, stirring speed: 307 rpm, volume of injectant: 5 µl, duration: 10 sec, spacing: 2000 sec, filter period: 2 sec.

The heat of hydrolysis for PP(V) was conducted with 10 mM of pyrophosphate drawn into the syringe whilst the cell contained 3 mM $MgCl_2$ and 1 x 10^{-9} M *E.coli* pyrophosphatase. Both the syringe and cell also contained 20 mM buffer at pH 8.40 or 7.50, 0.1 M ionic strength and the heat of dilution was subtracted from the isotherm.

The instrument parameters for the ITC experiments were:

Number of injections: 3, reference power: 15 µcal/sec, initial delay: 300 sec, stirring speed: 307 rpm, volume of injectant: 3 µl, duration: 6 sec, spacing: 1500 sec, filter period: 2 sec.

The enthalpy associated with the any reaction occurring in the sample cell can be represented by Equation 1.7[85].

$$\Delta H_{obs} = \frac{1}{[S]_i\, V_0} \int_{t=0}^{t=\infty} \frac{dQ(t)}{dt}\, dt$$

Equation 1.7

The observed enthalpy is then subtracted from the heat of dilution to give the enthalpy associated with the specific reaction (which would include any buffer protonations/deprotonations etc).

1.3 Results and discussion

1.3.1 Pyro-di-H-phosphonate identification

Samples of pyro-di-H-phosphonate (PP(III)) as the di-sodium salt were provided by T. Kee (University of Leeds) and prepared as stated within the experimental section. The reaction involves the dehydration of phosphorous acid as shown in Scheme 1.41.

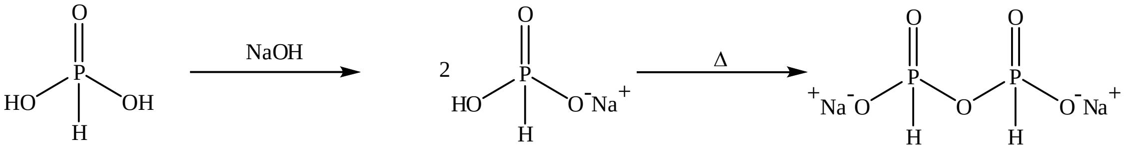

Scheme 1.41 Preparation of PP(III), firstly by treatment with sodium hydroxide to preparing the mono-sodium salt which is heated to give the product as the di-sodium salt.

Pyro-di-H-phosphonate is a chemically symmetrical compound which could either be magnetically equivalent or non-equivalent. The P nuclei (spin =1/2) are well separated from the proton nuclei and can be assigned as A and X of PP(III) di-anion in D_2O. The ^{31}P NMR (Figure 1.8) shows two apparent triplets separated by 666 Hz, this large coupling constant of $J_{P1H1} = J_{P2H2}$ is from the P-H bond. The 'triplets' are not true first-order couplings as the coupling constants are unequal 7.97 ± 0.03 Hz and 9.28 ± 0.03 Hz. They presumably reflect three bond coupling between P and the adjacent H and between the two P's. The two P's are magnetically non-equivalent because the coupling of P_1 to H_1 is different from that of P_2 to H_1. The P_1 to P_2 coupling is similar, but not identical, to that for P_1 to H_2 giving rise to an apparent triplet which in reality is probably a doublet of doublets (Figure 1.9) which could possibly be resolved on a high frequency NMR, this system can be referred to as an AA' XX' coupling system.

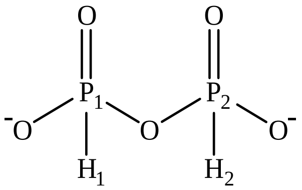

Scheme 1.42 Pyro-di-H-phosphonate di-anion.

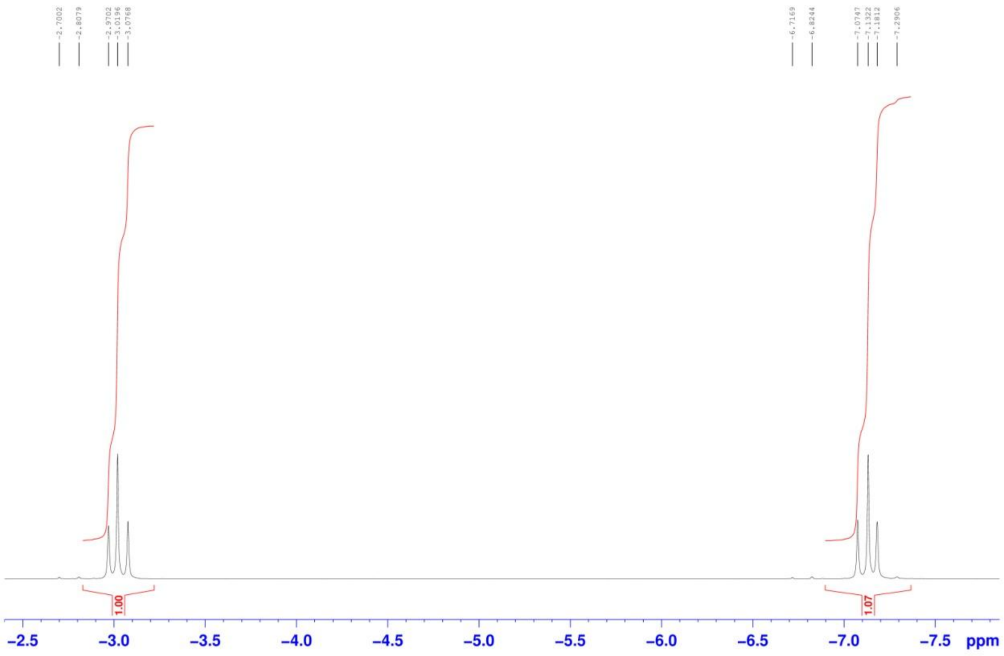

Figure 1.8 ^{31}P NMR of Pyro-di-H-phosphonate di-anion in D_2O at 161.97 MHz.

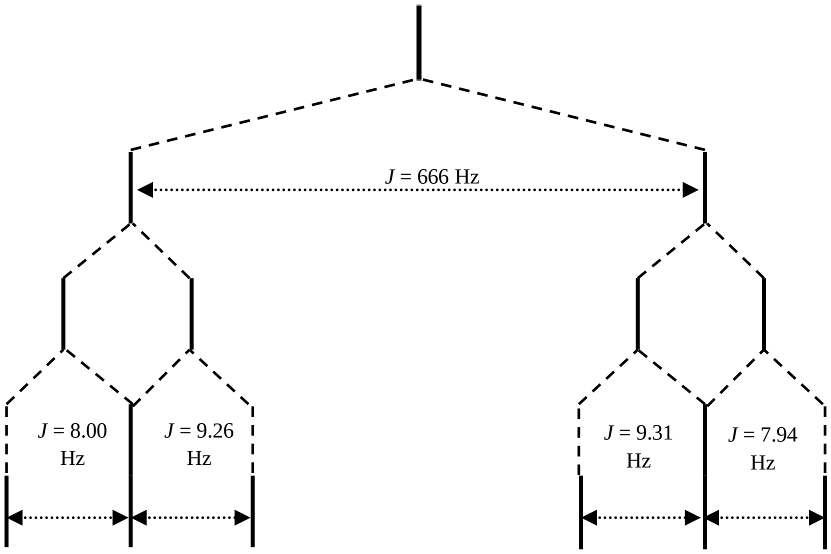

Figure 1.9 Splitting tree diagram of the coupling constants of pyro-di-H-phosphonate.

1.3.2 pK$_a$ of pyro-di-H-phosphonate (III) and ethyl-H-phosphonate

The pK$_a$s of the four dissociable protons of pyrophosphate are known[24] but not of the two dissociable protons in pyro-di-H-phosphonate. The decoupled ^{31}P{H} NMR of PP(III) di-anion in H_2O shows an invariant chemical shift from pH 2 to 13.5 indicating that the pK$_a$s are below 2 and that the dominant species over the majority of this pH range is the di-anion PP(III)$^{2-}$. But below pH 2 the chemical shift does change (Figure 1.10) but PP(III) unfortunately undergoes acid catalysis at low pH which makes difficult to measure the chemical shift below pH 0.6.

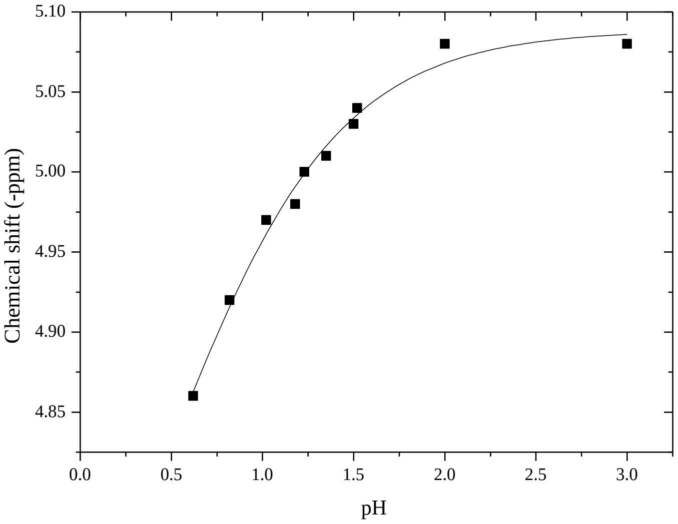

Figure 1.10 Decoupled ^{31}P{H} NMR chemical shift of PP(III) in H_2O against pH (I = 1.0 M, 25°C) with external reference to diphenyl phosphate.

Assuming that the observed data is sigmoidal in character, it can be fitted to a pK$_a$ of 0.44 ± 0.1 which is indicated by the solid line. This is assumed to be the second pK$_a$ of pyro-di-H-phosphonate as above pH 2 it exists as the di-anion. The first pK$_a$ may be very similar or lower than the second even though a limiting chemical shift has not been determined below pH 0.6.

The ^{31}P NMR spectrum of an analogous P(III) compound ethyl-H-phosphonate (EtO PH(O)OH) was measured as a function of pH (Figure 1.11) but a limiting chemical shift could also not been determined.

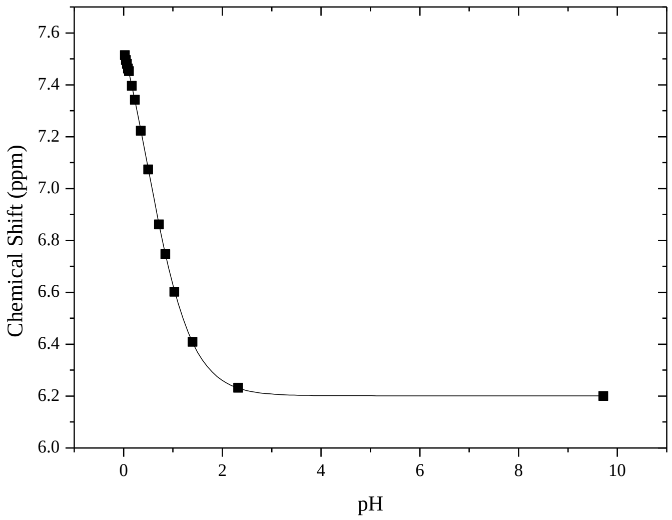

Figure 1.11 Decoupled ^{31}P{H} NMR chemical shift of ethyl-H-phosphonate in H_2O against pH at I = 1.0 M, 25°C with external reference to diphenyl phosphate.

Again assuming a sigmoidal chemical shift as a function of pH, a pK_a of 0.47 ± 0.01 was obtained. Ethyl phosphate has a pK_a of 1.60[86], which is thus higher than that of ethyl-H-phosphonate. The first pK_a of phosphoric acid is 2.12 which is also higher than that of phosphorous acid, 1.07[24] and a calculated value of 0.9[25]. It thus appears that phosphorous P(III) derivatives, as their H-phosphonates, are more acidic than the corresponding phosphoric P(V) compounds. Carroll and Mesmer studied isohypophosphate which contains both a P(III) and P(V) oxidation state bridged by an oxygen (Scheme 1.43). Interestingly, the first pK_a was estimated to be 0.6 followed by experimental determined of 1.67 and 6.26 for pK_{a2} and pK_{a3} [87]. A summary of the pK_as of various P(III) and P(V) acids is shown in Table 1.5.

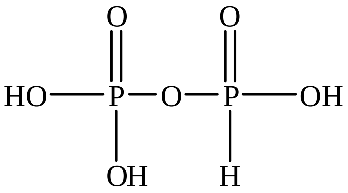

PP(III.V)

Scheme 1.43 Isohypophosphate, hybrid phosphorus anhydride which contains one phosphorus in a P(III) oxidation and the other in a P(V) oxidation state.

Acid	**pK_{a1}**	**pK_{a2}**	**pK_{a3}**	**pK_{a4}**
Phosphorous (H-phosphonic)	1.07	6.58		
Phosphoric	2.12	7.21	12.32	
Ethyl-H-phosphonate*	0.47			
Ethyl phosphate	1.60	6.62		
Pyro-di-H-phosphonic*	≤ 0.44	0.44		
Pyrophosphoric	0.9	2.0	6.6	9.4
Isohypophosphate	0.6	1.67	6.26	

Table 1.5 Summary of pK_as of phosphorous and phosphate acids at 25°C (* I = 1.0 M).

1.3.3 pH-rate profiles for the hydrolysis of PP(III) and PP(V)

The rates of hydrolysis of pyro-di-H-phosphonate PP(III) and pyrophosphate PP(V) (Scheme 1.44) are expected to change significantly with pH as their anionic state and reactivities vary.

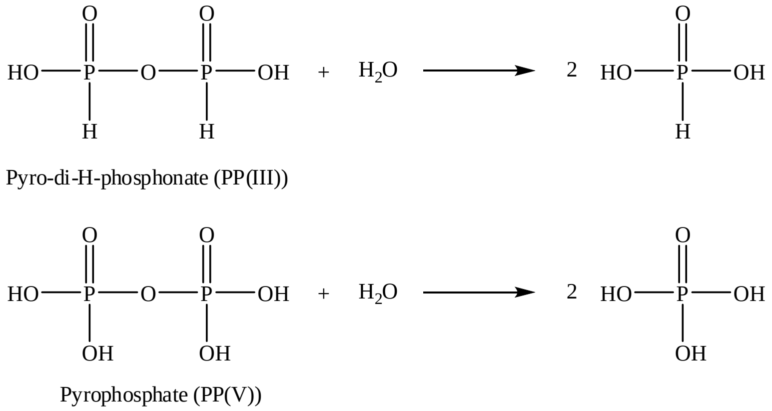

Scheme 1.44 Hydrolysis of pyro-di-H-phosphonate (PP(III)) and pyrophosphate (PP(V)).

pH-rate profiles are useful for determining any acid and base dependent and pH independent hydrolysis and the rate laws for ionising reactants. The rates of hydrolysis of pyrophosphate and pyro-di-H-phosphonate were determined by ^{31}P {H} NMR and auto-titration at a range of pHs using hydrochloric acid, sodium hydroxide and different buffers under pseudo first-order conditions at constant pH, ionic strength I = 1.0 M and temperature 25°C.

The observed pseudo first-order rate constants (k_{obs}) at different buffer concentrations at constant pH were extrapolated back to give a buffer independent rate constant. For example, without extrapolation to zero buffer concentration at higher pH the observed rate constant, if general base catalysed, could be a combination of the buffer([B]), hydroxide concentration ($[OH^-]$) and the independent rate constant (k_0) (Equation 1.8).

$$k_{\mathrm{obs}} = k_0 + k_{\mathrm{OH}}[\mathrm{OH}^-] + k_{\mathrm{B}}[\mathrm{B}]$$

Equation 1.8

The pseudo first-order rate constant (k_{obs}) measured at constant pH and buffer ratio but with different buffer concentrations allows a plot of k_{obs} against [B], which provides, from the intercept, the buffer independent rate constant k_0 + k_{OH} (Equation 1.9) and , from the slope, k_B.

$$\mathrm{Intercept} = k_0 + k_{\mathrm{OH}}[\mathrm{OH}^-] \text{ at } [\mathrm{B}] = 0$$

Equation 1.9

This is the case for the hydrolysis of PP(III), where, for example, at pH 8.0 the observed first order rate constant is dependent on the concentration of the buffer used to maintain constant pH (Figure 1.12)

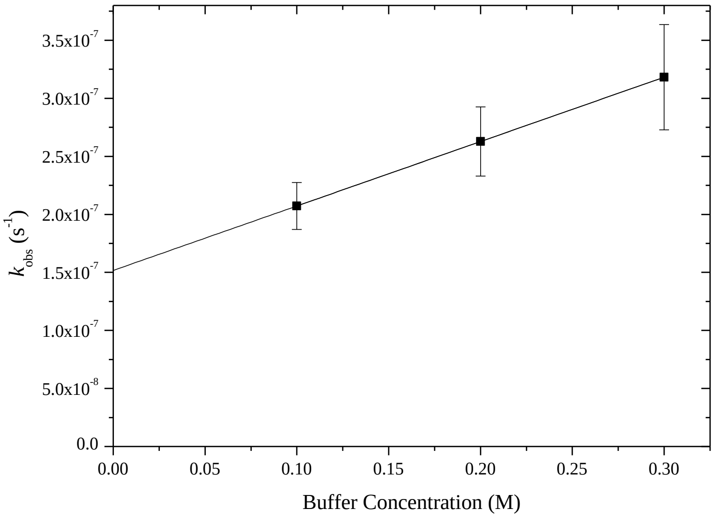

Figure 1.12 Plot of the observed pseudo first-order rate constants for the hydrolysis of PP(III) as a function of MOPS buffer concentration at pH 8.0 at I = 1.0 M (KCl) and 25°C.

However, when the reactants, such as PP(V) and PP(III) can ionise over the pH range studied, the pH rate profile may also indicate the relative reactivities of the various ionic states. A plot of the log of the pseudo first-order rate constants obtained at different pHs, independent of buffer concentration, against pH for the hydrolysis of pyro-di-H-phosphonate (PP(III)) and pyrophosphate (PP(V)) reflects the different ionic species present and their relative reactivities (Figure 1.13).

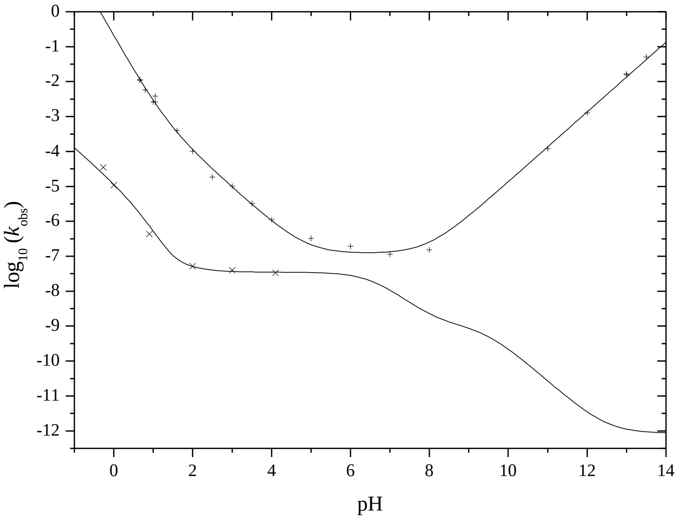

Figure 1.13 pH rate-profile for the hydrolysis of PP(III) (+) and PP(V) (×) at 25°C.

PP(III) is more reactive then PP(V) at all pHs and unlike PP(V) the hydrolysis of PP(III) shows a hydroxide-ion catalysed reaction at high pH. The rate of hydrolysis of pyrophosphate PP(V) steadily decreases with increasing pH as shown in Figure 1.13 - the rate constants for the tri- and tetra-anion are calculated from a recent report from measurements at high temperatures but extrapolated to 25^oC^{84} but those for the neutral, mono- and di-anionic species are from our ^{31}P NMR observations.

1.3.3.1 PP(III) hydrolysis

The observed pseudo first-order rate constant for the hydrolysis of PP(III) between pH 2 and 4 shows a first-order dependence on $[H^+]$ where the dominate species in solution is the di-anion ($PP(III)^{2-}$). Below pH 2 this changes to a second-order dependence on $[H^+]$ which is more clearly shown by the enlarged area between pH 0 and 4 (Figure 1.14) and by the changes in values of $k_{obs}/[H^+]$ as a function of pH (Figure 1.15).

Between pH 5 and 8 there is a pH independent term for the hydrolysis of the PP(III) di-anion which is then followed by a first-order dependence on hydroxide-ion at high pH. Thus the observed rate law is given in Equation 1.10 where k_1, k_2, k_0 and k_{OH} refer to the rate constants for the hydrolysis of PP(III) di-anion, the major species over the pH range studied, so k_1 refers to the reaction with PP(III) di-anion and $[H^+]^2$ or its kinetic equivalent, k_2 is that which is first-order in H^+ concentration, k_0 is the pH independent hydrolysis and k_{OH} is the second-order rate constant for the hydroxide catalysed hydrolysis of $PP(III)^{2-}$.

$$\mathrm{Rate}/[\mathrm{PP(III)}^{2-}] = k_{\mathrm{obs}} = k_1[\mathrm{H}^+]^2 + k_2[\mathrm{H}^+] + k_0 + k_{\mathrm{OH}}[\mathrm{OH}^-]$$

Equation 1.10

The pH-rate profile at low pH does not indicate any signs of levelling off of the pseudo first-order rate constant or a reversion to a first-order dependence on $[H^+]$ which may be expected if the PP(III) mono-anion or undissociated acid became the significant species in solution. The rate constants for the kinetic term k_1 and k_2 can also be obtained from the slope and intercept of a plot of $k_{obs}/[H^+]$ against $[H^+]$ which are 1.77 x 10^{-1} M^{-2} s^{-1} and 1.10 x 10^{-2} M^{-1} s^{-1} respectively (Figure 1.15). The first two terms in the rate law, k_1 and k_2 have kinetically equivalent expressions. For example the k_1 term could represent the spontaneous hydrolysis of the neutral PP(III), or the acid catalysed hydrolysis of the PP(III) mono-anion and the k_2 term could reflect either the spontaneous hydrolysis of the mono anionic species or even hydroxide-ion attack upon the neutral species, although the calculated rate constant for the latter $k_2.K_1.K_2/K_w$ is greater than that of a diffusion controlled rate and therefore can be excluded.

k_1	2.00 x 10^{-1} (*2.05 x 10^{-1}) (M^{-2} s^{-1})
k_2	9.40 x 10^{-3} (*8.32 x 10^{-3}) (M^{-1} s^{-1})
k_0	1.20 x 10^{-7} (*1.20 x 10^{-7}) (s^{-1})
k_{OH}	1.35 x 10^{-1} (*1.45 x 10^{-1}) (M^{-1} s^{-1})

Table 1.6 Rate constants for the hydrolysis of $PP(III)^{2-}$ at 25°C and I = 1.0 M (* obtained using Excel Solver to minimise the sum of the squared residuals).

The calculation of the rate constants for these kinetically equivalent mechanisms requires a knowledge of the two pK_a's of PP(III). The estimated value of pK_{a2} = 0.44 i.e. K_{a2} = 0.36 M is subject to error and there is no simple way to estimate pK_{a1}. Nonetheless it is a worthwhile exercise to enable a comparison with the PP(V) analogues. The third-order rate constant k_1 is kinetically equivalent to the spontaneous hydrolysis of the undissociated acid with a first-order rate constant equal to $k_1.K_{a1}.K_{a2}$. Based on the pH dependence of the ^{31}P {H} NMR chemical shifts (Figure 1.10) and the pH-rate profile (Figure 1.13) the product $K_{a1}.K_{a2}$ is $>10^{-1}$. The calculated rate constant for the hydrolysis of the undissociated PP(III) is thus > 0.073 s^{-1}. Presumably, the undissociated PP(III) is much more reactive than its mono- and di-anions so that between pH 1 and 2 it is the reactive hydrolytic species even though its concentration is small and falls off with a second-order dependence on $[H^+]$. Similarly, between about pH 2 and 5 where the rate of hydrolysis shows a first-order dependence on $[H^+]$ and the rate law is dominated by the k_2 term in (Equation 1.10), hydrolysis is probably occurring through the mono-anion of PP(III) even though, again, the dominant species in solution is the di-anion.

The calculated first-order rate constant for the hydrolysis of the mono-anion PP(III)$^-$ is given by $k_2.K_{a2} = 3.41 \times 10^{-3}$ s^{-1}. The rate constant for the spontaneous hydrolysis of the PP(III) di-anion is 1.20×10^{-7} s^{-1}, so the relative hydrolytic reactivities of the neutral, anionic and di-anionic PP(III) are approximately: $6 \times 10^5 : 3 \times 10^4 : 1.0$, respectively. The rates of hydrolysis of the neutral and mono-anionic PP(III) differ by a factor of 20 and presumably both involve nucleophilic attack by water in a concerted mechanism (S_N2(P)) (Scheme 1.45) or a associative mechanism involving a penta-coordinate intermediate on the more electrophilic neutral P centre although they require the expulsion of different leaving groups, the H-phosphonate mono- and di-anions, respectively (Scheme 1.45).

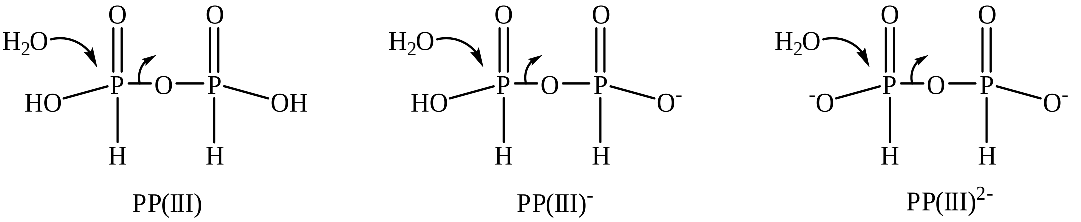

Scheme 1.45 Possible mechanism for the spontaneous hydrolysis of each PP(III) species.

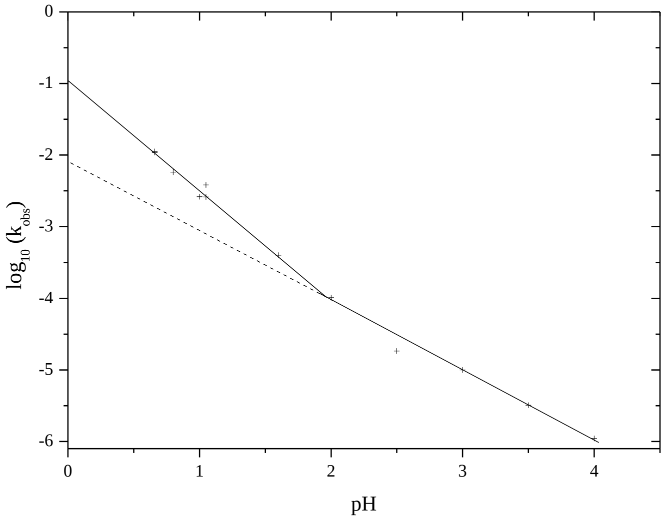

Figure 1.14 pH-rate profile enlarged from Figure 1.13 to show the change from first-order dependence on H$^+$ (dashed line is a continuation of a first-order dependence on H$^+$) to second-order dependence on H$^+$.

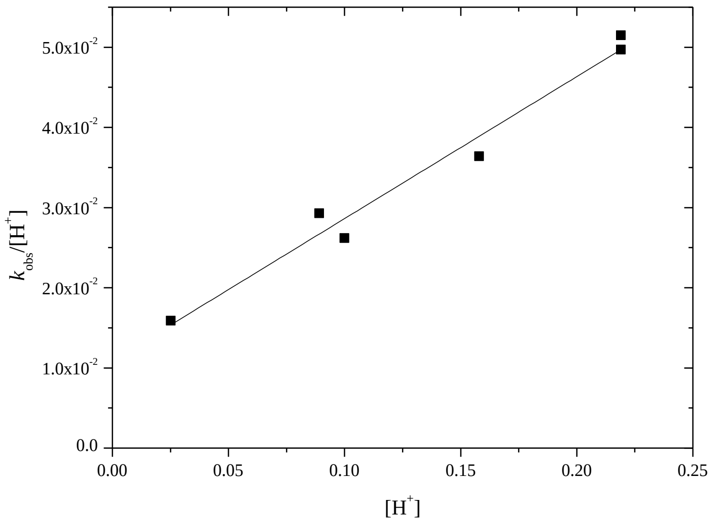

Figure 1.15 Plot of observed pseudo first-order rate constants divided by the hydrogen ion concentration against hydrogen ion concentration between pH 0.66 and 1.6, showing the second-order dependence on hydrogen ion concentration. The rate constant k_2 which is first-order in $[H^+]$ is given by the intercept. The third-order rate constant, k_1 which is second-order in hydrogen ion concentration was obtained from the slope.

There have been other studies of the hydrolysis of PP(III) using analytical techniques other than ^{31}P NMR. For example Mesmer and Carroll studied the hydrolysis of PP(III) at 30^{o}C (Figure 1.16), but only reported a hydrogen-ion and hydroxide-ion catalysed reaction. However, a re-analysis of their data in acidic media shows that the hydrolysis of PP(III) does not follow a first-order dependence on H^+, concentration which is demonstrated by the variation their first-order rate constants (k_{obs}) from 5.17 x 10^{-3} s^{-1} to 0.21 s^{-1} as hydrogen ion concentration from 0.0975 M to 0.975 M, respectively[88]. A plot of log k_{obs} against pH actually gives a slope = 1.56. Under basic conditions they found a first-order dependence of the rate of the hydrolysis of PP(III)$^{2-}$ on hydroxide-ion concentration and an average second-order rate constant (k_{OH-}) = 0.31 M^{-1} s^{-1} at 30^{o}C, compared with our value of 0.135 M^{-1} s^{-1} at 25^{o}C[88].

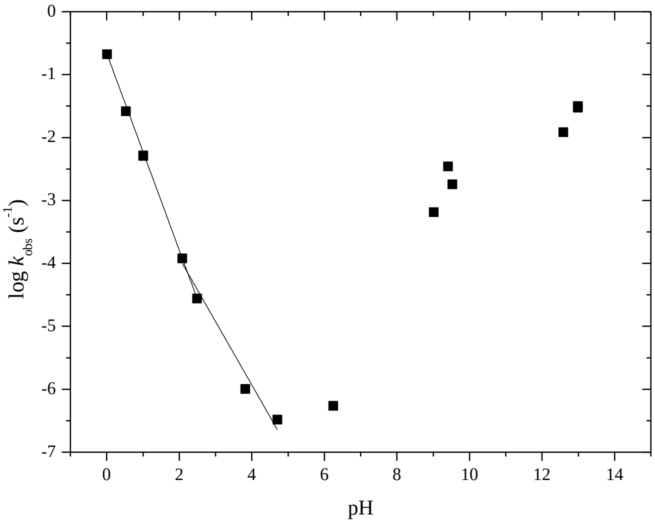

Figure 1.16 pH-rate profile constructed from the data of Mesmer and Carroll for the hydrolysis of PP(III) at 30°C[88].

1.3.3.2 PP(V) hydrolysis

In contrast to those for the hydrolysis of PP(III), the observed pseudo first-order rate constants for the hydrolysis of PP(V) continue to decrease with increasing pH (Figure 1.13) as the state of ionisation increases and PP(V) forms anions of increasingly lower reactivity.

The known pK_a values (0.79 (I = 1.0 M), 1.72 (I = 1.0 M), 6.6 and 9.4) of PP(V)[24, 89] and the rate constants obtained in this work over the pH range -2 – 4 (Table 1.7) have been used to generate the overall pH-rate-profile (Figure 1.13) using the overall rate-law for PP(V) (Equation 1.11). The rate constants for the tri- and tetra-anions of PP(V) are taken from the recent literature obtained by extrapolation from determinations at elevated temperatures[84] (Figure 1.17) and are compatible with other reports[45, 90, 91].

$$\text{Rate} = k_{\text{H}}[\text{PP(V)}][\text{H}^+] + k_0[\text{PP(V)}] + k_{1-}[\text{PP(V)}^-] + k_{2-}[\text{PP(V)}^{2-}] + k_{3-}[\text{PP(V)}^{3-}] + k_{4-}[\text{PP(V)}^{4-}]$$

Equation 1.11

k_H	1.30 x 10^{-5} (*1.33 x 10^{-5}) (M^{-1} s^{-1})
k_0 (I = 1.0 M)	1.00 x 10^{-7} (s^{-1})
k_{1-} (I = 1.0 M)	7.00 x 10^{-8} (s^{-1})
k_{2-} (I = 1.0 M)	3.50 x 10^{-8} (*3.59 x 10^{-8}) (s^{-1})
k_{3-}	1.07 x 10^{-9} (s^{-1}) ^
k_{4-}	8.59 x 10^{-13} (s^{-1}) ^

Table 1.7 Rate constants for the hydrolysis of PP(V) at 25°C. k_0 and k_{1-} have been estimated due to the lack of experimental data points. (* obtained using Excel Solver to minimise the sum of the squared residuals), (^ from [84]).

There is no base-catalysed hydrolysis observed in the hydrolysis of the PP(V) anions in alkaline solutions. This is unlike the behaviour of di-anionic PP(III) species which, despite its negative charges, does undergo a hydroxide-ion catalysed hydrolysis and, consequently PP(III) is much more reactive than PP(V) at high pH.

There are kinetically equivalent processes for the hydrolysis of PP(V). For example, if the reported rate constant for the spontaneous hydrolysis of PP(V) tri-anion[84] actually reflects the kinetically equivalent hydroxide-ion catalysed hydrolysis of the di-anion, then the corresponding second-order rate constant would be $K_{a3}.k_{3-}/K_w$ = 1.7 x 10^{-3} M^{-1} s^{-1} which can be compared with k_{OH} for $PP(III)^{2-}$ = 1.35 x 10^{-1} M^{-1} s^{-1}.

The hydrolysis of pyro-di-H-phosphonate is 79 fold higher compared with pyrophosphate, so the hydrolysis of the PP(V) tri-anion probably does occur through a mechanism involving hydroxide-ion attack on the di-anion.

Little work has been done regarding the hydrolysis of pyrophosphate around room temperatures due to its slow hydrolysis rate. Willard, Kim and Sullivan in 1984 published kinetic data on the hydrolysis of ammonium pyrophosphate at 25°C. At pH 4-6 where the major species is the di-anion, for which a k_{2-} rate constant of approximately 2.00 x 10^{-8} s^{-1} can be obtained which is in reasonable agreement with the results we obtained at 25°C[43] (Table 1.7).

The hydrolysis of PP(V) has been investigated by several researchers under acidic and basic conditions at high temperature and their reported rate constants (Table 1.8).

Contributor	Osterheld	Campbell and Kilpatrick	McGilvery and Crowther
Temp (°C)	60.0	59.9	65.5
Ionic Strength (M)	0.44	0.15	
Rate constants (s^{-1})			
$H_5P_2O_7^+$	≥ 1.92		
$H_4P_2O_7$	6.17 x 10^{-4}		3.83 x 10^{-3}
$H_3P_2O_7^-$	4.00 x 10^{-4}	2.00 x 10^{-4}	7.33 x 10^{-4}
$H_2P_2O_7^{2-}$	1.87 x 10^{-4}	1.59 x 10^{-4}	2.83 x 10^{-4}
$HP_2O_7^{3-}$	6.00 x 10^{-6}		5.25 x 10^{-5}
$P_2O_7^{4-}$			4.67 x 10^{-6}

Table 1.8 Summary of rate constants for the different anionic species of PP(V) at high temperature[44].

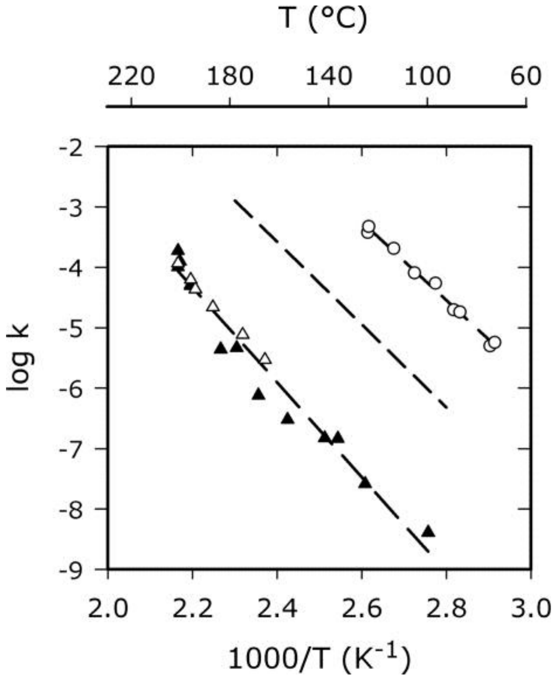

Figure 1.17 Arrhenius plot of pyrophosphate, o represent the hydrolysis of $H_2P_2O_7^{2-}$ at pH 5 and $P_2O_7^{4-}$ in 1 M KOH (▲) and 2 M KOH (Δ). The dashed line represents $HP_2O_7^{3-}$ [84].

1.3.3.3 Mixed P(III.V)

Interestingly a study carried out by Carroll and Mesmer in 1967 had examined the hydrolysis of isohypophosphate a compound which contains phosphorus atoms in P(III) and P(V) oxidation states which are bridged by oxygen (Figure 1.18).

This compound contains three dissociable protons, the first pK_{a1} was estimated to be 0.6 which is most likely to be of the P(III) phosphorus atom as the dissociable protons of PP(III) are more acidic than those of P(V). The second (pK_{a2}) and third (pK_{a3}) were determined by titration to be 1.67 and 6.26, respectively at 25°C[87].

The hydrolysis of isohypophosphate between pH 0.4 and 4.5 could be described by the rate law:

$$\text{Rate} = k_{1-}[\text{PP(III.V)}^{-}][\text{H}^{+}]^{2} + k_{2-}[\text{PP(III.V)}^{2-}][\text{H}^{+}]$$

Equation 1.12

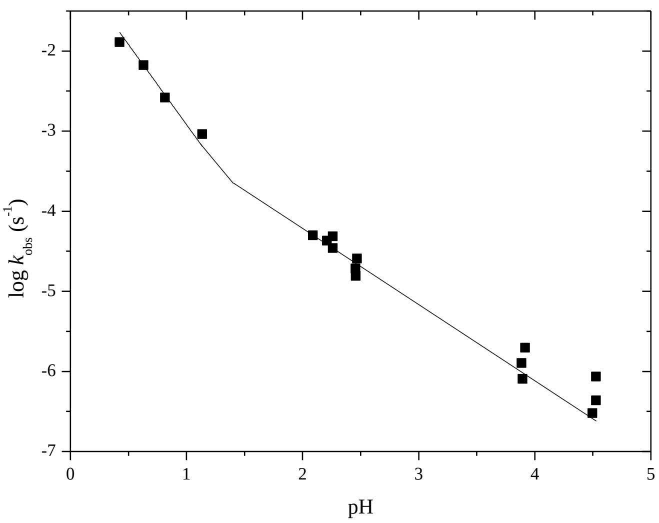

Figure 1.18 pH rate-profile for the hydrolysis of PP(III.V) at 25°C[87].

Between pH 2 and 4.5, the dominant species is the di-anion and although the observed first-order rate constants were not extrapolated to zero buffer concentration, it is observed that the rate of hydrolysis is first-order in hydrogen-ion concentration with a rate constant of 9.0 x 10^{-3} M^{-1} s^{-1}, which is kinetically equivalent to the spontaneous hydrolysis of the mono-anion (k_{2-} .K_{a2}) (Figure 1.18). Between pH 0.42 and 1.14 the dominant species is the mono-anion and the rate changes to a second-order dependence in hydrogen ion with a rate constant

(k_H) = 0.22 M^{-2} s^{-1}, which is kinetically equivalent to the acid catalysed hydrolysis of the undisscocated acid ($k_{1-}.K_{a1}$) (slope =1.65). If the first of pK_a is 0.6, as estimated one would expect the pseudo first-order rate constant to level off or revert back to a first-order dependence on [H^+], at pH < 0.6. In comparison to the hydrolysis of PP(III) mono-anion, the mixed PP(III.V) has a slower rate of hydrolysis by 18 fold, which would be expected as the rate of hydrolysis of pyrophosphate mono-anion is much lower than PP(III) and PP(III.V).

The rate constants for the hydrolysis of PP(III), PP(V) and PP(III.V) all at 25°C are summarised in Table 1.9.

Species	**Pyrophosphate PP(V)**	**Pyro-di-H-phosphonate PP(III)**	**Isohypophosphate PP(III.V)**
Acid catalysed	1.30×10^{-5} M^{-1} s^{-1}	-	5.5×10^{-2} M^{-1} s^{-1}
Neutral	1.00×10^{-7} s^{-1}	7.3×10^{-2} s^{-1}	-
Mono-anion	7.00×10^{-8} s^{-1}	3.41×10^{-3} s^{-1}	1.92×10^{-4} s^{-1}
Di-anion	3.50×10^{-8} s^{-1}	1.20×10^{-7} s^{-1}	-
Tri-anion	1.07×10^{-9} s^{-1}	-	-
Tetra-anion	8.59×10^{-13} s^{-1}	-	-

Table 1.9 Summary of rate constants for the hydrolysis of PP(III), PP(V) and PP(III.V) at 25°C.

1.3.4 Hydrolysis of other P(III) derivatives

The hydrolysis of diethyl pyro-di-H-phosphonate and diethyl H-phosphonate were studied as neither have dissociable protons to complicate the kinetics. They both produce the same mono-ester intermediate which can be hydrolysed further (Scheme 1.46).

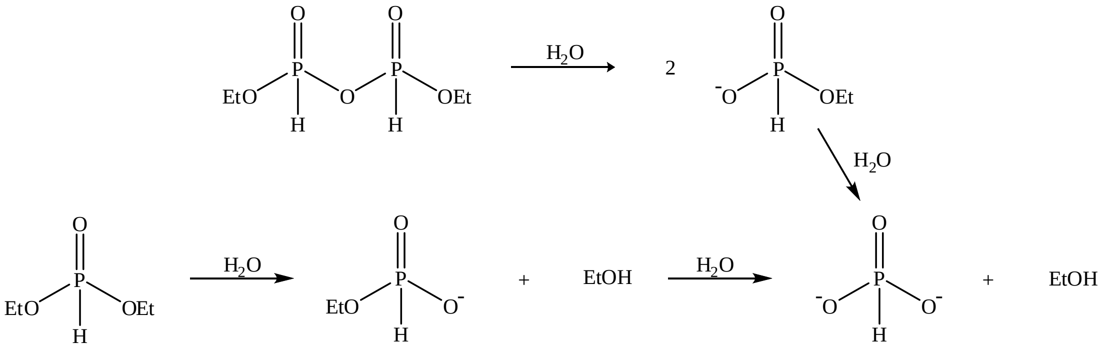

Scheme 1.46 Hydrolysis of diethyl pyro-di-H-phosphonate and diethyl-H-phosphonate.

The hydrolysis rate of di-ethyl pyro-di-H-phosphonate at pH 7 was too fast to measure by $^{31}P\{H\}$ NMR and is therefore > 0.1 s^{-1} [92].

Determined by ^{31}P NMR, di-ethyl H-phosphonate shows an acid catalysed hydrolysis to give ethyl H-phosphonate and ethanol with a second-order rate constant $k_{H+} = 1.21 \times 10^{-4}$ M^{-1} s^{-1} at 25°C (I = 1.0 M). It also shows a hydroxide-ion catalysed hydrolysis with a second-order rate constant $k_{OH-} = 81.3$ M^{-1} s^{-1} at 25°C (I = 1.0 M) which was obtained from the observed pseudo first-order rate constants, extrapolated to zero buffer concentration, at constant pH's.

Ethyl H-phosphonate also shows an acid catalysed rate of hydrolysis $k_{H+} = 6.90 \times 10^{-6}$ M^{-1} s^{-1} which is 18x slower than that for diethyl H-phosphonate, and a hydroxide-ion catalysed hydrolysis with a second-order hydrolysis rate $k_{OH^-} = 1.55 \times 10^{-5}$ M^{-1} s^{-1}, which is 5×10^6 less than that for diethyl H-phosphonate due to the additional negative charge repulsing the negatively charged nucleophile. The acid catalysed hydrolysis of ethyl H-phosphonate mono-anion is kinetically equivalent to the hydrolysis of the neutral ethyl H-phosphonate and, assuming the pK_a of ethyl H-phosphonate is approximately 0, the corresponding first-order rate constant would be 6.90×10^{-6} s^{-1}.

Using the above rate data, a Brønsted plot can be obtained for the calculated rate constants for the spontaneous hydrolysis of (HO)P(O)H-X (Table 1.10) by plotting log k_0 against pK_a of the leaving group (XH).

X	pK_a XH	k_0 (s^{-1})
H_2PO_3	1.1	> 0.073
HPO_3^-	6.6	3.41 x 10^{-3}
EtO	15.9	6.90 x 10^{-6}

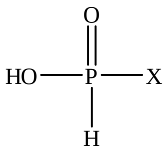

Table 1.10 Summary of the estimated kinetic data calculated for the spontaneous pH independent hydrolysis of H-phosphonate derivatives (HO)P(O)H-X at 25°C.

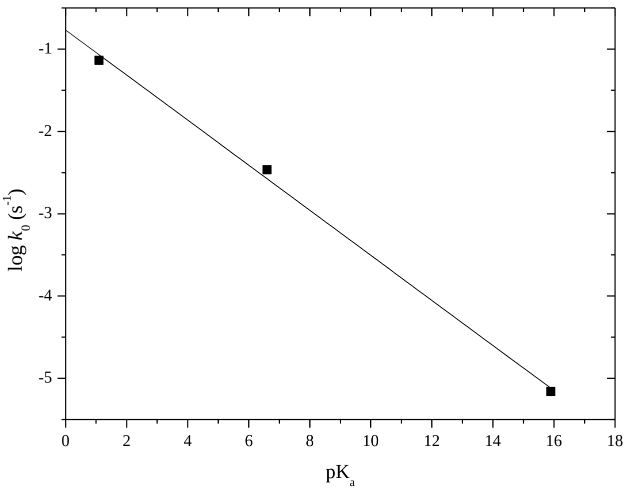

Figure 1.19 Brønsted plot for the spontaneous pH independent hydrolysis of H-phosphonate derivatives (HO)P(O)H-X at 25°C as a function of the pK_a of the leaving group XH.

Although only based on a three point Brønsted plot (Figure 1.19) it does cover a pK_a range of 14 and is linear giving a β_{lg} = -0.27. This indicates that there is little or no P-O bond cleavage in the transition state with a small development of charge on the oxygen relative to the reactant which is consistent of a rate limiting formation of a trigonal bipyramidal intermediate (Scheme 1.47).

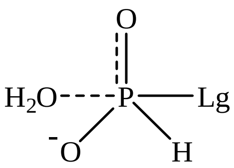

Scheme 1.47 Trigonal bipyramidal intermediate indicates little charge and bond cleavage in the transition state.

A summary of the kinetic data for the hydrolysis of H-phosphonates is given in Table 1.11:

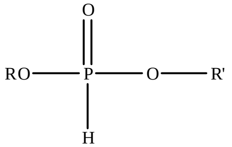	R’			
RO	-Et	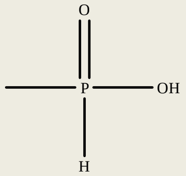	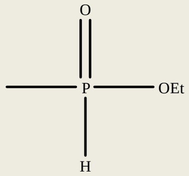	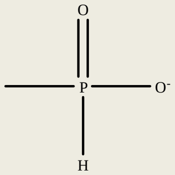
OH	$6.90 \times 10^{-6}\ s^{-1}$	$> 7.3 \times 10^{-2}\ s^{-1}$	-	$3.41 \times 10^{-3}\ s^{-1}$
EtO	$*81.3\ M^{-1}\ s^{-1}$	-	$> 0.1\ s^{-1}$	-
O^-	$*1.55 \times 10^{-5}\ M^{-1}\ s^{-1}$	$3.41 \times 10^{-3}\ s^{-1}$	-	$1.20 \times 10^{-7}\ s^{-1}$ $*1.35 \times 10^{-1}\ M^{-1}\ s^{-1}$

Table 1.11 Summary of rate constants for different H-phosphonates (* hydroxide catalysed rate constant) at 25°C, I = 1.0 M.

1.3.5 Mechanisms of hydrolysis of PP(III) and PP(V)

Pyro-di-H-phosphonate di-anion is the major species in water above pH 2. The pH-rate profile clearly shows a pH independent rate of hydrolysis from pH 4-8 and a reaction involving hydroxide-ion above pH 8 (Scheme 1.48, i, ii). It is likely that an associative mechanism is involved in the hydrolysis of PP(III) which involves the formation of a penta-coordinate phosphorane intermediate as there is small charge development in the transition state indicating little P-O bond cleavage (Figure 1.19).

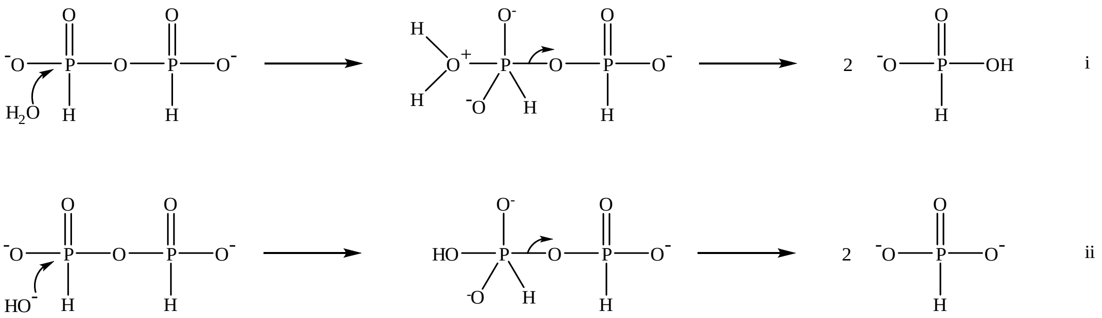

Scheme 1.48 Hydrolysis mechanism of PP(III) by water (i) and hydroxide (ii).

The second-order rate constant for the hydroxide-ion hydrolysis of PP(III) di-anion k_{OH} is 10^6, fold greater than that for k_0 the pH independent rate constant.

It is most likely that the undissociated and mono-anion of pyrophosphate PP(V) hydrolyse via an associative mechanism as an additional negative charge would be required to form the meta-phosphate intermediate[93]. There is a possibility that the di-anion can hydrolyse through a dissociative mechanism as long as the second dissociation occurs on the same phosphorus (Scheme 1.49)

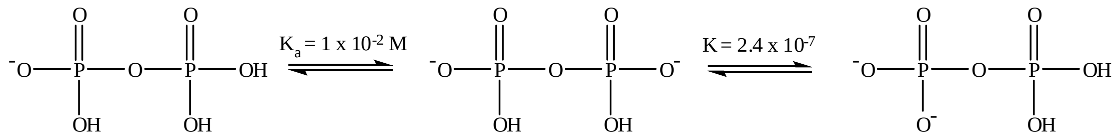

Scheme 1.49 Dissociation of a proton to form the pyrophosphate di-anion.

The equilibrium between the PP(V) di-anion with negative charges on different P-O's and the di-anion with them on the same P can be estimated as about 2.4×10^{-7} by analogy to the difference in the pK$_a$'s of ethyl phosphate. So a rough estimate of the rate of hydrolysis PP(V)$^{2-}$ with both negative charges on the same P is = 0.15 s^{-1} ($k_2 = 3.50 \times 10^{-8} / 2.4 \times 10^{-7}$).

An additional factor in-favour of the dissociative mechanism involves the departure of a good leaving group which has a pK$_a$ of 2 (Scheme 1.50).

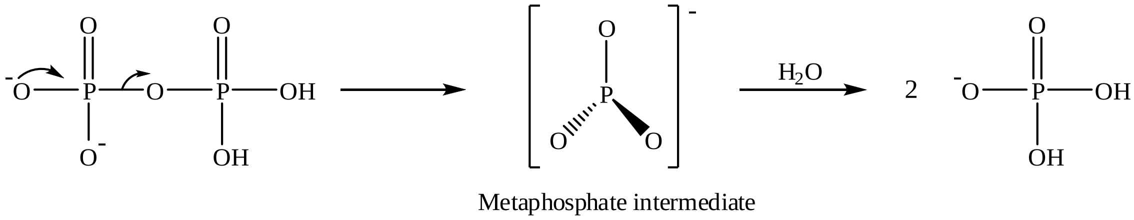

Scheme 1.50 A possible mechanism for pyrophosphate di-anion hydrolysing via a dissociative mechanism to yield phosphoric acid.

Pyrophosphate tri-anion may also hydrolyse via a dissociative mechanism although the leaving group is not as acidic. The hydrolysis of the tetra-anion involves the expulsion of a basic phosphate di-anion and a dissociative mechanism is still possible as the kinetically equivalent mechanism of hydroxide-ion attack on the tri-anion is electrostatically unfavourable.

1.3.6 Metal coordination to PP(III) and PP(V)

Many enzymes require one or more metal-ion(s) to aid hydrolysis and transesterification of phosphate esters. Although metal-ion binding has been studied extensively for pyrophosphate, there have been few reports on metal-ion coordination to pyro-di-H-phosphonate. The natural substrate of pyrophosphatase is pyrophosphate where metal-ions aid hydrolysis by facilitating the formation of a nucleophile and neutralising the negative charge on pyrophosphate. For pyrophosphatase to catalyse the hydrolysis of pyro-di-H-phosphonate, presumably the latter must be able to coordinate divalent cations such as magnesium. Isothermal titration calorimetry (ITC) shows that magnesium complexes 1:1 with pyrophosphate at pH 8.40 at 25°C (Figure 1.20). The majority of pyrophosphate at pH 8.40 exists as the tri-anion (~90%) and only ~9% as the tetra-anion. It is believed that the major species, magnesium pyrophosphate complex is the di-anion, $MgPP^{2-}$ with magnesium complexed to the tetra-anion which is thought to the true substrate of pyrophosphatase in solution[84]. The complexing of magnesium-ion to pyrophosphate tri-anion must therefore ionise by subsequently lowering the pK_a of the final hydroxyl group (Scheme 1.51).

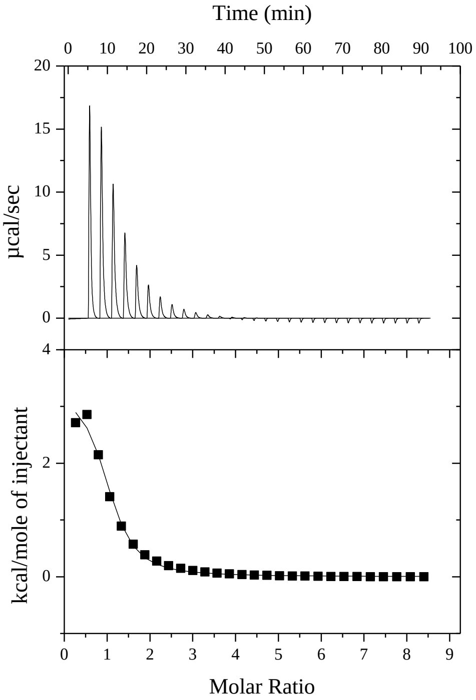

Figure 1.20 ITC isotherm of magnesium (21 mM) complexing with pyrophosphate (0.56 mM) buffered by HEPES at pH 8.40, I = 0.1 M and 25°C.

ITC provides the binding constant (K_b) = 1.64 x 10^4 M^{-1} and an enthalpy (ΔH_{obs}) of complexation = 13.9 kJ mol^{-1}. The binding constant is in reasonable agreement with the literature binding constant (K_b) of 2.0 x 10^4 M^{-1} for the $MgPP^{2-}$complex[84]. Given the thermodynamically favourable binding of Mg^{2+} to PP(V) one may expect the binding to show an exothermic change, but clearly the isotherm shows a large endothermic reaction. The endothermic heat observed is probably due to neutralisation by the buffer of the proton released by Mg^{2+} binding to $PP(V)^{3-}$ (Scheme 1.51), and desolvation of the water molecules which are coordinated to the magnesium-ion upon binding with pyrophosphate.

The titration of 8.5 equivalents of magnesium into pyrophosphate did not show any further complexation or precipitation.

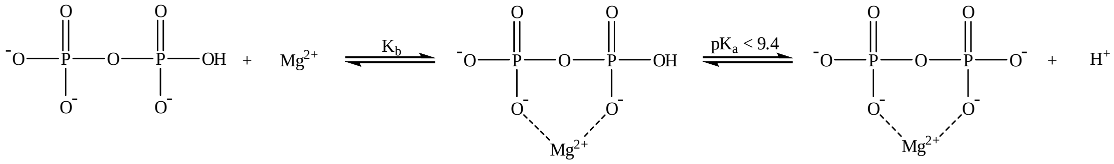

Scheme 1.51 Pyrophosphate tri-anion complexing with magnesium-ion and dissociation of the final proton which contributes to the overall enthalpy of complexation.

The enthalpy of association between A^- of the HEPES buffer and H^+ to form HA is -21.01 kJ mol^{-1} [94] which can be subtracted from the observed ITC enthalpy providing a enthalpy of magnesium complexation to pyrophosphate tri-anion of 34.88 kJ mol^{-1} at pH 8.40.

^{31}P NMR was used to confirm the ITC data which also showed that titrating different equivalents of magnesium-ion (0.5, 1 and 2) complexed with pyrophosphate (10 mM) in a 1:1 ratio without precipitation but on addition of 2 mole equivalents of magnesium, a white precipitate was formed. An NMR of the clear solution (Figure 1.21, purple) once the precipitate had settled confirmed all the pyrophosphate had complexed with magnesium.

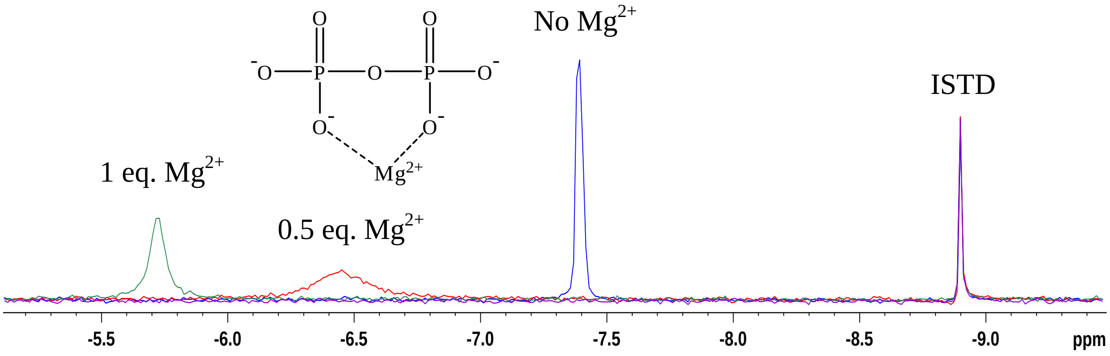

Figure 1.21 ^{31}P {H} NMR of Pyrophosphate before the addition of Mg^{2+} (blue) and after the addition of 0.5 (red), 1 (green) molar equivalents of Mg^{2+} at pH 8.40 and 25°C with reference to diphenyl phosphate.

For comparison, the possible magnesium complexing with PP(III) was investigated, using ITC, in water at pH 6 where pyro-di-H-phosphonate exits primarily as the di-anion. The isotherm (Figure 1.22) shows no signs of a sigmoidal trace associated with a binding event involving a heat change. This indicates no or very weak binding to PP(III) even after 9 mole equivalents of magnesium-ion were added.

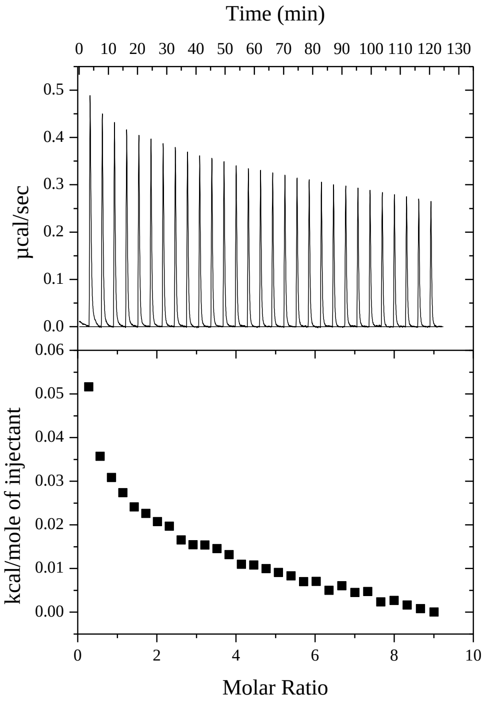

Figure 1.22 ITC isotherm titrating magnesium (20 mM) against pyro-di-H-phsophonate (0.5 mM) buffered by MES at pH 6.00, I = 0.1 M and 25°C

^{31}P NMR showed, upon addition of 2 mole equivalents of magnesium (Figure 1.23, purple), the NMR chemical shift did not alter significantly compared to the solution containing no magnesium, confirming little or no complexing.

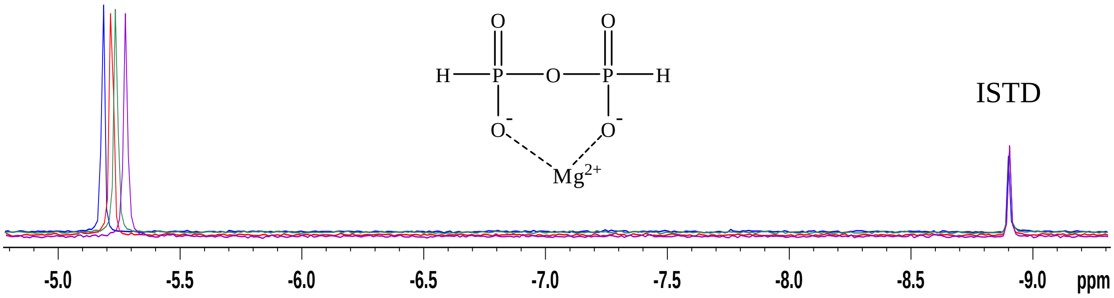

Figure 1.23^{31}P{H} NMR of Pyro-H-phosphonate before the addition of Mg^{2+} (blue) and after the addition of 0.5 (red), 1 (green) and 2 (purple) molar equivalents of Mg^{2+} at pH 8.40 and 25°C with reference to diphenyl phosphate.

Calcium ions were also titrated against PP(III) at pH 6 (Figure 1.24) which also showed no binding event no greater than the heats of dilution.

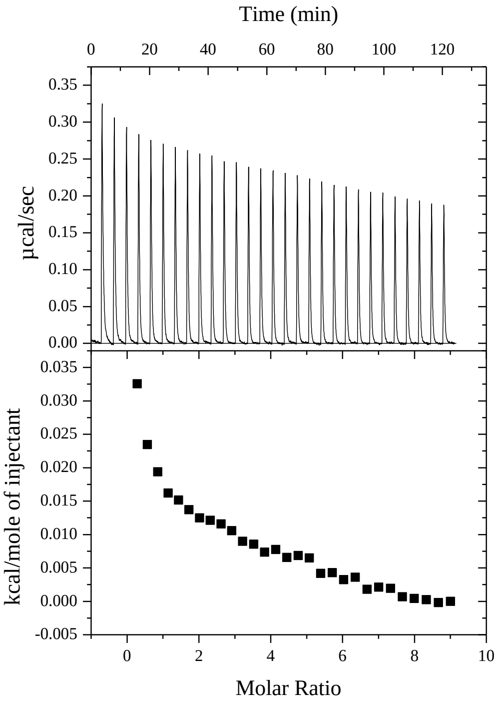

Figure 1.24 ITC isotherm of calcium (20 mM) complexing with pyro-di-H-phsophonate (0.5 mM) buffered by MES at, pH 6.00, I = 0.1 M and 25°C.

The weaker binding of PP(III)$^{2-}$ to metal-ions compared with PP(V)$^{3-}$/PP(V)$^{4-}$ is presumably due to the weaker basicity of PP(III)$^{2-}$ and less charge density (pK_a of PP(III) - < 0.5) compared with that of PP(V)$^{3-}$ (pK_a of PP(V)$^{2-}$ = 6.6).

1.3.7 Hydrolytic effect of metal-ions on pyro-di-H-phosphonate

The hydrolysis of pyrophosphate is enzymatically catalysed by pyrophosphatase, where the enzyme uses more than one magnesium-ion to aid catalysis. ATP is also a substrate for this enzyme but studies have shown that bivalent metal-ions catalyse the non-enzymatic transfer of phosphate from ATP to acceptors such as orthophosphate. When orthophosphate is the phosphate acceptor, it yields pyrophosphate as the product[95].

In order for pyrophosphatase to catalyse the hydrolysis of pyro-di-H-phosphonate presumably it must be able to complex magnesium-ion, as the enzyme complexes magnesium-ion to the natural substrate pyrophosphate. Although the addition of Mg^{2+} to PP(III)$^{2-}$ showed no observable binding, using ^{31}P {H} NMR and ITC, it does increase the rate of hydrolysis giving of PP(III)$^{2-}$ (Figure 1.25) a second-order rate constant of 2.20×10^{-5} M^{-1} s^{-1} at pH 7 (I = 1.0 M).

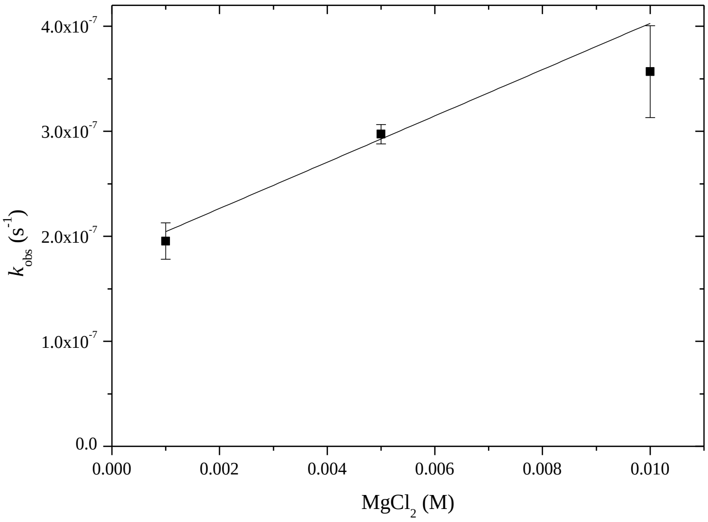

Figure 1.25 Pseudo first-order rate constants for the hydrolysis of PP(III)$^{2-}$ against $MgCl_2$ concentration at pH 7, I = 1.0 M at 25°C.

Ueda and Sasaki have investigated the effect of metal-ions on the hydrolysis of pyro-di-H-phosphonate at pH 4.6. A variety of metal-ions, including Mg^{2+}, showed no significant increase in the rate of hydrolysis of PP(III). The only exception was the addition of 0.5 mM Cu^{2+}, which increased the rate by 3 fold[96].

If it is assumed that Mg^{2+} catalysis is due to initial complexation of Mg^{2+} to PP(III) di-anion followed by nucleophilic attack by water and that metal-ion binding has a weak association constant of $<10^{-2}$, then the calculated rate constant for water attack on this complex is $> 2 \times 10^{-3}$ s^{-1} which is 4-orders of magnitude greater than that for the uncomplexed PP(III) di-anion. The Mg^{2+} catalysed hydrolysis of PP(V) at neutral pH is assumed[84] to be that of the tetra-anion, i.e. the overall di-anionic $MgPP^{2-}$ is the reactive species with an estimated rate constant at 25°C of 2.8×10^{-10} s^{-1}, three orders of magnitude greater than that of $PP(V)^{4-}$.

The process of phosphorylation and dephosphorylation that occur by associative type mechanisms usually have a penta-coordinate trigonal-bipyramidal geometry in the transition state, whereas in the case of the dissociative pathway it effectively involves a trigonal planar metaphosphate anionic species, PO^{3-}. The 3 orders of magnitude rate enhancement of the hydrolysis of PP(V) by Mg^{2+} is presumably due to the metal-ion binding to the tetra-anion and so neutralising some of the negative charge and facilitating nucleophilic attack by water. However, the hydrolysis of phosphate mono-esters proceeding through the dissociative pathway is not sensitive to the presence of Mg^{2+} ions in aqueous solution[97]. Although metal-ion coordination may enhance the electrophilicity of the phosphorus (Scheme 1.52) it will disfavour electron-donation from the non-bridging oxygens thus reducing their ability to assist in expelling the leaving group. Similarly, Mg^{2+} only enhances the rate of hydrolysis of ATP^{4-} by 3-fold and binds preferentially between the β and γ phosphates, making the di-anionic γ phosphate less effective at expelling the ADP leaving group, but it does not facilitate an alternative associative pathway[51]. An associative transition state can be sensitive to stabilization by Mg^{2+} ions if coordination occurs to the leaving group[50].

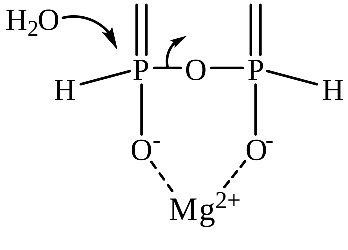

Scheme 1.52 Possible complexation of magnesium-ion to PP(III) which increases the rate of reaction.

1.3.8 Hydrolysis of PP(V) and PP(III) by pyrophosphatase

In primitive biological systems pyro-di-H-phosphonate or pyrophosphate may have acted as phosphoryl group donors[98]. In modern day organisms enzyme-catalysed hydrolysis is an important part of metabolism to remove PP(V) that is generated by biosynthetic reaction, yet on the other hand increasing phosphate levels can cause abnormal growth as in hypophosphatemia and rickets in children[99].

The pyrophosphatase catalysed hydrolysis of PP(V) was monitored by ITC as it provides a sensitive continuous assay compared to ^{31}P {H} NMR where PP(V) has limited solubility in the presence of magnesium-ion.

ITC can be used to follow the kinetics of an enzyme catalysed reaction because the amount of heat released is directly proportional to the amount of substrate that has reacted. The instrument output reflects the energy required to balance the heat generated by the reaction to maintain constant temperature (Figure 1.26). The initial positive spike probably represents the endothermic heat of injection/ dilution and magnesium-ion complexation to PP(V) as described earlier. The exothermic hydrolysis reaction gives a negative displacement from the baseline and as substrate is consumed, the rate at which heat is generated decreases and the output trace returns to the baseline.

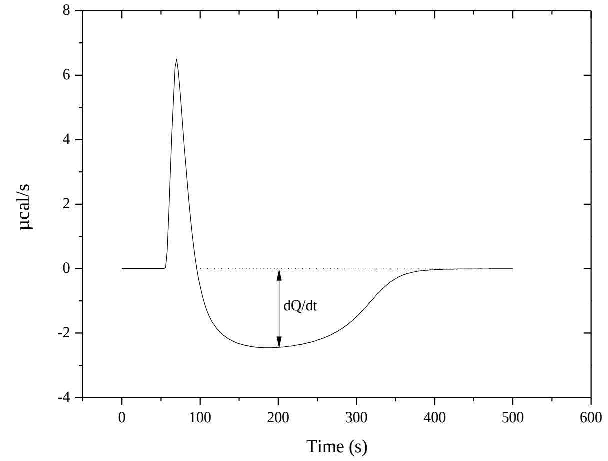

Figure 1.26 ITC trace of the enzymatic hydrolysis of pyrophosphate (PP(V)) with 1×10^{-9} M *E. coli* PPase, 3 mM $MgCl_2$, initiated with PP(V) to give a final concentration of 4.11×10^{-5} M at 25°C. The endothermic peak represents the heat of dilution and magnesium-ion complexation, followed by PP(V) consumption until the heat generated with respect to time (dQ/dt = power) returns to the baseline.

Using Equation 1.5, a plot of PP(V) concentration against time (Figure 1.27) was used to obtain the Michaelis-Menten kinetic parameters k_{cat} and k_{cat}/K_m. k_{cat} was obtained by dividing V_{max} by the enzyme concentration and the second-order rate constant k_{cat}/K_m was obtained by dividing k_{obs} by enzyme concentration.

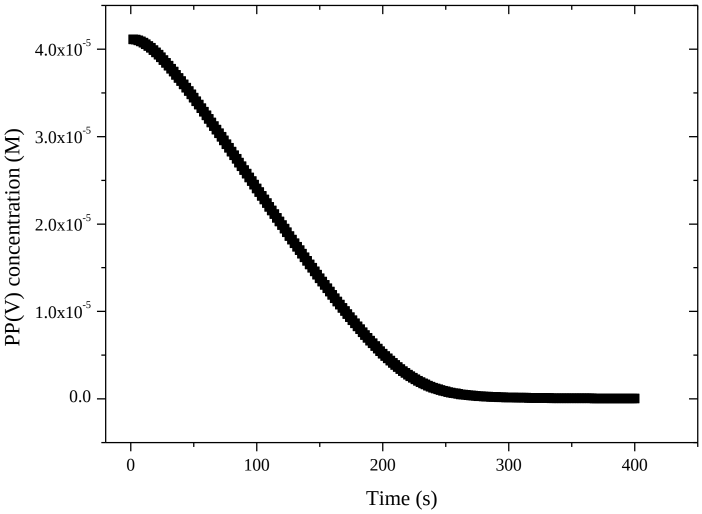

Figure 1.27 ITC trace converted to concentration of the enzymatic hydrolysis of pyrophosphate (PP(V)) with 1 × 10^{-9} M *E. coli* PPase at pH 8.40.

The k_{cat} values measured for PP(V) at 25°C at pH 8.40 and 7.55 were 208 s^{-1} and 82 s^{-1}, respectively. This is in good agreement with a value of k_{cat} = 290 s^{-1} at pH 8.40[84]. The second-order rate constant for the enzyme catalysed hydrolysis $k_{cat}/K_m = 3.68 \times 10^7$ M^{-1} s^{-1} and 2.89×10^7 M^{-1} s^{-1}, again at 25°C and, pH 8.40 and 7.55, respectively, and are very close to being diffusion-controlled enzymes which are characterised by having rate constants in the order of 10^8 M^{-1} s^{-1}[100].

As PP(III) has a very similar structure to PP(V) and it was thought possible that it may act as a substrate of pyrophosphatase and so, its hydrolysis was investigated using ^{31}P {H} NMR and ITC but neither method showed any observable reaction. Using pyrophosphatase from *E.coli* (2×10^{-7} M) there was no discernible rate difference from the background hydrolysis of PP(III) at pH 7.55 (300 mM buffer, 50 mM Mg^{2+}, I = 1.0 M), indicating that PP(III) is not a substrate and that k_{cat}/K_m is < 6 M^{-1} s^{-1}. This lack of reactivity may be due to PP(III) showing no significant binding to Mg^{2+} and/or having insufficient negative charge to bind to the positively charged active site of PPase.

PP(V) binds to the active site of *E.coli* PPase (Figure 1.28) through direct coordination of four magnesium-ions and three positively charged residues Lys_{142}, Lys_{29} and Arg_{43}. Shielding of the negatively charged oxygen atoms on pyrophosphate by magnesium and amino acid residues increases the electrophilcity of the phosphorus centre facilitating nucleophilic attack for hydrolysis.

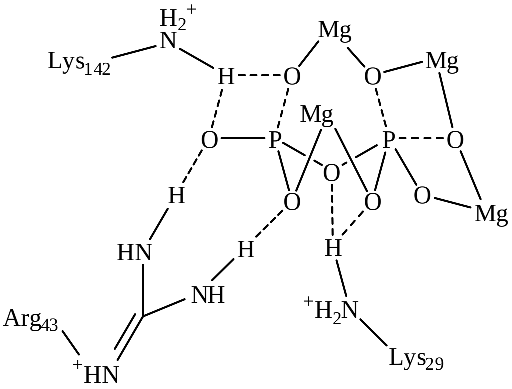

Figure 1.28 Active site of *E.coli* PPase coordinated to the natural substrate pyrophosphate[64].

1.3.9 Pyro-di-H-phosphonate as a potential inhibitor of pyrophosphatase

Although PP(III) is not an efficient substrate of *E.Coli* PPase, it may act as an inhibitor of the enzyme. Again using ITC, the cell contained 1×10^{-9} M *E.coli* PPase, 3 mM $MgCl_2$ and 1 mM PP(III). The reaction was initiated by the addition of PP(V) to give a final concentration of 4.11×10^{-5} M at 25 °C and pH 8.40 and 7.55. The kinetic parameters in the presence of PP(III) did show a small decrease compared with those in the absence of PP(III): at pH 8.40 $k_{cat} = 152\ s^{-1}$, $k_{cat}/K_m = 3.00 \times 10^7\ M^{-1}\ s^{-1}$ which represents a 27 % and 18 % decrease in k_{cat} and k_{cat}/K_m respectively. At pH 7.55 $k_{cat} = 60\ s^{-1}$, $k_{cat}/K_m = 2.48 \times 10^7\ M^{-1}\ s^{-1}$ this is a 26 % and 12 % decrease in k_{cat} and k_{cat}/K_m respectively. It is not possible to assign any significant inhibition of pyrophosphatase by PP(III) from these changes.

1.3.10 Heats of hydrolysis of PP(V) and PP(III)

The heat of hydrolysis of the P-O-P bond of pyrophosphate which is the product of hydrolysis of ATP has been investigated at high temperatures as at all pHs the reaction is too slow to be monitored calorimetrically. To overcome this problem, it has also been measured using an enzyme to catalyse hydrolysis. It was of interest to compare the heats of hydrolysis of PP(V) and PP(III).

The enthalpy of hydrolysis of pyrophosphate by pyrophosphatase was determined using ITC. As pyrophosphate has four dissociable protons with pK_as of 0.9, 2.0, 6.6 and 9.4 at 25^{o}C the enthalpy of hydrolysis is pH dependent as different ionic species exist in solution. When pyrophosphate is hydrolysed, two mole equivalents of phosphoric acid are produced which have pK_as of 2.15, 7.21 and 12.35 at 25^{o}C. At a fixed pH, there may thus be a change in the overall charge of the reactants and products as hydrolysis occurs, liberating or absorbing protons (Scheme 1.53).

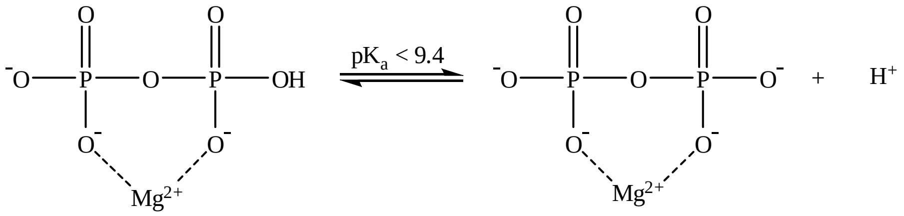

Scheme 1.53 Pyrophosphate tri-anion coordinating with magnesium-ion which consequently lowers the final pK_a of PP(V).

Deprotonation or protonation by the buffer would then also contribute to the observed enthalpy of hydrolysis (n). Consequently ΔH_{obs} can be expressed as:

$$\Delta H_{obs} = \Delta H_{pyrophosphate} + n\ (\Delta H_{buffer})$$

Equation 1.13

To eliminate the enthalpy contribution by the buffer, the hydrolysis of pyrophosphate was conducted in a series of buffers at constant pH 8.40 (Table 1.12) and 7.50 (Table 1.13) and ionic strength (I = 0.1 M) at 25^{o}C. The heat of hydrolysis of PP(V) was conducted using a single injection ITC method. Prior to injection the syringe contained 10 mM PP(V) and the cell contained 3 mM $MgCl_2$ and 1×10^{-9} M *E.coli* PPase. Both solutions were buffered either at pH 8.40 or 7.50 and I = 0.1 M. The heat of dilution and any other interactions were subtracted by using the same method described without the enzyme being present in the cell.

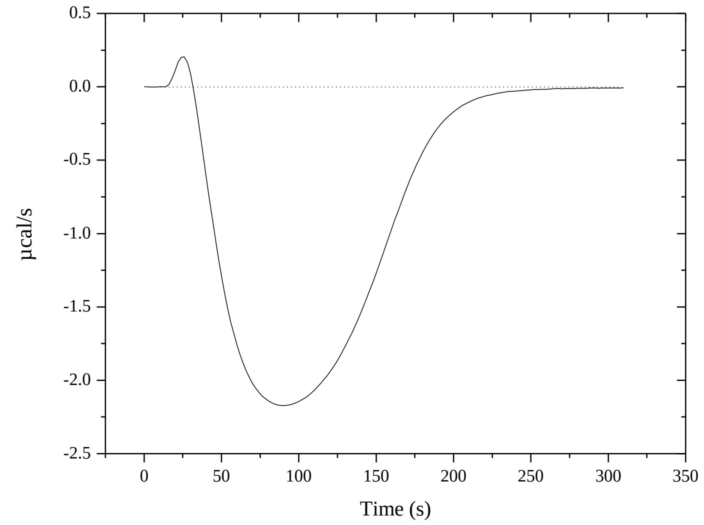

Figure 1.29 ITC trace of the enzymatic hydrolysis of pyrophosphate (PP(V)) with 1×10^{-9} M *E. coli* PPase, 3 mM $MgCl_2$, initiated with PP(V) to give a final concentration of 2.11×10^{-5} M at 25°C in 20 mM tricine, pH 8.40. The endothermic peak represents the heat of complexation of Mg^{2+} buffer effects and dilution followed by PP(V) consumption until the heat generated with respect to time (dQ/dt = power) returns to the baseline.

It is usually assumed that the substrate for PPase is the magnesium ion complex of the $PP(V)^{4-}$ tetra-anion in which case formally there should be no protons released on hydrolysis of PP(V) to two phosphate di-anions catalysed by the enzyme, in contrast to that expected for the hydrolysis of the $PP(V)^{3-}$ tri-anion at pH 8.4 (Scheme 1.54). Experimentally it was found that actually there is a small dependence on the heats of hydrolysis on the buffer used to maintain constant pH (Table 1.12). A plot of ΔH_{obs} against $\Delta H_{buffer\ ionisation}$ (Figure 1.30) is apparently linear and formally provides the number of protons reacting with the buffer from the slope which is -0.2. The intercept provides the true enthalpy of hydrolysis of $MgPP(V)^{2-}$ which is -27.1 ± 0.2 kJ mol^{-1}.

It seems probable that this apparent dependence on pH represents error, in which case the enthalpy of hydrolysis of $MgPP(V)^{2-} = -32.6 \pm 1.8$ kJ mol^{-1}, the average ΔH_{obs}.

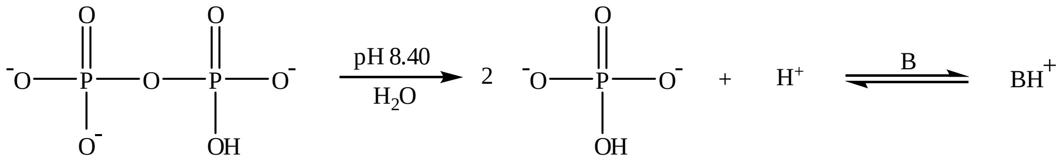

Scheme 1.54 Hydrolytic reaction of pyrophosphate tri-anion which liberates a proton, which is picked up by the buffer.

Buffer	ΔH_{obs} (kJ mol^{-1})	$\Delta H_{buffer\ ionisation}$ [94] (kJ mol^{-1})
HEPES	-30.75	21.01
Tricine	-32.81	31.97
TAPS	-34.35	41.49

Table 1.12 Enthalpies for the hydrolysis (ΔH_{obs}) of pyrophosphate (really $MgPP(V)^{2-}$) at pH 8.40, I = 0.1 M and 25°C in different buffers obtained using the PPase catalysed reaction, with the respective enthalpy of ionisation ($\Delta H_{buffer\ ionisation}$) for the specific buffer.

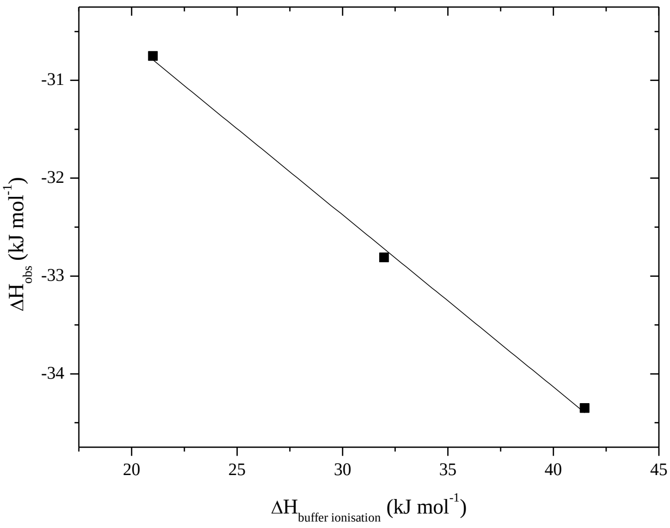

Figure 1.30 ΔH_{obs} against $\Delta H_{buffer\ ionisation}$ for the hydrolysis of pyrophosphate by pyrophosphatase at pH 8.40 (I = 0.1 M) and 25°C.

The hydrolysis was also conducted with similar buffers at pH 7.50 where pyrophosphate (Table 1.13) still exits as the tri-anion at approximately 88% in solution and approximately 11% as the di-anion. As before the actual substrate is $MgPP(V)^{2-}$ which is presumably formed rapidly and any heat changes in its formation are included in the initial endothermic spike (in HEPES buffer) at the beginning of the ITC output. However, in this case at pH 7.5 the hydrolysis of pyrophosphate yields phosphate as a mixture of mono-anion (~34%) and di-anion (~61%). In this case formally hydroxide-ion is released upon hydrolysis and so compensated by ionisation of the buffer. Interestingly, in contrast to the data at pH 8.40, ΔH_{obs} decreases as $\Delta H_{buffer\ ionisation}$ increases giving an apparent positive dependence of ΔH_{obs}

against $\Delta H_{buffer\ ionisation}$ with a slope of 0.2 indicative of no significant buffer protonation have occurred during the hydrolysis of pyrophosphate (Figure 1.31).

The 'true' enthalpy of hydrolysis of $MgPP(V)^{2-}$at pH 7.5 from the intercept is -33.5 ± 0.5 kJ mol^{-1}, whereas the average ΔH_{obs} = -28.0 ± 2.2 kJ mol^{-1}. Ging and Sturtevant obtained an enthalpy of -30.6 kJ mol^{-1} for the hydrolysis of pyrophosphate by yeast pyrophosphatase at pH 7.2, 0.1 M ionic strength and 25°C[78].

Buffer	ΔH_{obs} (kJ mol^{-1})	$\Delta H_{buffer\ ionisation}$ [94, 101] (kJ mol^{-1})
HEPES	-29.91	21.01
Tricine	-28.44	31.97
Tris	-25.53	47.53

Table 1.13 The dependence of the observed enthalpies for the hydrolysis (ΔH_{obs}) of pyrophosphate at pH 7.50, I = 0.1 M and 25°C on the nature of the buffer.

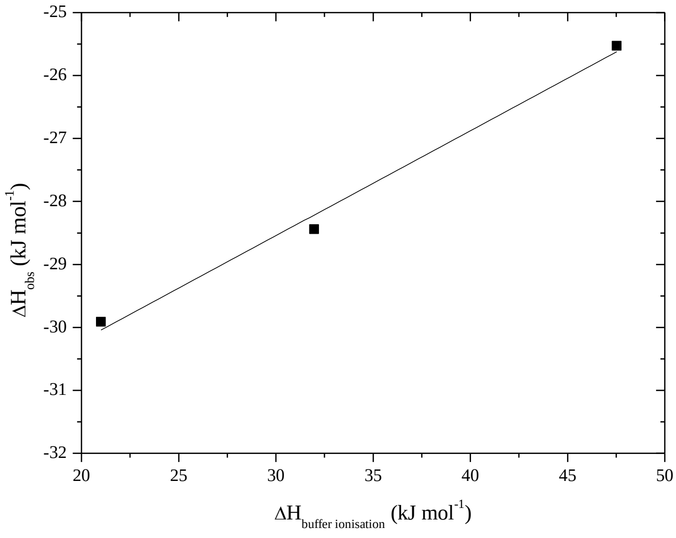

Figure 1.31 ΔH_{obs} against $\Delta H_{buffer\ ionisation}$ for the hydrolysis of pyrophosphate by pyrophosphatase at pH 7.50 (I = 0.1 M) and 25°C.

As PP(III) is not a substrate for PPase it was also hydrolysed in basic solutions at 25°C which showed a significantly exothermic reaction of -112.9 ± 9.3 kJ mol^{-1} of the di-anion (Figure 1.32). The heat of hydrolysis of PP(III)$^{2-}$ in basic conditions is not dependent on the hydroxide-ion concentration and can be represented by Scheme 1.55, where the ionisation of the final pK$_a$ of phosphorous acid is captured by excess hydroxide-ion to produce water. Therefore the true enthalpy of hydrolysis of PP(III)$^{2-}$ at pH 8.40 is -1.1 kJ mol^{-1} ($\Delta H_{PP(III)} = \Delta H_{obs} - 2H_{ion(H2O)}$), as the enthalpy of water ionisation at 25°C is 55.9 kJ mol^{-1} [102].

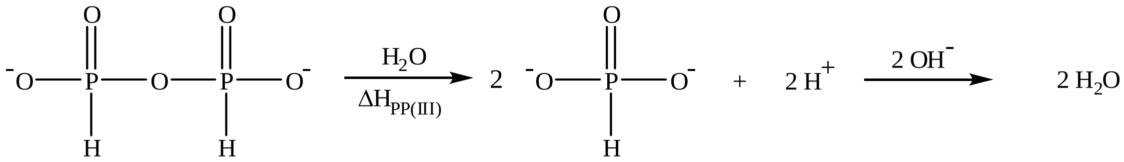

Scheme 1.55 Pyro-di-H-phosphate di-anion hydrolysing to form phosphorous acid di-anion and water.

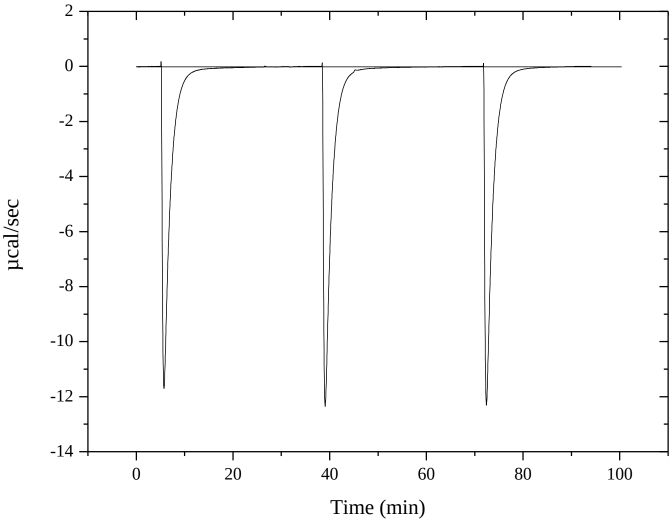

Figure 1.32 Three 5µl injections of PP(III)$^{2-}$ (syringe stock was 10.05 mM) into 0.1M NaOH, I = 1.0 M at 25°C.

Also, if the ΔH_{obs} for the hydrolysis of MgPP^{2-} is corrected for the initial heat of complexation the ‘true’ enthalpy of hydrolysis of pyrophosphate tetra-anion ($\Delta H_{PP(V)4-}$) is 0.9 kJ mol^{-1} (Scheme 1.56) which is significantly different to an approximate value of -14.7 kJ mol^{-1} [103].

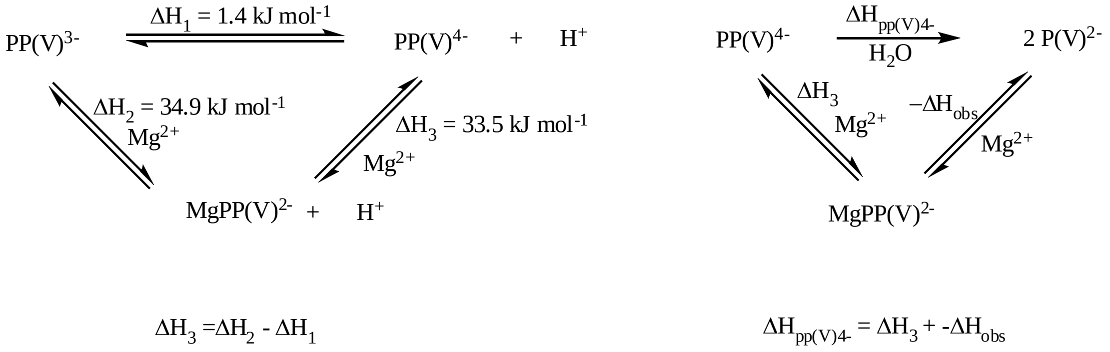

Scheme 1.56 Hydrolysis of pyrophosphate tetra-anion via the substrate of pyrophosphatase, $MgPP(V)^{2-}$.

At pH 8.40, the hydrolysis of pyrophosphate tetra-anion is 0.9 kJ mol^{-1} whilst the hydrolysis of pyro-di-H-phosphoante di-anion is slightly more exothermic with a value of -1.1 kJ mol^{-1}. Although the enthalpy of hydrolysis of both of these compounds requires further investigation it is possible to conclude that PP(III) could be a potential phosphorylating agent.

1.4 Conclusion

The hydrolysis of PP(III) and PP(V) are a complex function of pH. The rate of hydrolysis of PP(V) decreases steadily with increasing pH as the ionic species change. The hydrolysis of PP(III)$^{2-}$ which is the major species in solution is much more reactive than PP(V) at all pHs with a second-order dependence in [H^{+}] between pHs 0.6 and 2, kinetically representing the hydrolysis of the undissociated acid with a rate constant of 7.3×10^{-2} s^{-1}. The hydrolysis changes to a first-order dependence in hydrogen-ion concentration between pH 2 and 4 which could be kinetically represented by the mono-anionic species with a rate constant of 3.41×10^{-3} s^{-1}. The rate then becomes pH independent between pHs 5 and 8 corresponding to the spontaneous hydrolysis of PP(III) with a rate constant of 1.20×10^{-7} s^{-1}. Unlike PP(V), PP(III) shows a hydroxide-ion hydrolysed reaction with a rate constant of 1.35×10^{-1} M^{-1} s^{-1}. The pK_a of P(III) derivatives compared to P(V) appear to be more acidic with a reasonable pK_{a2} estimate of 0.44 ± 0.1for PP(III) and a pK_a for ethyl H-phosphonate of 0.47 ± 0.01. A Brønsted plot for the spontaneous hydrolysis of H-phosphonate derivatives signifies little charge development or no P-O cleavage to the leaving group in the transition state consistent with the formation of a trigonal-bipyrimidal intermediate and hydrolysis occurring via a associative ($A_N + D_N$) mechanism compared to a dissociative mechanism ($D_N + A_N$) for the hydrolysis of PP(V) di-, tri- and tetra-anion.

In addition to the hydrolytic studies the complexing abilities of PP(V) and PP(III) were analysed which showed that pyrophosphate tri-anion complex one equivalent of magnesium-ion with a binding constant of 1.64×10^{4} M^{-1} unlike PP(III) which shows negligible complexing ability with magnesium-ion. Although ITC and NMR showed no strong interaction between PP(III) and magnesium-ion a rate enhancement was observed with respect to the hydrolysis at pH 7 with a second-order rate constant of 2.20×10^{-5} M^{-1} s^{-1}.

The enzyme which catalyses the hydrolysis of pyrophosphate, pyrophosphatase does not catalyse the hydrolysis of PP(III) nor does it act as an inhibitor to the natural substrate pyrophosphate. This inability for pyrophosphatase to catalyse the hydrolysis of PP(III) is likely to be due to the positively charged amino acid residues unable to neutralise the negative charge which is usually present on pyrophosphate.

The enthalpy of hydrolysis of pyrophosphate tri-anion catalysed by pyrophosphatase is in reasonable agreement with literature data, although the enthalpy of pyrophosphate tetra-anion (0.9 kJ mol^{-1}) and pyro-di-H-phosphonate (-1.1 kJ mol^{-1}) require further investigation.

Chapter 2 – METHYLENE BIS-PYRIDINIUM DICATION

2 Background

2.1 Properties of pyridine and dichloromethane (DCM)/methylene chloride

Pyridine (C_5H_5N) is a 6-membered heterocyclic (Scheme 2.1) compound similar to benzene. It is an essential skeletal feature of pyridoxal phosphate an electron sink for elimination and transamination reactions due to resonance stabilisation. The electron withdrawing properties of the nitrogen enable pyridine to undergo nucleophilic addition/substitution reactions more readily than electrophilic addition/substitution reactions as carbons 2, 4 and 6 are strongly deactivated towards electrophiles (E^+). This is partly because most electrophilic substation reactions are done under acidic conditions to form a pyridinium ion.

The carbons and the nitrogen are sp^2 hybridised forming σ bonds with neighbouring atoms. The nitrogen atom possesses a lone pair of electrons which are not required as part of the aromatic π system (Scheme 2.1) allowing it to act as a weak base with a pK_a of 5.23 at 25°C for its conjugate acid[24]. Pyridine can also act as a nucleophile able to donate the pair of electrons on nitrogen to electrophiles creating pyridinium salts.

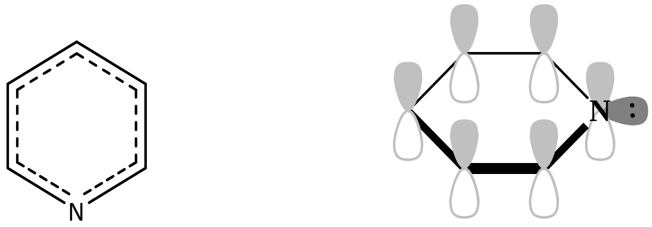

Scheme 2.1 Dashed line in pyridine represents the resonance throughout the molecule by the π-electron orbitals. The nitrogen contains a sp^2 lone pair of electrons shown by dark grey orbital.

DCM (CH_2Cl_2) is a volatile organic solvent and is a popular choice of solvent by chemists due to its low boiling point, density, polarity and relatively moderate toxicity but it is generally disregarded that DCM and chloroform are not inert and can act as alkylating agents[104].

2.1.1 Alkylation of pyridine

The salt formation between pyridine and alkyl halides results from nucleophilic substitution. The Menshutkin reaction, named after the Russian chemist Nikolai Menshutkin, converts tertiary amines including pyridine to quaternary ammonium salts with an alkyl halide by a S_N2 type mechanism where both bond breaking/making occur in the transition state (Scheme 2.2).

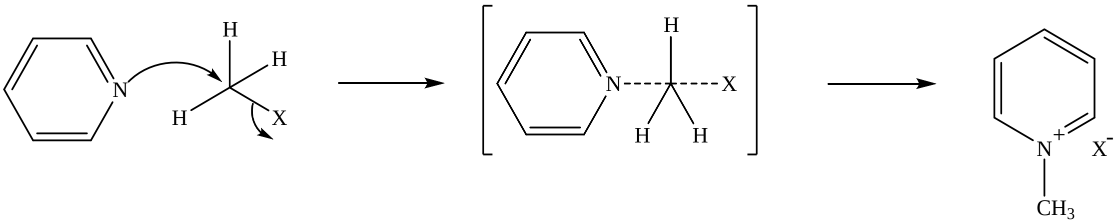

Scheme 2.2 Reaction of an alkyl halide with pyridine to form methyl pyridinium.

Studies of the effect of substituted pyridines on the N-alkylation of methyl iodide concluded that in the transition state, the bond from the alkyl group carbon to the pyridine is approximately 30% developed and that the bond to the leaving group is highly charged or polarised implying some positive charge development on the central carbon[105] (Scheme 2.3).

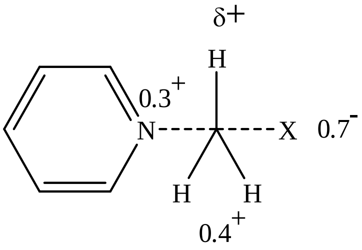

Scheme 2.3 Example of possible charge development on central carbon.

This statement is true when there is little steric hindrance or strong solvent hydrogen bonding, but a year later Kevill concluded that little charge would be present on the α-carbon and that the actual charge separation would depend on the reactants and the type of solvent[106].

In general reacting alkyl halides, such as methyl iodide or benzyl bromide, with pyridine forms the N-alkyl pyridinium salts which are useful reagents in organic synthesis and in the synthesis of many drugs. Due to their reactivity they may have potential toxic/mutagenic properties within humans as they readily react with nucleophiles within the body. Some pyridinium salts fluoresce and the use of pyridine derivatives may be used to detect low levels of alkylating agents in solution[107] (Scheme 2.4).

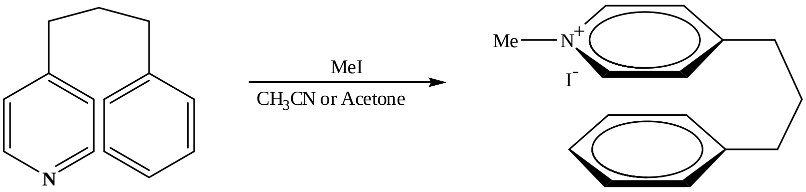

Scheme 2.4 Pyridinium compound which exhibits π-fluorescence once alkylated with methyl iodide[107].

2.1.2 Salts of pyridine and their preparation

Pyridinium salts are of great interest with cationic surfactants providing many applications in industry and a variety of medical applications[108]. Quaternisation of pyridine is relatively easy but can become more complex with ring substitution on pyridine.

2.1.2.1 N-alkyl pyridinium salts

Methylation of pyridine is relatively straightforward yielding N-methyl pyridinium (Scheme 2.5) which is carried out by mixing pyridine and methyl iodide in absolute ethanol, recrystallised in absolute ethanol to produce white crystals[109]. A simpler method involves no solvents and the addition of pyridine with excess alkyl halide or alkyl sulphate at 150°C for 2 hours produces the desired product dependent on the size of the alkyl halide[110].

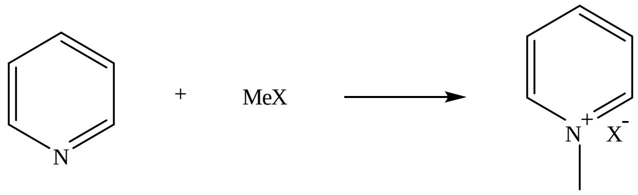

Scheme 2.5 Alkylation of pyridine with methyl halide to form methyl pyridinium[109].

2.1.2.2 Zincke procedure

In 1903-1905 Zincke reported the preparation of pyridinium salts, starting with pyridine and 2,4-dinitro-chlorobenzene produced the N-arylated pyridinium salt which are known as Zincke salts[111]. The addition of a primary amine to the Zincke salt produces a ring opened intermediate, presumed to be a glutaconaldehyde derivative, red in colour at room temperature; heating the mixture resulted in cyclisation to give the N-alkyl pyridinium salt[112] (Scheme 2.6).

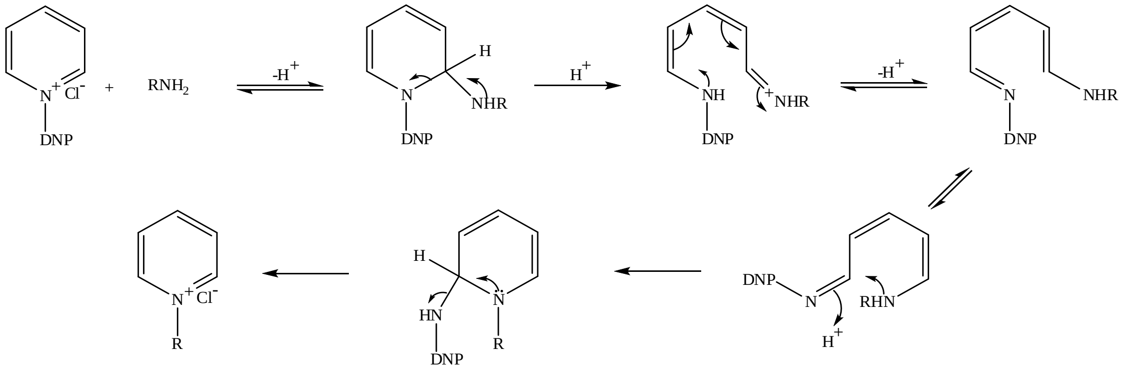

Scheme 2.6 Formation of an alkyl pyridinium salt which is brought about by ring opening of the Zincke salt[112].

2.1.2.3 N-acyl pyridinium salts

A pyridine derivative, dimethyl amino pyridine (DMAP) can be combined with an acyl halide to produce a reactive N-acyl pyridinium salt but in contact with H_2O or alcohol it undergoes hydrolysis giving the corresponding ester and protonated pyridine species (Scheme 2.7).

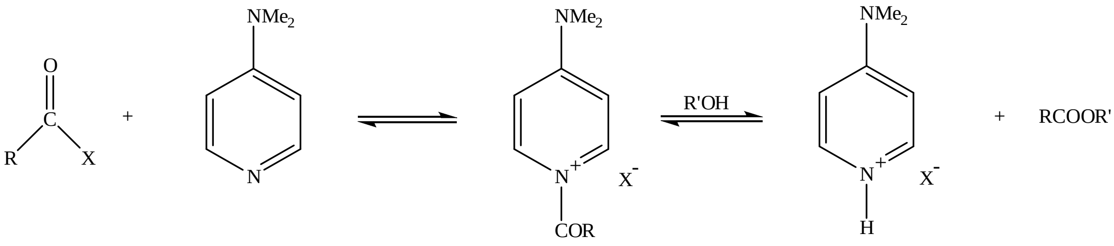

Scheme 2.7 N-acylation of DMAP[110].

2.1.2.4 N-trityl pyridinium salts

Tritylation with pyridine on the nitrogen also occurs, but with larger sterically hindered substituents such as triphenylmethyl chloride, the reaction requires increased temperatures (60-70°C) and pressures (4000-5000 atm) for 12-15 hours in which a white precipitate is formed[113] (Scheme 2.8).

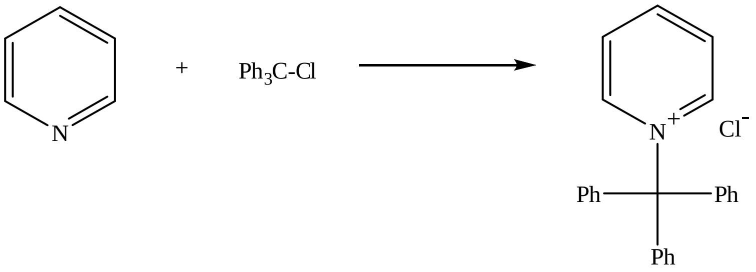

Scheme 2.8 Addition of a large substituent such as triphenyl to pyridine[113].

2.1.2.5 Paraquat

1,1'-Dimethyl-4,4'-bipyridinium dichloride has the trade name Paraquat (Scheme 2.9), which is one of the largest selling herbicides manufactured initially by ICI Chemicals and is still widely used today. Pyridine in reaction with sodium in liquid ammonia produces 4,4'-bipyridyl in which, after further treatment with CH_3Cl, produces Paraquat[114].

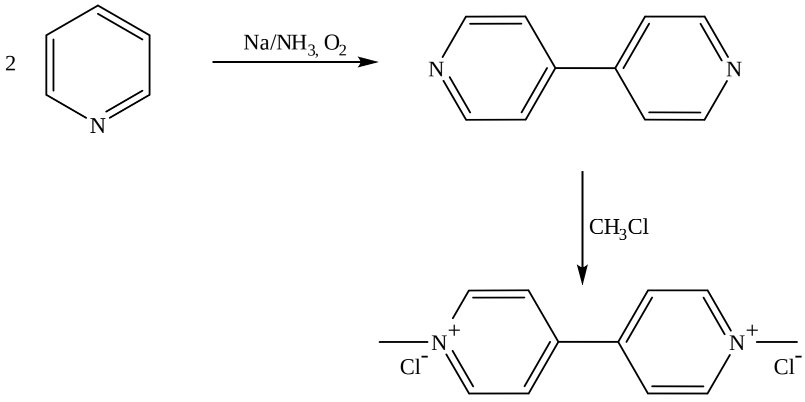

Scheme 2.9 Synthesis of Paraquat[114].

2.1.2.6 Pyridinium salts from pyrylium salts

Pyrylium salts react with primary amines to form pyridinium salts as another example of a reaction proceeding through opening of the aromatic ring. The α-position of the pyrylium salts is usually attacked by the primary amine forming intermediate **i** (Scheme 2.10) and in the presence of excess base usually in a ratio of 1:2 pyrylium:amine or triethylamine as an external catalyst leads to 2-amino-tetrahydropyran[115]. The ketodieneamine intermediate sometimes requires a little acid to form the pyridinium salt, although some unwanted products may also form such as vinyl amides or anilines[115].

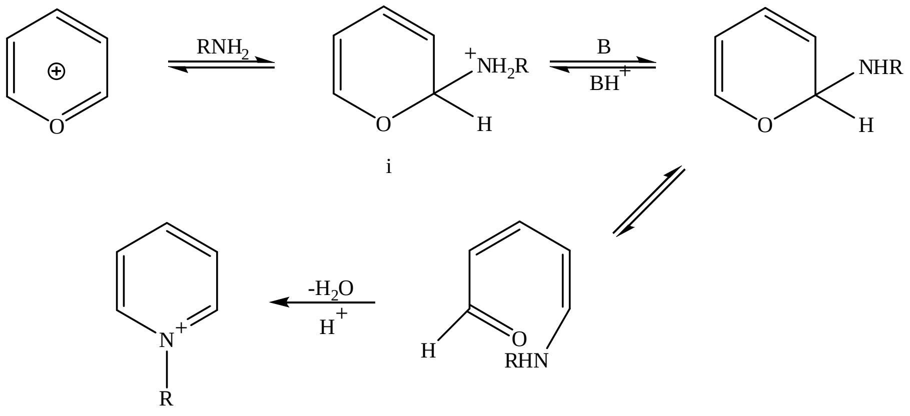

Scheme 2.10 Preparation of pyridinium salts from pyrylium salts[115].

2.1.2.7 Bis-pyridinium salts

The dibromide salt of 1,1'-(ethane) dipyridinium was formed by refluxing 1,2-dibromoethane (ethylene dibromide), pyridine and dimethylformamide. Within 2 hours a precipitate formed which was washed with diethyl ether and dried (Scheme 2.11)[116].

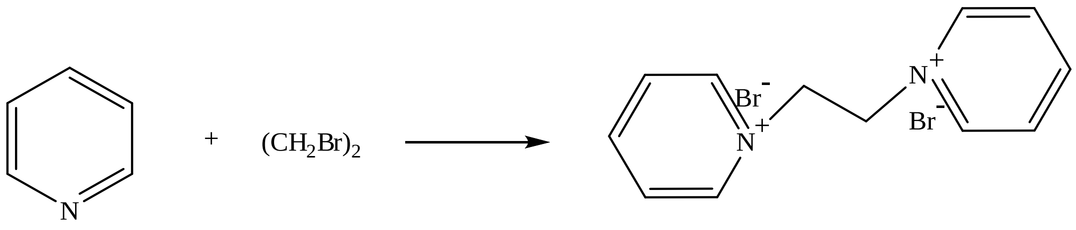

Scheme 2.11 Preparation of 1,1’-(ethane) dipyridinium dibromide[116].

2.1.3 Application of pyridinium compounds

A series of cationic sulphonamides have been developed for inhibiting carbonic anhydrase (CA), a zinc metallo enzyme. The main role of the enzyme is to provide homeostasis of water within the body but there have been connections between the enzyme and cancer[115]. There are some carbonic anhydrase isoforms which are only present in cancerous cell and the drug acetazolamide (Scheme 2.12), an inhibitor of carbonic anhydrase functions as a growth regulator in anticancer therapies. A series of pyridinium derivatives (Scheme 2.12) show nanomolar affinities towards CA II and IV and in addition they distinguish between membrane-bound versus cytosolic isozymes and therefore the use of classical inhibitors such as acetazolamide and pyridinium derivatives may provide selective cancer treatment[115].

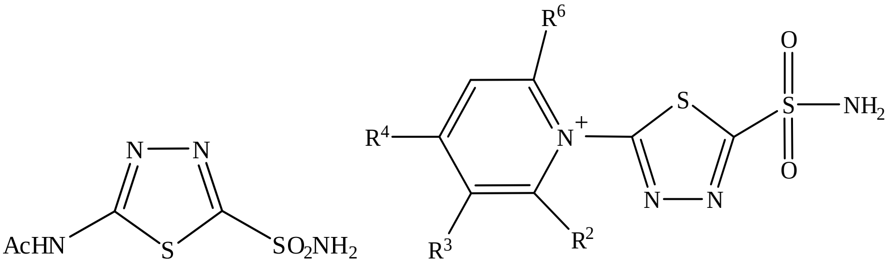

Scheme 2.12 Classical carbonic anhydrase sulfonamides inhibitors, acetazolamide (left) and a pyridinium derivative (right)[115].

Pyridinium salts also have an important role in providing cationic surfactants for use as corrosion inhibitors of ferrous materials in acidic media, textile softeners, antistatic agents and the use in the petroleum industry as additives. Cationic surfactants have a minimum of one hydrophobic group usually a long chained alkyl group, which is directly bonded to the positively charged nitrogen atom[110].

Cetylpyridinium chloride (CPC) (Scheme 2.13) has been used in mouthwashes and toothpastes as studies have shown that CPC prevents plaque production and gingivitis by penetrating the bacterial cell membrane causing leakage/inhibition of cell components/membrane[117].

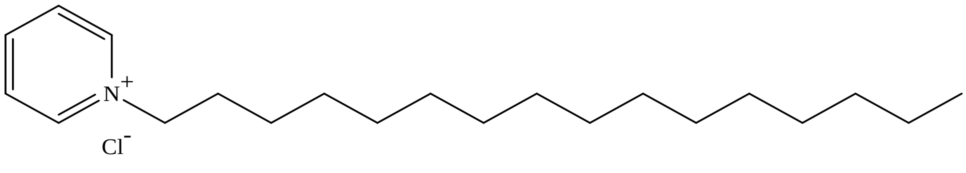

Scheme 2.13 Cetylpyridinium chloride (CPC), used in a variety of dental hygiene products.

A few pyridinium salts have been shown to be useful conductors in lithium-ions in batteries. 1-Butyl-4-methyl pyridinium tetrafluoroborate and 1-butyl-3-methyl imidazolium tertrafluroroborate (Scheme 2.14) or hexafluorophosphate in organic solvents such as butyrolactone or acetonitrile together with a lithium salt such as $LiBF_4$, provide low viscosity and high conductivity and making them an improved contender since the first lithium-ion battery commercialised by Sony in 1990[110, 118].

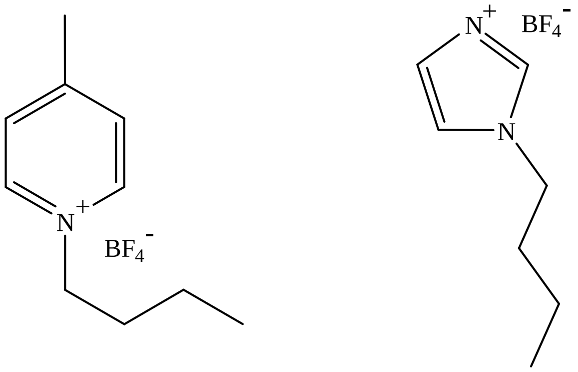

Scheme 2.141-butyl-4-methyl pyridinium tetrafluoroborate (left) and 1-butyl-3-methyl imidazolium tertrafluroroborate (right).

The medical industries are always on the search for new non-toxic, broad spectrum, safe antimicrobial sprays and disinfectants. Pyridinium salts have shown antimicrobial activity when used at the recommended concentrations with no odour or toxicity. The mode of action is dependent on various factors; and includes the salt being adsorbed or absorbed onto or into the cells membrane and causing the cell structure to alter, lyse or more commonly to halt or decrease a biochemical process such as respiration and glycolysis but more often they inhibit oxidative systems. Increasing the alkyl chain of alkylpyridinium salts usually increases the antimicrobial activity but is also dependent on additional groups and the substitution position on the pyridine ring. A bis-pyridinium compound, N,N'-hexamethylenebis-(4-carbamoyl-1-alkylpyridinium bromide) was analysed for antimalarial activity compared to quinine and chloroquine, the N1 alkyl moiety was altered and the highest activity was approximately 10 times more effective than quinine and half as effective as chloroquine[110, 119].

Ionic liquids are excellent reaction media due to their broad solvating ability, chemical stability, non-flammability and good thermal properties which make them safer than conventional solvents but not all ionic liquids have these ideal properties[120, 121].

Bittner *et al.* investigated the physical properties of a series of pyridinium ionic liquids, physical properties such as density, viscosity and surface tension were measured as a function of temperature at atmospheric pressure. It was found that lengthening the alkyl chain, reduces density and surface tension but the viscosity increases[121].

Cellulose is a bio-renewable material which has many applications in clothing, paper, polymer and the paint industry. Due to the high molecular weight of linear glucose polymer chains typically being 400-1000 units, cellulose is insoluble in water and many organic solvents[122]. In 1934 Graenacher used N-ethylpyridinium chloride to dissolve cellulose but it was not used as it was treated as novel and of little practical use[123]. Two ionic liquids although not pyridinium based compounds, dissolve cellulose without derivatisation which are 1-butyl-3-methylimidazolium chloride (BMIMCl) and 1-allyl-3-methylimidazolium chloride (AMIMCl)[123] but pyridinium salts with co-solvents DMSO or DMF have been used for dissolution and derivitisation of cellulose[124].

2.1.4 Preparation of Methylenebis-pyridinium

Baer and Prescott in 1896 were the first to prepare 1,1-bispyridinium dication (MDP) by the addition of pyridine to methylene iodide (Scheme 2.15). Various methods of preparation were used but on refluxing the components in alcohol, yellow crystals appeared on cooling. Once purified in 50% hot ethanol the fine crystals were soluble in water, and sparingly soluble in methanol and hot ethanol; but insoluble in cold ethanol, ether, chloroform and benzene[125]. In 1986 Almarzoqi *et al.* investigated different amines with di (chloro-, bromo- and iodo) methane, where it was found that the products were either a mixture of the mono- and di-substituted salt or one or the other. Tertiary amines such as triethylamine and diethylmethylamine produced only the mono-substituted chloromethane but pyridine substituted twice with dichloromethane to give methylenebis-pyridinium[126]. Another method for the preparation of MDP involves reaction of ω, ω-dibromoacetophenone and pyridine in ethanol to produce MDP and ethyl benzoate[127]. This presumably occurs by nucleophilic attack of ethanol on the carbonyl group of ω, ω-dibromoacetophenone which also implies the expulsion of the MDP carbanion (which forms part of this investigation) (Scheme 2.16). The ^1H NMR of the bridging CH_2 is strongly downfield due to being between two positively charged pyridine molecules with a chemical shift of 7.5 ppm in D_2O[126].

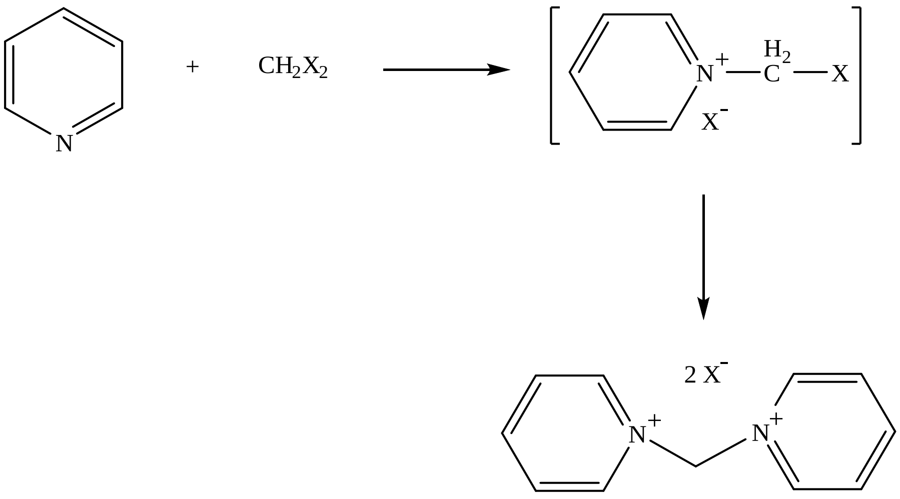

Scheme 2.15 Method of preparation of methylene bispyridinium by Almarzoqi[126].

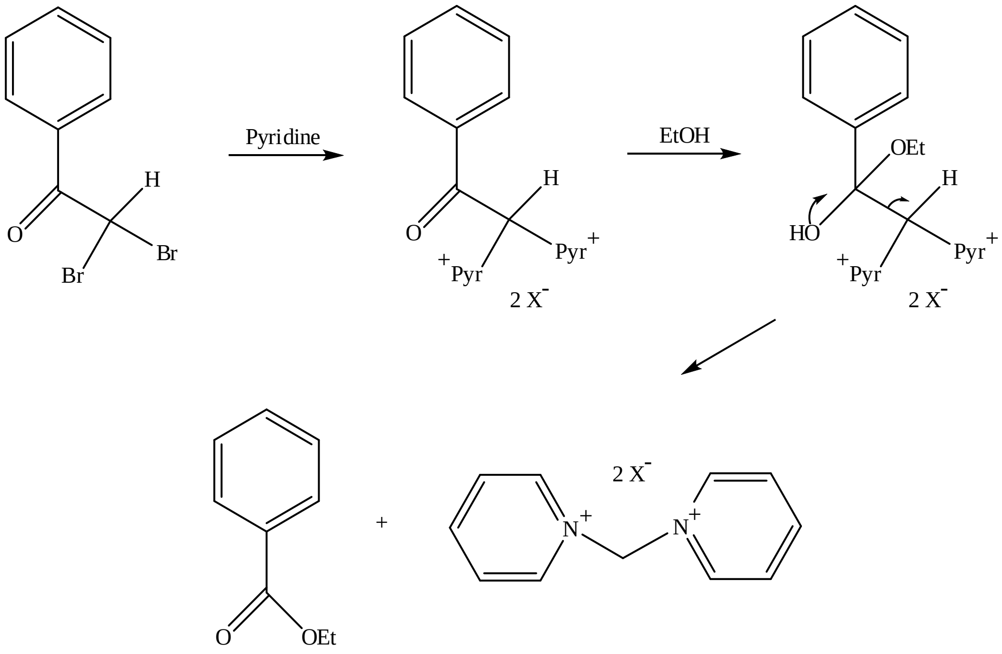

Scheme 2.16 Method of preparation of methylene bispyridinium by Krohnke[127].

The type of halogen attached to CH_2 has a dramatic effect on the rate of MDP production. The reactivity of the dihalomethane occurs in the order of $CH_2I_2 > CH_2Br_2 > CH_2Cl_2$, di-iodomethane having the greatest reactivity at low temperature and the least reactive CH_2Cl_2 requiring increased temperature and pressure for reaction to occur[126].

2.1.5 Crystal structures of Methylenebis-pyridinium

The first crystal structure of MDP was by Brudgam in 1986[128] but recently the MDP dichloride ($C_{11}H_{12}N_2^{2+}.2Cl^-.H_2O$) crystal structure was published as a monohydrate. The structure adopts a butterfly conformation (Figure 2.1) and does not show any unusual bond angles with the NCN of 110° and HCH 108° and the CH_2-N bond length of 147 pm[129].

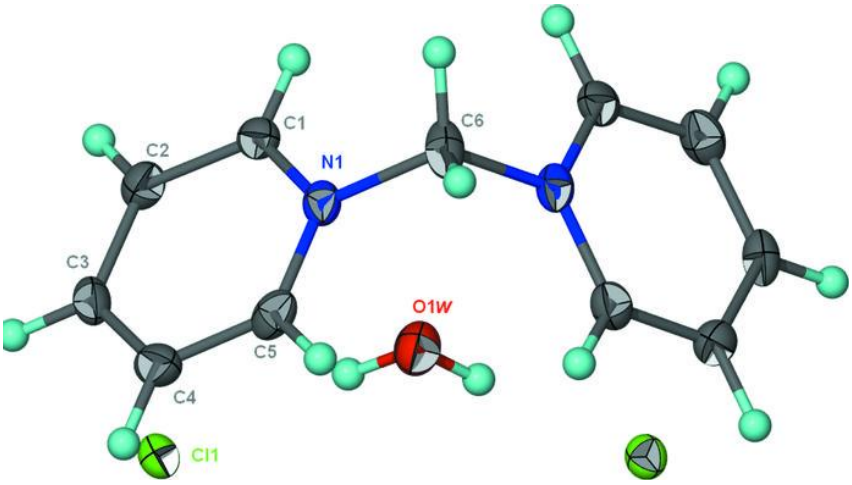

Figure 2.1 Crystal structure of MDP adopting the butterfly conformation[129].

Other salts of MDP have been produced such as methylene bispyridinium tertrachloroplatinate as organic-inorganic materials which are of interest to supra-molecular chemists and material scientists. Hybrid salts of MDP were made by treating it with the appropriate metal dichloride ($ZnCl_2$ or $CdCl_2$) in aqueous solution at room temperature (Figure 2.2)[130]. The salts are soluble in water but not in organic solvents. The parent structure and the hybrid salts are similar, both still consisting of the methylene attached to two positively charged nitrogen atoms of pyridine adopting a butterfly conformation which is roughly tetrahedral and the counter-ion $ZnCl_4^{2-}$ is nearly tetrahedral with bond angles of 113.8° and 105.9° (Cl-Zn-Cl) and for $CdCl_4^{2-}$ (Cl-Cd-Cl) 110.7° and 104.3°[130].

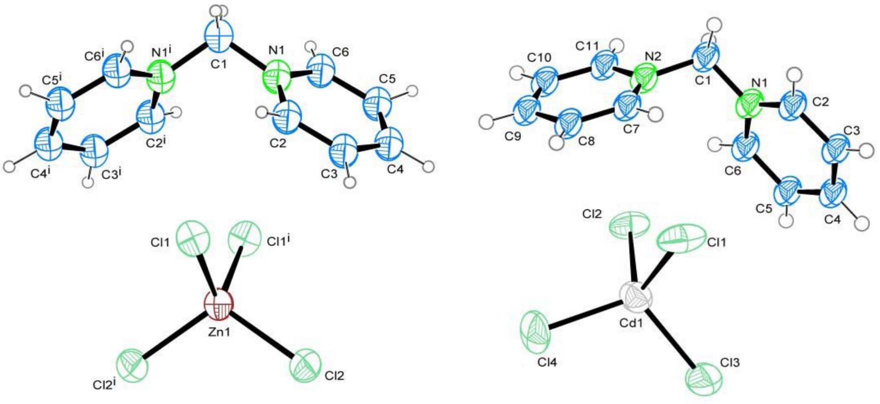

i ii

Figure 2.2 Crystal structures of N, N’-methylenedipyridinium tetrachlorozincate(II) (i) and N,N’-methylenedipyridinium tetrachlorocadmate (II) (ii)[130].

2.1.6 Reactivity of pyridinium compounds

Ring substituted N-pyridinium salts undergo a variety of reactions ranging from ring substitution reactions to hydrolysis and they undergo nucleophilic substitution reactions much easier than the corresponding N-oxides which are more reactive than the corresponding substituted pyridine. A series of 4-substituted N-methyl pyridinium salts react readily with sodium hydroxide in water at constant ionic strength, where the 4 position either contained F, Cl, Br, I, OCH_3. 4-methoxypyridine and 4-chloropyridine are very unreactive towards nucleophilic substitution by hydroxide[131]. For example 4-methoxypyridine shows no reaction after 43 days at 25°C which may be due to the expected intermediate not being able to support additional negative charge (Scheme 2.17)[131]. The 4-substituted N-methyl pyridinium salts are approximately a million fold more reactive than the corresponding 4-substituted pyridines.

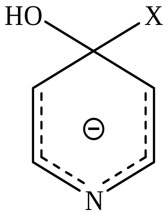

Scheme 2.17 Intermediate unable to support negative charge[131].

With 4-methoxy N-methyl pyridinium salt under certain conditions, the methyl groups at the N and O positions are susceptible to nucleophilic attack either forming 4-methoxypyridine or N-methyl-4-pyridone[131]. Nucleophilic substitution on the ring presumably occurs through the neutral intermediate adduct (Scheme 2.18) with the fluoride being the most reactive and the iodide and methoxide being the least reactive at the 4-position[131].

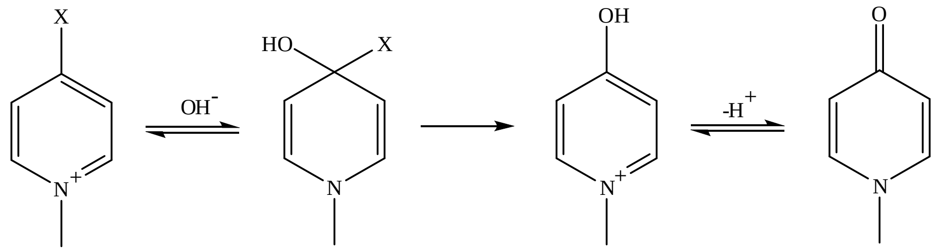

Scheme 2.18 Displacement of a halide by hydroxide forming a pyridone.

2.1.7 Hydrolysis of pyridinium compounds

Kosower and Patton investigated the alkaline hydrolysis of N-alkyl cyanopyridinium ions, the products of which are sensitive to the position of the cyano group on the ring. When the cyano group is at positions 2 or 4 of the pyridinium ring, attack by hydroxide-ion produces the corresponding pyridone by displacement of cyanide ion and carbamidopyridinium ion (Scheme 2.19, i, ii and Scheme 2.20), whereas 3-cyano pyridinium ion produces 3-carbamidopyridinium ion and the ring-opened 4-cyano-5-methylamino-2,4-pentadienal (Scheme 2.20, iii)[132]

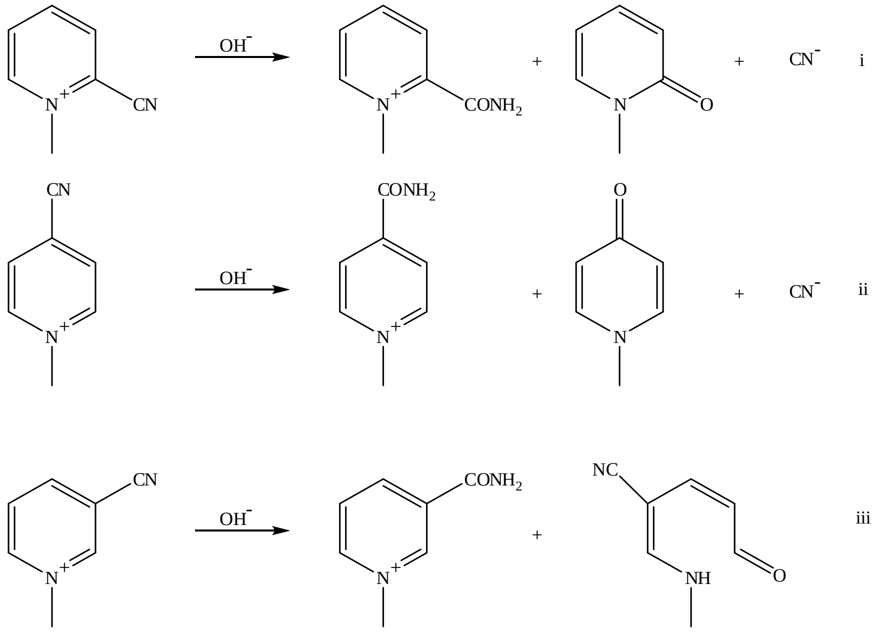

Scheme 2.19 Methyl pyridinium substituted with CN at different positions on the ring, reaction with hydroxide-ion produces the respective pyridone (i, ii) but substitution at position 3 produces a ring opened aldehyde (iii)[132].

The mechanism of forming pyridone and carbamidopyridinium ion for when the cyano group is attached at the 2 position of the pyridinium ring is shown in Scheme 2.20.

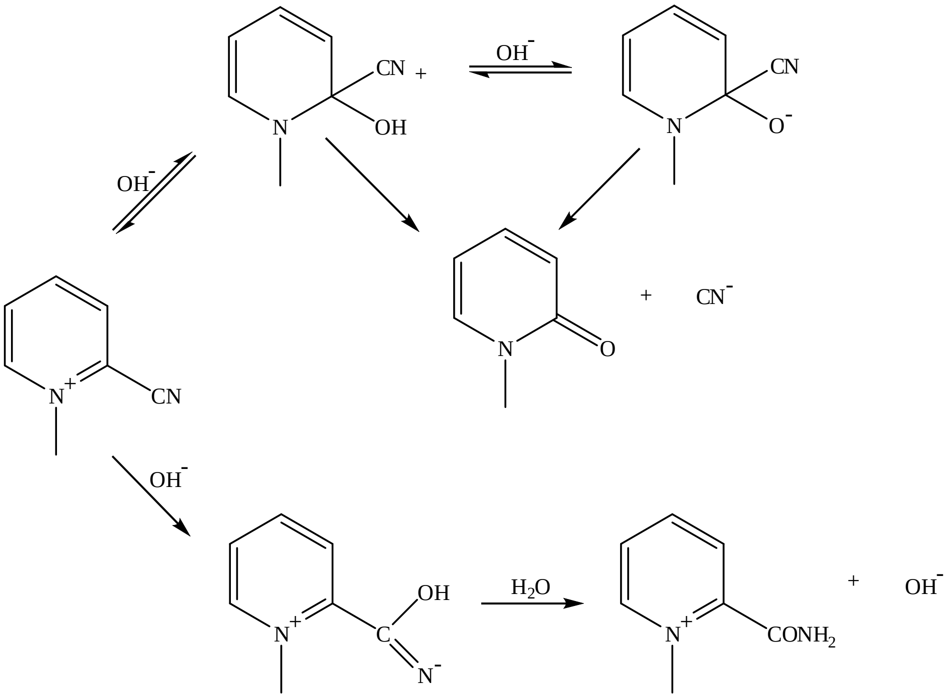

Scheme 2.20 Formation of pyridone and carbamidopyridinium ion at position 2 of the pyridinium ring[132].

Olofson and Zimmerman in 1967 reported the hydrolysis of 1,1'-(phenylmethylene) bispyridinium. Refluxing the pyridinium salt in water produced 2 equivalents of pyridine along with benzaldehyde[133]. In the presence of alkali, a solid precipitated intermediate (Scheme 2.21, i) was produced which was pale in colour and stable under N_2, in the dark and refrigerated. Returning this solid to basic solution forms benzaldehyde and a second equivalent of pyridine[133].

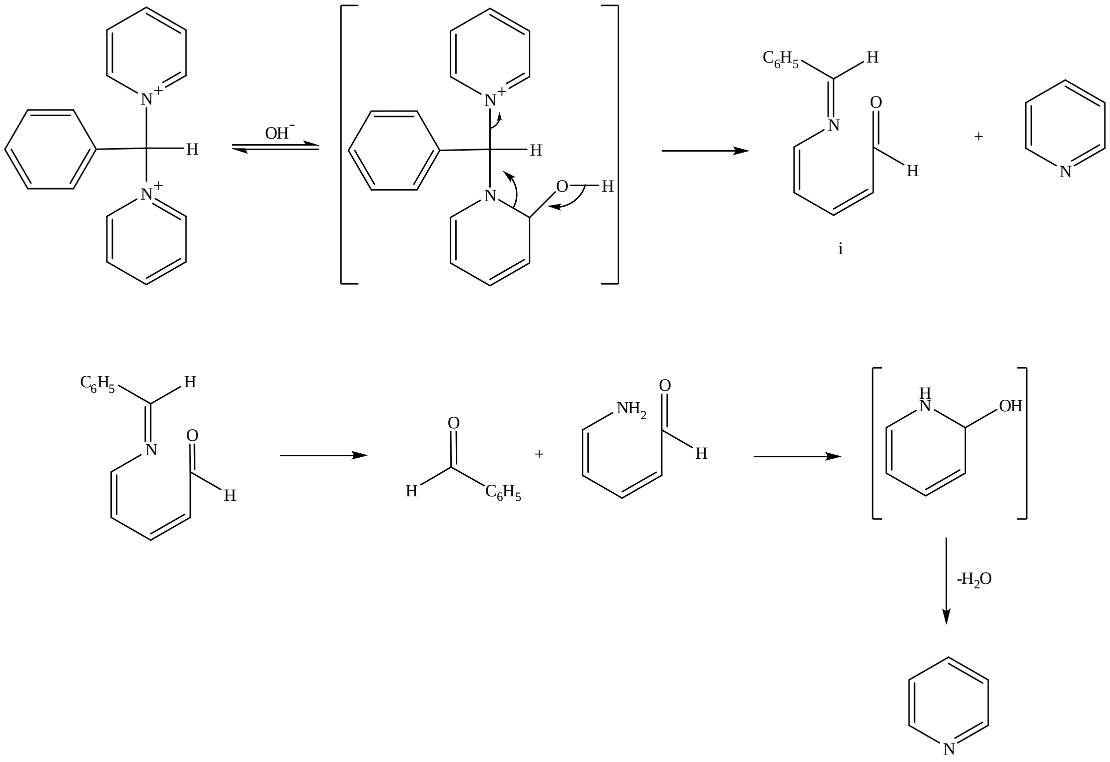

Scheme 2.21 Hydrolysis of 1,1'-(phenylmethylene) bispyridinium forming two equivalents of pyridine and benzyaldehyde[133].

Fernandez *et al.* investigated the reaction of hydroxide with a range of 1,ω-bis (2-bromopyridinium) alkanes, where the centres had a varying number of methylene groups. Five different methylene variants were used and the reaction with hydroxide produced the 1,ω-bis (2-pyridone)-alkane[134].

The reactions of the different methylene variants were monitored using a spectrophotometric method with hydroxide-ion which showed an isobestic point at 288 nm. Kinetic data obtained by monitoring the course of the reaction at 277 or 296 nm showed biphasic consecutive first-order reactions[134]. The pathway included fast attack of OH^- which yielded a mono reacted pyridone, followed by a slow OH^- attack on the intermediate giving the bispyridone product (Scheme 2.22).

The reaction at different pHs provided a set of rate constants for the two steps in the reaction, a plot of log k against pH (10.3-13) showed that k_1 and k_2 were both first-order in hydroxide concentration[134].

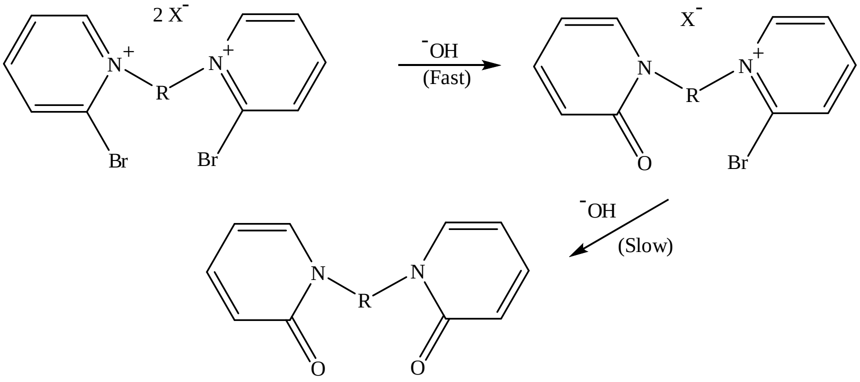

Scheme 2.22 Hydroxide-ion attack of 1,ω-bis (2-bromopyridinium) alkanes to produce the bispyridone product[134].

2.1.8 Ring opening reactions

Nucleophilic reactions with pyridine have been studied since the end of 19th century. The most popular reaction is the Zincke-Konig reaction or the cleavage of quaternary pyridine rings by amines[135].

The first reported behaviour of ring-opening was of 1-(2,4-dinitrophenyl) pyridinium chloride (Scheme 2.23, i) discovered by Zincke *et al*. This compound is stable in acid and at neutral pH but decomposes at 150°C upon heating to form pyridine and 2,4-dinitrophenol. Hydrolysis at higher pH produces a red coloured compound initially unknown in structure but later work revealed a ring opened derivative of 1-(2,4-dinitrophenyl) pyridinium chloride (Scheme 2.23, ii-iv)[136].

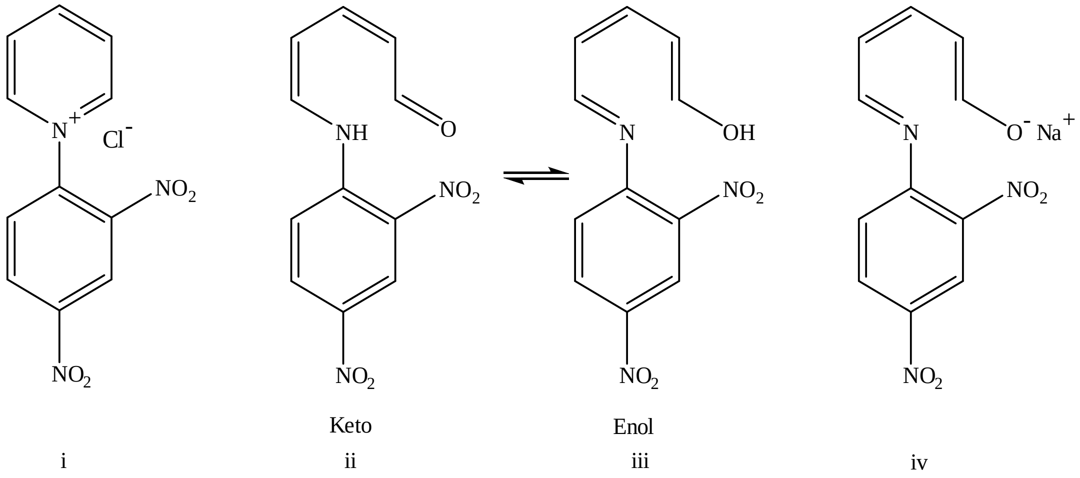

Scheme 2.231-(2,4-dinitrophenyl) pyridinium salt (i) to produce potential ring opened coloured compounds (ii-iv)[136].

Approximately 70 years later the reaction order of 2,4-dinitrophenyl pyridinium chloride with hydroxide-ion was found to be a maximum of 2 in hydroxide-ion in 50-90% aqueous ethanol but decreased with increasing OH^- ion and ethanol concentration[137].

At a similar time, in 1904 Konig showed that the addition of pyridine and cyanogen bromide produced N-cyanopyridinium ion[136]. This pyridinium salt was reacted with aniline which produced dinitroaniline and glutacondialdehyde dianil, (di-imine) but the reaction with hydroxide was not studied. The production of the glutaconaldehyde from many N-substituted pyridinium ions proved quite common but some reactions were inhibited by steric hinderance and electronegative substituents and even successful reactions have a tendency to recyclise to a pyridinium derivative[136].

A similar compound, pyridinium sulfonic acid was studied by Baumgarten in 1926, which was prepared by the addition of sulphur trioxide (SO_3) and chlorosulphuric acid with pyridine[136]. Addition of strong sodium hydroxide (5 M) produced an intermediate yellow in colour which was isolated (Scheme 2.24). Further treatment with hydroxide produced the final product glutaconaldehyde which was red/brown in colour. The reaction between pyridinium sulfonic acid and aniline produces glutaconic dialdehyde dianil, (the di-imine)[136].

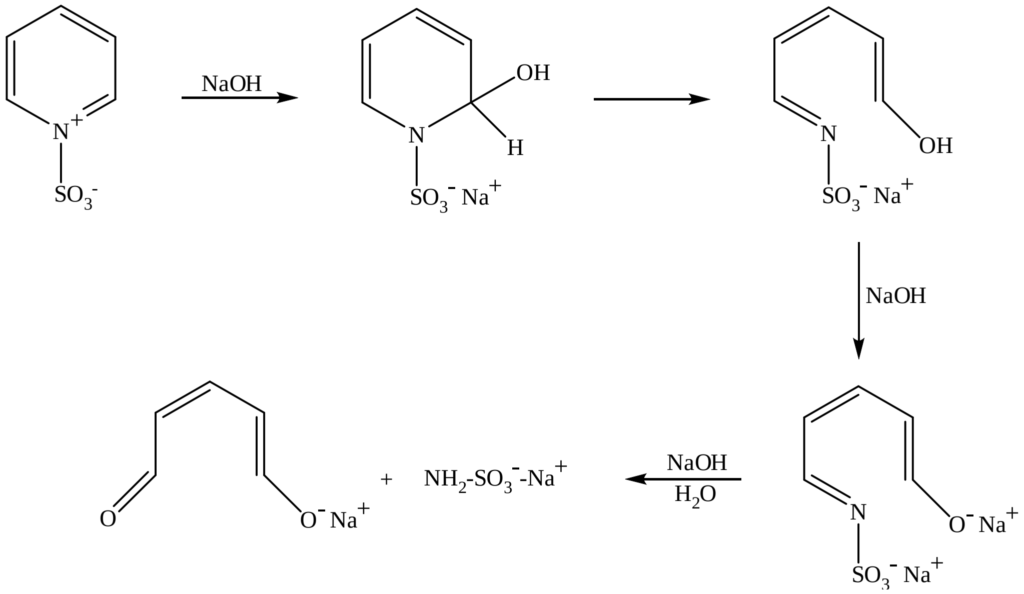

Scheme 2.24 Ring opening of pyridinium sulfonic acid by hydroxide to form glutaconaldehyde[136].

In 1965 Eisenthal and Katritzky studied the ring opening of N-methoxypyridinium perchlorate by hydroxide although N-alkoxypyridinium salts were initially investigated by Ochiai *et al.* in 1944 which showed that in the presence of hydroxide the salt produces pyridine and an aldehyde (Scheme 2.25)[138].

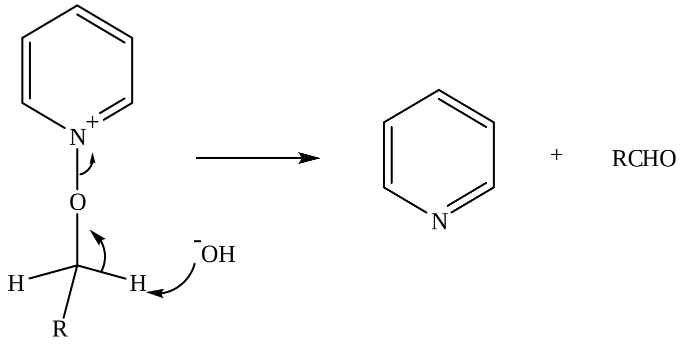

Scheme 2.25 N-methyloxypyridinium hydrolysis producing pyridine and an aldehyde[138].

Spectrophotometric kinetic evidence of N-methoxypyridinium perchlorate showed an absorbance at 343 nm in alkaline solution and attributed to the glutaconic aldehyde enolate (Scheme 2.26). The sodium enolate of glutaconic dialdehyde has a λ_{max} at 365 nm. Substituting the C=O by C=NH shifts the λ_{max} downfield about 35 nm but the addition of a methoxy group changes λ_{max} by 22 nm, presumably due to inductive effects. A plot of log initial rate against log concentration of hydroxide-ion showed a straight line with a second-order dependence on hydroxide-ion[138].

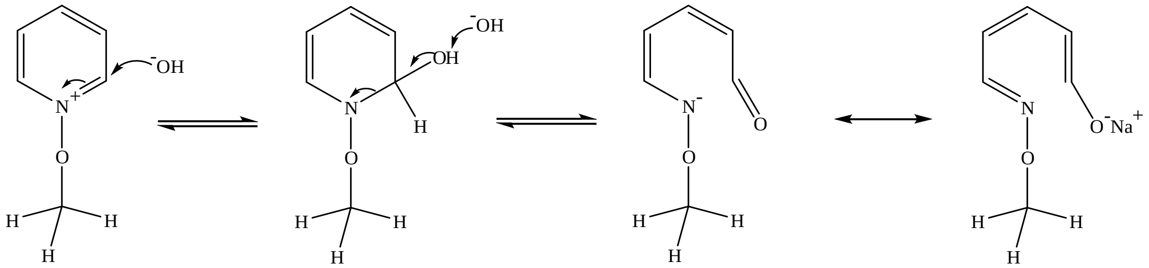

Scheme 2.26 Ring opening of N-methyloxypyridinium to form a sodium enolate[138].

In 1966 Johnson and Rumon synthesised 1-(N,N-dimethyl-carbamoyl) pyridinium (Scheme 2.27) which, when treated with hydroxide, is capable of following different mechanistic pathways dependent on pH. At a pH below 10, 1-(N,N-dimethyl-carbamoyl) pyridinium hydrolyses to give pyridine and dimethylcarbamic acid but above pH 10 an unstable intermediate is formed (Scheme 2.27)[139]. Further investigation of the intermediate demonstrated that it is capable of decomposing by two pathways; the intermediate was prepared and dissolved in aqueous solutions of varying pH. The predominant pathway above pH 13.5 yields glutacondialdehyde and 1,1-dimethylurea but between pH 8-13 the predominant pathway yields pyridine and dimethylamine[139].

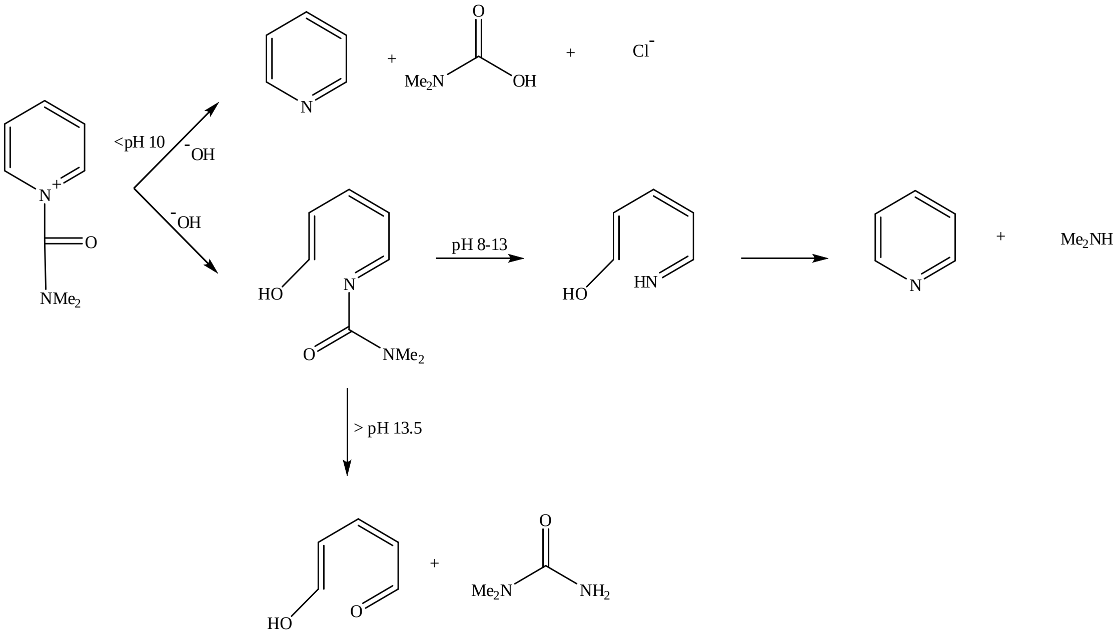

Scheme 2.27 Pathways for the hydrolysis of 1-(N, N-dimethyl-carbamoyl) pyridinium by hydroxide dependent on pH[139].

Another example involves the reaction of pyridine and thiophosgene producing the bispyridinium salt 1,1'-thioketone dipyridinium (Scheme 2.28). Treatment with hydroxide-ion, which attacks at the C-2 position, gives an anhydro-base where another hydroxide-ion ring opens the pyridine to produce pentadiene aldehyde and pyridine. The ring opening was considered to be due to hard-soft acid base theory and attack at C-2 is expected as the thiocarbonyl carbon atom has a soft centre[140].

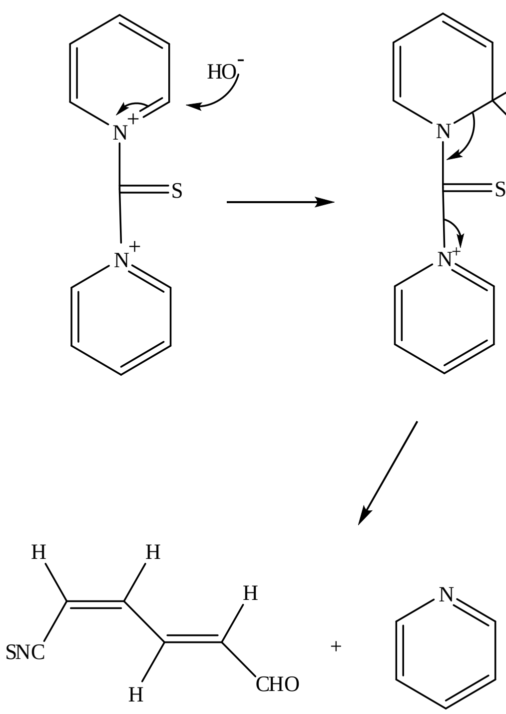

Scheme 2.28 Ring opening of 1,1'-thioketone dipyridinium by hydroxide-ion[140].

2.1.9 Acidity

2.1.9.1 Brønsted-Lowry acid-base model

In 1923 a Danish chemist, Johannes Brønsted, and Thomas Lowry, an English chemist, defined acids and bases. Brønsted-Lowry defined that an acid is a species which donates a proton whereas a base is a proton acceptor (Scheme 2.29).

$$\mathrm{HA} + \mathrm{B}^- \rightleftharpoons \mathrm{A}^- + \mathrm{BH}$$

Scheme 2.29 Deprotonation of a general acid.

When the acid donates its proton the species formed is known as the conjugate base (A^-) and the proton acceptor is known as the conjugate acid (BH). Compounds which are able to donate or accept a proton are known as amphoteric, examples include H_2O.

In addition to the Brønsted-Lowry definition, Gilbert N. Lewis also defines acids and bases further where Lewis acids are electron pair acceptors and a Lewis bases is an electron pair donors where protons are not necessarily involved in the reaction.

A compounds pK_a is a measure of how acidic a given proton is within a compound. Scheme 2.30 shows the deprotonation of a carbon acid to its corresponding conjugate base (a carbanion) in water. The equilibrium constant K_a is the relative stability of the conjugate base and the acid but more commonly the negative logarithm is taken giving the pK_a enabling comparison of acids easier. The pK_a in a given solvent is predominantly determined by resonance and inductive effects and if a compound is deprotonated and contains atoms which are electronegative, the charge ends up on the most electronegative atom as the lone pair is most tightly held providing the most stable conjugate base (Scheme 2.30).

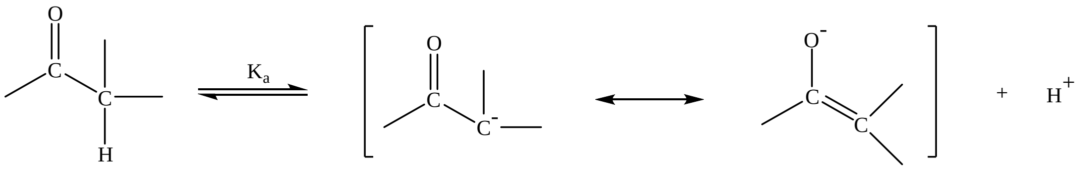

Scheme 2.30 Deprotonation of a ketone providing a keto-enol stabilised resonance structure.

2.1.9.2 Carbon acidity

Compound's containing a C-H bond are capable of losing a proton to form a carbanion. Strong carbon acids generally have pK_as in the range of 0-14 and the two main factors controlling acidity are resonance stabilisation of the conjugate base and inductive effects. These types of compounds which are able to stabilise the negative charge usually contain oxygen, nitrogen or sulphur which in turn, allows charge transfer from the carbanion to an electronegative atom. Nitro groups are strongly electron attracting and therefore the negative charge on nitro carbanions is mostly transferred to the oxygens from the carbon (Scheme 2.31, i). Carbonyl and sulfonic groups are also effective at transferring the negative charge from the carbanion (Scheme 2.31, ii, iii)[141].

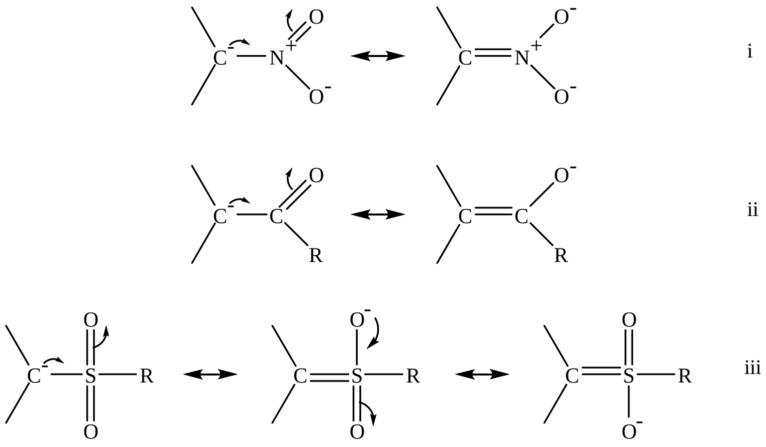

Scheme 2.31 Transfer of negative charge from carbon to electron withdrawing groups.

Carbanion stability can often be predicted from electronegativity or s character content of the orbitals involved in charge delocalisation. Hybridisation of the carbon is also an important factor determining the acidity of a compound, which increases as more s character is observed by the acidic atom and follows the trend $sp^3 < sp^2 < sp$ (Scheme 2.32). In alkynes, 50% s character is observed compared to only 25% in sp^3 bonds and the electrons associated with high s character increase the electronegativity of the carbon, making sp carbons more acidic compared to sp^3 [142].

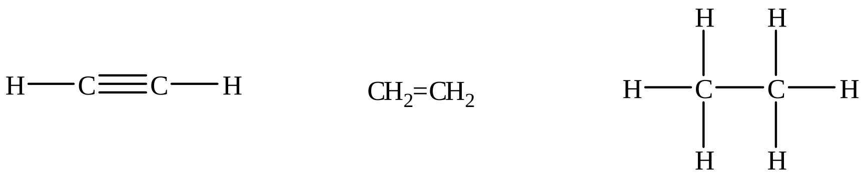

Scheme 2.32 Acidity of carbon acids is dependent on hybridisation with the most acidic being acetylene (pK_a 24) followed by ethene (pK_a 44)[143] and the least acidic being ethane (pK_a 50.6)[144].

Pyridinium carbon acids are also of great interest as ketimines, which are formed by the addition of 5'-pyridoxamine phosphate to α-ketoacids, are intermediates of enzyme catalysed transamination reactions. The α-carbon of the intermediate undergoes proton transfer which is activated by the pyridinium ring (Scheme 2.33)[145].

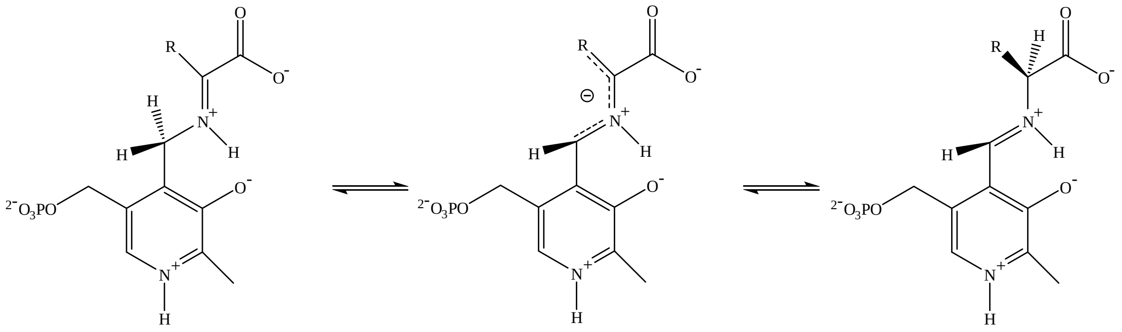

Scheme 2.33 Proton transfer mechanism of 5'-pyridoxamine phosphate[145].

The first α-proton pK_a of the methylene group within 4-(aminomethyl) pyridinium (Scheme 2.34, i) is between 17 and 19 in water at 25°C (I = 1.0 M) although it was thought to be a relatively strong carbon acid due to the strong electron withdrawing α-pyridinium and α-iminium groups. High carbon acidity has also been reported for malononitrile (Scheme 2.34, ii) and dimethyl malonate (Scheme 2.34, iii) which have pK_as of 11.2 and 13.3 respectively[145].

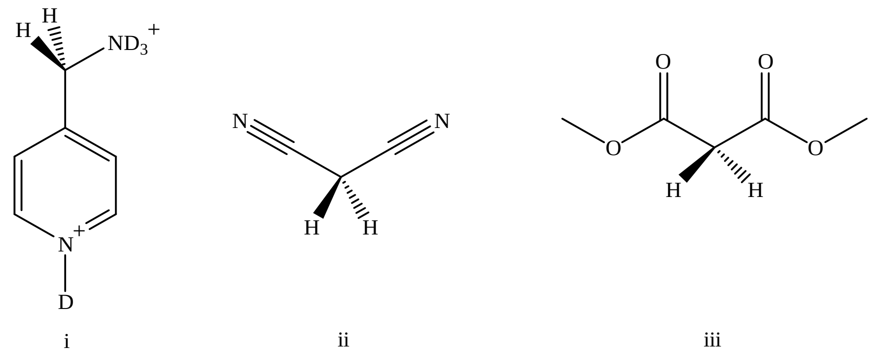

Scheme 2.34 4-(aminomethyl) pyridinium (i), malononitrile (ii) and dimethyl malonate (iii).

2.1.9.3 Enzyme catalysed proton transfer

Deprotonation of substrates by enzymes which have catalytic efficiency constants (k_{cat}/K_m) near diffusion ~10^8 are difficult to monitor. One method of deprotonation of 2-phosphoglycerate trianion by the enzyme enolase at the weakly α-carbon proton is by the utilisation of two divalent metal-ions to neutralise the highly negatively charged substrate[146]. Although the enolase superfamily are not very substrate specific, this general feature lies within the active site to which the substrate coordinates to the metal-ion and amino acid residues such as glu and lys to labilise the α-proton of the bound carboxylate anion (Scheme 2.35).

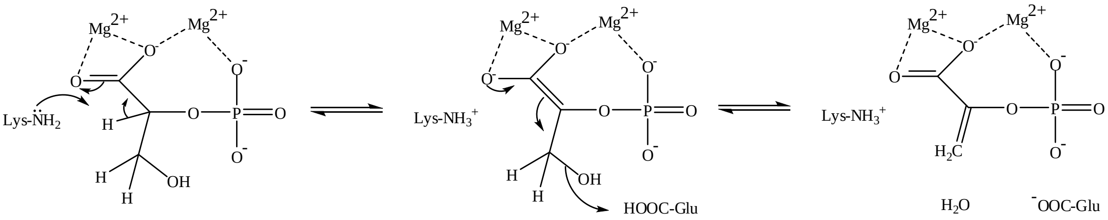

Scheme 2.35 Deprotonation mechanism of 2-phospho-D-glycerate by enolase[147.]

2.2 Experimental

2.2.1 Materials

1,1′-Methylenebis-pyridinium dichloride (MDP) was prepared by the addition of 130 ml DCM (2035.79 mmoles) to 30 ml pyridine (372.40 mmoles) which was then refluxed at $60^{o}C$ until a solid precipitate was formed. The precipitate was filtered and any remaining pyridine was removed by washing with excess DCM.

^{1}H NMR (500 MHz, D_2O) 9.38 ± 0.03ppm (dd, $J_{2,3}$ = 5.55 Hz, $J_{2,4}$ = 1.25 Hz, 4H), 8.85 ± 0.01 (tt, $J_{4,3}$ = 7.90Hz, $J_{4,2}$ = 1.28Hz, 2H), 8.33 ± 0.02 (m, 4H) and 7.47 ± 0.03 (s, 2H).

^{13}C NMR (500 MHz, D_2O) 149.89 ± 0.09 ppm (C_4), 145.15 ± 0.06 ppm ($C_{2/6}$), 129.55 ppm ± 0.05 ($C_{3/5}$), 78.0 ± 0.05 ppm (methylene).

ESI (+) for M^{2+} ($C_{11}H_{12}N_2$) found m/z = 86.0503 whilst the exact mass calculated using Masshunter software is 86.0495.

Sodium deuteroxide (30 wt%, 99+% D), deuterium chloride (37 wt%, 99+%D) and deuterium oxide (99.9% D) were from Aldrich. All other organic and inorganic chemicals were AnalaR grade and were used without further purification.

2.2.2 General methods

Phosphate, CAPS and borate buffers were prepared by dissolving the acid form and KCl in D_2O followed by the addition of NaOD to give the desired acid/base ratio at total I = 1.0 M (KCl). Solution pH was determined at 25°C using a Jenway 3510 pH meter equipped with a Mettler InLab Ultra-Micro electrode. Values of pD were obtained by adding 0.40 to the observed reading of the pH meter[148]. The concentration of deuteroxide-ion at any pD was calculated using Equation 2.1, where $K_w = 10^{-14.87}$ is the ion product of D_2O at 25°C[148].

$$\log[\mathrm{OD^-}] = \mathrm{pD} - \mathrm{pK_w}$$

Equation 2.1

^{1}H NMR spectra at 500 MHz were recorded in D_2O at 25°C using a Bruker Avance 500 NMR spectrometer. Chemical shifts are reported relative to TSP (sodium trimethylsilylpropionate 2,2,3,3-d_4 ($(CH_3)_3$ $SiCD_2CD_2CO_2^{-}Na^{+}$)) at 0.00 ppm and sodium acetate was used as an internal standard.

UV-Vis spectra were acquired using a Cary 4000, equipped with a 12 compartment cell block thermostatically maintained by using a peltier system.

An Agilent 7890A GC equipped with flame ionization detection (FID) or MS-QQQ. The column used was an Agilent HP-5 with dimensions 30 m x 0.25 mm x 0.25 µm. The inlet temperature was set at 250°C, with an injection volume of 1µl and split ratio of 50:1. The carrier gas was helium at a constant pressure of 16.1 psi and flow rate of 1.5 ml/min. The oven temperature was initially 45°C, holding for 2 minutes, before increasing the temperature at a ramping rate of 20°C/min. The final oven temperature was 320°C which was held for 2 minutes.

2.2.3 Kinetic measurements

All reactions were carried out in H_2O or D_2O at 25°C. The rate of hydrolysis of MDP was studied by injecting a stock solution of MDP (10 mM in H_2O) into a buffered solution, I = 0.1 M giving 1 x 10^{-4} M MDP and measuring the change in UV absorbance at 366 nm as a function of time. The biphasic change in absorbance was dissected into pseudo first-order rate constants for the formation and breakdown of the intermediate using Origin Labs software. The deuterium exchange reactions of MDP were followed by ^1H NMR and were initiated by mixing MDP into 1.0 M, 0.1 M DCl or buffered D_2O solutions at an ionic strength of 1.0 M (KCl) to give a final substrate concentrations ranging from 19.85-21.22 mM. The pD of the reaction mixture was closely monitored and was found to be constant to within 0.05 pD units during the time the isotope exchange reaction was followed by ^1H NMR analysis at 25^{o}C.

The exchange for deuterium of the methylene proton of MDP in D_2O buffered at pD 7.20 and 10.0 were followed by monitoring the disappearance of the singlet at 7.47 ± 0.03 ppm and the appearance of a poorly resolved triplet at 7.46 ± 0.03 ppm due to the α-CHD group of the product by ^1H NMR spectroscopy. The exchange for deuterium of the aromatic protons of MDP in D_2O buffered solutions at pD 7.20-10.0 were followed by the ^1H NMR using either C_4 or $C_{3/5}$ protons of the pyridinium ring.

To monitor the formation of pyridine by GC, 10.1 mM MDP was added to a 300 mM CAPS buffer at pH 10.0, I = 0.1 M, 25^{o}C with methoxybenzene at 5 mM as an internal standard. At intervals, 1 ml of this solution was added to 2 ml DCM, the layers were shaken to ensure maximum transfer of organic materials into the methylene chloride layer. The layers were left to separate and the DCM layer was analysed for pyridine.

2.2.4 Aim

The aim of this project involves investigation into the kinetics of hydrolysis and mechanism of MDP and secondly to determine the acidity of the central methylene group.

2.3 Results and Discussion

2.3.1 Structural properties of MDP

2.3.1.1 ^{1}H and ^{13}C NMR

The ^{1}H NMR spectrum of MDP in D_2O showed the expected signals of the pyridinium ring at 9.38 ± 0.03 ($C_{2/6}$), 8.85 ± 0.01 (C_4) and 8.33 ± 0.02 ppm ($C_{3/5}$) and at high chemical shift the bridging CH_2 singlet at 7.47 ± 0.03 ppm. This unusually high chemical shift for a CH_2 group is due to it being situated between two positively charged nitrogen atoms, it was also observed that the chemical shifts change slightly dependent on the buffer used to maintain the pH. The splitting pattern of the pyridinium ring protons are first-order with the $C_{2/6}$ protons being a doublet of doublets ($J_{2,3}$ = 5.55 Hz, $J_{2,4}$ = 1.25 Hz, 4H), C_4 proton being a triplet of triplets, ($J_{4,3}$ = 7.90 Hz, $J_{4,2}$ = 1.28 Hz, 2H), $C_{3/5}$ protons appear as a multiplet,(4H) and the bridging CH_2 is a singlet (2H) (Figure 2.3).

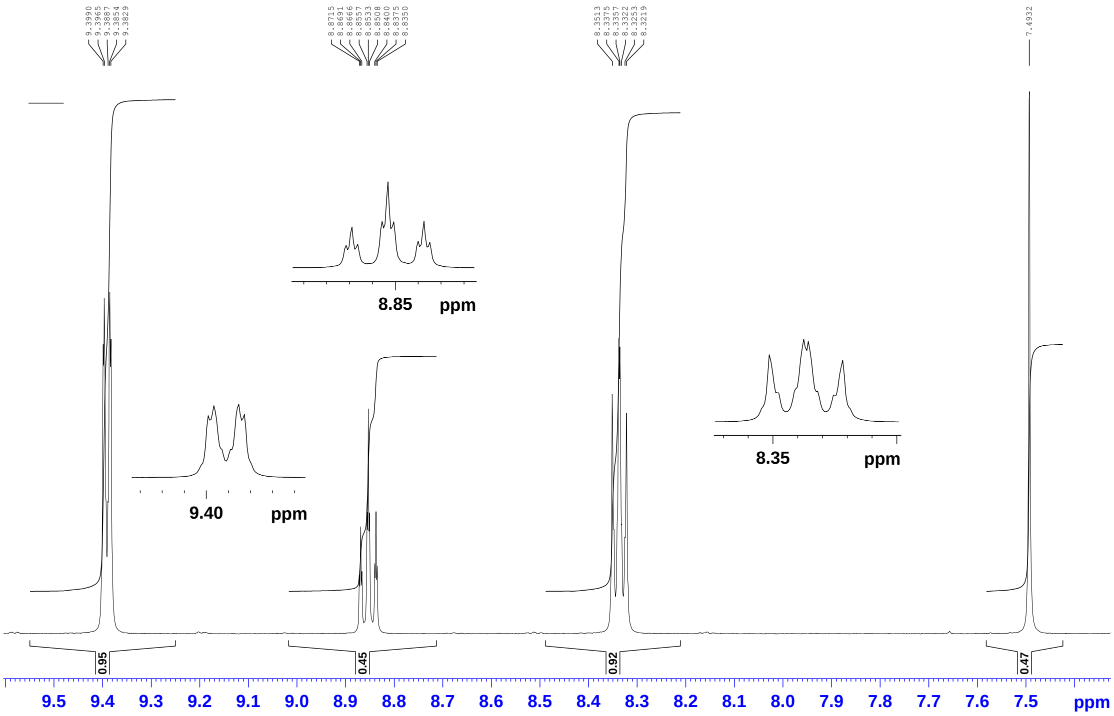

Figure 2.3 ^{1}H NMR of MDP at pD 7.20 (I = 1.0 M), 25°C in phosphate buffer.

In addition to the ^{1}H NMR, a ^{13}C DEPT-135 confirmed the presence of the methylene group between two positively charged nitrogen atoms at 78.0 ppm (Figure 2.4).

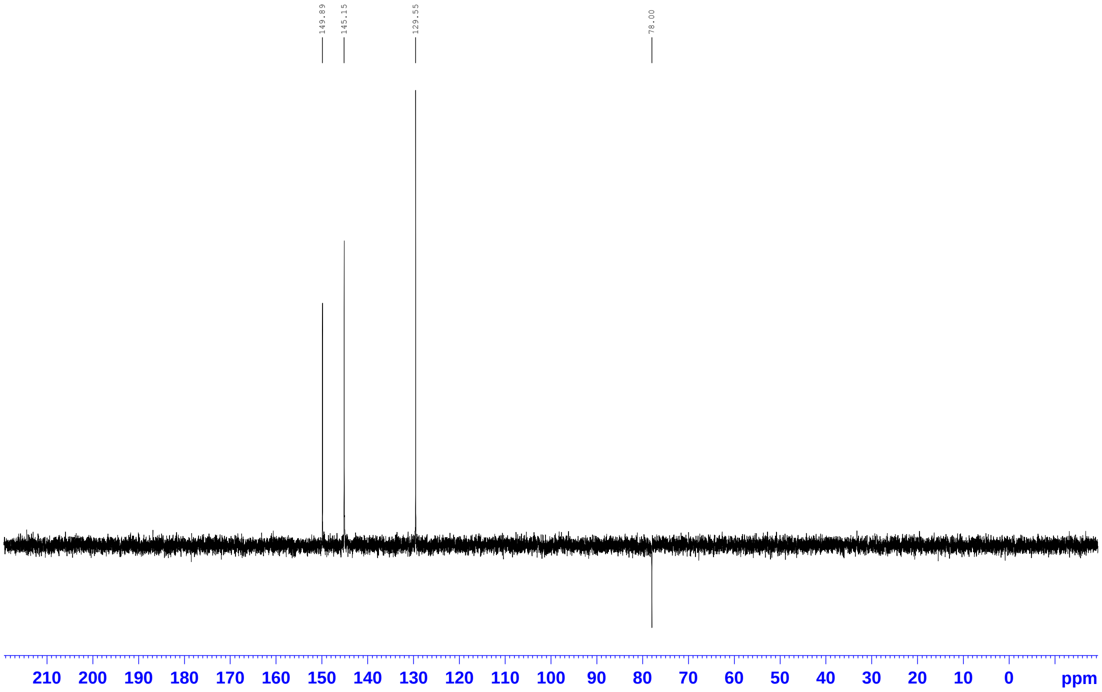

Figure 2.4 ^{13}C DEPT-135 of MDP at pD 7.20 (I = 1.0 M), 25°C in phosphate buffer.

The ^{13}C NMR clearly shows the pyridinium carbons and the bridging CH_2 carbon but not of the ratio one may expect (1:2:2:1). This phenomenon is due proton decoupled carbon-13 spectra which is known as Nuclear Overhauser Effect (NOE). This is observed when one nuclei is irradiated at its resonance frequency which causes the detected nuclei to be more intense or weaker than usual[149].

To correlate protons with their respective carbons a heteronuclear single quantum coherence (HSQC) spectrum was run which (Figure 2.5) indicated the high methylene proton at 7.49 ppm is connected to the carbon at 78.0 ppm. The proton situated within the pyridinium ring at $C_{2/6}$ next to the nitrogen atom has the highest ^{1}H downfield signal at 9.39 ppm, but the $C_{2/6}$ has the second highest carbon chemical shift at 145.15 ppm. The highest carbon chemical shift is C_4 of the pyridinium ring at 149.89 ppm whilst $C_{3/5}$ has the lowest proton and carbon chemical shift at 8.33 and 129.55 ppm, respectively.

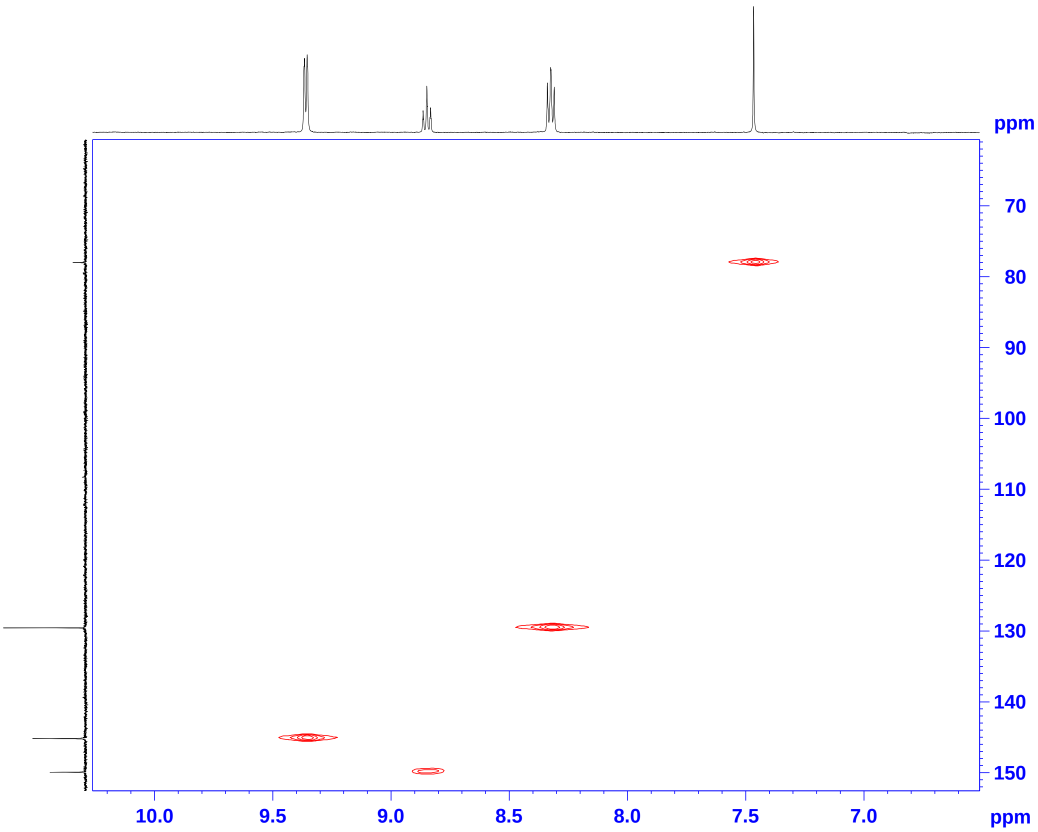

Figure 2.5 HSQC spectra of MDP in D_2O at 25°C.

For free pyridine itself, ^{1}H NMR (Figure 2.6) shows that the α-protons ($C_{2/6}$) are most electron deficient are the highest downfield signals, the second lowest field signal is the ɣ-proton (C_4) and the most upfield signal being of the β-protons ($C_{3/5}$). The ɣ-proton has a lower field signal compared with the β-protons due to inductive and resonance effects from the electron withdrawing nitrogen, as the resonance structures indicate partial positive charges on carbons $C_{2/6}$ and C_4 (Scheme 2.36) which is also concordant with the ^{13}C NMR spectrum.

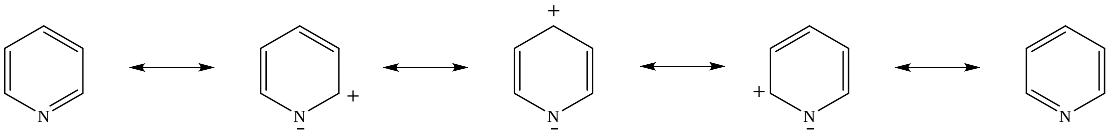

Scheme 2.36 Resonance structures of pyridine indicating partial positive charges of carbons 2, 4 and 6.

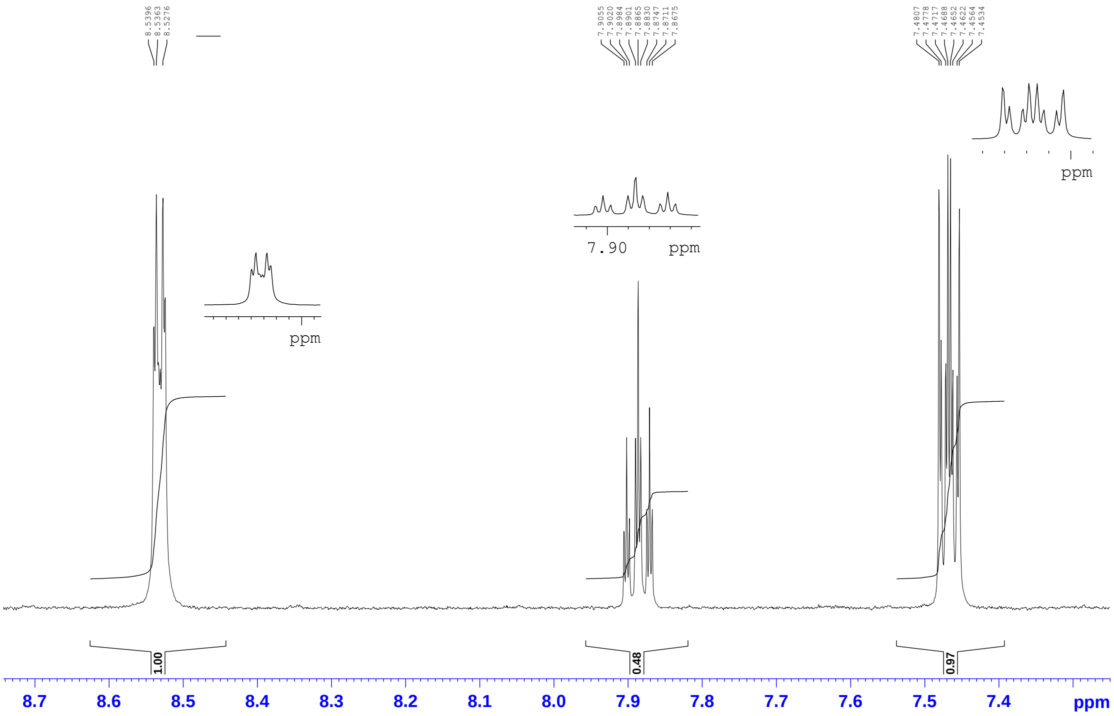

Figure 2.6 Pyridine in D_2O at pD 9.4 at 25°C.

A summary of the ^1H and ^{13}C chemical shifts of MDP and pyridine are shown in Table 2.1.

^1H / ^{13}C	**MDP chemical shift (ppm)**	**Pyridine chemical shift (ppm)**
$H/C_{2/6}$	9.38 (145.15)	8.53 (148.55)
$H/C_{3/5}$	8.33 (129.55)	7.47 (124.43)
H/C_4	8.85 (149.89)	7.89 (137.64)
Methylene (CH_2)	7.47 (78.00)	

Table 2.1 Summary of ^1H and ^{13}C NMR chemical shifts of MDP and pyridine at 25°C.

2.3.1.2 Mass spectrum of MDP

A mass spectrum of MDP (Mr = 172.10 (minus anion counter ions)) was taken using electron spray ionisation (ESI) in positive mode where a mass corresponding to half the molecular weight of MDP was observed at m/z = 86.0503 as there are two positive charges (z) on the molecule (Figure 2.7).

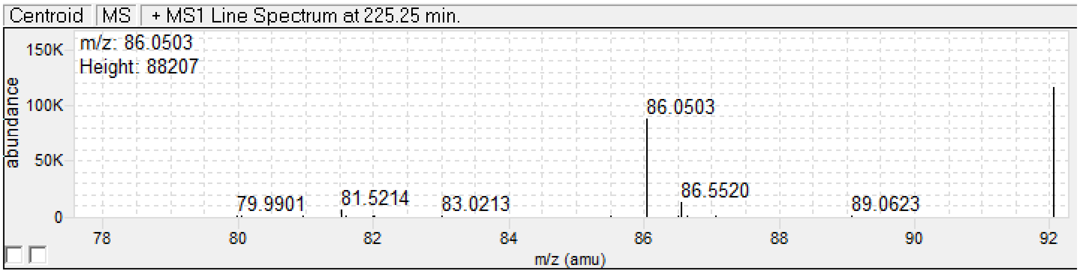

Figure 2.7 ESI mass spectrum corresponding to MDP.

2.3.2 Hydrolysis of MDP between pH 9 and 14

2.3.2.1 Kinetics

The UV-Vis spectrum of MDP in water is compatible with a recent publication and shows a maximum absorbance at 258 nm (Figure 2.8)[150]. At high pH, using 0.02 M CAPS buffer solutions at 0.1 M ionic strength at pHs 9.5, 10, 10.5 and 11.0 a reaction occurred as indicated by the appearance of a chromophore at 366 nm yet between pH 12-14 there was no observable chromophore at 366 nm. This absorbance changes with time and reaches a maximum and then decreases indicative of the formation of an unstable intermediate (Scheme 2.37).

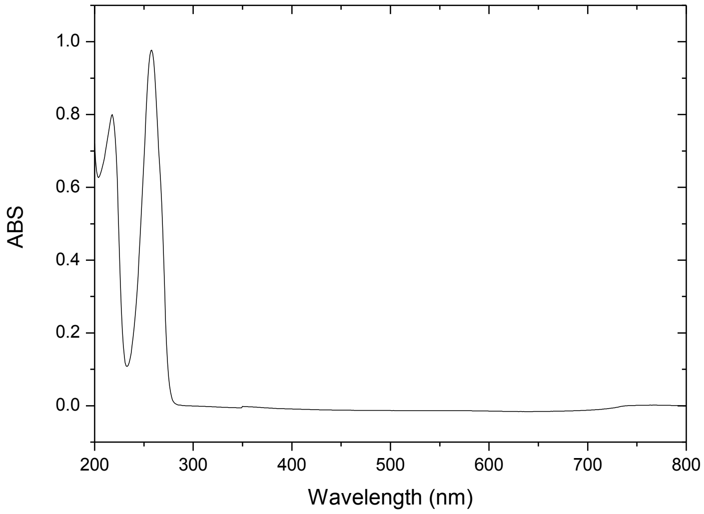

Figure 2.8 UV-VIS spectrum of MDP at 25°C (1.0×10^{-4} M) in water.

$$\mathrm{MDP} \xrightarrow{k_1} \mathrm{I} \xrightarrow{k_2} \mathrm{P}$$

Scheme 2.37 Proposed kinetic pathway for the hydrolysis of MDP.

The observed consecutive first-order rate constants associated with this biphasic behaviour were determined as a function of pH. The consecutive reaction was fitted in terms of the intermediate and the concentration of the intermediate at any time (t) is given by Equation 2.2.

$$[\mathrm{I}]_\mathrm{t} = \frac{k_1}{k_2 - k_1}\{\mathrm{e}^{(-k_1\mathrm{t})} - \mathrm{e}^{(-k_2\mathrm{t})}\}[\mathrm{A}_0]$$

Equation 2.2

The pseudo first-order rate constant k_1 corresponds to the first phase and appearance of the chromophore I, is shown by Figure 2.9. A plot of log k_1 against pH (slope = 1.8) shows a second-order dependence (Figure 2.10) on the concentration of hydroxide-ion (as $[\mathrm{OH}^-] = 10^{(\mathrm{pH-pKa})}$) giving a third-order rate constant = 5.47×10^4 $\mathrm{M}^{-2}\,\mathrm{s}^{-1}$ whereas that for the second phase and disappearance of the intermediate k_2 is pH independent = 6.0×10^{-5} s^{-1}.

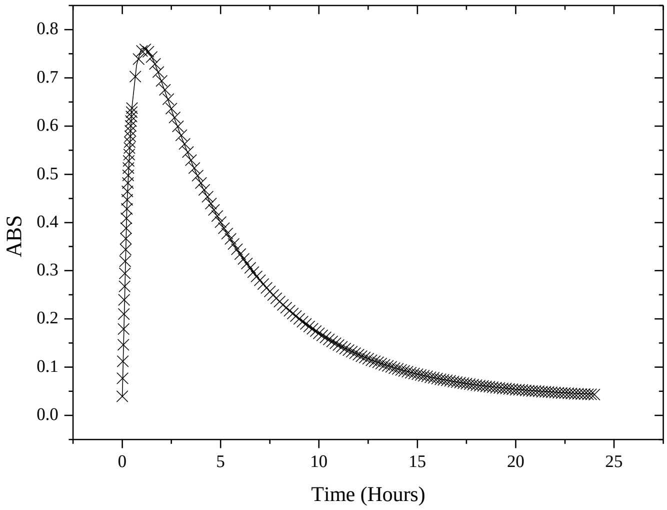

Figure 2.9 Change in absorbance at 366 nm with time for the hydrolysis of MDP (1.0×10^{-4} M) at pH 10.0 (0.02 M CAPS buffer) I = 0.1 M (KCl) at 25°C. The continuous line shows the model of Scheme 2.37 fit to data.

The pseudo first-order rate constants were not extrapolated to zero buffer concentration by altering the buffer concentration as there was no significant buffer catalysis. The total concentration of CAPS buffer was constant throughout the pH range and at constant ionic strength.

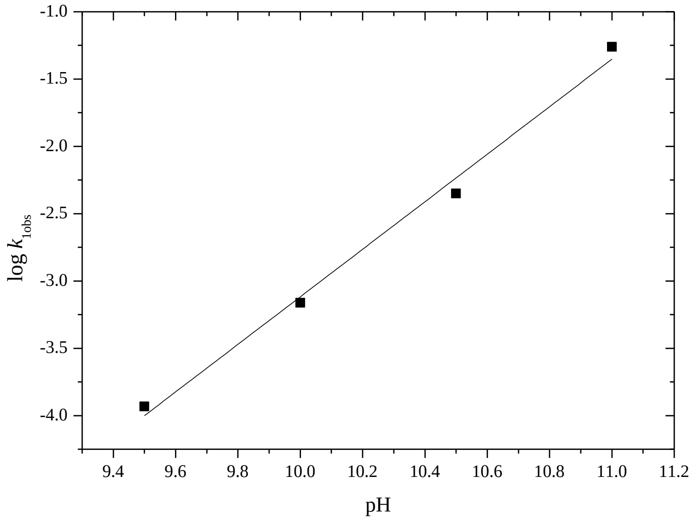

Figure 2.10 Plot of log k_1 against pH for the appearance of a chromophore at 366 nm at I = 0.1 M and at 25°C.

In addition to hydrolysis of MDP in water, the UV-Vis kinetic data of the hydrolysis of MDP in D_2O was slightly faster than that in H_2O ($k_{OD} > k_{OH}$). It is most likely that a solvent isotope effect has occurred as previous data showed that acid and base catalysed reactions proceeded more rapidly in D_2O than in H_2O by an order of 1.3-3.0 as acids are weaker in D_2O than H_2O ($pK_{wD2O} > pK_{wH2O}$), which makes (OD^-) a stronger base than (OH^-)[151].

Solvent effects are difficult to interpret as they can be a result of many factors:

(i) Water and deuterium oxide have different solvation properties.

(ii) A primary kinetic isotope effect is observed if an O-H or an O-D bond is broken in the rate determining step.

Isotopic substitution generally has no significant effect on the qualitative chemical reactivity of a given process, but a difference in the rate of isotopically substituted reactants is sometimes observed; this is known as the kinetic isotope effect (KIE)[151]. The lowest quantised vibrational state of a bond is its zero-point energy (ZPE), and the heavier the atom, the lower the zero-point energy. This is due to a lower frequency of vibration as ZPE = ½ hcω (h = Plank's constant (6.6 x 10^{-34} J s^{-1}), c = speed of light, ω = angular frequency) and is clearly shown by the difference between ^1H and ^2H (D) in the potential energy diagram (Figure 2.11)[151].

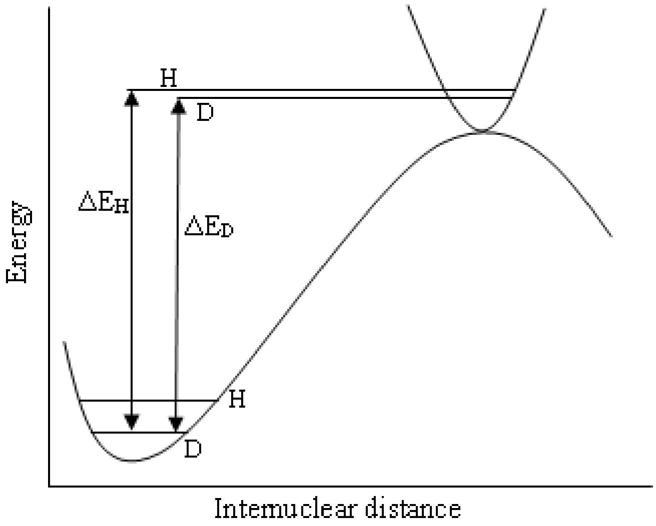

Figure 2.11 Reaction coordinate diagram for the difference in activation energy for C-H and C-D bond[151].

2.3.3 Hydrolysis products

Hydrolysis at pD 10 in D_2O yields pyridine on the disappearance of MDP as shown by ^{1}H NMR signals at 8.53 ppm ($C_{2/6}$) which appears to be a doublet (d, $J_{2,3}$ = 8.40 Hz, 2H). The peak at 7.88 ppm (C_4) is a triplet (t, $J_{4,3}$ = 7.70 Hz, 1H) and a multiplet at 7.47 ppm ($C_{3/5}$) (m, 2H) (Figure 2.12). Using sodium acetate as an internal standard, the changes in signal intensities with time were used to determine the pseudo first-order rate constants for the disappearance of MDP and the appearance of pyridine. Those for the latter were biphasic compatible with a stepwise formation of pyridine. This was also confirmed by monitoring the formation of pyridine by GC (Figure 2.13).

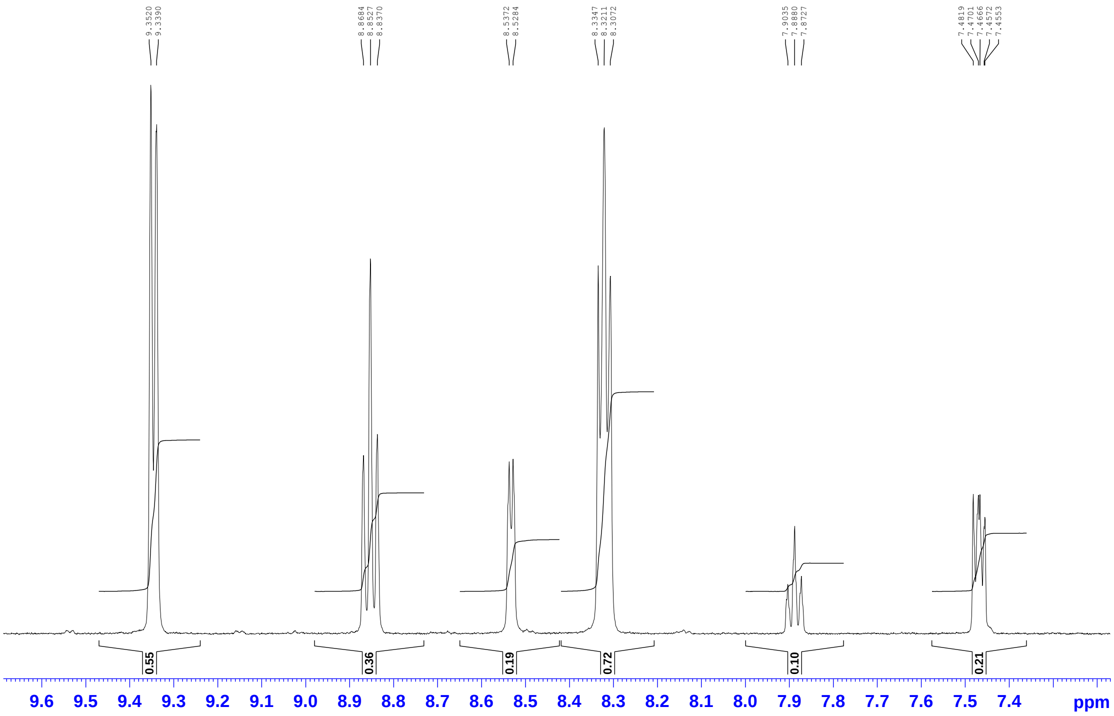

Figure 2.12 MDP hydrolysing to form pyridine at pD 10, I = 1.0 M and 25°C after 2.2 hours.

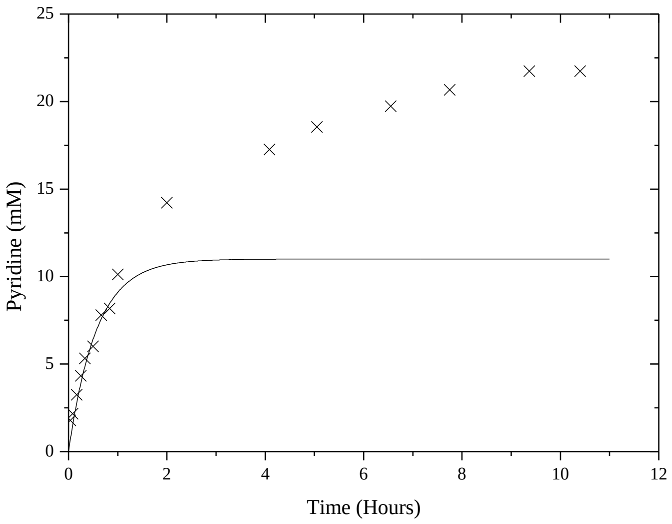

Figure 2.13 Change in concentration of pyridine with time for the hydrolysis of MDP (1.01 x 10^{-2} M) at pH 10.0 (0.3 M CAPS buffer) I = 0.1 M (KCl) at 25°C. The continuous line represents a first-order fit to 1 mole equivalent of pyridine.

A borate buffered solution at pH 9 containing MDP was heated to accelerate the reaction towards completion and monitored by ^1H and ^{13}C NMR. The ^1H NMR clearly showed the production of pyridine (8.53 ppm, dd, $J_{2,3}$ = 4.35 Hz, $J_{2,4}$ = 1.60 Hz, 2H), (7.89 ppm, tt, $J_{4,3}$ = 7.73 Hz, $J_{4,2}$ = 1.75 Hz, 1H), (7.47 ppm, m, 2H). A ^{13}C spectrum showed the presence of an unknown species underneath the water signal at 4.8 ppm, a HSQC confirmed a masked carbon compound under the H_2O ^1H spectrum at 81.99 ppm (Figure 2.14) and a ^{13}C DEPT-135 confirmed it to be a CH_2.

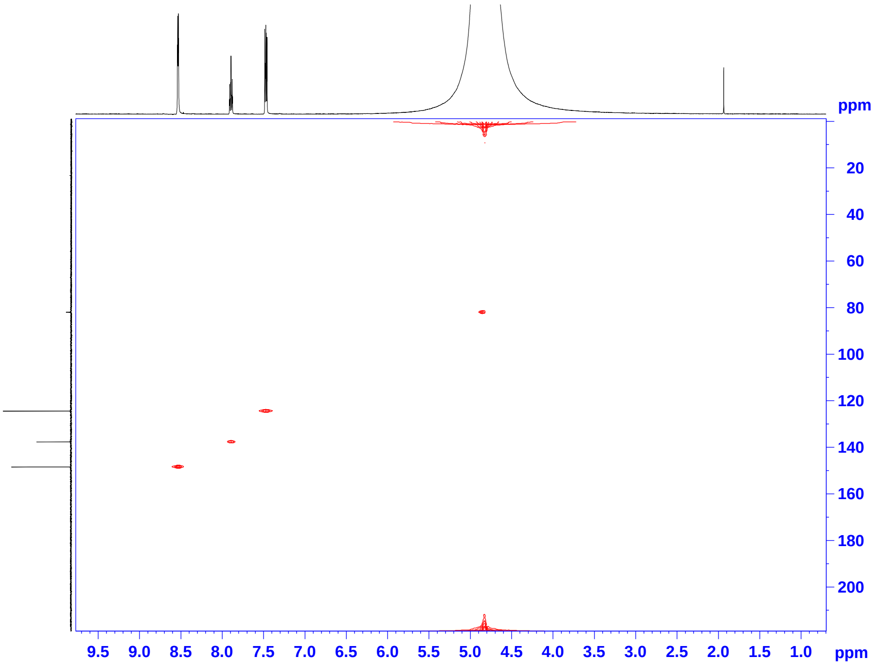

Figure 2.14 HSQC of the hydrolysed MDP forming pyridine and the unknown compound in pH 9 borate buffer, I = 1.0 M at 25°C.

The possibility of formaldehyde forming from the hydrolysis of MDP is relatively high and an identical buffered solution containing formaldehyde (without MDP) resulted in the ^{13}C chemical shift at 82.00 ppm and a ^{13}C DEPT-135 confirmed the signal to be a CH_2 confirming formaldehyde hydrate (Figure 2.15).

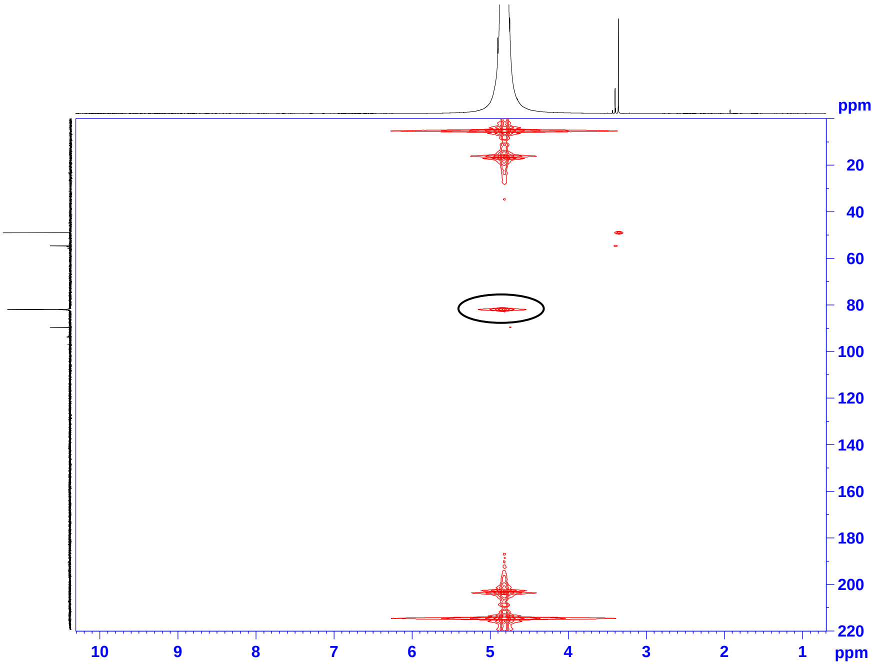

Figure 2.15 HSQC of the formaldehyde in pH 9 borate buffer, I = 1.0 M at 25°C.

2.3.4 Intermediate identification

The hydrolysis of MDP showed a maximum UV-Vis absorption at 366 nm which was shown in Figure 2.9. Investigation of this chromophore was carried out with a solution of MDP (22 mM) in 1 ml CAPS buffer pH 10, which was incubated at 25°C for 30 minutes corresponding to the maximum formation of the chromophore after which 2 ml DCM was added to the solution. The organic layer was separated from the aqueous layer and showed a UV-Vis absorption at 330 nm (Figure 2.16), presumably corresponding to the intermediate seen in water with a λ_{max} = 366 nm. There is also an absorption at 252 nm corresponding to free pyridine. Using a $\varepsilon = 2000$ l.mol.cm^{-1} for pyridine at 252 nm and an absorbance of 0.503 indicated that 5 mM (1 mole equivalent) of pyridine had been released, assuming the majority of pyridine had transferred into the DCM which is dependent on its partition coefficient. A similar compound to MDP which could resemble an intermediate is N-methylpyridinium chloride, the UV-Vis spectrum at pH 10 showed a chromophore at 258 nm and not 366 nm which eliminates N-methylpyridinium as a possible intermediate (Figure 2.17). In addition to the UV-Vis data a GC-MS showed an m-1= 108 corresponding to the mass of the intermediate (Figure 2.18).

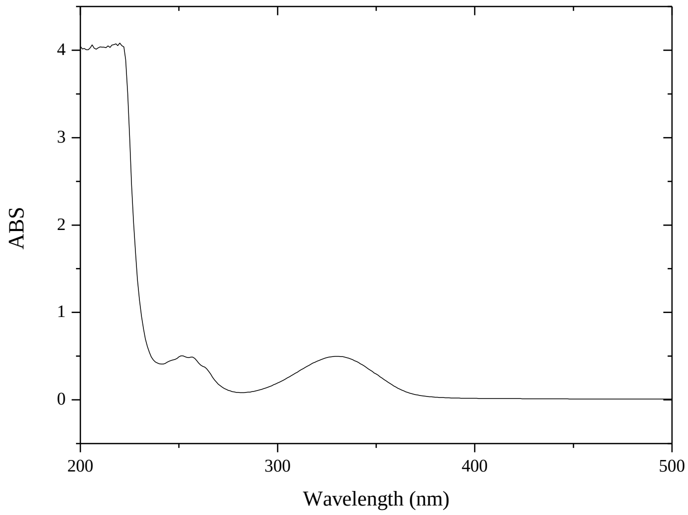

Figure 2.16 UV-VIS spectrum at 25°C of MDP (22.0 x 10^{-3} M) in CAPS buffer pH 10 and then extracted into DCM after 30 minutes.

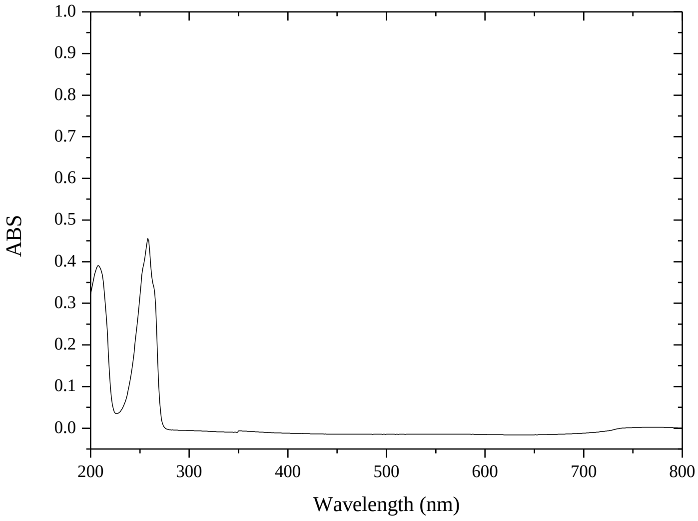

Figure 2.17 UV-VIS spectrum at 25°C of N-methylpyridinium (1.0 x 10^{-4} M) in 0.02 M CAPS buffer pH 10.

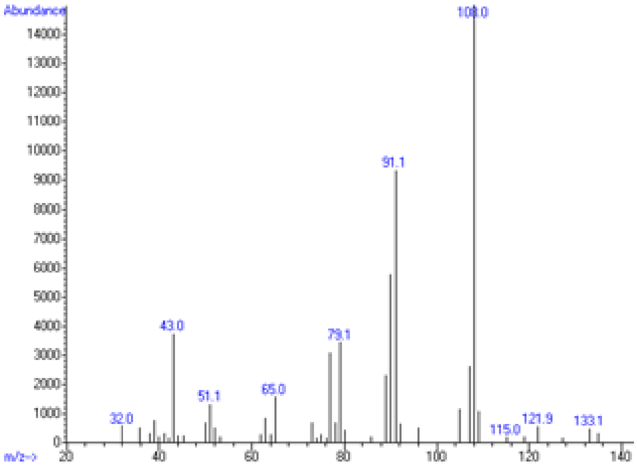

Figure 2.18 MS from GC peak showing the formation of the intermediate m-1 = 108.

2.3.5 Mechanism of hydrolysis

A reaction scheme compatible with these observations is shown in Scheme 2.38. It is known that some substitution reactions of pyridines and azines proceed by initial nucleophilic addition to the ring to form a 1:1 σ-adduct via a nucleophilic aromatic substitution addition-elimination (S_NAr-AE) or a nucleophilic aromatic substitution elimination-addition (S_NAr-EA) mechanism[135]. It also appears that some substitution reactions previously thought to occur by an aryne-type mechanism actually involve ring opening of the 1:1 σ-adduct followed by ring closure commonly known as the Addition of Nucleophile, Ring Opening and Ring Closure (S_N(ANRORC)) mechanism which was first observed mechanistically by Van der Plas[135, 152].

The first step within the S_N(ANRORC) mechanism involves addition of a nucleophile at the C_2 position producing the 1:1 σ-adduct, although it may be sterically inhibited by having large substituents on the ring[152]. The proposed species then undergoes ring-opening and expulsion of the first pyridine to generate the conjugated unsaturated imino-aldehyde **I** which is the chromophore observed at 366 nm. The unsaturated iminno-aldehyde undergoes ring closure to produce the second molar equivalent of pyridine and formaldehyde Scheme 2.38. At high pH the chromophore is not observed as the intermediate is in resonance between the imine and immonium ion (Scheme 2.39 i, ii) and hydroxide attacks quicker than the rate of formation of the intermediate (k_5).

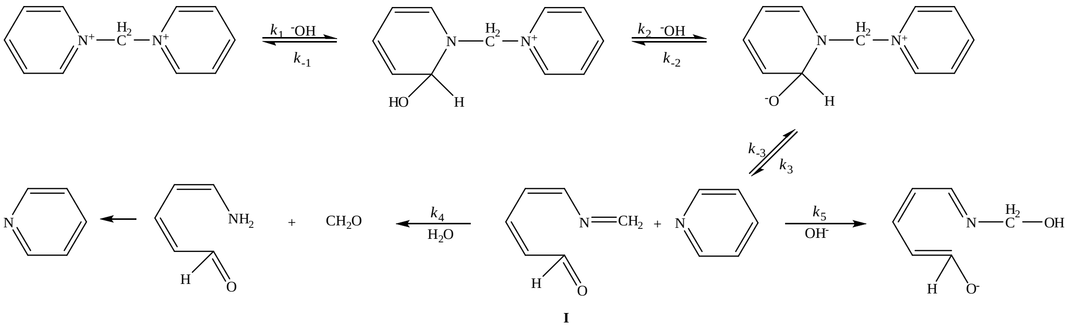

Scheme 2.38 Hydrolytic mechanism of MDP at high pH.

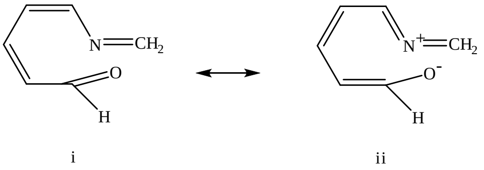

Scheme 2.39 Resonance between the imine and the immonium ion.

2.3.6 Hydrolysis products of MDP below pH 9

The chromophore at 366 nm was not observed below pH 9 but the reactions of MDP at lower pH/pD could be monitored in D_2O by the changes in the ^1H and ^{13}C NMR spectra. Under pseudo first-order conditions in 1.0 M and 0.1 M DCl at 25°C MDP remained unchanged after 4 weeks and at 50°C after 2 weeks which shows remarkable stability of MDP dication in solution.

After 2.4 weeks of MDP incubation at 25°C at pD 8.0 (I = 1.0 M) the ^1H NMR signals of MDP at 9.40 ppm ($C_{2/6}$) (dd, $J_{2,3}$ = 6.90 Hz, $J_{2,4}$ = 1.25 Hz), 8.85 ppm (C_4) (dt, $J_{4,3}$ = 7.88 Hz, $J_{4,2}$ = 1.5 Hz, 2H) and 8.33 ppm ($C_{3/5}$) (d, $J_{4,3}$ = 7.90 Hz, 4H) hydrolyse to show the appearance of pyridine at 8.55 ($C_{2,6}$) (dd, $J_{2,3}$ = 4.35 Hz, $J_{2,4}$ = 1.63 Hz), 7.92 (C_4) (dt, $J_{4,3}$ = 7.70 Hz, $J_{4,2}$ = 1.6 Hz, 1H) and 7.47 ($C_{3,5}$) ppm (m, 2H). The signals at 9.01 ppm ($C_{2/6}$) (d, $J_{2,3}$ = 6.45 Hz), 8.63 ppm (C_4) (dt, $J_{4,3}$ = 7.85 Hz, $J_{4,2}$ = 1.43 Hz, 1H) and 8.14 ($C_{3/5}$) (t, $J_{3,4}$ = 5.73 Hz, 2H) ppm are compatible with the formation of N-hydroxymethyl pyridinium-ion (Scheme 2.40) although the hydroxymethyl group was not visable due to it being deuterated (Figure 2.19) and splitting is lost due to other protons being exchanged with deuterium in MDP, pyridine and N-hydroxymethyl pyridinium.

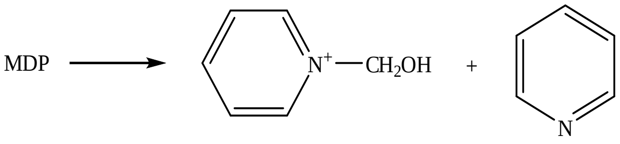

Scheme 2.40 Formation of N-hydroxymethyl pyridinium-ion from the hydrolysis MDP at low pH/pD.

A HSQC spectrum correlated the protons of N-hydroxymethyl pyridinium ion to its respective carbon which showed that the compound is hybrid between MDP and pyridine as shown by the Figure 2.20.

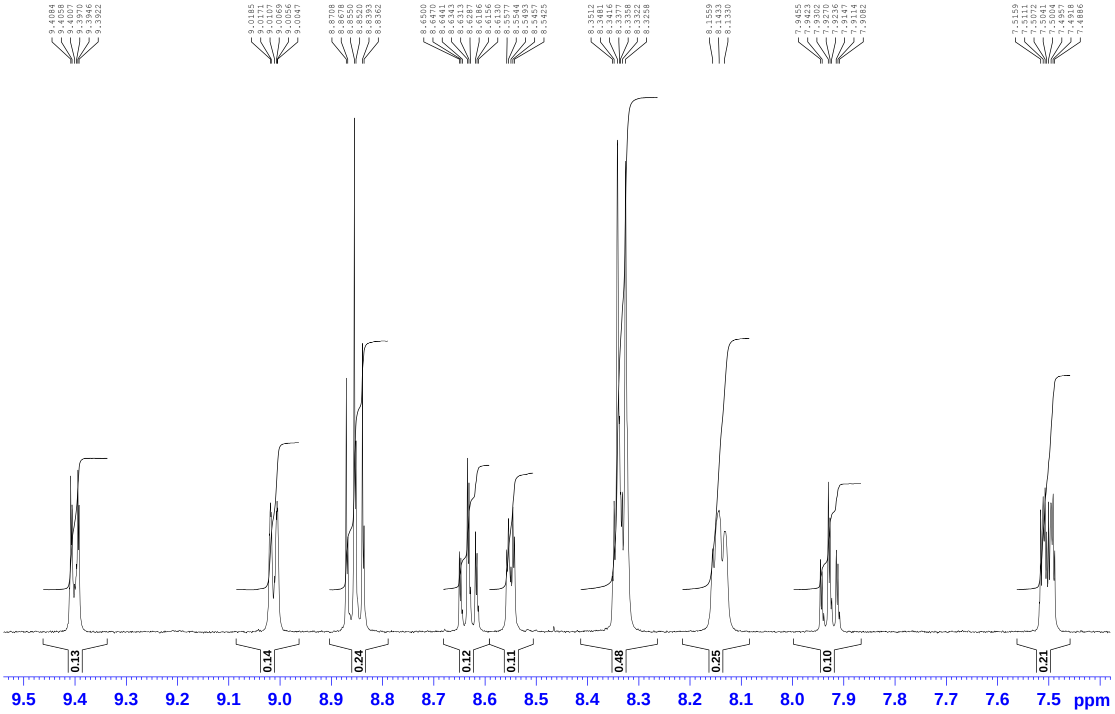

Figure 2.19 ^{1}H spectrum of the hydrolysis of MDP to form pyridine and N-hydroxymethyl pyridinium-ion at pD 8.0 (I = 1.0 M) at 25°C after 2.4 weeks.

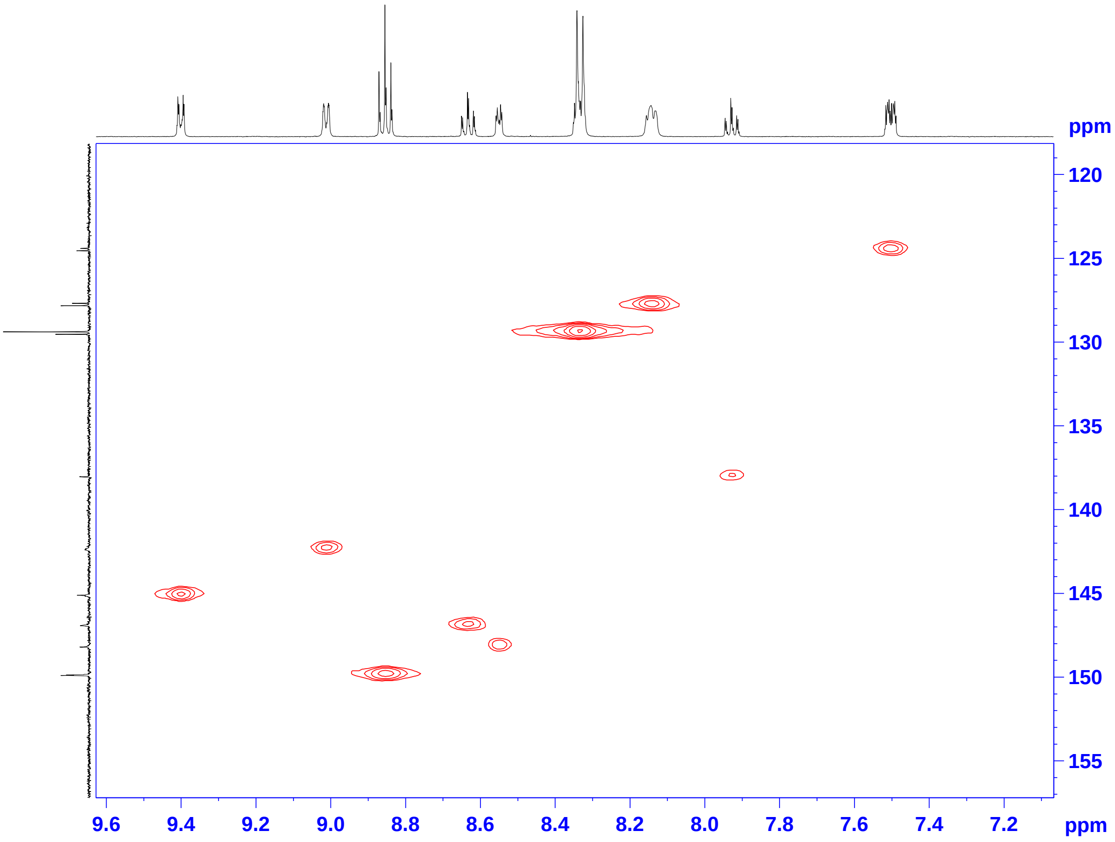

Figure 2.20 HSQC hydrolysis of MDP at pD 8.0 (I = 1.0 M) at 25°C after 2.4 weeks.

2.3.7 Summary

2.3.7.1 Overall pH-rate profile

The pseudo first-order rate constants obtained using the analytical techniques above were used to produce a pH-rate profile (log k_{obs} against pH) for the hydrolysis of MDP (Figure 2.21).

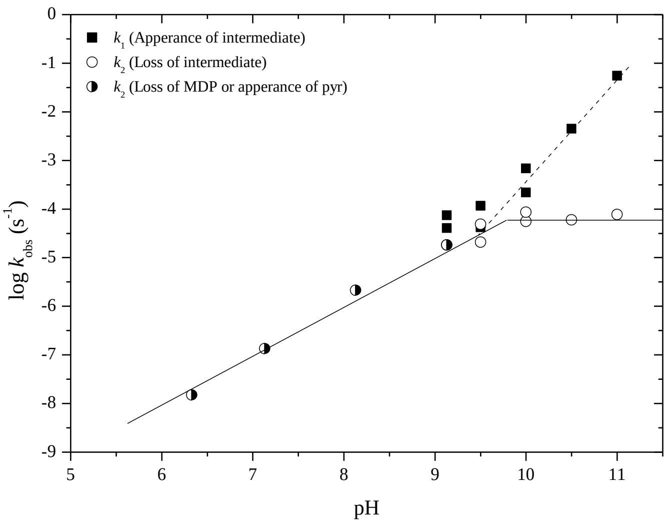

Figure 2.21 pH-rate profile of the hydrolysis of MDP which show the two different pathways. Below pH 9 the pathway is first-order (○ and ◑, k_2) and above pH 9 is second-order (■, k_1).

The pH-rate profile shows three different events which take place over a pH range of 6-11. Below pH 9 the pH-rate profile of k_2 shows a first-order linear dependence on hydroxide-ion concentration but above pH 9 becomes the rate becomes pH independent. The hydrolysis rate constant, k_1 shows a second-order dependence in hydroxide-ion concentration and assuming the reaction pathway given in Scheme 2.41 a steady state approximation can be used (Equation 2.3).

$$\mathrm{MDP} \underset{k_{-1}}{\overset{k_1\ \mathrm{OH^-}}{\rightleftharpoons}} \mathrm{M} \xrightarrow{k_2\ \mathrm{OH^-}} \mathrm{P}$$

Scheme 2.41 Proposed degradation pathway of MDP.

$$\frac{\mathrm{d[M]}}{\mathrm{dt}} = 0 = k_1[\mathrm{MDP}][\mathrm{OH^-}] - k_2[\mathrm{OH^-}][\mathrm{M}] - k_{-1}[\mathrm{M}]$$

$$k_1[\mathrm{MDP}][\mathrm{OH^-}] = k_2[\mathrm{OH^-}][\mathrm{M}] + k_{-1}[\mathrm{M}]$$

Equation 2.3

Solving for [M] using Equation 2.3 leads to the rate law:

$$[\mathrm{M}] = \frac{k_1[\mathrm{OH^-}][\mathrm{MDP}]}{k_2[\mathrm{OH^-}] + k_{-1}}$$

$$\frac{\mathrm{d[P]}}{\mathrm{dt}} = k_2\,[\mathrm{OH^-}][\mathrm{M}]$$

$$\frac{\mathrm{d[P]}}{\mathrm{dt}} = \frac{k_1 k_2[\mathrm{OH^-}]^2[\mathrm{MDP}]}{k_2[\mathrm{OH^-}] + k_{-1}}$$

Equation 2.4

Therefore if $k_{-1} >> k_2[\mathrm{OH^-}]$ in Scheme 2.42, rate $= \frac{k_1 k_2\,[\mathrm{OH^-}]^2}{k_{-1}} = k_2 \mathrm{K}_1\,[\mathrm{OH^-}]^2$ making k_2 the rate limiting step and the observed rate second-order in hydroxide-ion concentration. At high $[\mathrm{OH^-}]$, if $k_2[\mathrm{OH^-}] >> k_{-1}$,the rate $= k_1[\mathrm{OH^-}]$ i.e. a first-order dependence on hydroxide-ion concentration, there could be a change in rate limiting step to k_1. At lower $[\mathrm{OH^-}]$ (< pH 9) the rate of MDP disappearance or appearance of pyridine is first-order in hydroxide-ion concentration and corresponds to a change in mechanism to give N-hydroxymethyl pyridinium (Scheme 2.42).

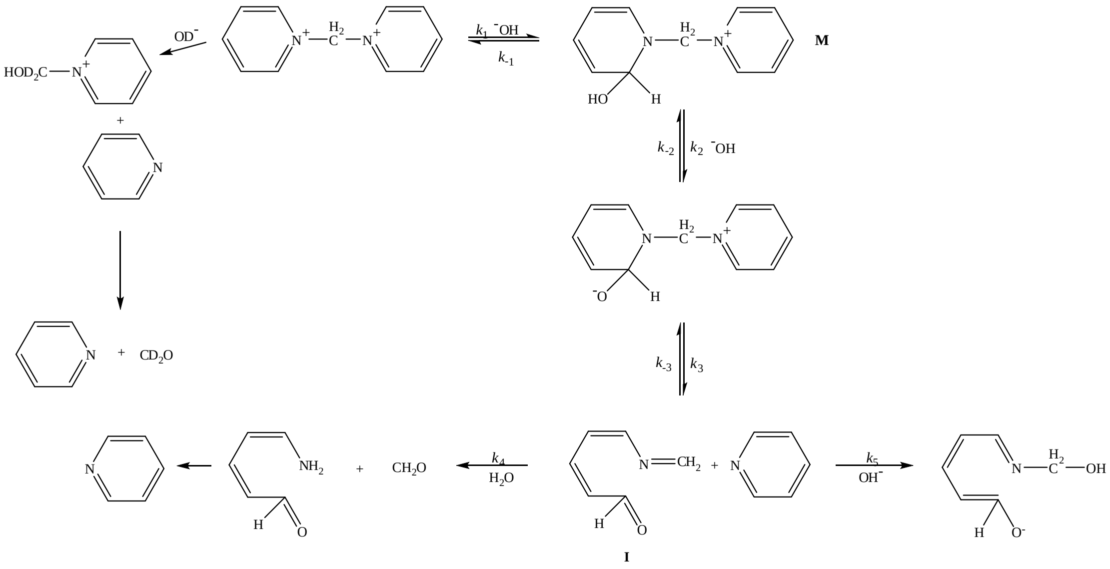

Scheme 2.42 Proposed mechanism of hydrolysis of MDP.

2.3.8 D-exchange

A compound's pK_a is an important physicochemical property and its determination for strong acids/weak bases is relatively easy between the pH regions of 2-10. Conventional methods for determining the pK_a of a compound include UV-Vis spectroscopy, providing the compound contains a chromophore, and NMR spectroscopy, but potentiometric titration has been the standard method for many years.

Many carbon acids have very high pK_a values and an alternative to the above methods involves a measurement of a kinetic pKa. The acidity constant (K_a) is the ratio of rate constants of the forward (k_f, M^{-1} s^{-1}) and reverse (k_r, s^{-1}) directions of an equilibrium process (Scheme 2.43).

$$\mathrm{HA} \underset{k_\mathrm{r}}{\overset{k_\mathrm{f}}{\rightleftharpoons}} \mathrm{H^+ + A^-}$$

$$\mathrm{K_a} = \frac{k_\mathrm{f}}{k_\mathrm{r}}$$

Scheme 2.43 Deprotonation of a simple acid.

A technique to calculate the forward rate constant is by using isotopic exchange techniques which can be followed by mass spectrometry or NMR. Commonly a proton is replaced by a deuterium atom although this process can be investigated in reverse. Deuterium oxide is usually present in excess compared with the non-deuterated carbon acid or compound of interest. In basic solution, deprotonation occurs when a deuteroxide ion removes a proton producing HOD and the carbanion which is then captured by a deuteron[153, 154]. For example, a carbonyl compound yields an enolate anion and if k_2 (D_2O) > k_{-1} (HOD) then the rate of deuteration corresponds to the rate of the formation of the carbanion (Scheme 2.44).

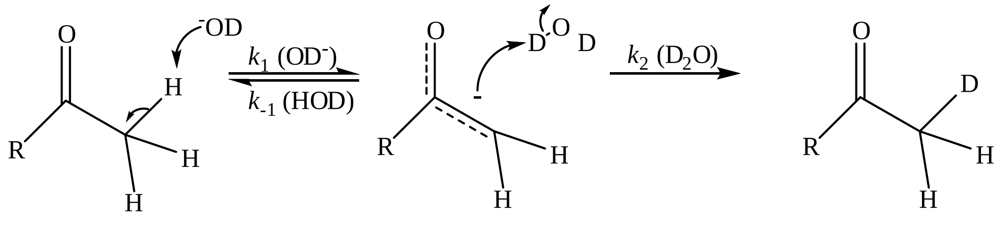

Scheme 2.44 Deprotonation of a carbon acid by deuterium oxide-ion[154].

In water, carbon acids may undergo deprotonation by the solvent (Scheme 2.45, i), by a buffer base (Scheme 2.45, ii), or by hydroxide ion (Scheme 2.45, iii). In general it is expected that the stronger a carbon acid is the more likely it is that deprotonation will occur by solvent or by buffer rather than by hydroxide ion at lower pHs.

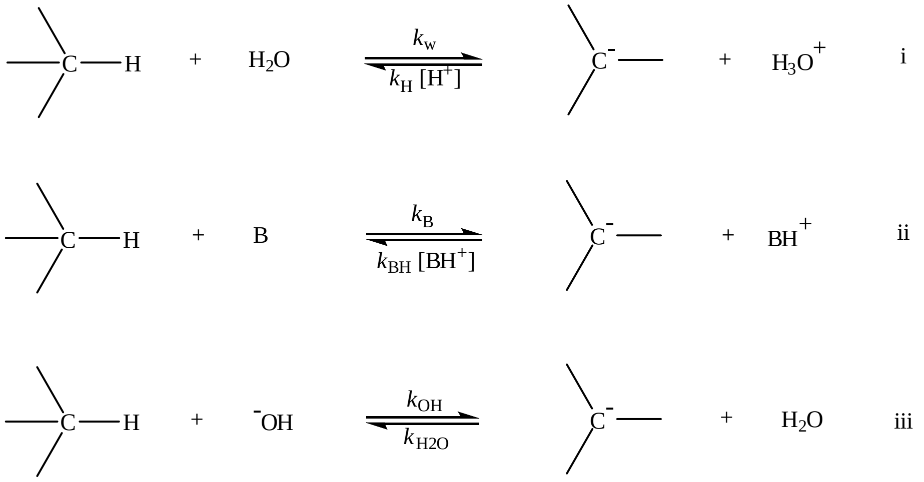

Scheme 2.45 Deprotonation of the carbon acid by the solvent, buffer base or hydroxide-ion.

Conversely, weak carbon acids, particularly those giving charge localised carbanions and subject to internal return in the initially formed ion-pair, may only show observable deprotonation by strong bases such as hydroxide-ions[154]. Once deprotonation occurs by the solvent, buffer or hydroxide-ion when $k_2 > k_{-1}$ an INT-H carbanion intermediate is formed. The reaction can then proceed either by regenerating the initial carbon acid and base, (k_{-1}) or can exchange the BH with BD within the bulk solvent to form INT-D which then would form the C-D bond of the carbon acid (Scheme 2.46)[155].

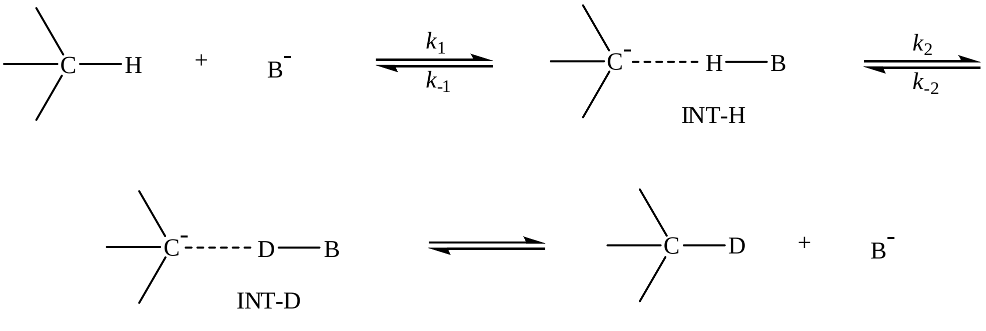

Scheme 2.46 Deprotonation of a carbon acid stabilised by internal return mechanism[155].

2.3.8.1 Methylene D-exchange

It was anticipated that the central methylene of 1,1′-methylenebis-pyridinium dication (MDP) would be a moderately strong carbon acid as ionisation yields what appears to be a fairly stable carbanion ylide (Figure 2.22).

The rate of exchange for deuterium of the methylene of 1,1′-methylenebis-pyridinium dication (MDP) in buffered D_2O (pD 7.20–10) at 25 °C and I = 1.0 M (KCl) was followed by ^1H NMR spectroscopy at 500 MHz. Deuterium exchange results in the disappearance of the singlet at 7.47 ± 0.03 ppm due to the CH_2 group of the substrate and the appearance of a poorly resolved upfield-shifted triplet at 7.46 ± 0.03 ppm due to the CHD group of the initially-formed mono-deuterated product. The loss of the methylene signal, which required deconvoluting, followed first-order kinetics and the associated first-order rate constants k_{obsd} (s^{-1}) were determined at pD 7.20-10.0, maintained at various phosphate and CAPS buffer concentrations at I = 1.0 M.

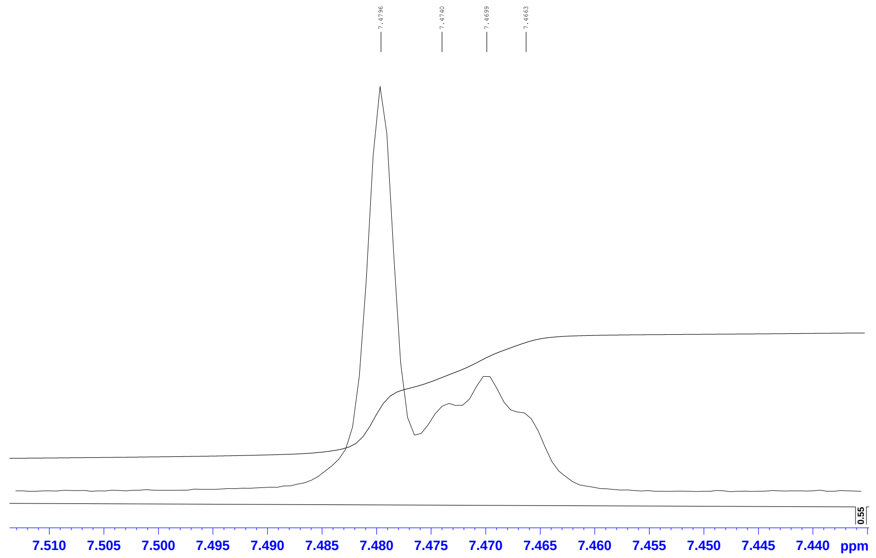

Figure 2.22 Methylene peak of MDP in phosphate buffer after 2 days at pD 7.2 at 25^{o}C (I = 1.0 M).

There was a small amount of buffer catalysis of the D-exchange reaction and the observed pseudo-first-order rate constants k_{obsd} (s^{-1}) were plotted against the buffer concentration to give the buffer independent rate constant k_{int} (s^{-1}) at zero buffer concentration (Equation 2.5). A plot of k_{int} against the deuteroxide-ion concentration [OD^-], calculated from Equation 2.6 where $pK_w = 14.87$[156] is linear and the slope of which gives the second-order rate constant for exchange of the methylene proton of MDP catalysed by OD^- $k_{OD} = 297.1 \pm 23.1$ dm^3 mol^{-1} s^{-1} (Figure 2.23).

$$k_{\mathrm{obs}} = k_{\mathrm{OD}}[\mathrm{OD}^-] + k_{\mathrm{B}}[\mathrm{B}]$$

Equation 2.5

$$\log[\mathrm{OD}^-] = \mathrm{pD} - \mathrm{pK_w}$$

Equation 2.6

Furthermore, the intercept was indistinguishable from zero, indicating an insignificant, pD independent, water catalysed D-exchange reaction. This was confirmed by there being no detectable D-exchange of MDP in 1.0 M and 0.1 M DCl/D_2O at 25°C after 7.5 weeks, indicating that the rate constant k_w (Scheme 2.45, i) for the spontaneous deprotonation of MDP is $< 4.38 \times 10^{-9}$ s^{-1}, assuming less than 2% exchange.

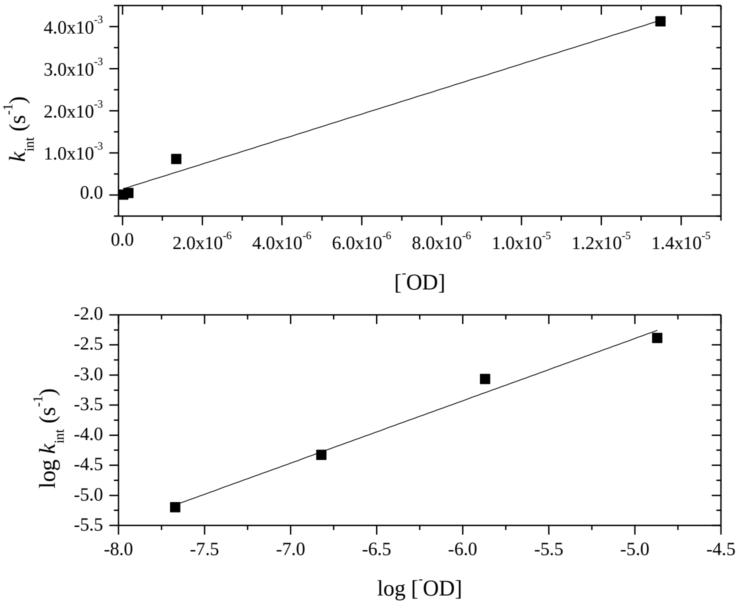

Figure 2.23 Plot of k_{int} against deuteroxide-ion concentration to give a second-order rate constant for the CH_2 exchange of MDP and a log-log plot (below).

The fact that there is no detectable spontaneous deprotonation of MDP (Scheme 2.45, i) indicates that its pK_a must be > 17 as the equilibrium constant for ionisation is the ratio of the deprotonation rate $< 4.38 \times 10^{-9}$ s^{-1} to the protonation rate of the carbanion by D^+ which is expected[157] to be near diffusion controlled $k_D \approx 10^9$ M^{-1} s^{-1}. The buffer catalysed deprotonation of MDP by DPO_4^{2-} and CAPS in D_2O can also be used to estimate the pK_a of MDP from the rate constants for its deprotonation by a buffer base (Scheme 2.45, ii) to give the free carbanion (k_B) and for the reverse protonation of the carbanion by the conjugate acid of this base (k_{BH}) according to Equation 2.7, where pK_{BH} is the pK_a of the buffer base.

$$\mathrm{pK_a} = \mathrm{pK_{BH}} + \log\left(\frac{k_{\mathrm{BH}}}{k_{\mathrm{B}}}\right)$$

Equation 2.7

The second-order rate constant for the deprotonation of MDP by DPO_4^{2-} in D_2O is $k_B = 4.86 \times 10^{-6}$ M^{-1} s^{-1}, and it can be assumed that the rate constant for HPO_4^{2-} in H_2O would be very similar because the kinetic solvent isotope effect for this type of reaction is close to unity. Combining this value of k_B with the upper limit of $k_{BH} \approx 10^9$ M^{-1} s^{-1} for the diffusion-limited reverse protonation of the carbanion by $H_2PO_4^-$ and the value $pK_{BH} = 6.5$ for $H_2PO_4^-$ in H_2O (I = 1.0M)[158] gives $pK_a = 20.8$ for the methylene ionisation of MDP in H_2O. The data using CAPS buffer ($pK_a = 10.15$ in H_2O, I = 1.0 M) give $k_B = 3.36 \times 10^{-3}$ M^{-1} s^{-1}, from which a similar calculation yields $pK_a = 21.6$, giving a mean value of 21.2. The maximum value of the rate of reprotonation of the carbanion by water (limited by solvent reorganisation) is 10^{11} s^{-1}, which can be combined with the observed second-order rate constant for exchange of the methylene proton of MDP catalysed by DO^- ($k_{OD} = 297$ M^{-1} s^{-1}; Scheme 2.45, iii) to give an MDP carbon acid pK_a of ≤ 22.5, in reasonable agreement with that obtained from the buffer-catalysed rate constants.

To compare MDP with N-methyl pyridinium, the rates of D-exchange in 0.1 M and 1 M NaOD/D_2O (I = 1.0M) under pseudo first-order conditions at 25°C was determined. The ^1H NMR showed the methyl group of N-methyl pyridinium as a singlet at 4.41 ppm. A broad triplet (Figure 2.24) was observed after 1 week confirming that one proton had exchanged with a deuteron forming CH_2D (Scheme 2.47). The deuterium exchange rate of a single hydrogen for deuteron of the methyl group was obtained by deconvoluting the singlet at 4.41 ppm.

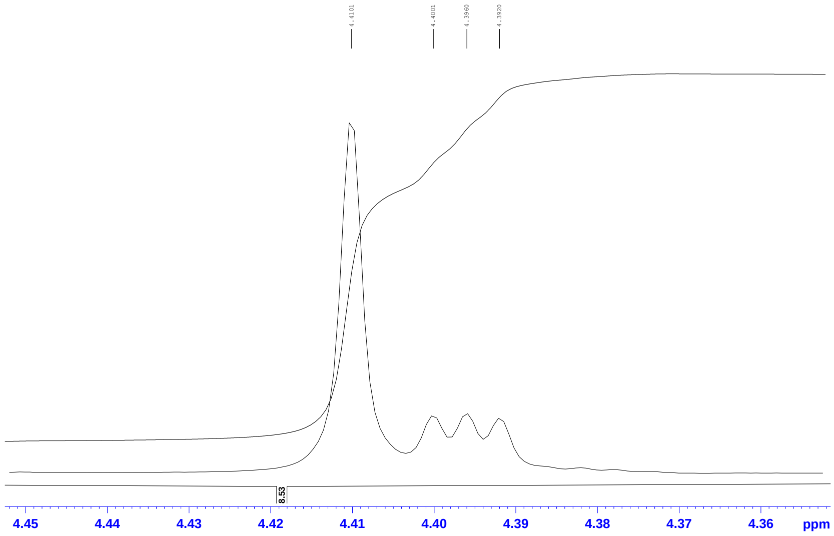

Figure 2.24 Methyl group of N-methylpyridinium becoming CH_2D in 1.0 M NaOD/D_2O solution at 25°C after 1week.

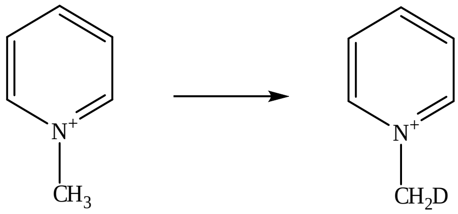

Scheme 2.47 N-methylpyridinium becoming CH_2D.

The appearance of another set of signals in 1.0 M NaOD/D_2O solution appeared after 4.7 weeks (Figure 2.25). A quintet up-field from the triplet is the most likely to be associated with a second proton being exchanged for deuterium, as no signals would appear if all three protons exchanged for deuterium to form CD_3 in a ^1H NMR.

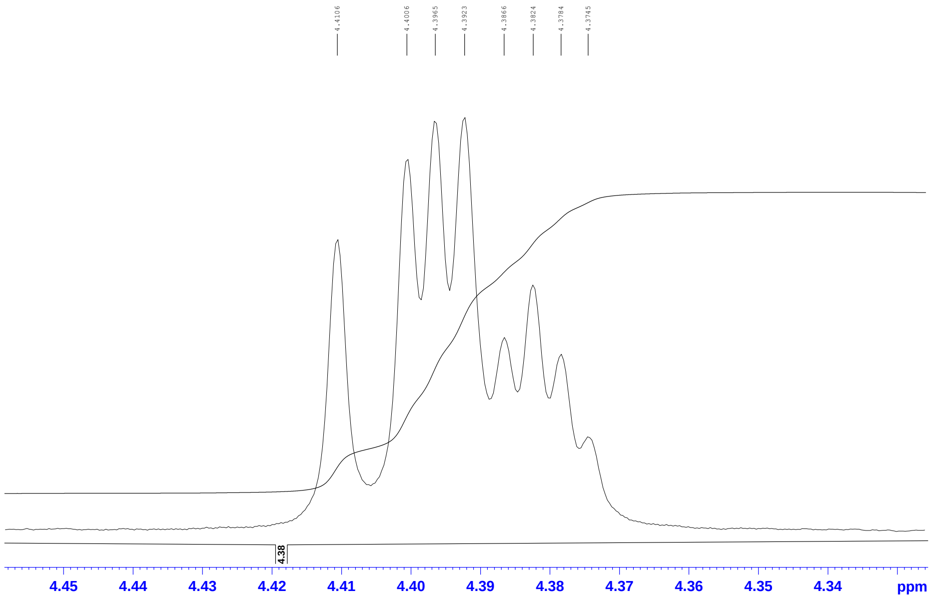

Figure 2.25 Methyl group of N-methylpyridinium becoming CD_2H in 1.0 M D_2O/NaOD at 25°C after 4.7 weeks.

The second-order rate constant for deprotonation of N-methylpyridinium ion to form CH_2D (Scheme 2.48, iii) by deuteroxide ion at 25 °C ($k_{OD} = 4.74 \times 10^{-7}$ M^{-1} s^{-1}) is much smaller than that for MDP. The calculation of the pK_a of N-methylpyridinium ion from this value requires knowledge of the rate constant k_{H2O} for the reverse reaction, the protonation of the carbanion by solvent water (Scheme 2.45, iii). If the pK_a of N-methylpyridinium ion is >25, it is likely[159] that $k_{H2O} \approx 10^{10}$ s^{-1}, giving an estimated pK_a of 30.3 for N-methylpyridinium ion in water, again assuming no significant isotope effect and using $pK_w = 14.0$[156]. Deuterium exchange of the methyl hydrogens of tetramethylammonium ion is not observed in 1.0 M deuteroxide solution over several weeks[160], which may indicate that the zwitterionic ylidic conjugate base of N-methylpyridinium ion is relatively stabilized by the aromatic pyridinium ring compared with that of Me_4N^+ or that Me_4N^+ is additionally stabilized.

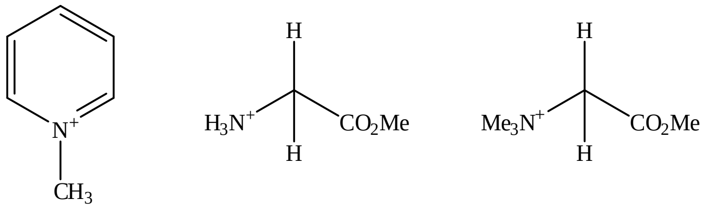

i ii iii

Scheme 2.48 Methyl pyridinium (i), N-protonated glycine methyl ester (ii) and N-quaternary cationic methyl glycine ester (iii).

The value $k_B = 4.86 \times 10^{-6}$ M^{-1} s^{-1} for deprotonation of MDP by DPO_4^{2-} is ca. 10-fold larger than the value $k_B = 5.6 \times 10^{-7}$ M^{-1} s^{-1} for carbon deprotonation of N-protonated glycine methyl ester (Scheme 2.48, ii) by the same base; for N-protonated glycine methyl ester the carbon acid pK_a in water is 21.0[161]. The second-order rate constant $k_{OD} = 297$ M^{-1} s^{-1} for deprotonation of MDP by deuteroxide-ion can be compared with those for some monocationic carbon acids. The k_{OD} values for deprotonation of N-protonated glycine methyl ester and the quaternary cation (Scheme 2.48, iii) are 6.0 and 570 M^{-1} s^{-1}, respectively[145]. The kinetic acidities for the carbon ionization of N-protonated glycine methyl ester and (Scheme 2.48, iii) in water are $pK_a = 18.0$ and 21.0, respectively[145].

The unusual stability of the central methylene which is attached to two hetero-atoms must bring about the stability and slow hydrolysis rates of MDP. This behaviour has been reported in XCH_2Y systems where X and Y are first-row substituents such as N, O and F[162]. The anomeric effect which may have contributing factors such as no bond resonance and negative hyperconjugation have been associated with this phenomenon, Brockway had observed that CF bonds are shorter (60 pm) when going from CH_3F to CF_4 and that di-fluorinated species are much more stable than mono-fluorinated carbon species[163]. This shortening had strengthened the bond which involves double bond-no bond resonance (Scheme 2.49).

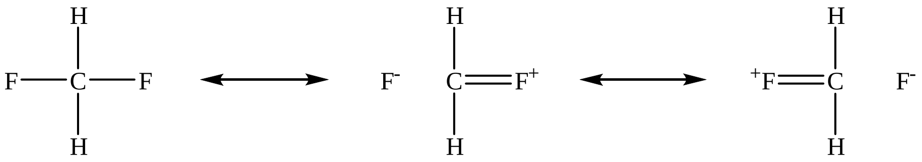

Scheme 2.49 Hyperconjugation of CH_2F_2[162].

In addition to the bond shortening of the anomeric effect, electrostatic interactions C^--N^+ and C^+-F^- shorten bonds although the H_2C-N bond length in MDP of 147 pm is not significantly different from the 146-148 pm seen in N-methylpyridinium ions[164, 165].

2.3.8.2 Deuterium exchange of MDP ring protons

Previous work has shown that protons of N-heterocyclic compounds can exchange with deuterium which may be aided by the presence of acid and base[166]. Pyridine protons exchange with deuterium under harsh conditions (10% NaOD, 200°C) at positions 2 and 6 whereas activated derivatives such as pyridine N-oxide, 3-chloropyridine and 3,5-dichrolopyrine have been described to exchange under milder conditions. Under these conditions exchange at positions 2 and 6 occurs fastest, followed by positions 3 and 5 with position 4 being the least susceptible to H/D exchange. [167, 168].

A similar compound to one of the precursors within the reaction Scheme 2.50 is N-methylpyridinium which has shown rapid exchange of hydrogen by deuterium at positions 2 and 6 at 75°C (I = 1.0 M)[154].

In addition to the methylene protons exchanging for deuterium in MDP the pyridinium ring protons at positions 2 and 6 also exchange for deuterium in solutions of D_2O. The rate of this was determined in buffered D_2O (pD 7.20–10) at 25°C and I = 1.0 M (KCl) and followed by ^1H NMR spectroscopy at 500 MHz either by using protons $C_{3/5,}$ C_4 of the pyridinium ring as a reference. There was negligible buffer catalysis of the D-exchange reaction (Equation 2.5) and a plot of the log of the observed first-order rate constants against pD were linear and of slope near unity (Figure 2.26), indicative of a rate first-order in deuteroxide-ion concentration with a second-order rate constant $k_{OD} = 2.84\ M^{-1}\ s^{-1}$.

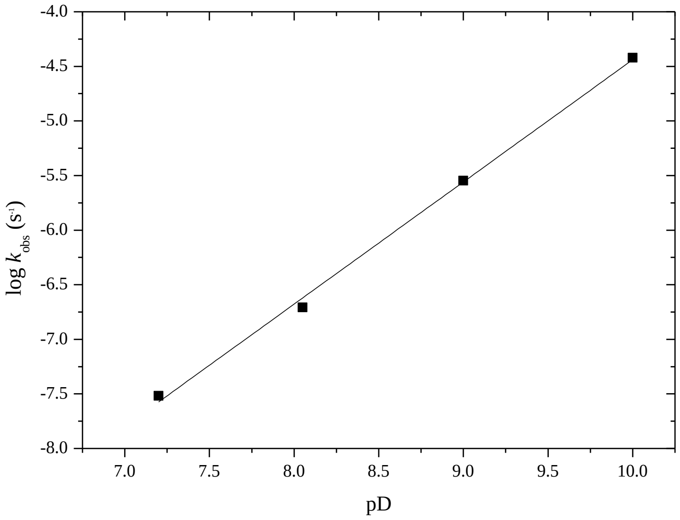

Figure 2.26 Plot of log k_{obs} against pD for the H/D exchange at position 2 and 6 of the pyridinium ring of MDP at 25°C (I = 1.0 M).

This value at 25°C is about two orders of magnitude greater than that for the similar reaction of N-phenylpyridinium-ion, $k_{OD} = 5.4 \times 10^{-2}\ M^{-1}\ s^{-1}$ at 50°C, and about 10-fold greater than that for N-methylpyridinium ion at 75°C[154]. The exchange of the pyridinium ion ring protons probably occurs through the intermediate formation of a zwitterion (Scheme 2.50).

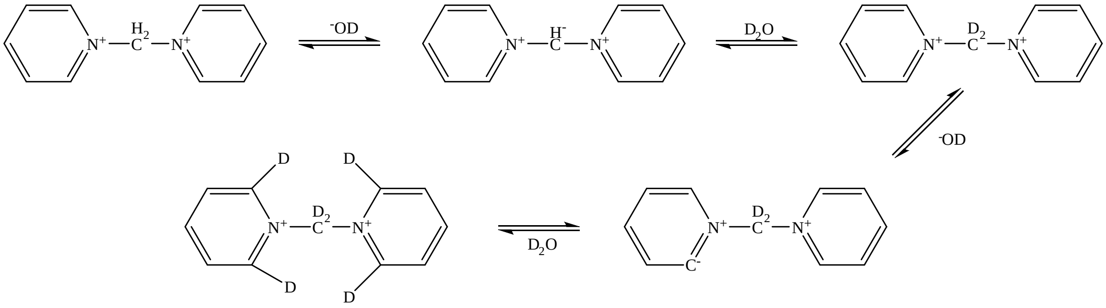

Scheme 2.50 Deuteration of the methylene group and of $C_{2/6}$ of the pyridinium ring.

2.3.9 Conclusion

Although 1,1′-methylenebis(pyridinium) dication (MDP) has two formal positively charged substituents attached to a central carbon, it is remarkably stable to hydrolysis at low pH (<7). It undergoes a complex series of reactions that vary with pH. Below pH 7 there is a very slow degradation (e.g., at pH 7 and 25°C it has a half-life of about 10 weeks) that is first-order in hydroxide-ion, liberates only one equivalent of pyridine, and forms N-(hydroxymethyl) pyridinium ion.

Above pH 9 there is a change in the reaction pathway, with expulsion of one of the pyridines and the formation of an unsaturated iminoaldehyde intermediate which is observed at 366 nm in water by UV-Vis between pH 9-12. This intermediate is formed by an ANRORC-type mechanism that involves opening the other pyridine ring. This intermediate subsequently undergoes ring closure back to pyridine with formation of formaldehyde hydrate. The rate of the first phase is second-order in hydroxide-ion, while the second is pH-independent.

Deuterium exchange of the central methylene in D_2O is faster than the breakdown of MDP and is predominantly OD^--catalysed with a small amount of buffer catalysis. The estimated pK_a of MDP dication in H_2O is unexpectedly high at 21.2 at 25°C and I = 1.0 M (KCl), compared with an estimated value of 30.3 for the monocationic *N*-methylpyridinium ion. Deuterium exchange also occurs at the 2 and 6 positions of the pyridinium rings, but at a lower rate that is first-order in deuteroxide-ion and only competitive with the breakdown of MDP below pD 11.

Chapter 3 – β-LACTAMASES

3 History

At St. Mary's Hospital, London, in 1928, Sir Alexander Fleming noticed partial lysis of colonies of *Staphylococci* on a plate which had been contaminated by *Penicillium notatum*. Attempts at separating the active substance were abandoned as it was unstable, but in 1940, E. Chain and H. Florey were able to isolate the crude active substance, penicillin. It was used for a preliminary clinical trial in 1941, and represented a turning point in the struggle against pathogenic bacteria[169].

The β-lactam ring (Figure 3.1) within penicillin was not accepted as part of the chemical structure until an x-ray crystallographic image was produced in 1943[170].

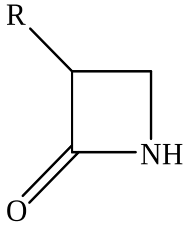

Figure 3.1 β-lactam ring.

All β-lactam antibiotics contain a β-lactam ring but are classified dependent on the ring structure attached to the β-lactam ring (Scheme 3.1)[170].

These include penams (1) which contain thiazolidine rings such as those found in penicillins, cephems (2) containing thiazine rings, cephamycins (3), oxacephems (4) and penems (5) containing thiazole rings. Oxapenams (6) which contain oxazolidine rings such as clavulanic acid, carbapenems (7), nocardicins (8), monobactams (9) are compounds which have no ring fused to the ring and ɣ-lactams such as lactivicin (10) (Scheme 3.1).

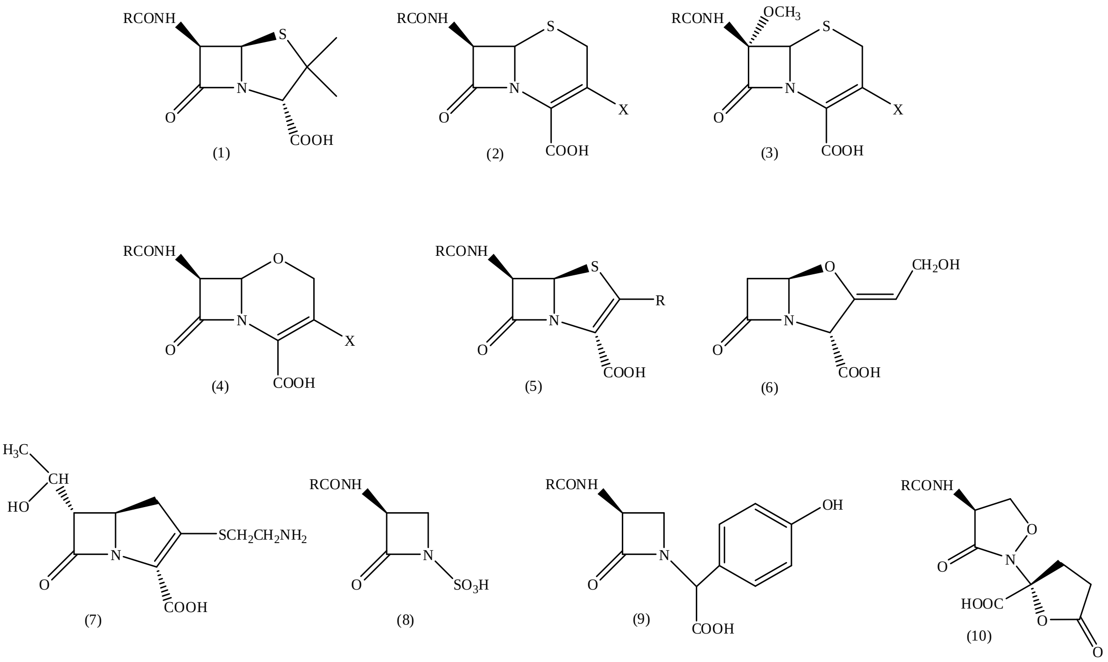

Scheme 3.1 Some β-lactam antibiotics (1-9)[170].

3.1 Antibiotics and bacteria

Antibiotics can be bactericidal or bacteriostatic and work by interfering with intracellular functions which may be endogenous or exogenous. When targeting any invasive agent such as bacteria (prokaryotes) within humans (eukaryotes), the larger the difference between the two types, of cell the greater the selectivity that can be achieved, thus reducing damage to prokaryotic cells.

Common targets for bacterial cells are cell metabolism inhibition, inhibition of protein synthesis, inhibition of the cell wall and inhibition of transcription and replication.

β-Lactams inhibit cell wall synthesis causing bacterial lyses due to changes in osmotic potential, but a slight difference in the cell wall structure of Gram-negative bacteria makes β-lactam antibiotics less effective towards them compared with Gram-positive bacteria (Figure 3.2).

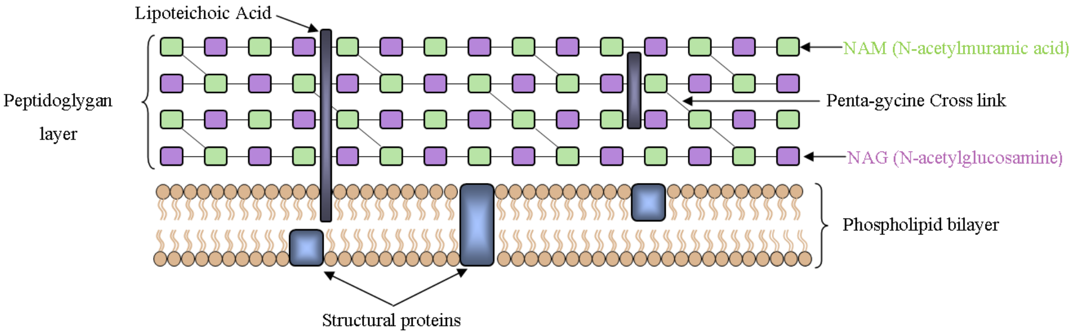

Figure 3.2 Gram-positive bacterial cell wall.

The Gram-positive bacterial cell wall (Figure 3.2) contains multiple layers of murein (peptidoglycan) which is also present in Gram-negative bacteria, sandwiched between the inner and outer lipid bilayers, but in addition there is a lipopolysaccharide layer which proves to be a better barrier against antibiotics (Figure 3.3).

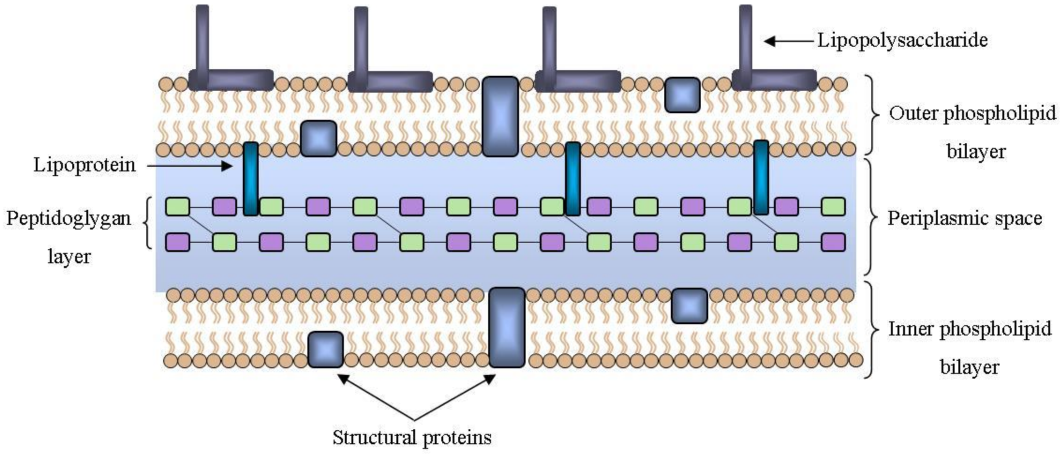

Figure 3.3 Gram-negative bacterial cell wall.

3.1.1 Peptidoglycan layer biosynthesis

Biosynthesis of peptidoglycan begins in the cytoplasm using N-acetylglucosamine-1-phosphate and uridine triphosphate (UTP) forming UDP-N-acetylglucosamine which is catalysed by a transferase enzyme. The nucleotide reacts with a phosphoenolpyruvate which undergoes reduction to form UDP-N-acetyl muramic acid which is an amino acid derivative only found in the peptidogylcan cell walls[171].

L-Alanine is added to the carboxyl group of UDP-N-acetyl muramic acid followed by D-glutamic acid then either L-lysine or meso-diaminopimelic acid which is completed with the addition of the dipeptide, D-alanyl-D-alanine (D-ala-D-ala)[171].

The UDP-N-acetyl muramic pentapeptide is translocated to a lipid carrier (bactoprenol) located in the cytoplasmic membrane where N-acetylglucosamine (NAG) is transferred to the complex to form bactoprenol-N-acetylglucosamine-N-acetylmuramic acid-penta-peptide. This complex moves across the membrane to lie on the outside of the cell[172].

Adjacent glycan strands are cross linked to form the rigid cell wall. The enzyme transpeptidase contains a serine residue to cleave the terminal D-alanine residue forming an acyl-enzyme intermediate. The cross-linking peptide deacylates the intermediate by nucleophillic attack which in Gram-negative bacteria occurs via the γ-amino group of lysine but in Gram-positive bacteria via the ε-amino group of lysine which bridges five glycine residues across the glycan stands.

3.1.2 Penicillin mode of action

Penicillin and cephalosporins inactivate the transpeptidase enzyme which is responsible for the cross-linking of the cell wall. The structure of penicillin (Figure 3.4, black) and cephalosporins resemble that of D-ala-D-ala side chain (Figure 3.4, blue) which is cleaved to form a stable acyl-enzyme intermediate sterically hindering subsequent nucleophillic attack[173].

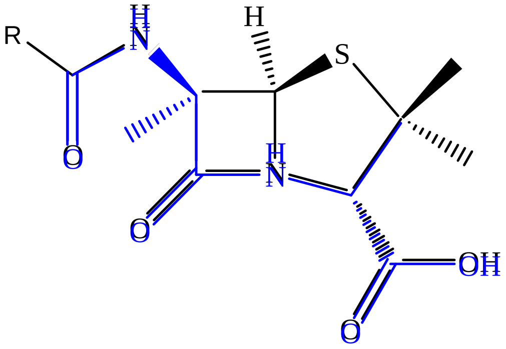

Figure 3.4 Superimposed D-ala-D-ala with penicillin.

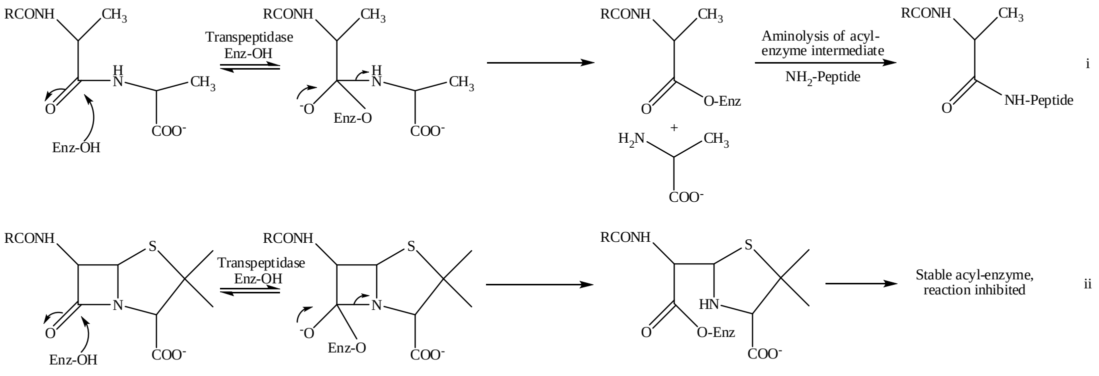

Scheme 3.2 Transpeptidase reaction of D-ala-D-ala (i) compared to penicillin (ii).

In both mechanisms the first step involves a serine residue attacking a carbonyl group to form an acyl-enzyme intermediate. Formation of the cross linked cell wall involves attack of a NH_2-peptide on the acyl-enzyme intermediate to form the rigid cell wall and the enzyme is released (Scheme 3.2, i). Penicillin however attaches to the enzyme within the active site as the acyl-enzyme which sterically hinders the incoming peptide and prevents release of the enzyme (Scheme 3.2, ii).

3.1.3 Antibiotic resistance

Without doubt antibiotics have been the most successful drugs deployed over the past 100 years, but over prescribing by physicians, veterinarians and use within agriculture have caused microbes to develop mechanisms to resist the action of β-lactam antibiotics. Many resistant elements are readily passed on both vertically and horizontally from one bacteria to another and with affordable global travel, resistance is inevitably able to spread through microbial populations across the world[174].

There are many mechanisms which confer resistance but the most common is the ability of bacteria to produce β-lactamase enzymes which rapidly catalyse the hydrolysis of the β-lactam.

A recent metallo-β-lactamase, New Delhi metallo-β-lactamase (NDM-1) was first found in *Klebsiella pneumonia* in 2008 when a Swedish resident visited India. The gene for the enzyme was increasingly found in *E.coli*, a major cause of diarrhoea due to inadequate sanitation and environmental contamination with faecal matter. The transfer of these resistant genes is mainly responsible for increased antibiotic resistant infections[175].

Vertical gene transfer involves transfer of genetic information from generation to generation i.e. from parent to offspring during replication whilst horizontal gene transfer involves genetic information to be passed one bacterium to another by transformation, transduction or conjugation[176].

3.1.3.1 Transformation

Transformation is the ability of a bacterial cell to take-up genetic information usually DNA on lysis of another organism and incooperate the naked DNA into its own genome or plasmid (Figure 3.5)[176, 177].

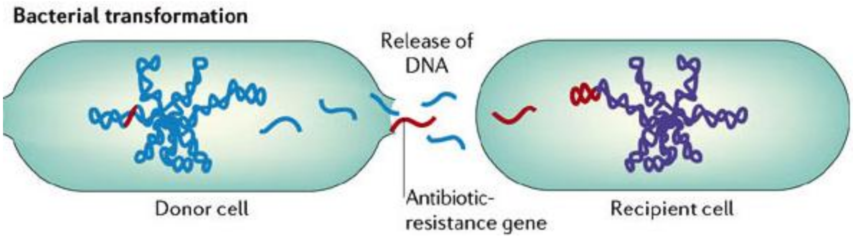

Figure 3.5 Mechanism of bacterial transformation[177].

3.1.3.2 Transduction

Transduction involves the introduction of exogenous DNA into a bacterial cell by a bacterial phage (usually a virus), once injected, the DNA can incorporate itself into the chromosomal DNA (Figure 3.6)[176, 177].

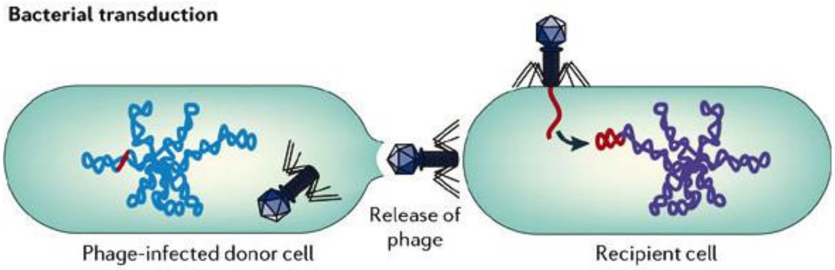

Figure 3.6 Mechanism of transduction by a bacteriophage[177].

3.1.3.3 Conjugation

Conjugation is the last method of horizontal gene transfer which bacteria may use to transfer genetic information. The F factor (fertility factor) is a sequence of DNA which enables the cell to act as a donor during conjugation. This F factor can be taken-up from an independent replicating plasmid or is already in the chromosomal DNA, if the bacterium contains this F factor they are known as F^+ and those who lack the factor are F^-. The F^+ bacterial cells produce sex pili which bind to the recipient’s cell forming a cytoplasmic mating bridge where genetic information such as transposons (genetic information which can change position within a genome) can be transferred to a plasmid (Figure 3.7)[176].

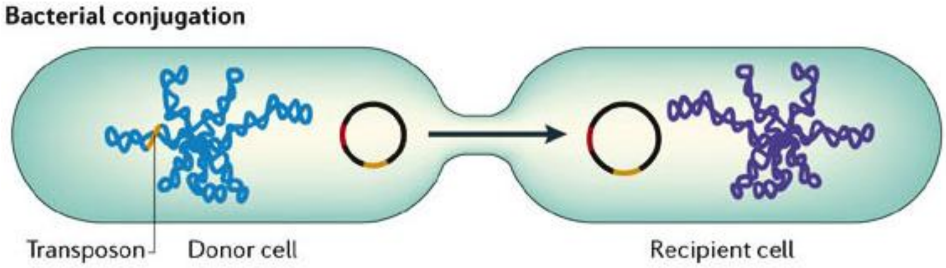

Figure 3.7 Conjugation mechanism of genetic information transfer[177].

3.1.4 Mechanisms of antibacterial resistance

Mechanisms which microbes have evolved include efflux pumps (or decreased entry), target modification and chemical modification[174].

3.1.4.1 Efflux pumps

Protein pumps within the membrane actively pump out the antibiotic faster than it can diffuse and accumulate in the cell to a therapeutic level. The bacteria may also change/alter the cytoplasmic membrane permeability to the drug lowering the total concentration within the cell[174].

3.1.4.2 Target modification and pathway alteration

A bacterial cell may alter its target active site where usually the antibiotic would bind but a slight change in conformation or amino acid residues would render the antibiotic inactive and the target modification may be by chance i.e. a single point mutation[178].

3.1.4.3 Chemical modification

The most efficient means of chemical modification is with the use of a catalyst such as an enzyme. β-Lactamases are secreted into the periplasm (Gram-negative) and outer membrane (Gram-positive) and hydrolytically deactivates the β-lactam ring. The β-lactam ring is readily opened rendering the antibiotic inactive[179].

3.1.5 β-Lactamases

β-Lactamases are the most common cause of bacterial resistance to β-lactam antibiotics. Benzylpenicillin (penicillin G) was the first compound used for clinical use which was effective against Gram-positive bacteria but after only three years resistance was observed[180].

Bush-Jacoby-Medeiros in 1995 devised a classification through groups 1 to 4 (Table 3.1) based on substrate and inhibitor profiles but the more popular Ambler classification divides β-lactamases into four distinctive groups dependent on their amino acid sequences A, B, C and D (Figure 3.8)[181].

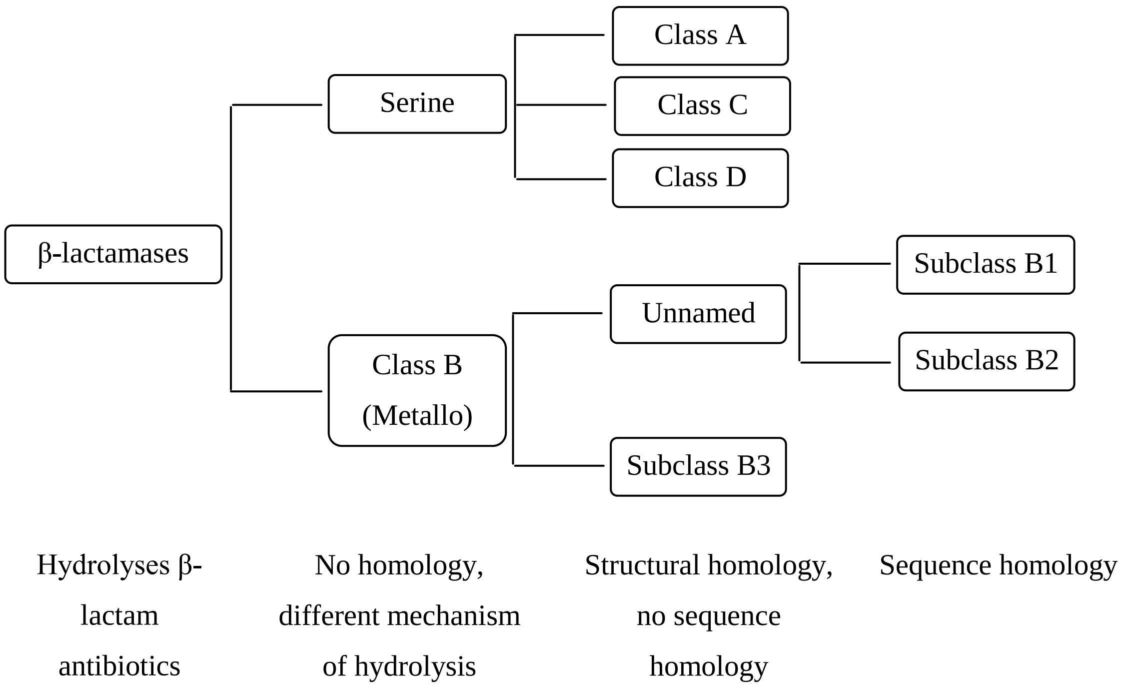

Figure 3.8 Ambler classification system[181].

Ambler Classification	Bush-Jacoby-Medeiros Class	Substrates	Representative enzymes
A	2a	Penicillins	PC1
	2b	Penicillins, Cephalosporins	TEM-1, TEM2, SIV-1
	2be	Penicillins, Cephalosporins, Monobactams	TEM-3, SIV-2, VEB-1
	2br	Penicillins	TEM-30, SHV-10
	2c	Penicillins	PSE-1, CARB-3
	2e	Cephalosporins	CepA
	2f	Penicillins, Cephalosporins, Carbapenems	KPC-2, IMI-1, SME-1
B	3	β-lactams including carbapenems	CcrA, IMP-1, BcII, IND-1
C	1	Cephalosporins	MIR-1, FOX-1
D	2d	Penicillins, Cloxacillin	OXA-1, OXA-10

Table 3.1 Classification of the Bush-Jacoby-Medeiros and Ambler scheme[182].

The Bush-Jacoby-Medeiros class also has a fourth group (group 4) which does not appear in the Ambler classification, the enzymes of this class may be included in an existing classification as they have not be well characterised such as *Pseudomonas cepacia*[182].

3.1.6 Serine β-Lactamases

3.1.6.1 Class A β-Lactamases

Class A β-lactamases use an active-site serine to hydrolyse the β-lactam ring of antibiotics. This class was the first to be identified in bacteria just after the clinical introduction of penicillin. The first plasmid mediated β-lactamase was identified in *E.coli* in 1963 (reported in 1965) and has been characterised as penicillinases as they are good at hydrolysing penicillin and ampicillin[183, 184].

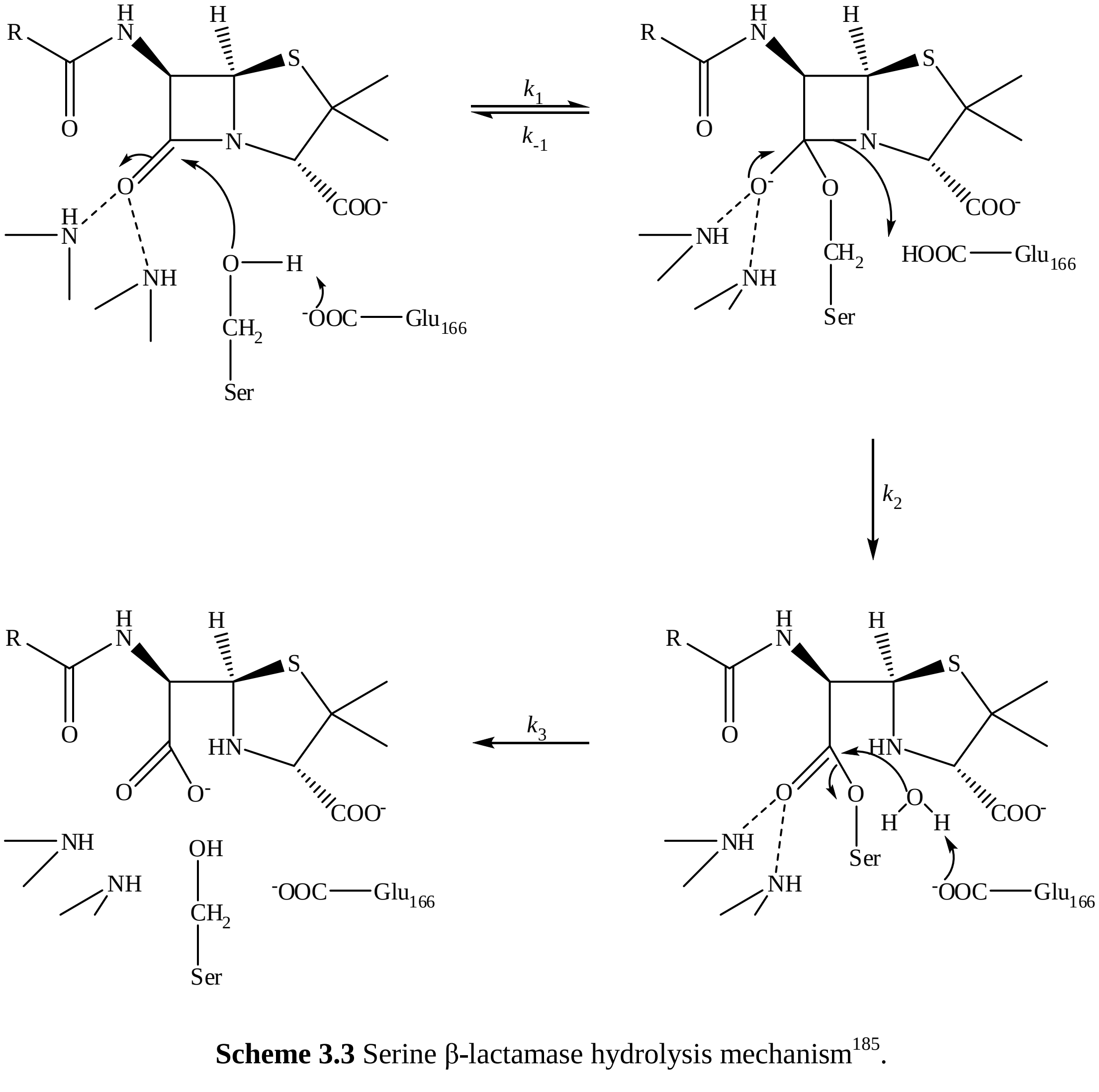

Scheme 3.3 Serine β-lactamase hydrolysis mechanism[185].

The mechanism of serine β-lactamases involves the formation of an acyl enzyme. The cleavage of the β-lactam requires several proton transfer steps, but the identity of the general acid-base catalyst(s) is controversial[185]. Scheme 3.3 shows the first step involves acylation, a Glu_{166} acts to deprotonate the serine hydroxyl to aid nucleophilic attack on the carbonyl group of the β-lactam ring. The C-N bond is cleaved by the formation of the double bond oxygen and deacylation occurs with the aid water being deprotonated by the general base to regenerate the enzyme and release the inactive β-lactam.

3.1.6.2 Class C β-Lactamases

The second most common class of β-lactamase is class C which are also serine enzymes and historically known as cephalosporinases as they prefer cephalosporins as a substrate although they have high hydrolytic activity towards penicillins too (Table 3.2)[186].

Ambler Class **(*Bush-Jacoby-Medeiros Class*)**	**Enzyme**	**β-Lactams to which resistance is conferred**	
		Primary	**Secondary**
A (*2b*)	Penicillinase	Penicillins, early cephalosporins	β-lactamase inhibitor combinations
A (*2be*)	Extended-spectrum β-lactamase	Penicillins, cephalosporins, monobactams	None
A (*2f*)	Carbapenemase	All current β-lactams	None
B (*3*)	Metallo β-lactamase	All current β-lactams except monobactams	None
C (*1*)	Cephalosporinase	Penicillins, cephalosporins	Carbapenems and monobactams
D (*2d*)	Cloxacillinase	Penicillins, Oxacillin and cloxacillin	None
D (*2df*)	Carbapenemase	Carbapenems and β-lactams	None

Table 3.2 The different classes of β-lactamases and their preferred substrate[187].

Amongst this class of enzymes, the most common is, AmpC and they are usually found in *Enterobacteriaceae* (a large family of Gram-negative bacteria) as chromosomal enzymes which are usually present at basal levels but higher levels are produced once induced by the presence of clavulanic acid (inhibitor of serine β-lactamases) or amoxicillin[188]. Plasmid-encoded AmpC is capable of transferring across species by conjugation[184].

3.1.6.3 Class D β-Lactamases

This class of β-lactamases are also serine enzymes and share the general hydrolytic mechanism of the Ambler classification enzymes A and C and are known as oxacillinases or OXAs. They differ from other serine β-lactamases because of their lack of amino acid comparison and usually are not inhibited by clavulanic acid[189], bactam (except OXA-29) and sulbactam whereas the hydrolytic activity can be inhibited by sodium chloride, 100 mM sodium chloride completely inactivates most class D β-lactamases. The mechanism is not fully understood but has been related to the Tyr residue at position 144, as mutation to Phe prevents sodium chloride inhibition[190]. Class D β-lactamases are often found in *Acinetobactor baumannii*, *Pseudomonas aeruginosa*, *Escherichia coli* and *K. pneumoniae*[191].

3.1.7 Metallo β-Lactamases

3.1.7.1 Class B β-Lactamases

This class of bacterial enzymes hydrolyse the β-lactam ring with the help of a metal cofactor which is zinc in its natural form and are known as metallo β-lactamases (MBL). In 1966, Sabath and Abraham discovered the first MBL in the Gram-positive bacteria *Bacillus cereus*[192]. In the last 20 years several pathogenic strains have developed MBL-mediated resistance which has been spread by horizontal transfer, involving both plasmid and integron-borne genetic elements[193].

The metallo family is divided into subclasses B1, B2 and B3 (Figure 3.8) which was devised by Rasmussen and Bush where the enzymes are grouped according to amino acid sequence and substrate profile.

Subclass B1 is the largest of the three groups and contains four comprehensively studied β-lactamases, BcII (*Bacillus cereus*), CcrA (*Bacteroides fragilis*), BlaB (*Chryseobacterium meningosepticum*) and IMP-1 (*Pseudomonas aeruginosa*) which show broad spectrum activity against penicillins, cephalosporins and carbapenems.[193, 194] This subclass of enzymes requires one or two zinc-ions at the active site and they catalyse the hydrolysis of many β-lactam compounds which include some which inhibit serine β-lactamases such as clavulanic acid and tazobactam.

Subclass B2 which contains CphA from *Aeromonas hydrophila*, ImiS and AsbM1 from *Areomonas* spp. and Sfh-I from *Serratia fonticola*. This group of enzymes are efficient at hydrolysing carbapenems but poor against penicillins and cephalosporins.[195, 196] This class consists of mono-zinc enzymes and the binding of the second zinc-ion usually inhibits enzyme activity.

Subclass B3, the least studied of the three groups include L1 from *Stenotroptromonas maltophilia* and FEZ-1 from *Legionella gormanii* hydrolyse numerous β-lactam antibiotics like that of subclass B1, although B3 enzymes differ greatly in their amino acid sequence and structure compared to B1 and B2. FEZ-1 has much lower catalytic rate constants (k_{cat}) towards penicillins compared to L1 (the first enzyme to be subclassed as B3) but greater values towards cephalosporins.[193, 197]

3.1.7.2 Structure of metallo β-lactamases

Despite the low sequence similarity between the various MBLs, the tertiary structure is very similar where they all exhibit the αβ/βα sandwich structure composed of two β-sheets at the core and five α-helices on the external faces[198]. In all known structures, the active site is located at the edge of the ββ sandwich in a shallow groove potentially binding two zinc-ions[199].

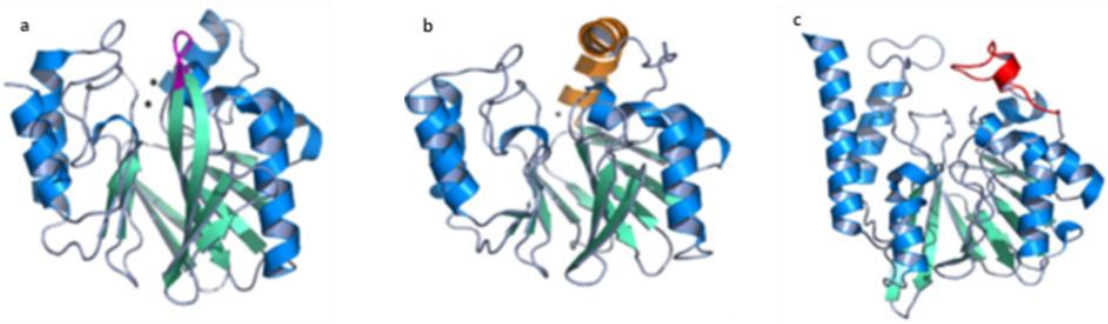

Figure 3.9 Adapted ribbon representations of the three subclasses; (a) BcII, (b) CphA and (c) FEZ-1. Helices represented in blue, strands in green and loops in grey[199].

Four residues among all metallo subclasses are strictly conserved which involve the coordination of metal-ion(s) and are His$_{118}$, Asp$_{120}$, His$_{196}$ and His$_{263}$, other residues are also involved in binding but these vary (Table 3.3).[180]

Subclass	Zn1 Ligands			Zn2 Ligands		
B1	His$_{116}$	His$_{118}$	His$_{196}$	Asp$_{120}$	Cys$_{221}$	His$_{263}$
B2	Asn$_{116}$	His$_{118}$	His$_{196}$	Asp$_{120}$	Cys$_{221}$	His$_{263}$
B3	His/Gln$_{116}$	His$_{118}$	His$_{196}$	Asp$_{120}$	His$_{121}$	His$_{263}$

Table 3.3 Zinc ligands of class B β-Lactamases[180].

The first metallo β-lactamase enzyme known as BcII which required metal-ions for activity was isolated from bacteria *Bacillus cereus.* Two strains of bacteria *Bacillus cereus* 569/H/9 and *Bacillus cereus* 5/B/6 both produce the metallo enzyme and only differ by 17 amino acids which are not part of the metal-active site coordination of the enzyme[200].

Both enzymes have two sites to which the metal can bind known as sites 1 and 2, at site 1 also known as the histdine site, zinc is tetrahedrally coordinated by the imidazoles of three histidine residues (His_{116}, His_{118} and His_{196}) and a water molecule (Wat_1)[201, 202]. At site 2 or the cysteine site His_{263}, Asp_{120}, Cys_{221} and one water pentacoordinate (trigonal bipyramidally coordinated) the metal, with water usually as the fifth ligand which, in the case of water, is referred to as the apical water or Wat_2 (Figure 3.10) [202, 203].

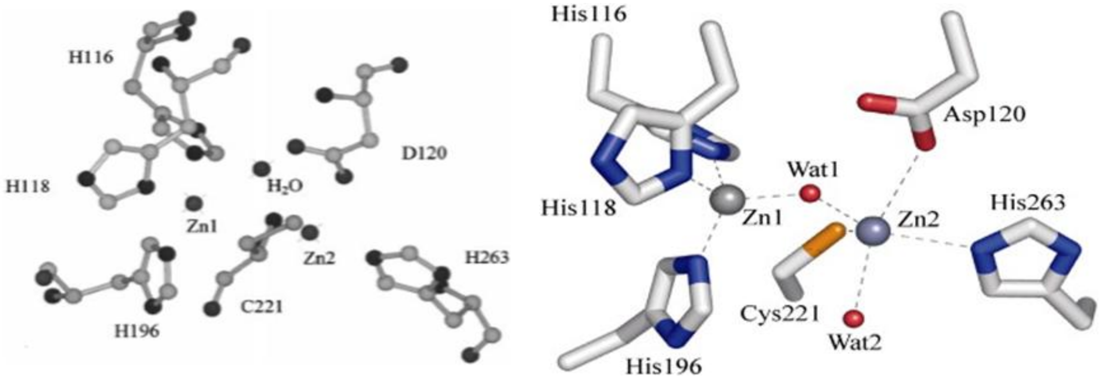

Figure 3.10 Atomic model of the active site of BcII[203, 204].

CphA (wild type) a class B2 enzyme consists of 227 amino acids with a calculated molecular mass of 25.2KDa[205] and has the capability of binding two zinc-ions but is only active in the mono-zinc form as binding the second zinc-ion inhibits the enzyme in a non-competitive manner[196, 206]. A long α3 helix (Arg_{140}-Leu_{161}) is located near the active site groove which provides a hydrophobic wall which explains the narrow activity profile of the enzyme[207]. Initially it was thought that the first zinc bound to site 1 containing Asn_{116}, His_{118} and His_{196} but X-ray crystallography has shown that the first zinc is located in the cysteine site/site 2 which has ligands Asp_{120}, Cys_{221} and His_{263} and not the histidine site[208].

3.1.7.3 Why Zinc?

Zinc the second most abundant first row transition metal in biology and is the choice metal for many enzymes[209]. Unlike some transition metals such as V^{2+}, Cr^{2+}, Ni^{2+}, Fe^{2+} and others zinc contains a filled d orbital (d^{10}) and does not participate in redox reactions[210]. The $zinc^{2+}$-ion in metallo enzymes can in-turn adopt four-, five- or six-coordinate geometries (Figure 3.11) as the energy barrier is relatively small for conversion[199]. Many zinc metallo enzymes have the binding geometry of a slightly distorted tetrahedron with the metal centre(s) coordinating to three or four protein side chains.

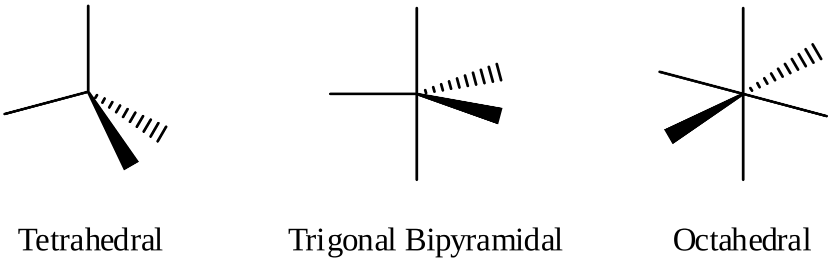

Figure 3.11 Zinc ligand geometry.

A combination of variable coordination geometries, rapid ligand exchange, Lewis acidity, intermediate hard-soft behaviour and strong binding with substrates allows zinc to be involved in a wide range of hydrolysis reactions[209]. Some class B metallo β-lactamases such as BcII have di-nuclear active sites present for activity and rapid exchange for kinetically labile zinc-bound water is an important feature in these classes of hydrolases[209].

3.1.8 Metallo hydrolysis mechanisms

The mechanism of hydrolysis compared to serine active site β-lactamases is considerably different, Scheme 3.4 shows one of the first proposed mechanisms by Bounaga *et al* in 1998 for BcII where a zinc-ion is used to catalyse the hydrolysis of the β-lactam ring. Initially water that is bound to the zinc-ion, acting as a Lewis acid lowers the pK_a of the water facilitating nucleophilic attack on the carbonyl centre forming a tetrahedral intermediate which is also stabilised by the zinc-ion. Asp_{120} acts as a general base to deprotonate the tetrahedral intermediate and subsequently it can act as a general acid to donate a proton to the β-lactam nitrogen facilitating C-N bond cleavage, followed by enzyme dissociation[211].

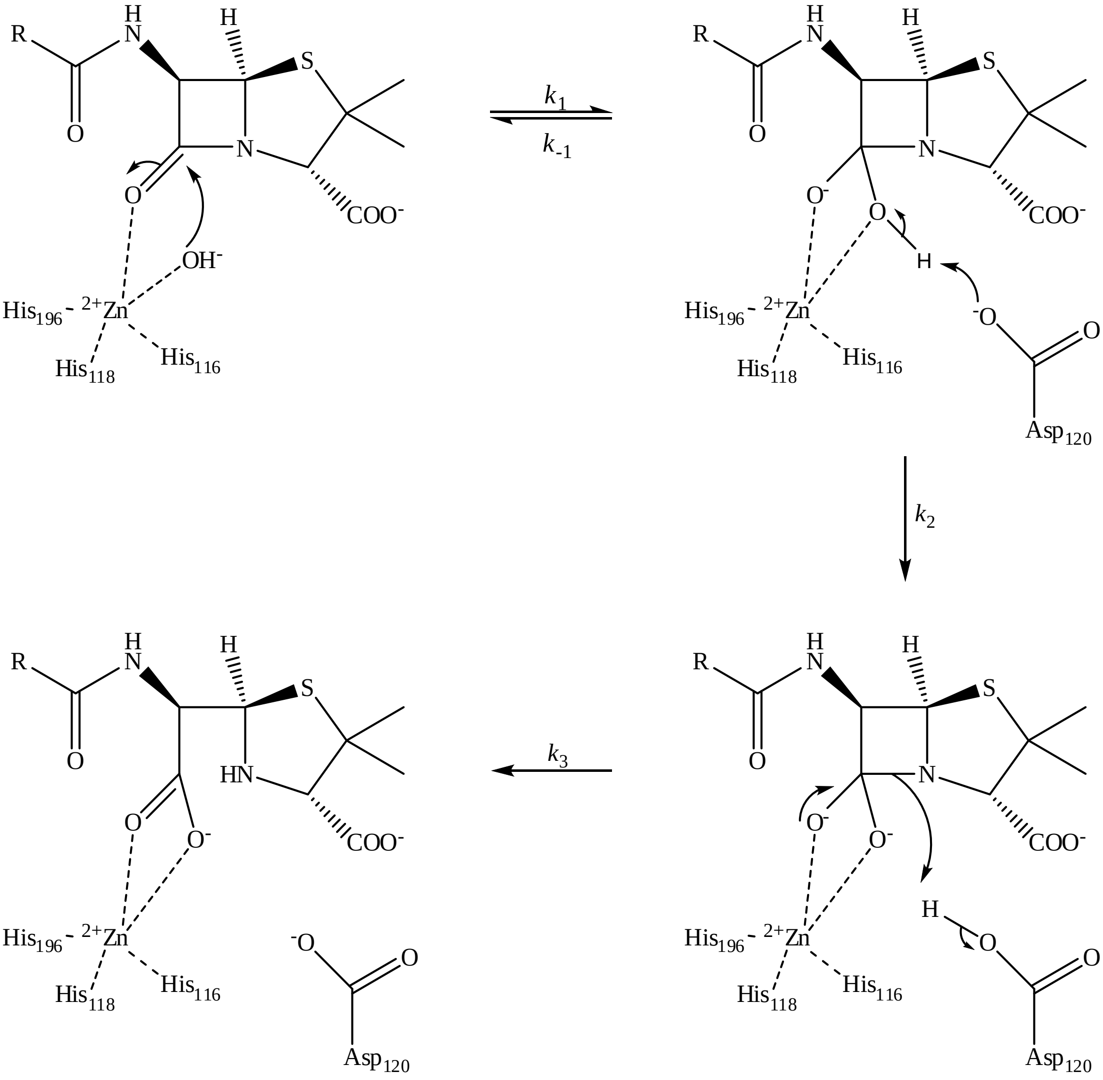

Scheme 3.4 Mono-zinc β-lactamase hydrolysis mechanism[211].

In contrast to the mono-zinc mechanism which is the main mode of hydrolysis of subclass B2 β-lactamases Scheme 3.5 uses a di-zinc-ion to catalyse the hydrolysis of the β-lactam ring where the two zinc-ions are bridged by a hydroxide-ion which is used to attack the carbonyl centre of the β-lactam ring generating a negatively charged tetrahedral intermediate which is stabilised by positively charged residues. The C-N bond is then cleaved as a proton is transferred to the amide nitrogen by Wat_2 which then is able to become the bridged hydroxide-ion Wat_1, the product finally undergoes displacement from the enzyme[193].

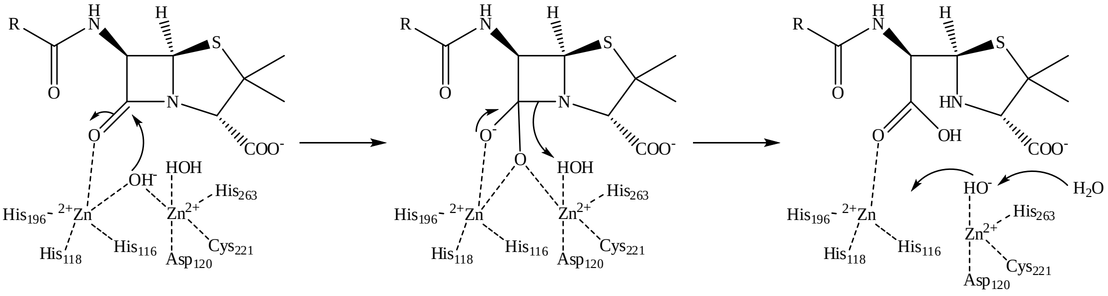

Scheme 3.5 Di-zinc β-lactamase hydrolysis mechanism[193].

3.1.9 Binding of metal-ions to enzymes

Metal-ions are essential to many life processes; many enzymes require metal-ions for their activity. Understanding the properties of enzymes by acquiring data from 3D structures, biochemical properties and kinetics and mechanism require studies into the binding of metal-ions to the active site of the enzyme[212].

For any metallo-protein the affinity of the metal-ion (M) for the enzyme (E) is a key requirement for its biological activity and is defined by the dissociation constant (K_d) (Equation 3.1)[212]:

$$\mathrm{E + M} \overset{K_b}{\rightleftharpoons} \mathrm{EM}$$

Scheme 3.6 Simple 1:1 complexing between E and M to for EM.

$$K_d = \frac{[E][M]}{[EM]}$$

Equation 3.1

The binding constant (K_b) is simply $1/K_d$ (Equation 3.2).

$$K_b = \frac{[EM]}{[E][M]} = \frac{1}{K_d}$$

Equation 3.2

Under *in vitro* conditions binding of metal-ions to protein surfaces often have a $K_d \geq 10^{-6}$ M whereas metal-ion binding to enzyme active sites often have a higher affinity as high metal-ion concentrations *in vitro* would by toxic to many cells[212].

Dependent on experimental techniques, the variation often seen in binding constants for a particular enzyme may reflect a few parameters which should be kept under control. For example, the class B β-lactamases, BcII which has reported binding constants for K_{b1} (first zinc binding) and K_{b2} (second zinc binding) range from $1.7 \times 10^9\ M^{-1}$ to $8.3 \times 10^3\ M^{-1}$ and $6.7 \times 10^8\ M^{-1}$ to $41.7\ M^{-1}$, respectively. These discrepancies are most likely due to inadequate pH control, buffer-metal interactions, secondary interactions with proteins or contaminates in solution and incorrect interpretation and processing of experimental data[200]. Subgroup B2 enzyme, CphA exists mainly as the mono-zinc enzyme and full catalytic activity is obtained with a binding constant for the first zinc-ion $\leq 5 \times 10^7\ M^{-1}$ and $2.2 \times 10^4\ M^{-1}$ for the second zinc-ion, which shows that the second zinc is less tightly bound (negative cooperativity) to the active site of the enzyme[196, 213].

3.1.9.1 Microscopic and Macroscopic Binding

A microscopic binding scheme is necessary when there is more than one binding process which can be clearly distinguished. As shown be Scheme 3.7 an enzyme (E) which contains two binding sites (1 and 2), the first metal-ion (M) can bind to site 1 of the enzyme, the microscopic binding constant characterised by K_1 or M can bind to site 2 which is characterised by the microscopic binding constant K_2. The second M can occupy the empty site either by microscopic equilibrium constants K_3 or K_4. The macroscopic binding constant for populating the enzyme with one M can be given by Equation 3.3 and the second macroscopic binding constant by Equation 3.4, as some analytical methods such as ITC are unable to measure the microscopic binding constants[214].

$$\frac{[\mathrm{EM}]}{[\mathrm{E}][\mathrm{M}]} = \mathrm{K}_1 + \mathrm{K}_2 = \mathrm{K}_{\mathrm{b1}}$$

Equation 3.3

$$\frac{[\mathrm{EM}_2]}{[\mathrm{EM}][\mathrm{M}]} = \mathrm{K}_3 + \mathrm{K}_4 = \mathrm{K}_{\mathrm{b2}}$$

Equation 3.4

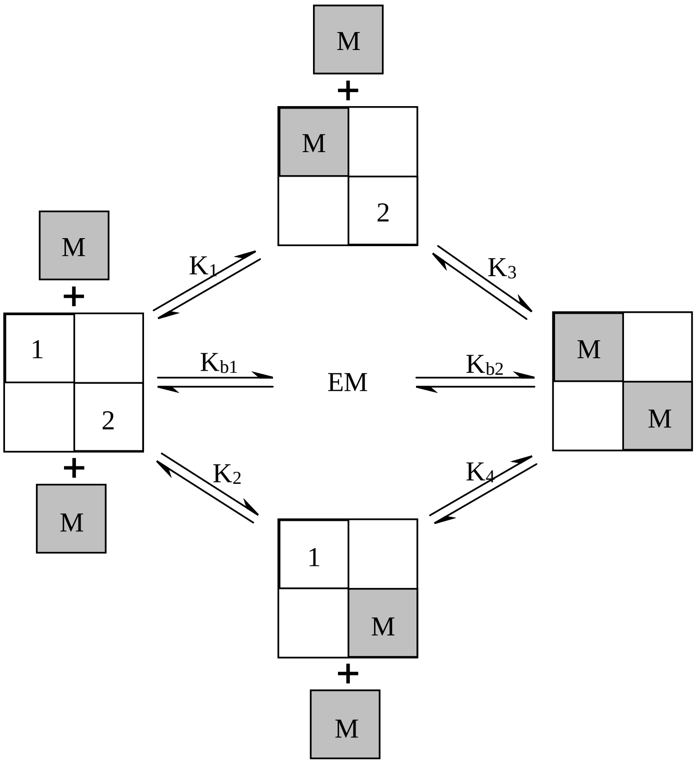

Scheme 3.7 Macroscopic and microscopic binding of an enzyme which contains two binding sites[214].

3.1.10 Cooperativity

Cooperativity has been well known to occur in enzymes which have multiple binding sites or domains. There are two types of cooperativity, positive, where the affinity for the first binding site increases subsequent ligand(s) binding. Negative cooperativity is where the binding affinity for the next ligand is decreased when the first site is already occupied. The most common example of cooperativity is the binding of oxygen to haemoglobin, where the four binding sites are gradually increased in oxygen affinity as each oxygen binds[215].

A consequence of cooperativity in proteins is that there is often a change in conformation. A β-lactamase which showed a slight conformational change on titration with zinc-ion compared to the apo-enzyme was CphA from *A. hydrophila*, observed using circular dichroism and fluorescence emission. Treatment of the enzyme with increasing concentrations of urea showed that the di-zinc enzyme is much more stable than the mono-zinc enzyme to thermal and urea denaturation[216]. For many enzymes, zinc, or the native metal-ion, is required to correctly fold the protein to its active structure.

The presence of metallo-β-lactamases in their physiological conditions does raise questions to the available concentrations of zinc in their natural habitat because of the range of binding constants of the mono- and bi-nuclear species. Production of metallo β-lactamases in the laboratory usually occurs by over expression in *E.coli* and, during purification excess zinc is used to fold and stabilise the protein into the active form of the enzyme. Removal of zinc to form the apo-enzyme would be monitored to ensure little of negligible concentrations of zinc remained in solution prior to titrating zinc[216].

Bacillus cereus 569/H/9 β-lactamase BcII is an enzyme where the metal-ion to protein stoichiometry remains controversial, it has been proposed that under physiological conditions β-lactamase catalyses its substrate aided by one zinc-ion. The mononuclear form of BcII has been shown to be catalytically active as the first detailed crystal structure[199, 201].

Using stop-flow, the kinetics of metal binding has been monitored by observing the metal-ion-induced fluorescence changes of the protein. The association rate constants for binding of the second zinc-ion were two orders of magnitude lower than that of the first metal-ion therefore suggesting that negative cooperativity was occurring[216].

Mass spectrometry has been used to identify the different masses corresponding to the apo-, mono- and di-enzyme. At pH 7 three different masses were observed at different [Zn]/[E] ratios, the apo-enzyme has a Mr = 24,961 ± 2 Da which was the dominant species before zinc addition. The di-zinc species, which is 128 Da (Mr = 25,089 ± 2 Da) higher compared to the apo-enzyme, predominates at $[Zn]/[E] \geq 2$. Although the mono-zinc species appears with an intermediate mass Mr = 25,025 ± 2 Da throughout the titration, its relative abundance remains below 20%. It was suggested positive cooperativity occurs such that binding at the first zinc site increases the affinity at the second site or the affinity for the second zinc site is much greater than the first[200].

To assess the binding nature and cooperativity of BcII an identical experiment with cadmium as the ligand was used. NMR and PAC (perturbed angular correction) spectrometries were used to confirm the MS data which indicated that the process is non-cooperative and the dominate species is the mono-cadmium enzyme in the presence of 1 molar equivalent of cadmium[200].

Isothermal titration calorimetry (ITC) has also been used to assess the binding of zinc to the apo-BcII at 30°C in MOPS buffer, pH 7.06 which showed an apparent single binding event with a stoichiometric ratio of 1.9 indicating the two binding sites have very similar binding constants or the second binding constant is much greater than the first collapsing the binding event into a single observable event, or the first stronger binding site gives the same heat as the second weaker binding site (Figure 3.12). The association constant was determined by fitting the data to a single binding event where K_b was found to be 3.3×10^7 M^{-1}[202].

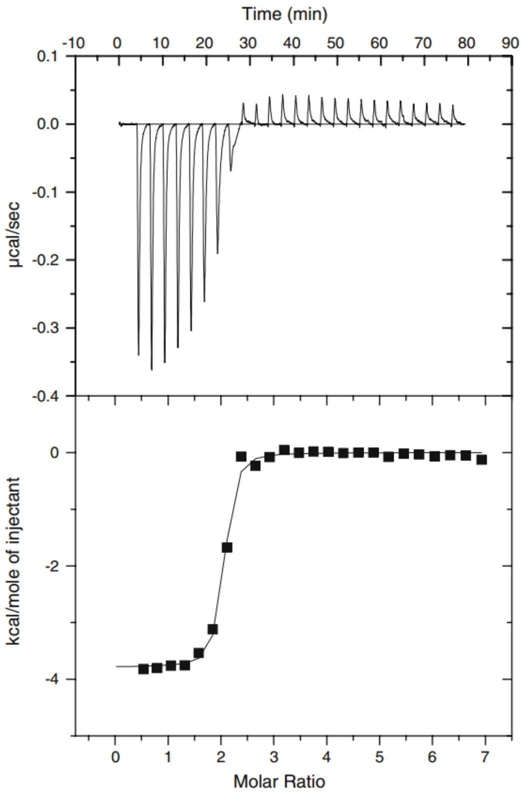

Figure 3.12 ITC trace for the titration of zinc-ion into BcII in 25 mM MOPS, I = 0.25 M, pH 7.06 at 30°C[202].

3.1.11 Calorimetry

Calorimetric measurements can be performed in three different ways: temperature change, heat conduction and power compensation, also known as isothermal[217].

In a temperature change instrument, heat is evolved or consumed by the reaction within the calorimeter resulting in a change in the temperature in the measuring cell as a function of time[217].

With heat conduction measurements, the cell is passively maintained at a constant temperature which is controlled be sensors and heat sinks. As the reaction produces heat, a small voltage is applied which is proportional to the very small ΔT that is developed across the heat flow sensors[217].

Power compensation calorimeters will be discussed in detail in this chapter.

ITC is the current method of choice when characterising binding and thermodynamic properties of chemical and biological systems. Although ITC dates back over 40 years, instruments have been developed and smaller volumes of samples now provide accurate thermodynamic and binding information[218].

3.1.12 Power compensation calorimeter

The power compensation calorimeter used within this work is the VP-ITC which is manufactured by GE-Healthcare (previously known as MicroCal). Modern instruments such as the VP-ITC work in an energy compensation mode where the sample cell and the reference cell are maintained at a constant temperature (isothermal) relative to the adiabatic jacket (Figure 3.13). The sample cell and the reference cell are identical which are composed of sensitive heat conducting material such as hasteloy or gold[219].

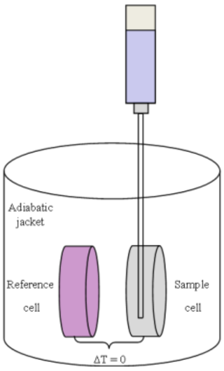

Figure 3.13 Typical isothermal titration calorimeter which shows zero temperature difference between the reference and sample cell.

In a typical ITC experiment the sample cell is filled with a macromolecule (which will be referred to as the enzyme (E)) and the syringe with the ligand/metal-ion (referred to as the titrant), the reference cell contains ultrapure water or buffer. Prior to any aliquots of the metal-ion being injected into the sample cell, the differential power is stabilised. As aliquots of titrant are titrated into the sample cell, each injection yields a deflection in relative power versus time as the instrument compensates for the heat which is evolved or absorbed[220].

If heat is generated by the reaction (exothermic) ΔT increases and the feedback loop responds by reducing the power to the heaters around the sample cell to restore ΔT to 0 therefore a negative deflection from the baseline is observed in a power versus time plot. For an endothermic reaction this is opposite. After each titration the temperature difference between the sample cell and the reference cell returns back to zero[221].

3.1.13 ITC output

The raw output of the ITC is a power versus time plot. Each injection is represented by a peak in a negative direction from baseline (Figure 3.14) or positive direction from baseline. The area under each peak is integrated to obtain the heat per injection which is plotted against molar ratio (added titrant/enzyme)[222].

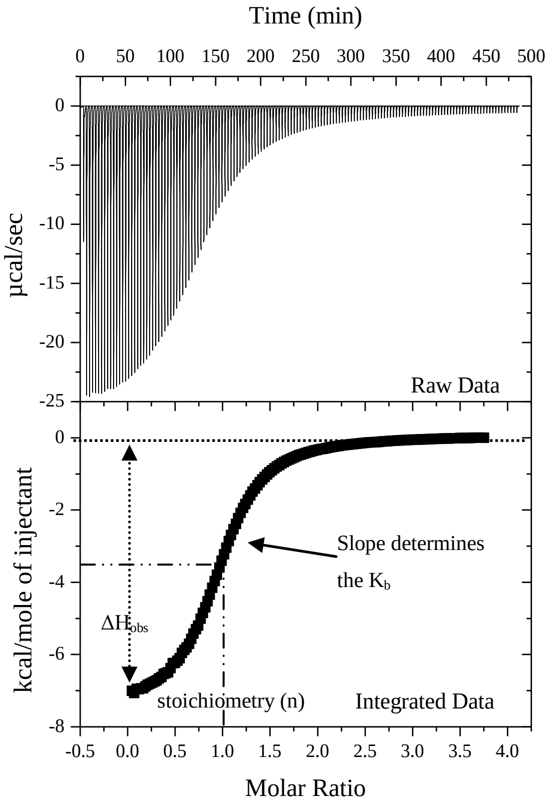

Figure 3.14 ITC output, raw data (top), integrated data (bottom).

The integrated isotherm provides three crucial parameters, firstly the enthalpy of all the reactions (ΔH_{obs}) occurring within the cell is obtained from the first few injections. As additional titrant is added and equilibrium is reached, the reaction heat falls until no more enzyme reacts with the metal-ion and only the heats of dilution are observed. The stoichiometry can be obtained from the intercept or inflection point of the reaction and the binding constant (K_b) from the slope (Figure 3.14), the steeper the slope the greater the binding constant.

3.1.14 Calculating the binding constant K_b and other parameters

The position of the equilibrium is dependent on the binding constant K_b, where K_b is the concentration of products over reactants, shown in a simple 1:1 ratio reaction (Equation 3.5).

$$\mathrm{E + M} \xrightleftharpoons{\mathrm{K_b}} \mathrm{EM}$$

Scheme 3.8 Simple 1:1 complexing to form EM.

$$\mathrm{K_b} = \frac{[\mathrm{EM}]}{[\mathrm{E}][\mathrm{M}]}$$

Equation 3.5

Once the binding constant is calculated the Gibbs free energy (Equation 3.6) is related to K_b where R is the gas constant (8.314 J mol^{-1}) and T is the absolute temperature (K).

$$\Delta \mathrm{G} = -\mathrm{R\,T} \ln \mathrm{K_b}$$

Equation 3.6

MicroCal software is provided with the VP-ITC to be used as the data analysis program for the raw ITC data. It integrates the area under each peak and the heat which is obtained per injection is plotted against the molar ratio. The $K_{b,}$ enthalpy and stoichiometry are determined by applying non-linear least square fitting and therefore indirectly obtaining the Gibb's Free energy and the entropy of the reaction (Equation 3.7).

$$\Delta \mathrm{G} = \Delta \mathrm{H} - \mathrm{T} \Delta \mathrm{S}$$

Equation 3.7

ΔG = Standard Gibbs free energy (kJ mol^{-1})

ΔS = Entropy (kJ mol^{-1} K^{-1})

ΔH = Enthalpy (kJ mol^{-1})

T = Absolute temperature (K)

The heat is directly proportional to the extent of binding and as the enzyme is saturated by the titrant, the heat per injection decreases until no more binding occurs, the total heat (Q) within the active sample volume (V_0) is governed by Equation 3.8 where EM is the concentration of enzyme bound to the metal-ion, ΔH is the enthalpy of binding and E_i is the initial enzyme concentration.

$$Q = V_0[EM][E]_i \, \Delta H$$

Equation 3.8

The initial concentrations of enzyme and metal-ion are an important factor as the binding isotherm is characterised by a unitless parameter *c* (Equation 3.9) also known as the Wiseman parameter, which is the binding constant (K_b),the initial concentration of enzyme ($[E]_i$) and the stoichiometry (n)[223]:

$$c = K_b[E]_i \, n$$

Equation 3.9

For accurate determination of the very high binding constant (K_b) the optimum *c* values are between 10-100 and those <1 and >1000 are excluded[224].

Those *c* values >1000 the binding constant is not resolved well as the transition is very sharp to the end point or equivalence point (saturation may be obtained in a single injection) and those *c* values <1 loose sigmoidal shape becoming nearly linear causing the equivalence point hard to determine (Figure 3.15)[219].

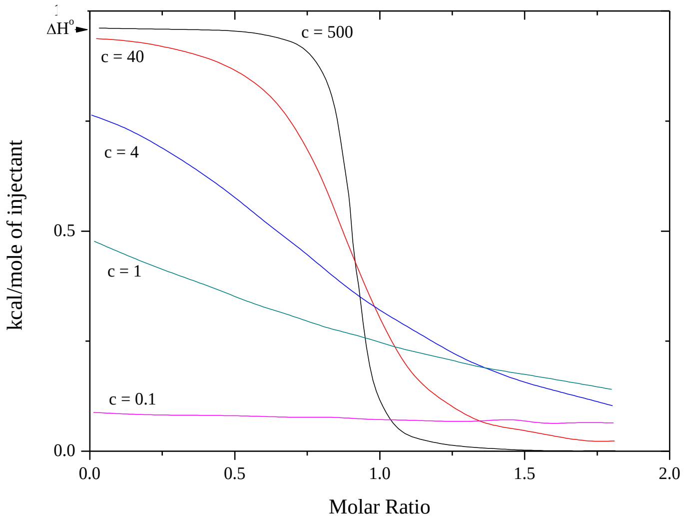

Figure 3.15 How the c value affects K_b[219].

3.1.15 Calibration of the ITC

The VP-ITC was calibrated (y-axis) once a month using the specific onboard software, this is achieved by dissipating a known power through a resistive heater located on the cell wall which then adjusts the software for differential power. The calibration power was 1 µcal/sec, pulse duration was 300 sec and the spacing was 600 sec. The reported error in deflection or energy was less than 1%.

3.1.16 Subtraction of heats of dilution

The heats of dilution are those which are seen after full saturation of the enzyme and additional titrations show heat which are from the titrant adding into the cell. These heats are removed from each of the titration peaks either by the subtraction after each experiment or by a separate background titration which does not incorporate the enzyme.

3.1.17 Aim

The aim of this project is firstly to develop a model for simulating ITC data based on two metal-ions binding to an enzyme by a 'concerted' (direct formation of EM_2 with no formation of EM) and a simple sequential mechanism and, secondly, use these binding models to interpret experimental ITC data for metal-ions binding to apo-BcII. Reference will also be made to the MicroCal software available with the ITC instrumentation.

The model which will be considered is shown in Scheme 3.9:

$$E + M \overset{K_{b1}}{\rightleftharpoons} EM \overset{K_{b2}\ \ M}{\rightleftharpoons} EM_2$$

Scheme 3.9 Scheme to show the formation of the mononuclear species EM and the di-nuclear EM_2.

In extreme cases:

When $K_{b1} >> K_{b2}$, a truly <u>sequential</u> binding event is observed and all the metal (M) is bound to the enzyme (E) in the form of EM up to one equivalent of M, then excess metal (M) forms EM_2.

When $K_{b1} = K_{b2}$, both EM and EM_2 are formed with less than 1 equivalent of metal-ion.

A '<u>concerted'</u> binding event is observed when $K_{b2} >> K_{b1}$ and only EM_2 is formed even with less than 1 equivalent of metal-ion added and so there is no EM produced.

Between these extreme cases, there may be intermediate ones showing mixed behaviour.

3.2 Results and discussion

3.2.1 Single binding site, formation of the mononuclear enzyme

The simplest model used to simulate ITC data involves one enzyme binding site (E) and one metal-ion (M), complexing to form EM. The commercial system (by MicroCal and others) is available for this system but, as part of this project the single binding site model was developed and checked against the commercial software. The equilibrium characterised by this 1:1 complexing has an association constant (K_b) (Equation 3.10).

$$\mathrm{E} + \mathrm{M} \overset{K_b}{\rightleftharpoons} \mathrm{EM}$$

$$K_b = \frac{[\mathrm{EM}]}{[\mathrm{E}][\mathrm{M}]}$$

Equation 3.10

The initial concentrations of enzyme (E_i) in the analyte solution in the calorimetric cell and metal (M_i) in the titrant solution are critical to ensuring accurate thermodynamic and stoichiometric values. The titration is carried out in defined steps and the heat released or absorbed is measured after each injection of titrant into the sample cell. The object is to predict the concentration of EM produced in the cell with each injection. From this, with a suitable value of ΔH the heat against added titrant profile can be calculated.

The equilibrium constant (K_b) for the equilibrium concentration of EM produced after the first injection can be defined by Equation 3.11 with respect to the initial concentrations of enzyme $[E]_i$ and metal-ion $[M]_i$ in Equation 3.10.

$$K_b = \frac{[\mathrm{EM}]}{([\mathrm{E}]_i - [\mathrm{EM}])([\mathrm{M}]_i - [\mathrm{EM}])}$$

Equation 3.11

For subsequent injections the concentration of E and M (Equation 3.10) are calculated from the remaining concentrations of enzyme and metal in the cell, this equation is a quadratic in terms of [EM] (Equation 3.12).

$$K_b[\mathrm{EM}]^2 - K_b[\mathrm{E}]_i[\mathrm{EM}] - K_b[\mathrm{M}]_i[\mathrm{EM}] - [\mathrm{EM}] + K_b[\mathrm{E}]_i[\mathrm{M}]_i = 0$$

Equation 3.12

The quadratic equation is easily solved for EM (Equation 3.13)

$$\mathrm{EM} = \frac{-\mathrm{b} \pm \sqrt{\mathrm{b}^2 - 4\mathrm{ac}}}{2\mathrm{a}}$$

Equation 3.13

Where:

$\mathrm{a} = \mathrm{K_b}$

$\mathrm{b} = [-\mathrm{K_b E_i} - \mathrm{K_b M_i} - 1]$

$\mathrm{c} = \mathrm{K_b E_i\ M_i}$

The increase in [EM] as the titration proceeds can be converted to a heat output using a suitable value for ΔH. The heat can be converted to a differential heat (heat per mole of injectant) and plotted against the molar ratio of added metal to enzyme concentration.

The solution to the quadratic equation yields two roots where only one root is relevant - the concentrations of EM cannot exceed the initial concentrations of enzyme and metal for any injection.

From the concentration of EM produced for the first injection of metal-ion titrated, the moles of EM formed (ΔN_{EM}) is given by Equation 3.14 where [EM] is the concentration of product of the first injection, V_0 is the active cell volume (V_0 = 1.4194 ml) and ΔV is the injection volume.

$$\Delta \mathrm{N_{EM}} = [\mathrm{EM}]_1 \, (\mathrm{V_0} + \Delta \mathrm{V})$$

Equation 3.14

For additional injections (***i***) of metal, the moles of EM ($\Delta N_{EM\,\boldsymbol{i}}$) formed can be calculated using Equation 3.15.

$$\Delta \mathrm{N}_{\mathrm{EM}_{\boldsymbol{i}}} = [\mathrm{EM}]_{\boldsymbol{i}} \, (\mathrm{V_0} + \Delta \mathrm{V}) - ([\mathrm{EM}]_{\boldsymbol{i}-1} \, \mathrm{V_0})$$

Equation 3.15

The heat (Q) in terms of kcal mol^{-1} of injectant for any injection $\boldsymbol{i}$, can be calculated using Equation 3.16 where $\Delta N_{EM\boldsymbol{i}}$ is the moles of EM formed of the $\boldsymbol{i}$th injection, ΔH is the observed enthalpy, ΔV is the injection volume for each injection into the cell and M_i is the initial metal concentration in the syringe.

$$Q_{\boldsymbol{i}} = \frac{\left(\frac{\Delta N_{EM_{\boldsymbol{i}}} * \Delta H}{1000}\right)}{\Delta V * M_i}$$

Equation 3.16

A problem associated with consecutive injections into the sample cell causes volume to be driven out of the cell into a reservoir which does not contribute to additional titrations which are not picked up by the thermocouples (Figure 3.16).

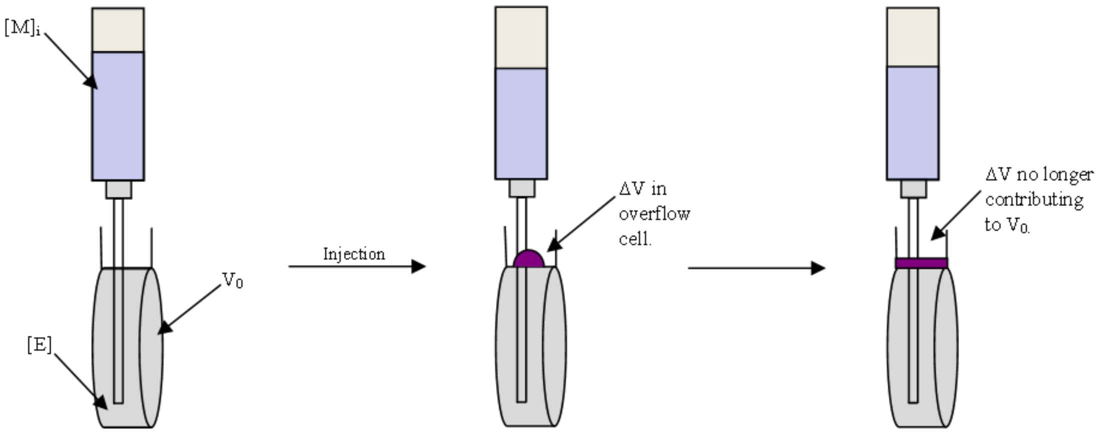

Figure 3.16 Schematic showing how an injection causes volume to be driven out of the active volume (V_0) into the overflow cell.

This constantly alters the concentrations of enzyme and metal-ion prior to the next injection which is accounted for by Equation 3.17-Equation 3.19.

$$D_{fM} = \frac{\Delta V}{V_0 + \Delta V}$$

Equation 3.17

$$D_{fE} = \frac{V_0}{V_0 + \Delta V}$$

Equation 3.18

$$[\mathrm{M}]_1 = [\mathrm{M}]_\mathrm{i}\mathrm{D}_{\mathrm{fM}} \qquad [\mathrm{E}]_1 = [\mathrm{E}]_\mathrm{i}\mathrm{D}_{\mathrm{fE}}$$

$$[\mathrm{M}]_2 = ([\mathrm{M}]_\mathrm{i}\mathrm{D}_{\mathrm{fM}}) + ([\mathrm{M}]_1\mathrm{D}_{\mathrm{fE}}) \qquad [\mathrm{E}]_2 = [\mathrm{E}]_1\mathrm{D}_{\mathrm{fE}}$$

$$[\mathrm{M}]_i = ([\mathrm{M}]_\mathrm{i}\mathrm{D}_{\mathrm{fM}}) + ([\mathrm{M}]_{i-1}\mathrm{D}_{\mathrm{fE}}) \qquad [\mathrm{E}]_i = [\mathrm{E}]_{i-1}\mathrm{D}_{\mathrm{fE}}$$

Equation 3.19

Assuming the reaction between the metal-ion and enzyme occurs faster than the volume driven out of the cell, Equation 3.17 is the dilution factor used to calculate the concentration of metal-ion (D_{fM}) for a single injection into the active volume of the cell. The metal-ion concentration for the first injection is given by Equation 3.19 ($[M]_1$), the second by Equation 3.19 ($[M]_2$) and subsequent metal-ion concentrations is given by Equation 3.19 ($[M]_i$). Dilution factor D_{fE} (Equation 3.18) calculates the concentration of enzyme for each injection i.e. the first injection by Equation 3.18 ($[E]_1$), the second by Equation 3.18 ($[E]_2$) and subsequent concentrations using Equation 3.18 ($[E]_i$) within the active cell volume (V_0).

A system which exhibits the typical 1:1 stoichiometry is barium-ion complexing to 18-crown-6-ether (Scheme 3.10) for which the parameters the number of metal-ions bound per crown ether, n = 1.00, $K_b = 5900\ M^{-1}$ and $\Delta H = -7.4\ kcal\ mol^{-1}$ were generated using the MicroCal model (Figure 3.17 and Figure 3.18).

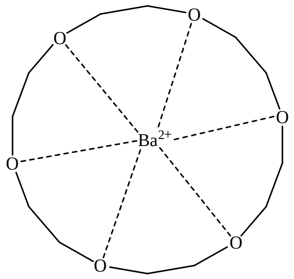

Scheme 3.10 Complex between barium ion and 18-crown-6-ether.

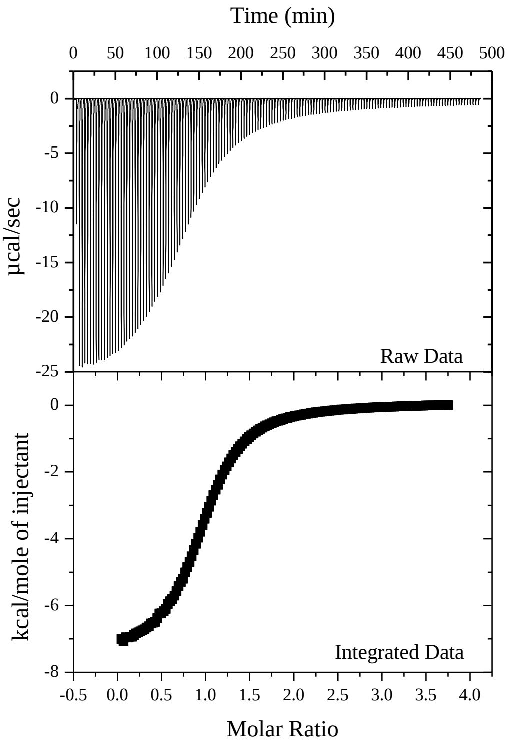

Figure 3.17 ITC titration of 50 mM barium chloride into 3 mM 18-crown-6-ether experimental isotherm at 25°C.

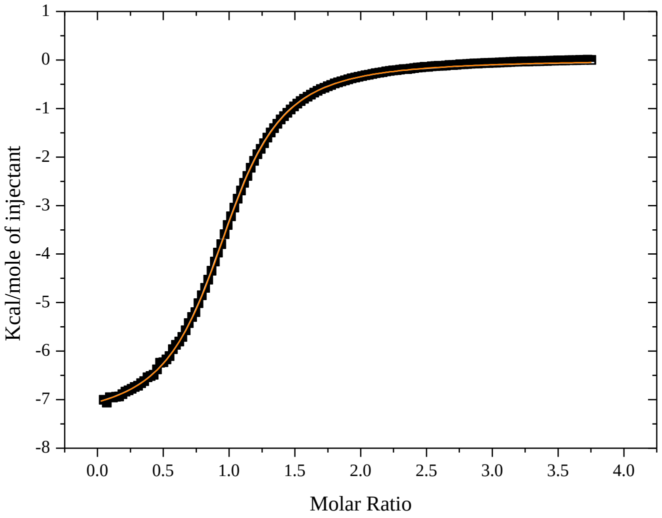

Figure 3.18 Experimental isotherm of 50 mM barium chloride into 3 mM 18-crown-6-ether (black) with theoretical fits by MicroCal model (white line) and our simulated model (orange).

Exactly the same curve was generated using our single binding site model developed here to form a mononuclear 1:1 complex as the MicroCal model. The experimental data (Figure 3.18, black) was simulated using our single binding model (Figure 3.18, orange) using the parameters which were calculated by MicroCal (as our model does not contain a fitting algorithm). It is assumed that these superimposable fits confirm that our methodology is robust. The calculated parameters (Figure 3.18, white) are in agreement with literature data at 25^{o}C for the 1:1 complex between barium-ion and 18-crown-6-ether where n = 0.97, K_b = 5610 M^{-1} and ΔH = -7.5 kcal mol^{-1} [225].

3.2.2 Binuclear binding model with the formation of both EM and EM_2 (Sequential binding).

Formation of the binuclear enzyme EM_2 may occur in two sequential steps. First the metal-ion binds to the apo-enzyme to form the mononuclear enzyme EM and subsequently this binds more metal-ion to give the binuclear enzyme EM_2. At equilibrium, the fractions of the enzyme species existing as E, EM and EM_2 are functions of the two binding constants K_{b1} and K_{b2} and the concentrations of E, M and EM.

The sequential binding of metal-ions can be represented by Scheme 3.11. Large variations of zinc-ion affinity K_{b1} and K_{b2} values have been reported for BcII and have either indicated positive cooperativity where the second metal-ion binds more strongly than the first or negative cooperativty, where the second metal-ion binds more weakly than the first. The two association constants (K_{b1} and K_{b2}) are given by Equation 3.20 and Equation 3.21.

When $K_{b1} >> K_{b2,}$ the addition of metal-ion to the apo-enzyme will convert it all to EM, so with a molar ratio (M:E) of 1:1only the mono-nuclear enzyme EM will be present – the first binding site is filled completely before the second site is populated

$$E + M \overset{K_{b1}}{\rightleftharpoons} EM \overset{K_{b2}\ \ M}{\rightleftharpoons} EM_2$$

Scheme 3.11 Sequential binding model forming both EM and EM_2.

$$K_{b1} = \frac{[EM]}{[E][M]}$$

Equation 3.20

$$K_{b2} = \frac{[EM_2]}{[EM][M]}$$

Equation 3.21

The two equations were treated independently to obtain the concentrations of EM and EM_2. For a single injection of metal-ion into the cell containing the enzyme, in the first step to form EM the system was allowed to equilibrate to give concentrations of E, EM and M. These concentrations were then used in the second modelling step to form EM_2 and allowed to come to equilibrium. The concentrations of EM and EM_2 at equilibrium were established in an iterative process until there was negligible change in metal-ion (M) concentration (10^{-17} M) in Equation 3.20 and Equation 3.21. The concentrations of E, M, EM and EM_2 for each injection were fed back into Equation 3.20 and Equation 3.21 to calculate the binding constants K_{b1} and K_{b2}.

For each injection, as before the change in the concentrations of EM ($\Delta N_{EM\boldsymbol{i}}$) and EM_2 ($\Delta N_{EM2\boldsymbol{i}}$) are calculated. These two values are then converted to heat outputs, based on the two ΔH values used for the two formation reactions (Equation 3.22). Note that, in the first equation ($Q_{EM\boldsymbol{i}}$), the heat depends on the amount of EM formed. Some of the EM present before the injection is converted into EM_2 at the same time, the overall amount of EM formed is the change in EM concentration ($\Delta N_{EM_{\boldsymbol{i}}}$) plus the amount of EM that is simultaneously converted to EM_2 (i.e. $\Delta N_{EM2_{\boldsymbol{i}}}$) the overall heat output is calculated for the ***i***th injection, $Q_{Total\boldsymbol{i}}$. This is converted to a differential heat with respect to the added metal-ion.

$$Q_{EM_{\boldsymbol{i}}} = \frac{(\Delta N_{EM_{\boldsymbol{i}}} + \Delta N_{EM2_{\boldsymbol{i}}}) * \Delta H}{1000}$$

$$Q_{EM2_{\boldsymbol{i}}} = \frac{\Delta N_{EM2_{\boldsymbol{i}}} * \Delta H}{1000}$$

Equation 3.22

The total heat for the ***i***th injection is given by Equation 3.23:

$$\mathrm{Q_{Total}}_{\boldsymbol{i}} = \mathrm{Q_{EM}}_{\boldsymbol{i}} + \mathrm{Q_{EM2}}_{\boldsymbol{i}}$$

Equation 3.23

The heat for the ***i***th injection can be represented in terms of differential heat per mole of metal-ion added (Equation 3.24).

$$\Delta \mathrm{H}_{\boldsymbol{i}} = \frac{\mathrm{Q_{Total}}_{\boldsymbol{i}}}{\Delta \mathrm{V} * \mathrm{M_i}}$$

Equation 3.24

3.2.3 Binuclear binding model without the formation of the mononuclear species EM (‘concerted’, positively cooperative binding).

Just to reiterate, cooperativity in the formation of binuclear enzymes can either be positive where binding of the first metal-ion enhances the binding of the second metal-ion or negative where binding of the second metal-ion binds less tightly to the enzyme than the first metal-ion.

The enzyme of interest in this work is the metallo-β-lactamase from *Bacillus cereus* (BcII) which is a non-pathogenic strain of bacteria which has β-lactam resistance. BcII has two metal-ion binding sites to which the natural ligand zinc is capable of binding. Work by Jacquin et al. in 2009 suggested that BcII 569/H/9 binds zinc in a positively cooperative manner and the di-anion is the only relevant form for catalysis[200]. It is proposed to investigate this by ITC but an appropriate model is needed to allow for strong cooperativity.

Cooperative binding is characterised by Scheme 3.12 when $K_{b2} >> K_{b1}$ and in this extreme case intermediate EM is not formed in significant quantities and the binding equilibrium constant (K_b) can then be represented by Equation 3.25.

$$\mathrm{E + M \xrightleftharpoons{K_{b1}} EM \xrightleftharpoons{K_{b2}\ \ M} EM_2}$$

If $K_{b2} >> K_{b1}$ the above equilibrium is reduced to a single binding event:

$$\mathrm{E + 2\,M \xrightleftharpoons{K_b} EM_2}$$

Scheme 3.12 Sequential binding of metal-ion to enzyme which contains two binding sites which is reduced to one event when $K_{b2} >> K_{b1}$.

$$\mathrm{K_b = \frac{[EM_2]}{[E][M]^2}}$$

Equation 3.25

If this is the situation, the equilibrium constant (K_b) for the concentration of EM_2 produced after the first injection can be defined by Equation 3.26 with respect to the initial concentrations of enzyme $[E]_i$ and metal-ion $[M]_i$. The initial concentration of the enzyme (E_i) is that in the analyte solution in the calorimetric cell and that of the metal-ion (M_i) is that added from the titrant solution.

$$\mathrm{K_b = \frac{[EM_2]}{([E]_i - [EM_2])([M]_i - 2\,[EM_2])^2}}$$

Equation 3.26

Both binding sites are filled even when there is less than 1 equivalent of metal-ion to the enzyme, so that the only species present are E and EM_2. For subsequent injections the concentration of E and M (Equation 3.25) are calculated from the remaining concentrations of enzyme and metal in the cell, this equation is a cubic in terms of $[EM_2]$ (Equation 3.27).

$$\mathrm{-(4K_b)[EM_2]^3 + 4K_b([E]_i + [M]_i)[EM_2]^2}$$

$$\mathrm{-\left(4K_b[E]_i[M]_i + K_b[M]_i^2 + 1\right)[EM_2] + K_b[E]_i[M]_i^2 = 0}$$

Equation 3.27

The roots (Equation 3.28) of the cubic equation (Equation 3.27) for the concentration of EM_2 for each injection were solved analytically using Derive 6 which is a mathematical system used for processing algebraic variables, functions etc.

$$\mathrm{Root}_1 = \frac{\mathrm{E_i} + \mathrm{M_i}}{3} - \frac{\sqrt{\mathrm{P}}\ \cos\left(\dfrac{\cos^{-1}\left(-\dfrac{\mathrm{N}\sqrt{\mathrm{P}}}{\mathrm{O}}\right)}{3}\right)}{3}$$

$$\mathrm{Root}_2 = \frac{\mathrm{E_i} + \mathrm{M_i}}{3} + \frac{\sqrt{\mathrm{P}}\ \sin\left(\dfrac{\sin^{-1}\left(\dfrac{\mathrm{N}\sqrt{\mathrm{P}}}{\mathrm{O}}\right)}{3} + \dfrac{\pi}{3}\right)}{3}$$

$$\mathrm{Root}_3 = \frac{\mathrm{E_i} + \mathrm{M_i}}{3} - \frac{\sqrt{\mathrm{P}}\ \sin\left(\dfrac{\sin^{-1}\left(\dfrac{\mathrm{N}\sqrt{\mathrm{P}}}{\mathrm{O}}\right)}{3}\right)}{3}$$

Equation 3.28

Where:

$$\mathrm{N} = \mathrm{K_b}\left(8\,[\mathrm{E}]_\mathrm{i}{}^3\mathrm{K_b} - 12\,[\mathrm{E}]_\mathrm{i}{}^2[\mathrm{M}]_\mathrm{i}\mathrm{K_b} + 3\,[\mathrm{E}]_\mathrm{i}\left(2\,[\mathrm{M}]_\mathrm{i}{}^2\mathrm{K_b} - 3\right)[\mathrm{M}]_\mathrm{i}\left([\mathrm{M}]_\mathrm{i}{}^2\mathrm{K_b} + 9\right)\right)$$

$$\mathrm{O} = \left(4\,[\mathrm{E}]_\mathrm{i}{}^2\mathrm{K_b} - 4\,[\mathrm{E}]_\mathrm{i}[\mathrm{M}]_\mathrm{i}\mathrm{K_b} + [\mathrm{M}]_\mathrm{i}{}^2\mathrm{K_b} - 3\right)^2$$

$$\mathrm{P} = \left(\frac{4\,[\mathrm{E}]_\mathrm{i}{}^2\mathrm{K_b} - 4[\mathrm{E}]_\mathrm{i}[\mathrm{M}]_\mathrm{i}\mathrm{K_b} + [\mathrm{M}]_\mathrm{i}{}^2\mathrm{K_b} - 3}{\mathrm{K_b}}\right)$$

The cubic expression has three roots, but the root which has a physical meaning (i.e. not imaginary) was obtained using a branched statement as the correct root for EM_2 lies between 0 and $M_i/2$ and cannot be greater than the initial concentration of enzyme and metal for a given injection. The dilution equations (Equation 3.17-Equation 3.19) were incorporated and the differential heats/kcal/mole of injectant was calculated using Equation 3.16 with respect to EM_2.

Titration curves of different binding constants were simulated with initial enzyme (E_i) and metal (M_i) concentrations of 1.8 x 10^{-5} M and 3.6 x 10^{-4} M respectively and a metal increment volume (ΔV) of 1.0 x 10^{-5} L (Figure 3.19).

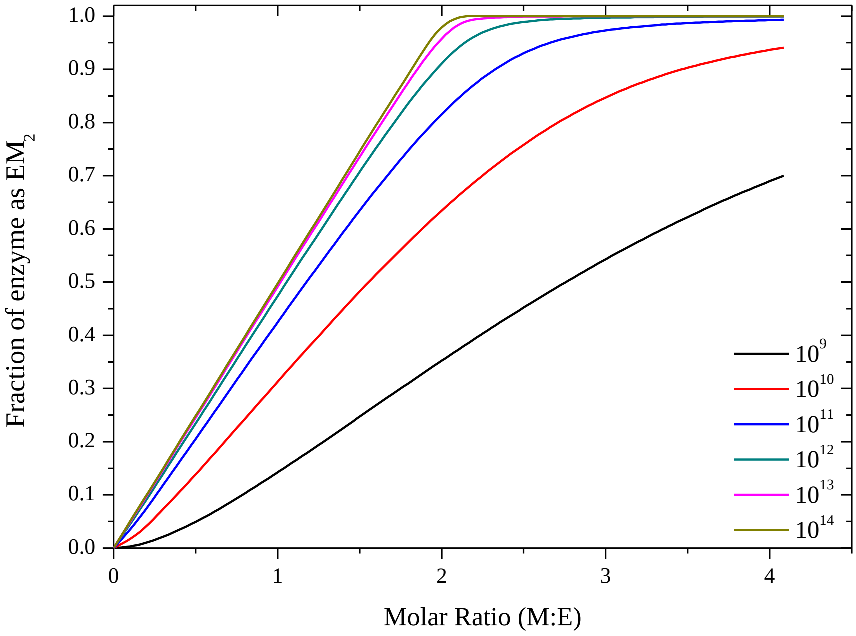

Figure 3.19 Simulated fraction of enzyme bound to metal-ion as EM_2 as a function of molar ratio (metal added/enzyme) at different binding constants K_b= 10^9 to 10^{14} M^{-2}. Using initial enzyme (E_i) and metal (M_i) concentrations of 1.8 x 10^{-5} M and 3.6 x 10^{-4} M respectively and a metal increment volume (ΔV) of 1.0 x 10^{-5} L

Figure 3.19 shows how the binding constant alters the profile of the fraction of enzyme bound to metal-ion as a function of molar ratio (M:E). At a high binding constant 10^{12} to 10^{14} M^{-2} the fraction of enzyme bound to the metal as EM_2 is near completion with a slope of 0.50 as a function the molar ratio (M:E). The enzyme is fully saturated as EM_2 at a molar ratio of about 2 for binding constants of 10^{14} and 10^{13} M^{-2}, but a binding constant of 10^{12} M^{-2} requires a little more metal-ion with 99% saturation occurring at 2.5 molar equivalents. Even with what appears to be a high binding constant of 10^{11} M^{-2} there is a decreasing amount of the enzyme bound to the metal-ion to form EM_2. At a 1:1 (M:E) molar ratio there is 42% of enzyme bound as EM_2 and 58% free enzyme. At a molar ratio of 2:1 (M:E) 81% of the enzyme exists as EM_2 yet 19% still remains as E. Substantial saturation of the enzyme (> 90%) starts to occur at 3.5 equivalents of total metal-ion added. Further reducing the binding constant to 10^{10} M^{-2} starts to show an initial downward curvature at low metal:enzyme ratio which may be slightly surprising with this ‘high’ binding constant, only 31% of the enzyme exists as EM_2

at a molar ratio of 1:1 (M:E) and at a molar ratio of 2:1 (M:E) 63% of enzyme exists as EM_2, complete saturation (> 99%) requires more than 4 molar equivalents of metal-ion. A binding constant of 10^9 M^{-2} shows a definite sigmoidal shape graph with an increasing concave line until a molar ratio of 1 after which the fraction of EM_2 becomes linear up until a molar ratio of 2. At molar ratios of 1:1 and 2:1 (M:E) only 14% and 35% of enzyme exists as $EM_{2,}$ respectively. Even after 4 molar equivalents of metal-ion have been added, only 70% of the enzyme exists as EM_2 when the binding constant is 10^9 M^{-2}. Some examples of the fraction of enzyme bound to the metal as EM_2 as a function of the molar ratio (M:E) and various binding constants are given in Table 3.4.

The initial increasing concave behaviour at low binding constants is surprising and could arise because at the beginning of the titration, the concentration of metal-ion added to the sample cell is low but as the concentration of the metal-ion is squared in the denominator of the equation for equilibrium (Equation 3.25) it makes the effective concentration of metal-ion even smaller therefore very low concentrations of EM_2 form. This also accounts for the apparent low fractions of conversion to EM_2 despite what appear to be large binding constants.

K_b	% EM_2	
	1:1 (M:E) molar ratio	2:1(M:E) molar ratio
10^{14}	49	97
10^{13}	48	95
10^{12}	47	90
10^{11}	42	81
10^{10}	31	63
10^{9}	14	35

Table 3.4 Percentage of the enzyme existing as EM_2 at different binding constants at molar ratios (M:E) of 1:1 and 2:1.

The data in Figure 3.20 was transformed to differential heats per mole of injectant using an enthalpy $\Delta H = 10.0$ kcal mol^{-1} per mole of product EM_2 formed. As two moles of metal-ion are required for each mole of EM_2 formed, 5.0 kcal mol^{-1} would be the maximum heat released per mole of metal-ion injectant if all the metal complexed with the enzyme to form EM_2. This is shown with a very high binding constant of 10^{14} M^{-2} even at a molar ratio of less than 2:1. A binding constant of 10^{13} M^{-2} initially shows a kink where the enthalpy of binding is lower than the maximum, compatible with less than full conversion of the added metal-ion to EM_2. As the binding constant is decreased the binding enthalpy decreases which is shown clearly by binding constant 10^{11} and 10^{12} M^{-2} and the initial values increase then decrease again as decreasing fraction of enzyme is converted toEM_2 with increasing added metal-ion as equilibrium is approached.

The initial increase in binding enthalpy, as explained previously using Figure 3.19 must be due to the formation of very low concentrations of EM_2 due to the initial low concentration of metal-ion within the sample cell.

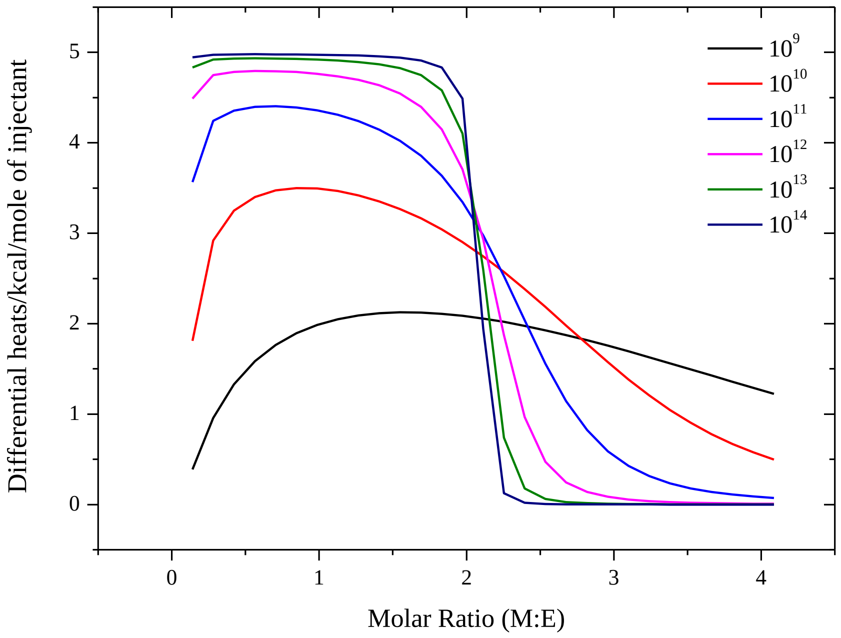

Figure 3.20 Simulation of the differential heats per kcal per mole of injectant metal-ion as a function of molar ratio (M:E) at different binding constants.

3.2.4 Comparison of the sequential and concerted models

Before considering the simulation of experimental ITC data, the sequential and concerted models were compared using various binding constant ratios (K_{b2}/K_{b1}) termed α (Equation 3.29)[215]. The fraction of enzyme existing as either EM or EM_2 and the total fraction of both species ($EM+EM_2$), θ, Equation 3.30) were plotted against molar ratio (M:E) at α = 10,000, 1000, 100, 10 and 1, 0.1 and 0.01.

$$\alpha = \frac{K_{b2}}{K_{b1}}$$

Equation 3.29

and:

$$\theta = \frac{[\mathrm{EM}] + [\mathrm{EM}_2]}{\mathrm{E_i}}$$

Equation 3.30

The resulting plots of the fraction of enzyme bound as EM and EM_2 are then converted to differential heat outputs using a trial ΔH value of 5.0 kcal mol^{-1} for both EM and EM_2 in the sequential binding model. Using an initial enzyme concentration (E_i) in the cell (1.4194 ml) of 1.8×10^{-5} M and injecting 1.0×10^{-5} l of titrant metal-ion concentration of 3.6×10^{-4} M for a total of 29 injections provides simulation plots from Figure 3.21-Figure 3.27.

Equivalent plots are shown for the concerted binding event simulation of $\mathrm{E} + 2\mathrm{M} \rightleftharpoons \mathrm{EM}_2$ using the same heat (i.e.ΔH = 10.0 kcal mol^{-1} for the overall reaction) for comparison. In Figure 3.21-Figure 3.25 for the sequential model, K_{b1} is kept at 10^5 M^{-1} and K_{b2} is altered to achieve different plots for α except when K_{b1} is greater than $K_{b2,}$ which is shown in Figure 3.26 and Figure 3.27.

An α value of 10,000 (Figure 3.21) shows that the fraction of EM (black line) present in solution is negligible compared to the fraction of enzyme bound as EM_2 (red line) which is consistent with the concerted binding model (direct formation to EM_2). The maximum enthalpy of 5.0 kcal mol^{-1} is produced initially as all of the metal-ion added is converted to EM_2 without significant formation of EM. At α = 1000 (Figure 3.22), a similar fraction of EM_2 is formed again with negligible concentrations of the mono-enzyme and the total heat per mole of product is 5.0 kcal mol^{-1}.

α = 10,000

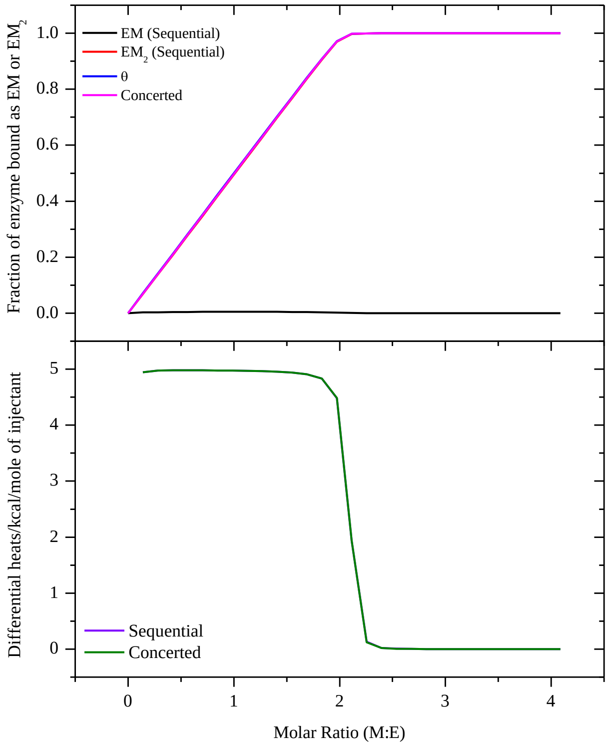

Figure 3.21 Fraction of EM (▬), EM$_2$ (▬) and θ (▬) against molar ratio (M:E) for the sequential binding model using $K_{b1} = 10^5$ M^{-1} and $K_{b2} = 10^9$ M^{-1} (α = 10,000), but are in fact indistinguishable from the concerted model (▬) using a $K_b = 10^{14}$ M^{-2}. The bottom graph shows the differential heats per kcal per mole of injectant against molar ratio for the sequential (▬) and concerted (▬) models.

α = 1000

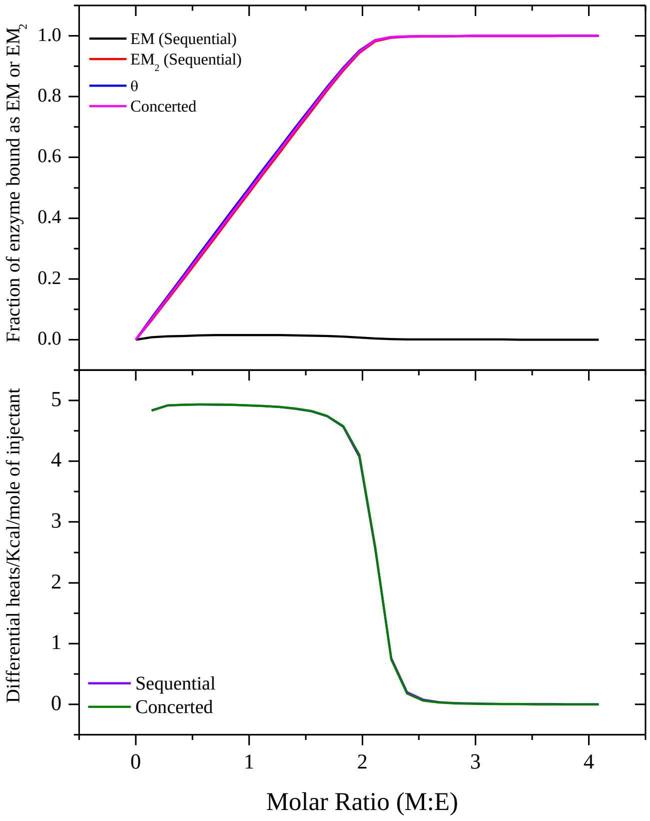

Figure 3.22 Fraction of EM (—), EM$_2$ (—) and θ (—) against molar ratio (M:E) for the sequential binding model using $K_{b1} = 10^5$ M^{-1} and $K_{b2} = 10^8$ M^{-1} (α = 1000). The concerted model (—) is shown using a $K_b = 10^{13}$ M^{-2}. The smaller graph shows the differential heats per kcal per mole of injectant against molar ratio for the sequential (—) and concerted (—) models.

$\alpha = 100$

When α is reduced to 100 (Figure 3.23) a difference appears between the concerted and the sequential model. For the latter, at a molar ratio of 1:1 (M:E) there is 5% EM (black line) and 45% EM_2 (red line) formed and at a molar ratio of 2:1 (M:E) there is 3% EM and 88% EM_2. The concerted model (magenta line) at molar ratios of 1:1 and 2:1 (M:E) shows 47% and 91% of the enzyme is as EM_2, respectively. Conversion to EM_2 in the sequential model (red line) is lower than in the concerted model but in addition there is significant EM produced even up to a molar ratio of almost 3:1. Consequently, the total fraction of enzyme converted to metallo enzyme species θ at a fixed molar ratio (M:E) is greater in the sequential than in the concerted model.

A very striking feature of the differential enthalpies plot is that in both models, the differential heat is relatively low at the beginning of the reaction which shows up as a 'kink' in the plot.

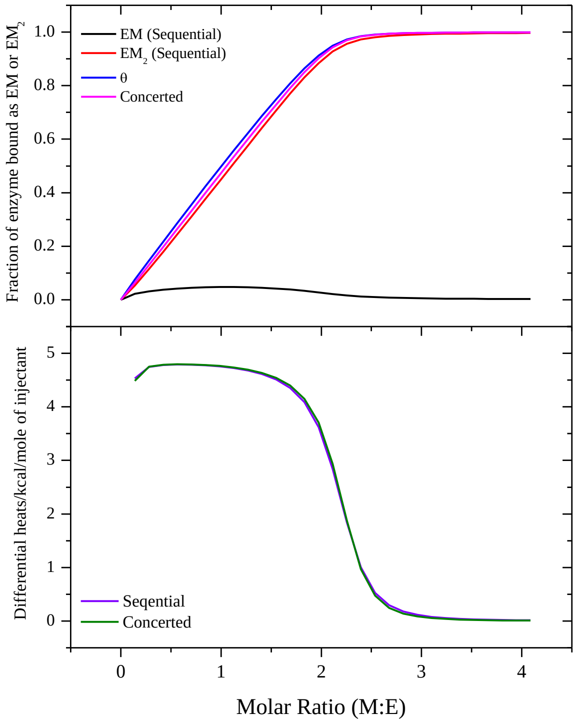

Figure 3.23 Fraction of EM (—), EM_2 (—) and θ (—) against molar ratio (M:E) for the sequential model using $K_{b1} = 10^5$ M^{-1} and $K_{b2} = 10^7$ M^{-1} ($\alpha = 100$). The concerted model (—) is shown using a $K_b = 10^{12}$ M^{-2}. The bottom graph shows the differential heats per kcal per mole of injectant against molar ratio for the sequential (—) and concerted (—) models.

When α = 10 then as expected, there is a large difference between two models because the sequential model predicts a relatively high EM concentration at molar ratios of 1:1 and 2:1 (M:E) of 14% and 11%, respectively, until a molar ratio of metal to enzyme of 3:1. The percentage of EM_2 at molar ratios 1:1 and 2:1 (M:E) in the sequential and concerted model are 35, 74 and 42 and 81%, respectively. Again, the total fraction of enzyme converted at a fixed molar ratio (M:E) is greater in the sequential than in the concerted model.

α = 10

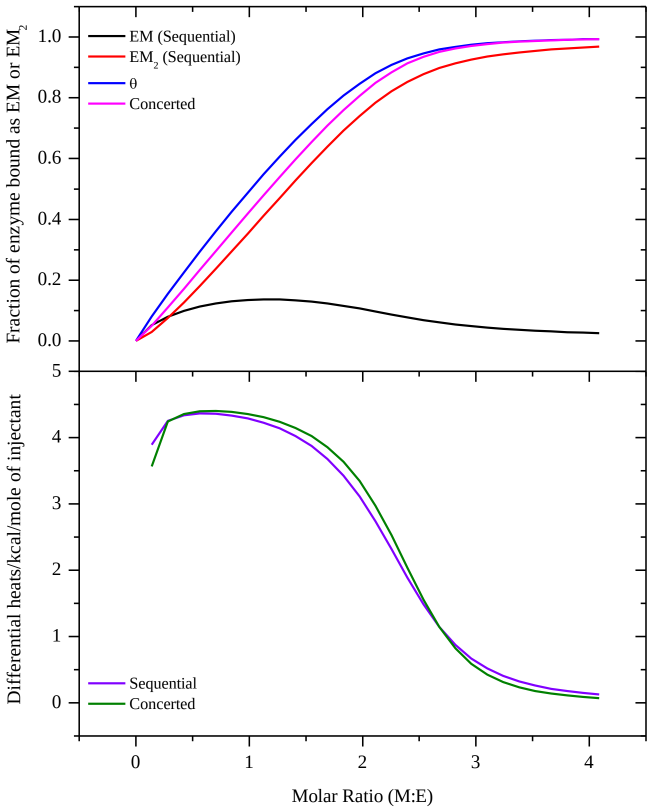

Figure 3.24 Fraction of EM (—), EM_2 (—) and θ (—) against molar ratio for the sequential model using $K_{b1} = 10^5\ M^{-1}$ and $K_{b2} = 10^6\ M^{-1}$ (α = 10). The concerted model (—) shown using a $K_b = 10^{11}\ M^{-2}$. The bottom graph shows the differential heats per kcal per mole of injectant against molar ratio for the sequential (—) and concerted (—) models.

A $\alpha = 1$, using $K_{b1} = 10^5$ M^{-1} and $K_{b2} = 10^5$ M^{-1}, shows that both EM and EM_2 are produced in the sequential model at least up to molar ratios (M:E) of 4:1. At low metal-ion concentrations the fraction of EM_2 in the sequential process (red line) shows a 'concave' feature until a molar ratio (M:E) of 1.5:1 where the fraction of EM is at a maximum (33%). At a molar ratio of 2:1 (M:E) 32% of the enzyme exists as EM and 44% as EM_2. Saturation at this relatively low overall binding constant (10^{10} M^{-2}) requires high concentrations of metal-ion. The concerted model shows a completely different profile compared to the sequential model with 31% of the enzyme as EM_2 at a M:E of 1:1 and at a molar ratio of 2:1 (M:E) 63%. This difference between the two models is reflected in the differential heats.

$\alpha = 1$

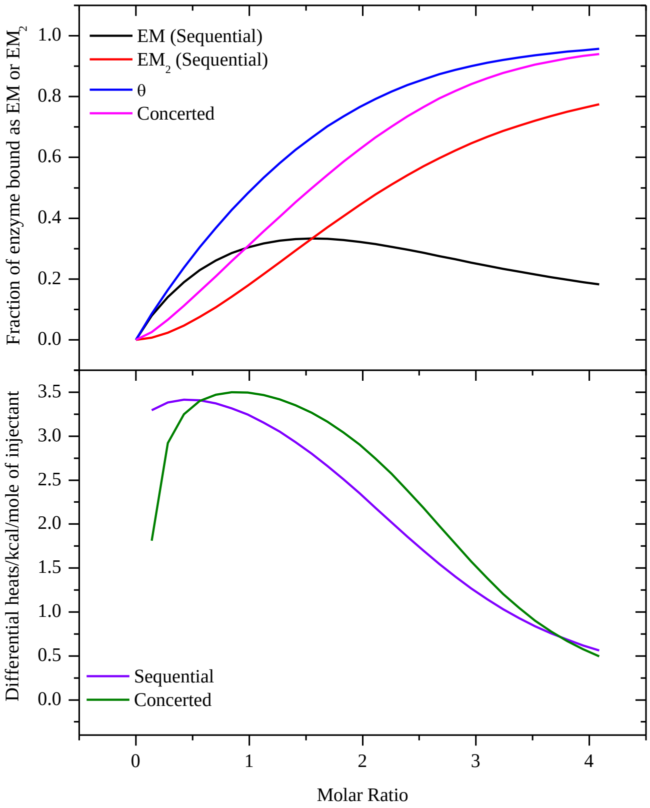

Figure 3.25 Fraction of EM (—), EM_2 (—) and θ (—) against molar ratio for the sequential model using $K_{b1} = 10^5$ M^{-1} and $K_{b2} = 10^5$ M^{-1} ($\alpha = 1$). The concerted model (—) is shown using a $K_b = 10^{10}$ M^{-2}. The bottom graph shows the differential heats per kcal per mole of injectant against molar ratio for the sequential (—) and concerted (—) models.

In the case where the first binding constant is greater than the second, $K_{b1} > K_{b2}$ i.e. $\alpha < 1$, formation of the mononuclear enzyme is favoured over that of the binuclear enzyme. At $\alpha = 0.1$ and at a molar ratio of 1:1 (M:E) 60% of the enzyme exists as EM and 13% as EM_2 in the sequential model compared to 42% EM_2 in the concerted model. At a molar ratio of 2:1 (M:E) in the sequential model 48% and 47% of the enzyme exists as EM and EM_2, respectively whereas in the concerted model there is 81% EM_2. The overall fraction, θ in the sequential model is higher than that of the fraction existing as EM_2 in the concerted model which indicates the stability of the mononuclear species is favoured over that of the binuclear enzyme.

$\alpha = 0.1$

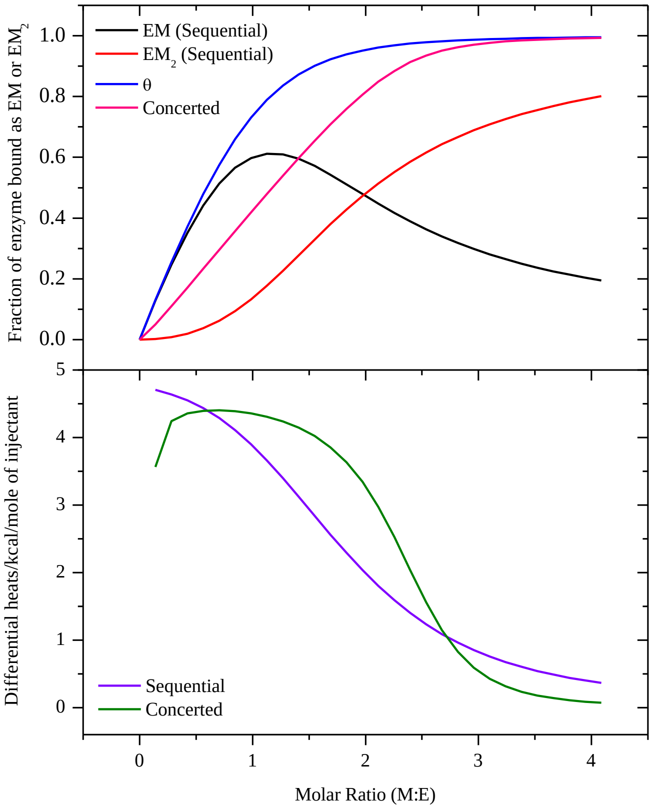

Figure 3.26 Fraction of EM (—), EM_2 (—) and θ (—) against molar ratio for the sequential model using $K_{b1} = 10^6\ M^{-1}$ and $K_{b2} = 10^5\ M^{-1}$ ($\alpha = 0.1$). The concerted model (—) is shown using a $K_b = 10^{11}\ M^{-2}$. The bottom graph shows the differential heats per kcal per mole of injectant against molar ratio for the sequential (—) and concerted (—) models.

When $\alpha = 0.01$ using $K_{b1} = 10^8$ M^{-1} and $K_{b2} = 10^6$ M^{-1} the formation of the mononuclear complex is the dominant species at a molar ratio of 1:1 (M:E) with 83% in the form of EM and only 7% as EM_2 and only when the molar ratio is > 1, is the fraction of EM_2 significant in the sequential model. At a molar ratio of 2:1 (M:E) 22% of the enzyme exists as EM and 78% as EM_2 in the sequential model. As shown previously the concerted model at $K_b = 10^{14}$ M^{-2} predicts a total conversion of metal-ion to EM_2 even at molar ratios (M:E) below 1. The overall fraction of the enzyme that has reacted, (θ, ($EM+EM_2/E_i$)) in the sequential model is greater than the fraction of enzyme as EM_2 in the concerted model at all molar ratios.

A single binding event is produced when the enthalpy of the two binding site are the same or very similar although $K_{b1} > K_{b2.}$

$\alpha = 0.01$

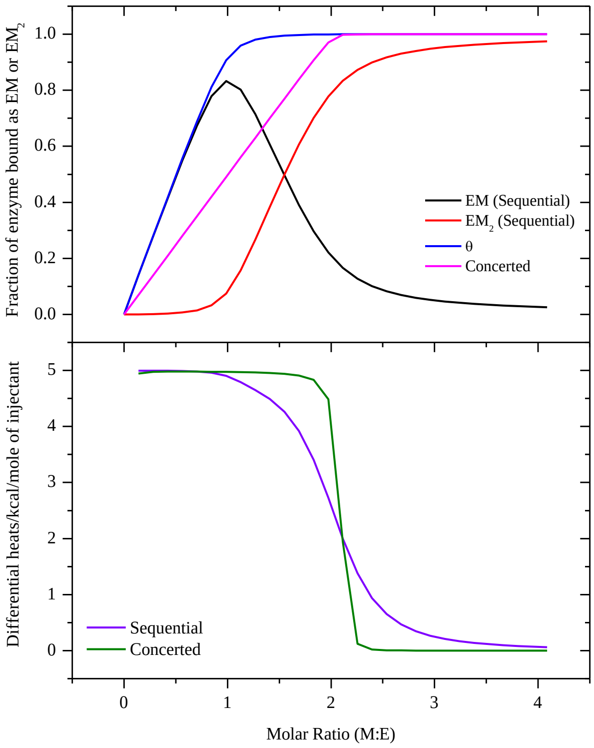

Figure 3.27 Fraction of EM (—), EM_2 (—) and θ (—) against molar ratio for the sequential model using $K_{b1} = 10^8$ M^{-1} and $K_{b2} = 10^6$ M^{-1} ($\alpha = 0.01$). The concerted model (—) is shown using a $K_b = 10^{14}$ M^{-2}. The bottom graph shows the differential heats per kcal per mole of injectant against molar ratio for the sequential (—) and concerted (—) models.

3.2.5 Comparison of differential heat isotherms with respect to different binding constants and enthalpies using the sequential model.

This section involves comparing different enthalpies at α values of 0.02, 0.1, 1, 10 and 50 using the sequential model. At α = 1 ($K_{b1} = K_{b2} = 10^6$ M^{-1}) when ΔH_1 is kept constant at 5.0 kcal mol^{-1} and ΔH_2 is gradually decreased an upwards concave kink is produced as expected, as the first enthalpy is having a greater effect than the second enthalpy on the overall profile. When ΔH_1 is lower than ΔH_2 (kept at 5.0 kcal mol^{-1}), the enthalpy starts off at the given ΔH_1 value, which gradually increases which decreases again as metal-ion is added.

α = 1

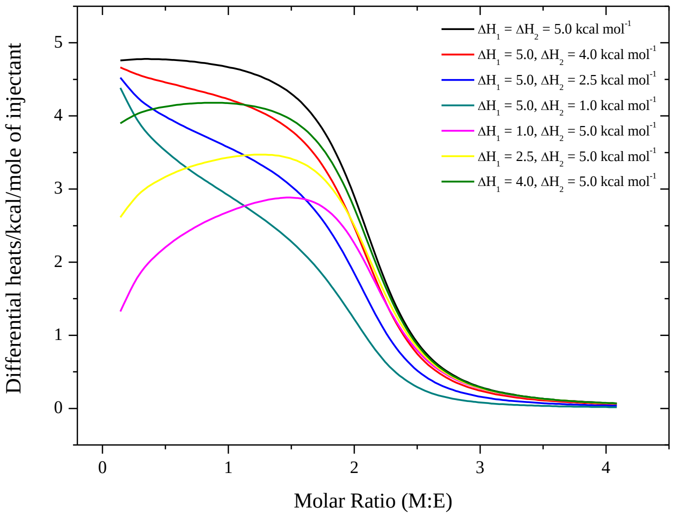

Figure 3.28 $K_{b1} = K_{b2} = 10^6$ M^{-1} (α = 1) at different ΔH_1 and ΔH_2 values, shown as differential heats per kcal per mole of injectant against molar ratio (M:E).

When $\alpha = 0.1$ i.e. $K_{b1} = 10^7$ M^{-1} and $K_{b2} = 10^6$ M^{-1} (Figure 3.29) and when the first enthalpy is greater than the second, again a similar effect is seen in the differential heats per kcal per mole of injectant plot against molar ratio (M:E). When ΔH_1 is 5.0 kcal mol^{-1} and ΔH_2 is 2.5 kcal mol^{-1} the difference of 2.5 kcal mol^{-1} is observed as a kink in the plot at a molar ratio of about 1.75 which is less profound when there is a difference between ΔH_1 and ΔH_2 of 4.0 kcal mol^{-1} (▬). When ΔH_1 is smaller than ΔH_2, the enthalpy gradually increases which decreases as all the enzyme in the cell becomes saturated.

$\alpha = 0.1$

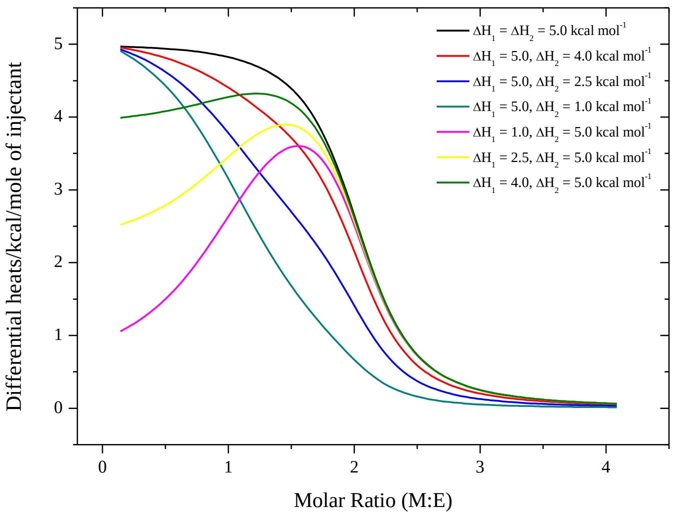

Figure 3.29 $K_{b1} = 10^7$ M^{-1} and $K_{b2} = 10^6$ M^{-1} ($\alpha = 0.1$) at different ΔH_1 and ΔH_2 values, shown as differential heats per kcal per mole of injectant against molar ratio (M:E).

When K_{b1} is 50 times higher than K_{b2} a similar curve is observed to Figure 3.29 when ΔH_2 is kept constant at 5.0 kcal mol^{-1} and ΔH_1 is decreased. When ΔH_1 is kept at 5.0 kcal mol^{-1} and ΔH_2 is changed the kink becomes more pronounced to where the second enthalpy has a major contribution to the overall profile. A difference of 1.0 kcal mol^{-1} is clearly seen compared to Figure 3.29 and is even more apparent with a larger difference between the two ΔH values.

$\alpha = 0.02$

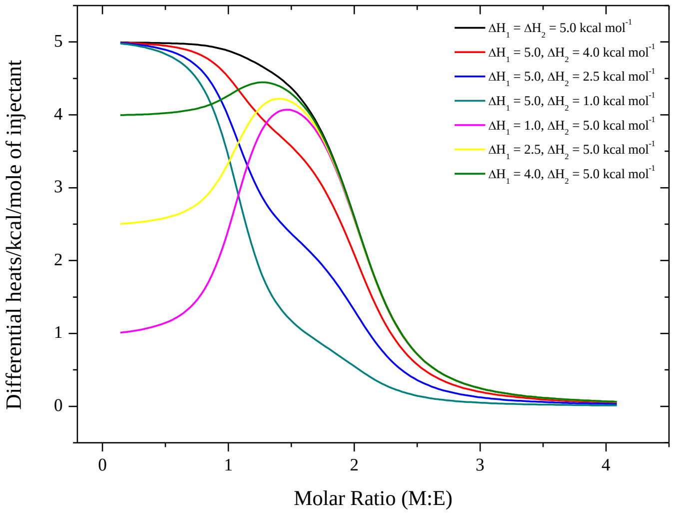

Figure 3.30 $K_{b1} = 5 \times 10^7$ M^{-1} and $K_{b2} = 10^6$ M^{-1} ($\alpha = 0.02$) at different ΔH_1 and ΔH_2 values, shown as differential heats per kcal per mole of injectant against molar ratio (M:E).

When K_{b2} is greater than K_{b1} ($\alpha = 10$ and 50) and the enthalpies are the same, a single binding event is observed. When ΔH_1 is constant at 5.0 kcal mol^{-1} and ΔH_2 is decreased, similar to when $\alpha = 1$, a upwards concave kink is produced yet when the second enthalpy is constant at 5.0 kcal mol^{-1} and ΔH_1 is changed initially up to approximately a molar ratio (M:E) of 0.5 a sharp concave downwards kink is observed which gradually increases due to the higher second enthalpy value which then diminishes as the enzyme becomes saturated. If the binding constant is increased by 5 fold as shown in Figure 3.32, the first enthalpy has a slightly larger contribution to the profile as the initial kink up to a molar ratio of 0.5 is less than when $K_{b1} = 10^6$ M^{-1} and $K_{b2} = 10^7$ M^{-1} (Figure 3.31).

$\alpha = 10$

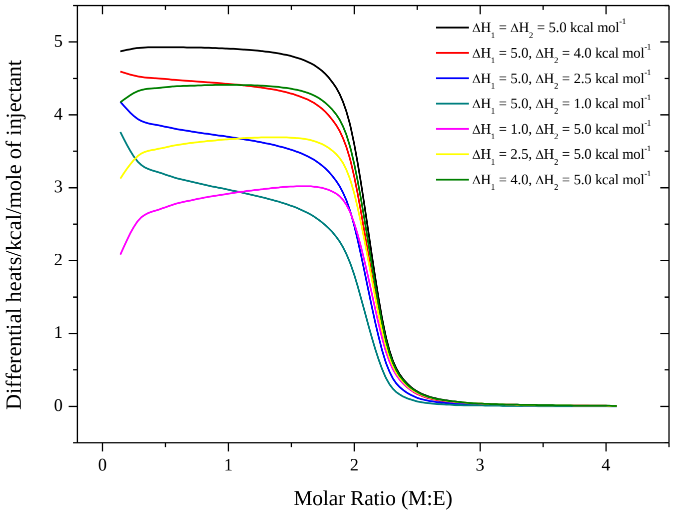

Figure 3.31 $K_{b1} = 10^6$ M^{-1} and $K_{b2} = 10^7$ M^{-1} ($\alpha = 10$) at different ΔH_1 and ΔH_2 values, shown as differential heats per kcal per mole of injectant against molar ratio (M:E).

$\alpha = 50$

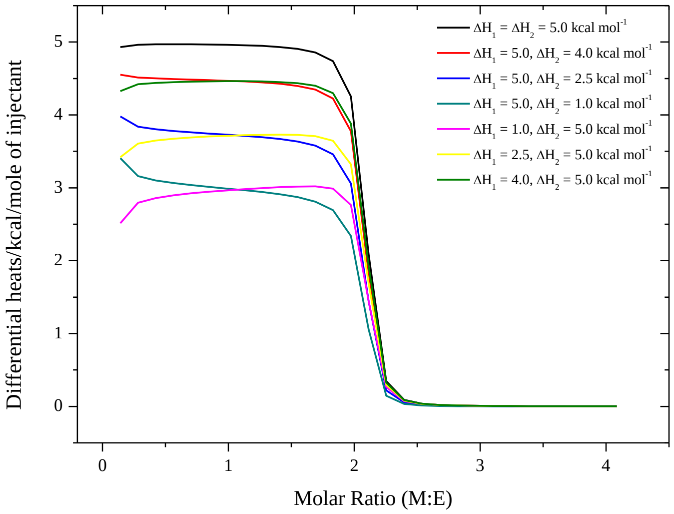

Figure 3.32 $K_{b1} = 10^6$ M^{-1} and $K_{b2} = 5 \times 10^7$ M^{-1} ($\alpha = 50$) at different ΔH_1 and ΔH_2 values, shown as differential heats per kcal per mole of injectant against molar ratio (M:E).

3.2.6 Metal-ion binding to BcII

Before analysing the experimental ITC data, it is worth mentioning the fitting models which MicroCal have available with the VP-ITC[217].

The first model involves n number of non-interacting but equivalent sites. This model is used for a simple n:1 (M:E) ratio systems or when the binding sites are the same. This fitting model only provides *one* binding constant (K_b) and enthalpy (ΔH, per mole of injectant). If there are several binding sites on a molecule i.e. 2, the single K_b value would refer to one of the sites, therefore K_b must be squared and the enthalpy multiplied by two.

The second binding model has independent non-interacting sites and a fit provides, if n = 2, K_{b1} and ΔH_1 for the first binding site and K_{b2} and ΔH_2 for the second binding site.

The final MicroCal model, sequential binding, is the same as our sequential model developed here, dependent on the relevant values of K_{b1} and K_{b2}, EM and EM_2 are possible. If the number of binding sites on the enzyme is two, the fitting system consists of two binding constants (K_{b1} and K_{b2}) and two enthalpies (ΔH_1 and ΔH_2). This model can be difficult to distinguish compared to the independent non-interacting sites and may require other techniques to confirm the experimental data.

These various modelling schemes were applied to the experimental data in which various metal-ions were titrated against apo-BcII at a fixed pH maintained by different buffers, most of which had been previously carried out in our laboratory by Hasina Motara.

The titration of zinc-ion into apo-BcII showed that above pH 6.80 (in MES buffer) two zinc-ions bind per enzyme molecule and the ITC output appeared to indicate a single binding event. The various modelling schemes described herein were applied to this data to try to distinguish between cooperative binding, which would definitely appear as a single event, and sequential binding which just happens to appear as a single binding event.

The first attempt to simulate the titration data was based on two independent but equivalent sites per enzyme molecule provided by MicroCal. This is shown in Figure 3.33 and a best fit in terms of the binding constant for each site K_b is $2.0 \pm (0.4) \times 10^6$ M^{-1} and an enthalpy ΔH_{obs} of 2.6 ± 0.7 kcal mol^{-1} per mole of injectant for the formation of both EM and EM_2. However, it is likely that the two sites in BcII are not equivalent as they involve different binding sites/ligands.

Furthermore, there is the possibility of positive cooperativity in binding the two metal-ions. Using ITC to detect cooperativity can be difficult especially when two or more binding site have very similar binding constants or similar enthalpies of association.

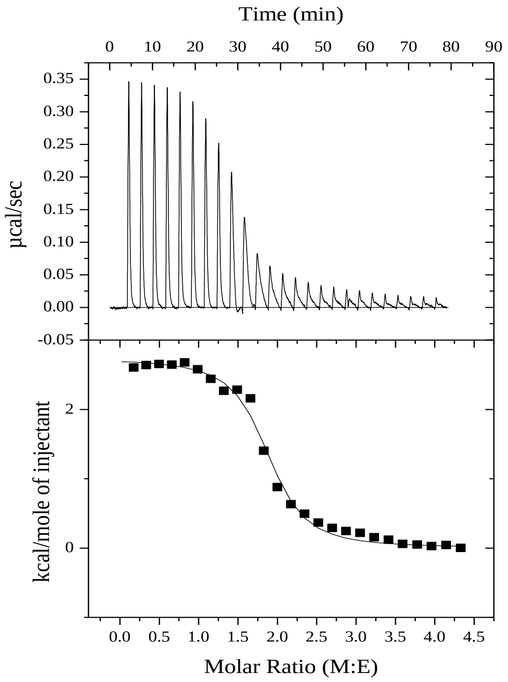

Figure 3.33 Isotherm of $ZnSO_4$ solution (3.6×10^{-4} M) titrated into apo-BcII solution (1.8×10^{-5} M) in MES buffer at pH 6.80 at 25°C. The single line is calculated assuming two independent but equivalent sites per enzyme molecule.

The ITC trace was also simulated using a model in which the two sites are not equivalent. The experimental data was fitted to a sequential binding model using MicroCal software. The number of sites was fixed at two and the parameters $K_{b1} = 4.33 \pm (3.5) \times 10^6$ M^{-1}, $\Delta H_1 = 2.7 \pm 0.07$ kcal mol^{-1}, $K_{b2} = 8.85 \pm (1.7) \times 10^5$ M^{-1} and $\Delta H_2 = 2.9 \pm 0.1$ kcal mol^{-1} were obtained from the simulation.

The simulation using the MicroCal program is shown in Figure 3.34 (○) compared to the experimental data (■). The value for the initial enzyme concentration used in the program was slightly changed in order to obtain a stoichiometric ratio of exactly 2. In order to compare the sequential model developed in this work with the MicroCal model, these same values for K_{b1}, ΔH_1, K_{b2} and ΔH_2 were used. The resultant plot is shown as the solid red line in Figure 3.34 and is in excellent agreement with the MicroCal model for sequential binding. The two models provide similar results in terms of the first binding constant and enthalpy. As expected the second binding constant ($K_{b2} = 8.85 \pm (1.7) \times 10^5$ M^{-1}) and enthalpy ($\Delta H_2 = 2.9 \pm$

0.1 kcal mol^{-1}) would be different from the independent but equivalent model (K_b = 2.0 ± (0.4) x 10^6 M^{-1} and ΔH = 2.6 ± 0.7 kcal mol^{-1}). The difference is not great and could represent error in the experimental data/fit or that the second binding site of BcII is slightly different to the first.

The individual species concentrations could be calculated which shows that a significant concentration of the mono-zinc species is formed during the titration (Figure 3.34, bottom).

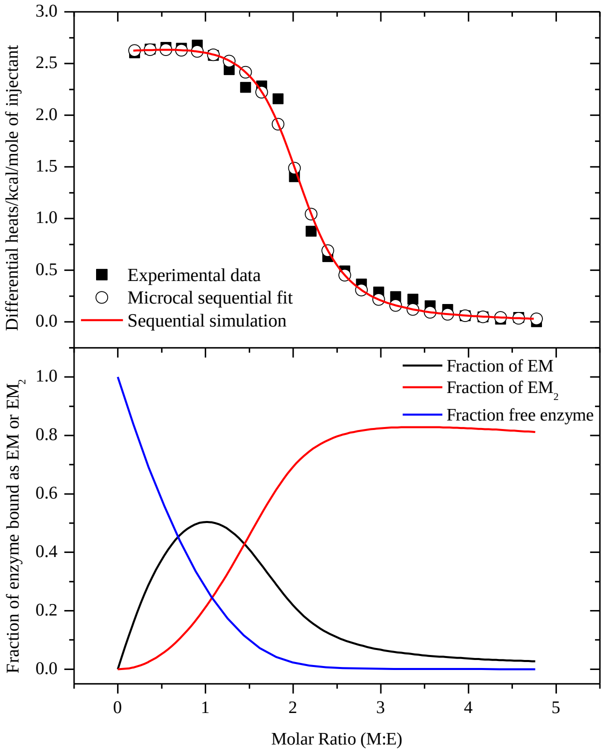

Figure 3.34 Isotherm of $ZnSO_4$ solution (3.6 x 10^{-4} M) titrated into apo-BcII solution (1.5 x 10^{-5} M) in MES buffer at pH 6.80 at 25°C fitted to MicroCals sequential model (○), our sequential simulation (▬). The bottom graphs show the fraction of enzyme bound as either EM (▬), EM_2 (▬) or free enzyme (▬) using the sequential model.

Also shown in Figure 3.34 is the fraction of the enzyme bound as the mononuclear EM and the binuclear EM_2 as the ratio of M:E changes. At 1:1 ratio of M:E, 50% of the enzyme is present as EM and 25% as EM_2 i.e. 25% is still free apo-enzyme. As the ratio increases to 2:1 (M:E) the proportion of EM_2 increases to 70% and that of EM decreases to 22% (8% free apo-enzyme).

An attempt was made to simulate the experimental results based on a positive cooperative model i.e. 'concerted', $E + 2M \rightleftharpoons EM_2$ without forming EM. To do this a binding constant K_b of 3.83 x 10^{12} M^{-2} (as the product of the two bind constants $K_{b1}.K_{b2}$) and the combined ΔH of 5.6 kcal mol^{-1} were used (Figure 3.35 (▬)).

Many attempts were made to simulate the experimental data by varying K_b and ΔH but it is clear that a concerted model is not appropriate for this system.

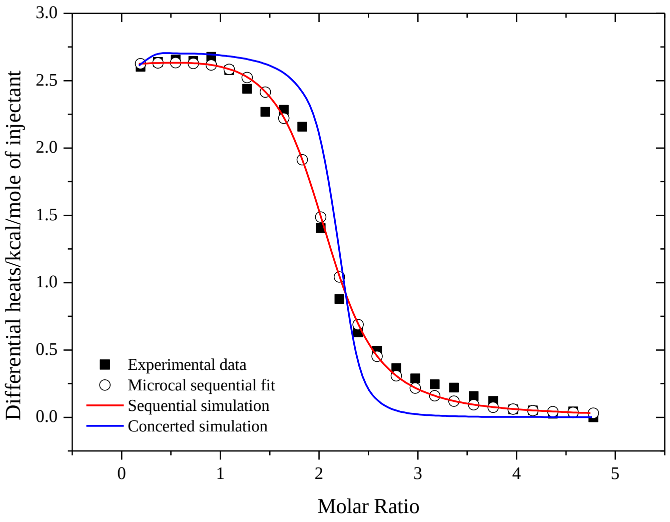

Figure 3.35 Isotherm of $ZnSO_4$ solution (3.6 x 10^{-4} M) titrated into apo-BcII solution (1.5 x 10^{-5} M) in MES buffer at pH 6.80 at 25°C fitted to MicroCals sequential model (○), our sequential simulation (▬) and the concerted model (▬) for the formation of EM_2.

A summary of the simulated binding constants for the two non-interacting but equivalent and the sequential model are shown in Table 3.5 for zinc-ion at pH 6.80.

MicroCal Two non-interacting but equivalent sites		MicroCal/our sequential model			
K_b (M^{-1})	**ΔH_{obs} (kcal mol^{-1})**	**K_{b1} (M^{-1})**	**ΔH_1 (kcal mol^{-1})**	**K_{b2} (M^{-1})**	**ΔH_2 (kcal mol^{-1})**
2.0 ± (0.4) x 10^6	2.6 ± 0.7	4.33 ± (3.5) x 10^6	2.7 ± 0.07	8.85 ± (1.7) x 10^5	2.9 ± 0.1

Table 3.5 Summary of binding constants and enthalpies using the non-interacting but equivalent model and the sequential model for $ZnSO_4$ titrated into apo-BcII in MES buffer at pH 6.80 at 25°C.

Another example where BcII exhibits a stoichiometric ratio of 2 from ITC experiments with respect to zinc-ion per enzyme is in cacodylate buffer at pH 6.35, 25°C. The ITC experimental data shown in Figure 3.36 was firstly fitted using the MicroCal single binding model (two independent and equivalent binding processes). This gives a binding constant K_b of 2.3 ± (0.3) x 10^6 M^{-1} and an enthalpy (ΔH_{obs}) of 6.2 ± 1.9 kcal mol^{-1}, for the formation of both EM and EM_2.

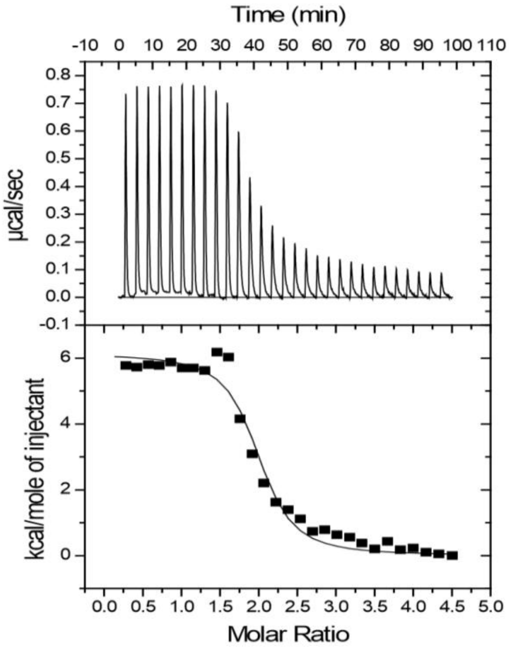

Figure 3.36 ITC output for $ZnSO_4$ solution (3.6 x 10^{-4} M) titrated into apoBcII solution (1.8 x 10^{-5} M) in cacodylate buffer at pH 6.35 at 25°C.

The second simulation used the MicroCal sequential model where the molar ratio was fixed at two. This model is shown in Figure 3.37 and the best fit parameters for K_{b1} = 1.37 ± (1.1) x 10^7 M^{-1}, ΔH_1 = 5.8 ± 0.07 kcal mol^{-1}, K_{b2} = 5.14 (± 0.55) x 10^5 M^{-1} and ΔH_2 = 6.7 ± 0.1 kcal mol^{-1}. Again these values were used in our model for a sequential process simply to check whether our model corresponded to MicroCals model. Exactly the same profile as the MicroCal model was produced. The values obtained from the sequential fit are slightly different compared to the single non-equivalent but identical model, this difference is most likely due to the goodness of the fit. Also shown again is the fraction of EM and the EM_2 as the molar ratio of M:E changes. At a ratio of 1:1, there is 69% of EM and 14% of EM_2. At a 2:1 M to E ratio there is 64% EM_2 and 27% of EM.

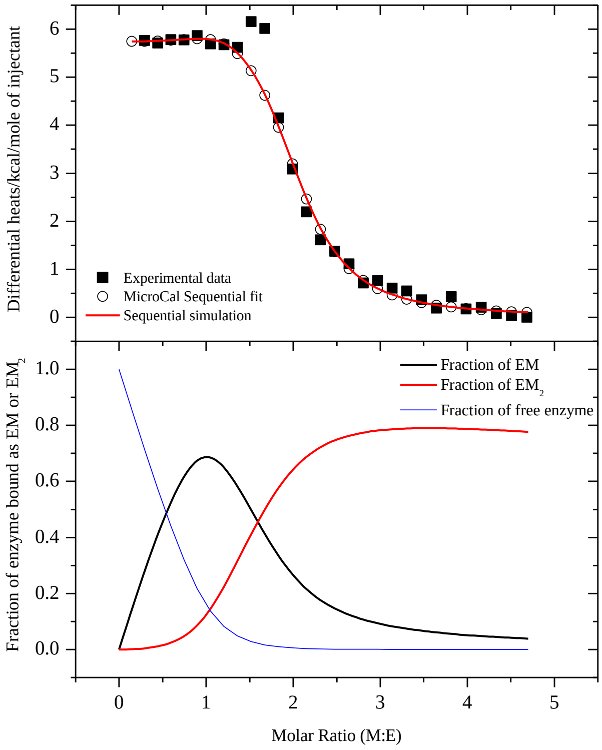

Figure 3.37 Isotherm of $ZnSO_4$ solution (3.6 x 10^{-4} M) titrated into apo-BcII solution (1.7 x 10^{-5} M) in cacodylate buffer at pH 6.35 at 25^{o}C fitted to MicroCals sequential model (○) and our sequential simulation (—). The bottom graph show the fraction of enzyme either bound as EM (—), EM_2 (—) or free enzyme (—) for the sequential model.

A simulation of the data assuming a positive cooperative binding model i.e. concerted formation of EM_2 with no detectable formation of EM using our cubic equation, used the product of the two binding constants and the sum of the two separate enthalpies (Figure 3.38, (—)). The simulation showed that a binding constant of 7.02 x 10^{12} M^{-2} was too steep and produced slightly more heat upon the metal complexing to enzyme to form EM_2. Reducing the binding constant by 10 fold (Figure 3.38, (—)) produces less heat as expected but the shape of the curve still does not reflect the experimental data and again many attempts were made to fit the experimental data by varying K_b and ΔH, but were unsuccessful.

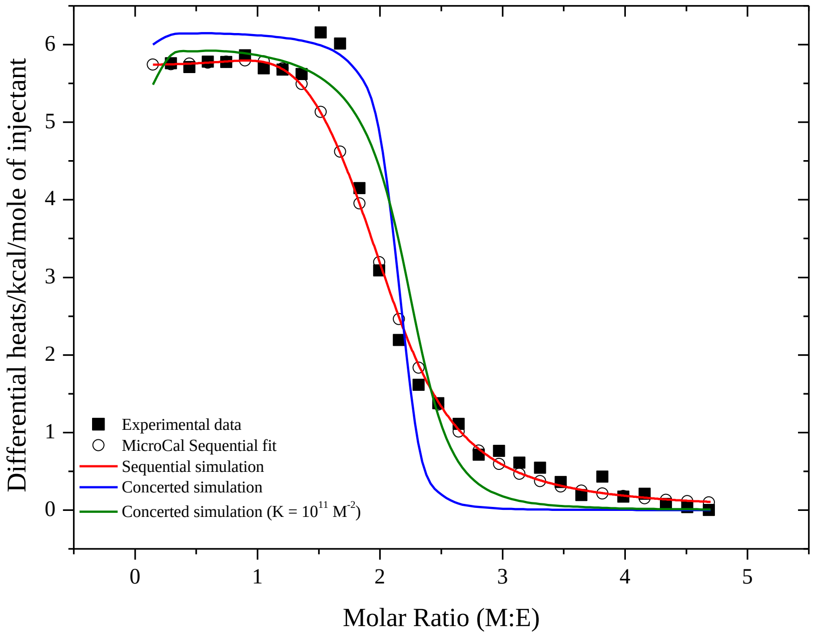

Figure 3.38 Isotherm of $ZnSO_4$ solution (3.6 x 10^{-4} M) titrated into apo-BcII solution (1.7 x 10^{-5} M) in cacodylate buffer at pH 6.35 at 25°C fitted to MicroCals sequential model (○), sequential simulation (▬) and concerted simulation (▬ , ▬).

A summary of the simulated binding constants for the two non-interacting but equivalent and the sequential model are shown in Table 3.6 for zinc-ion at pH 6.35.

MicroCal Two non-interacting but equivalent sites		MicroCal/our sequential model			
K_b (M^{-1})	**ΔH_{obs} (kcal mol^{-1})**	**K_{b1} (M^{-1})**	**ΔH_1 (kcal mol^{-1})**	**K_{b2} (M^{-1})**	**ΔH_2 (kcal mol^{-1})**
2.3 ± (0.3) x 10^6	6.2 ± 1.9	1.37 ± (1.1) x 10^7	5.8 ± 0.07	5.14 (± 0.55) x 10^5	6.7 ± 0.1

Table 3.6 Summary of binding constants and enthalpies using the non-interacting but equivalent model and the sequential model for $ZnSO_4$ titrated into apo-BcII in cacodylate buffer at pH 6.35 at 25°C.

Cobalt complexing with apo-BcII results in a similar ITC trace in which it is not easy to identify two discrete binding events. It is clear however that the ultimate stoichiometry of cobalt:enzyme complex is 2:1. The experimental data was first fitted to MicroCals single binding model where there are two independent but equivalent binding sites on each enzyme molecule, which gave a binding constant (K_b) of 2.49 ± (0.4) x 10^6 M^{-1} and a ΔH_{obs} of 15.6 ± 2.9 kcal mol^{-1} for the formation of both EM and EM_2.

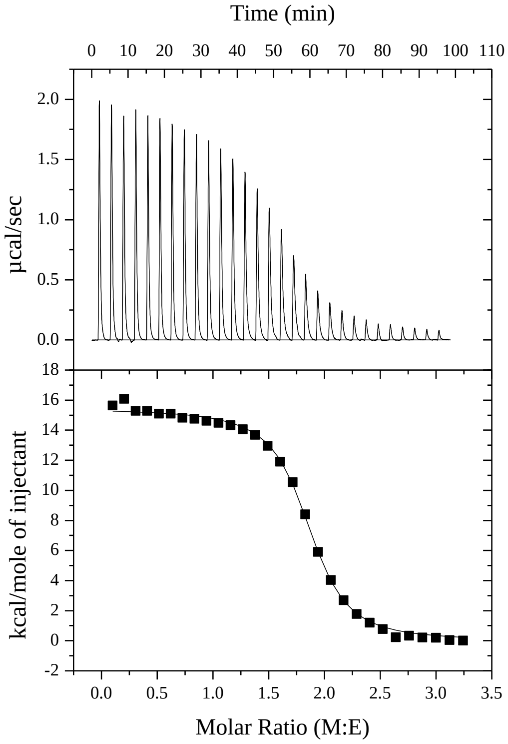

Figure 3.39 ITC output for $CoCl_2$ solution (3.6 x 10^{-4} M) titrated into apoBcII solution (1.8 x 10^{-5} M) in cacodylate buffer at pH 6.80 at 25°C.

The second simulation assuming two sites which bind metal-ions sequentially using the MicroCal software gave K_{b1} = 8.97 ± (1.3) x 10^5 M^{-1}, ΔH_1 = 16.8 ± 0.3 kcal mol^{-1}, K_{b2} = 1.70 ± (1.3) x 10^6 M^{-1} and ΔH_2 = 14.1 ± 0.3 kcal mol^{-1} (Figure 3.39 (○)). Again the difference between the single non-equivalent but identical model and the sequential model is very small, the theoretical fit for both models are good but there is less error in the enthalpies for the sequential model. A simulation using the model developed in this work based on the sequential model gave an identical ITC trace to that from the MicroCal (Figure 3.40). At 1:1 ratio of Co^{2+}, BcII corresponds to 25% of EM and 35% of EM_2 but increasing the ratio to 2:1 gives 11% EM and 75% EM_2.

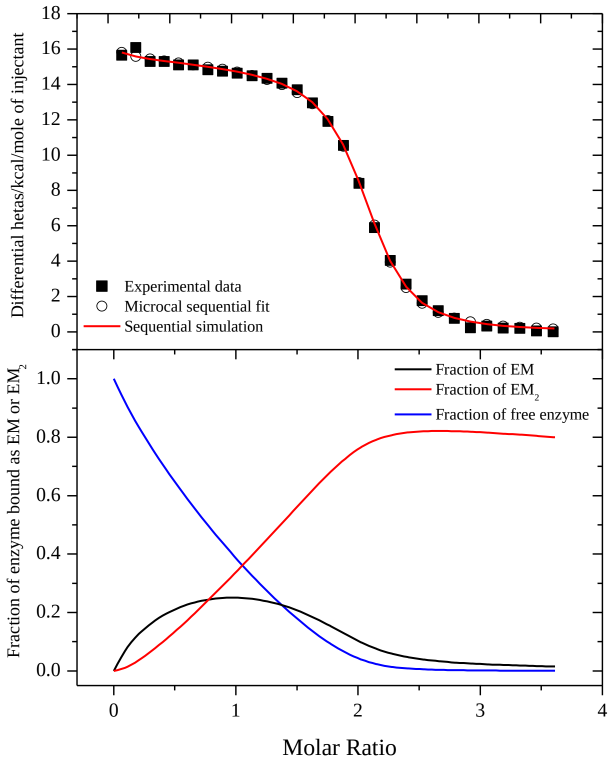

Figure 3.40 Isotherm of $CoCl_2$ solution (3.6 x 10^{-4} M) titrated into apo-BcII solution (2.2 x 10^{-5} M) in cacodylate buffer at pH 6.80 at 25°C fitted to MicroCals sequential model (○) and our sequential simulation (▬). The bottom graphs show the fraction of enzyme bound as either EM (▬), EM_2 (▬) or free enzyme (▬) using the sequential model.

A final attempt to simulate the experimental data using our concerted binding model assuming positive cooperativity with no formation of EM proved to be unsuccessful as shown by one of the simulations in Figure 3.41 (▬) using $K_b = 1.5 \times 10^{12}$ M^{-2} and an enthalpy (ΔH) = 30.9 kcal mol^{-1}.

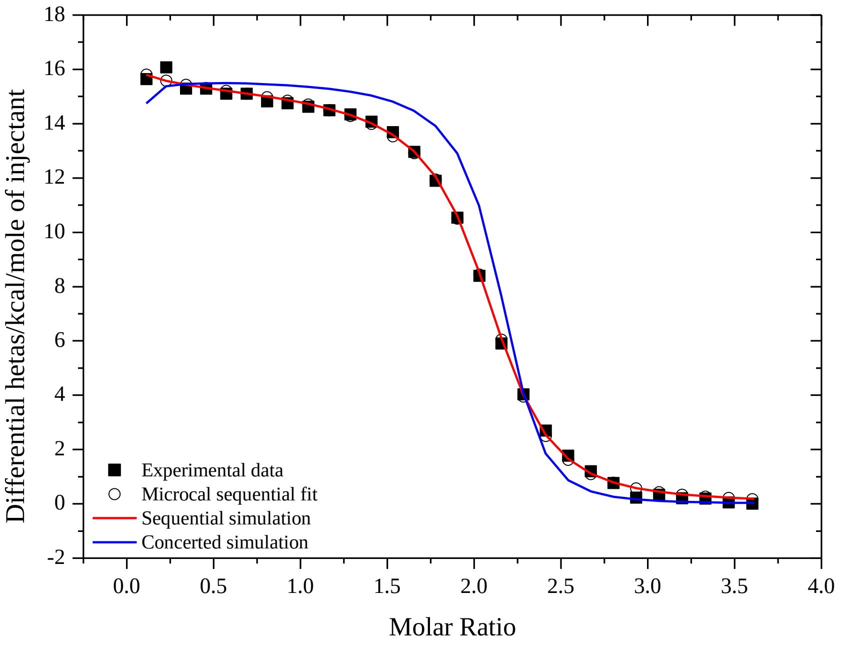

Figure 3.41 Isotherm of $CoCl_2$ solution (3.6×10^{-4} M) titrated into apo-BcII solution (2.2×10^{-5} M) in cacodylate buffer at pH 6.80 at 25°C fitted to MicroCals sequential model (○), sequential simulation (▬) and concerted simulation (▬).

A summary of the simulated binding constants for the two non-interacting but equivalent and the sequential model are shown in Table 3.7 for cobalt-ion at pH 6.80.

MicroCal Two non-interacting but equivalent sites		MicroCal/our sequential model			
K_b (M^{-1})	**ΔH_{obs} (kcal mol^{-1})**	**K_{b1} (M^{-1})**	**ΔH_1 (kcal mol^{-1})**	**K_{b2} (M^{-1})**	**ΔH_2 (kcal mol^{-1})**
2.49 ± (0.4) x 10^6	15.5 ± 2.9	8.97 ± (1.3) x 10^5	16.8 ± 0.3	1.70 ± (1.3) x 10^6	14.1 ± 0.3

Table 3.7 Summary of binding constants and enthalpies using the non-interacting but equivalent model and the sequential model for $CoCl_2$ titrated into apo-BcII in cacodylate buffer at pH 6.80 at 25°C

A completely different profile is observed at pH 7.20 for the titration of cadmium-ion to apo-BcII (Figure 3.42), the isotherm shows two distinctive binding events. Binding of cadmium-ion occurs non-cooperatively and independently, the enzyme binds the first cadmium-ion and then the second cadmium-ion.

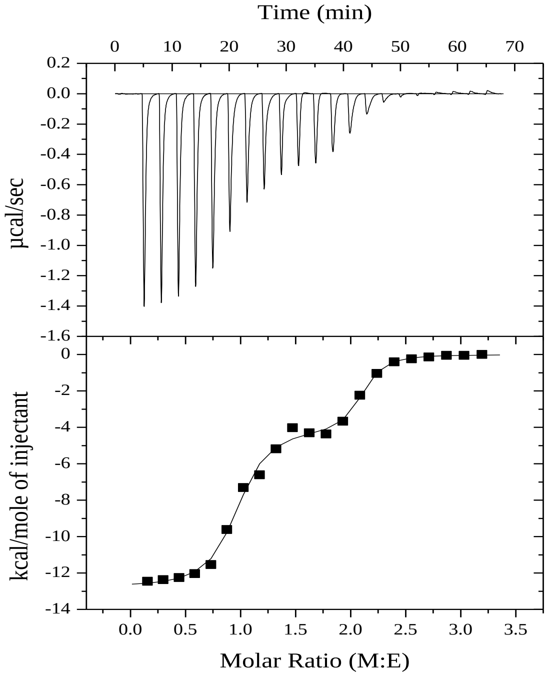

Figure 3.42 ITC output for $CdCl_2$ solution (3.6×10^{-4} M) titrated into apoBcII solution (1.8×10^{-5} M) in HEPES buffer at pH 7.20 at 25°C

The experimental data was fit to the MicroCal two independent non-interacting sites which produced $K_{b1} = 3.65 \times 10^8\ M^{-1}$, $\Delta H_1 = -12.4$ kcal mol^{-1}, $K_{b2} = 5.29 \times 10^6\ M^{-1}$ and $\Delta H_2 = -4.8$ kcal mol^{-1}. It may be difficult to distinguish between completely independent or slightly interacting; an attempt was made to simulate the experimental data to the sequential model (Figure 3.43). The MicroCal sequential fit produced $K_{b1} = 5.23\ (\pm 6.1) \times 10^8\ M^{-1}$, $\Delta H_1 = -12.3 \pm 0.3$kcal mol^{-1}, $K_{b2} = 1.35\ (\pm 1.6) \times 10^7\ M^{-1}$ and $\Delta H_2 = -3.7 \pm 0.4$ kcal mol^{-1}.

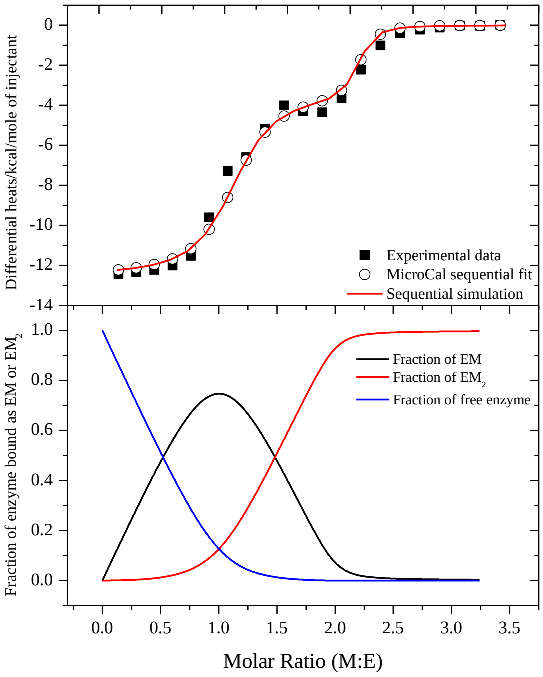

Figure 3.43 Isotherm of $CdCl_2$ solution (3.6 x 10^{-4} M) titrated into apo-BcII solution (1.8 x 10^{-5} M) in HEPES buffer at pH 7.20 at 25°C fitted to MicroCals sequential model (○) and our sequential simulation (▬). The bottom graphs show the fraction of enzyme bound as either EM (▬), EM_2 (▬) or free enzyme (▬) using the sequential model.

A summary of the simulated binding constants for the two non-interacting but equivalent and the sequential model are shown in Table 3.8 for cobalt-ion at pH 7.20.

MicroCal Two independent non-interacting sites				MicroCal/our sequential model			
K_{b1} (M^{-1})	**ΔH_1 (kcal mol^{-1})**	**K_{b2} (M^{-1})**	**ΔH_2 (kcal mol^{-1})**	**K_{b1} (M^{-1})**	**ΔH_1 (kcal mol^{-1})**	**K_{b2} (M^{-1})**	**ΔH_2 (kcal mol^{-1})**
3.65 x 10^8	-12.4	5.29 x 10^6	-4.8	5.23 (± 6.1) x 10^8	-12.3 ± 0.3	1.35 (± 1.6) x 10^7	-3.7 ± 0.4

Table 3.8 Summary of binding constants and enthalpies using the two independent non-interacting model and the sequential model for $CdCl_2$ titrated into apo-BcII in HEPES buffer at pH 7.20 at 25°C.

Metal, buffer, pH	MicroCal Two non-interacting but equivalent sites		MicroCal/our sequential model			
	K_b (M^{-1})	**ΔH_{obs} (kcal mol^{-1})**	**K_{b1} (M^{-1})**	**ΔH_1 (kcal mol^{-1})**	**K_{b2} (M^{-1})**	**ΔH_2 (kcal mol^{-1})**
$ZnSO_4$, MES, pH 6.80	2.0 ± (0.4) x 10^6	2.6 ± 0.7	4.33 ± (3.5) x 10^6	2.7 ± 0.07	8.85 ± (1.7) x 10^5	2.9 ± 0.1
$ZnSO_4$, cacodylate, pH 6.35	2.3 ± (0.3) x 10^6	6.2 ± 1.9	1.37 ± (1.1) x 10^7	5.8 ± 0.07	5.14 (± 0.55) x 10^5	6.7 ± 0.1
$CoCl_2$, cacodylate, pH 6.80	2.49 ± (0.4) x 10^6	15.5 ± 2.9	8.97 ± (1.3) x 10^5	16.8 ± 0.3	1.70 ± (1.3) x 10^6	14.1 ± 0.3

Table 3.9 Summary of the binding constants and enthalpies for the three isotherms which show a single binding event fitted to MicroCals two non-interacting but equivalent model and MicroCals/our sequential model.

Fitting the different models to experimental data has shown that investigating positive cooperativity is difficult. Titrating metal-ions such as zinc and cobalt, a single binding event is observed and simulating the curves using MicroCals non-interacting but equivalent sites does fit the data with binding constants ranging from 2.0 x 10^6 – 2.5 x 10^6 M^{-1} therefore the overall binding constant for the two sites of BcII range from 4.0 x 10^{12} – 6.25 x 10^{12} M^{-2}. Using the sequential model the first binding constant (K_{b1}) varies much more from 9.0 x 10^5 – 1.4 x 10^7 M^{-1} and the second binding constant (K_{b2}) from 5.1 x 10^5 – 1.7 x 10^6 M^{-1}. The overall binding constant for BcII using the sequential model range from 1.5 x 10^{12} – 7.0 x 10^{12} M^{-1}, this is a larger range than the non-interacting but equivalent binding model but between the two models the values are in the same order of magnitude. It is likely that BcII has different binding constants as the two sites contain different amino acids. Many attempts were made at fitting the experimental data to our positively cooperative (concerted) model by using various values of K_b and ΔH, but were unsuccessful, which suggests that BcII binds metal-ions in a sequential manner producing both EM and EM_2 as metal-ion is titrated.

3.2.7 Conclusion

We have been able to develop and confirm the commercial MicroCal software is capable of determining simple 1:1, sequential and independent but not interacting reactions between metal-ion and enzyme or host-guest chemistry. A striking feature of the positively cooperative (concerted) model without any formation of the intermediate EM is at ‘low’ binding constants such as 10^{10} M^{-2} where a slight concave character is observed when plotting the fraction of enzyme as EM_2 against molar ratio (M:E). This feature is transferred to the differential heats plot against molar ratio (M:E) and is most likely due to low concentrations of EM_2 being formed as the metal-ion concentrations in the cell within the initial stages of the titration are very low. The sequential model on the other hand is capable of forming both EM and EM_2 dependent on the relative values of the two binding constants. Comparing our sequential and positively concerted model, the two simulations clearly demonstrate that the sequential model converges into a positively cooperative model when $K_{b2} >> K_{b1}$ and when $\alpha \geq 100$. When α is below 100, the fraction of enzyme existing as EM dominates and the overall fraction of enzyme as either species ($EM+EM_2$) is greater in the sequential simulation then the fraction of EM_2 in the concerted model, which may indicate the overall stability of the mononuclear species is more stable than the binuclear species.

The two models were used in conjunction with the MicroCal sequential simulation to re-analyse the experimental data of titrating metal-ions such as zinc and cobalt into BcII solution, which provide a single binding event with a stoichiometric ratio of 2. Using the MicroCal sequential model, the binding constants K_{b1} and K_{b2} were obtained with their relevant enthalpies dependent on the buffer used. The values suggest slight negative cooperativity between the two binding sites or it is possible that the two sites are independent and identical. The overall binding constants for the two sites are within experimental error using either the independent but identical model or the sequential model. Although initially suggesting that BcII only binds metal-ions in a positively cooperative event, the ITC data does not fit a positively concerted model and therefore can be considered a sequential processes with the two sites have similar binding constants within error or slight negative cooperativity upon binding of the second metal-ion. The isotherm of cadmium complexing with apo-BcII shows two distinct events and can be simulated with either the sequential model or independent non-interacting sites model. Both models fit the experimental data but the independent non-interacting model does fit better than the sequential model, which suggests when apo-BcII complexes with cadmium, it does via an independent non-interacting process.

Chapter 4 – PUBLISHED PAPERS

‘The relative hydrolytic reactivities of pyrophosphites and pyrophosphates’

D. Mistry and N. Powles, *Organic & Biomolecular Chemistry*, 2013, **11**, 5727-5733.

‘Unusual Stability and Carbon Acidity of a Dicationic Carbon Species’

D. Mistry, N. Powles and M. I. Page, *The Journal of Organic Chemistry*, 2013, **78**, 10732-10736.

'pH and Basicity of Ligands Control the Binding of Metal-ions to *B.cereus* B1 β-Lactamase'

H. Motara, D. Mistry, D. R. Brown, R. A. Cryan and M. I. Page, *Chemical Science*, 2014, DOI: 10.1039/C4SC00601A.

Chapter 5 – REFERENCES

1. M. W. Bowler, M. J. Cliff, J. P. Waltho and G. M. Blackburn, *New Journal of Chemistry*, 2010, **34**, 784-794.
2. J. D. Watson and F. H. C. Crick, *Cold Spring Harbor Symposia on Quantitative Biology*, 1953, **18**, 123-131.
3. S. Mikkola, E. Stenman, K. Nurmi, E. Yousefi-Salakdeh, R. Stromberg and H. Lonnberg, *Journal of the Chemical Society, Perkin Transactions 2*, 1999, 1619-1626.
4. R. H. Horton, *Principles of Biochemistry*, 4th ed.,International edn., Pearson Prentice Hall, Upper Saddle River, N.J, London, 2006.
5. Z. Shabarova and A. Bogdanov, in *Advanced Organic Chemistry of Nucleic Acids*, Wiley-VCH Verlag GmbH, Editon edn., 2007, pp. 1-32.
6. M. A. Pasek, T. P. Kee, D. E. Bryant, A. A. Pavlov and J. I. Lunine, *Angewandte Chemie International Edition*, 2008, **47**, 7918-7920.
7. J. Sutton, *Biology*, Macmillan Publishers Limited, 1998.
8. A. P. H. J. J. Zuckerman, ed., *Inorganic Reactions and Methods, The Formation of Bonds to Group VIB (O, S, Se, Te, Po) Elements, Part 1*, John Wiley & Sons, 2009.
9. W. Gerrard, M. J. D. Isaacs, G. Machell, K. B. Smith and P. L. Wyvill, *Journal of the Chemical Society (Resumed)*, 1953, 1920-1926.
10. S. A. Todd, *Proceedings of the National Academy of Sciences*, 1959, **45**, 1389-1397.
11. V. M. Clark, G. W. Kirby and A. Todd, *Nature*, 1958, **181**, 1650-1652.
12. V. M. Clark, G. W. Kirby and A. Todd, *Journal of the Chemical Society (Resumed)*, 1957, 1497-1501.
13. Z. Shabarova and A. Bogdanov, in *Advanced Organic Chemistry of Nucleic Acids*, Wiley-VCH Verlag GmbH, Editon edn., 2007, pp. 93-180.
14. K. D. Troev, in *Chemistry and Application of H-Phosphonates*, Elsevier Science Ltd, Amsterdam, Editon edn., 2006, pp. 1-291.
15. H. A. Sober and W. P. Jencks, *Handbook of Biochemistry ed*, Chemical Rubber Co., Cleveland, OH, 1968.
16. A. Kraszewski, *Pure and Applied Chemistry*, 2007, **79**, 2217-2227.
17. N. Powles, J. Atherton and M. I. Page, *Organic & Biomolecular Chemistry*, 2012, **10**, 5940-5947.
18. R. B. Martin, *Journal of the American Chemical Society*, 1959, **81**, 1574-1576.
19. Z. Luz and B. Silver, *Journal of the American Chemical Society*, 1961, **83**, 4518-4521.
20. B. Silver and Z. Luz, *Journal of the American Chemical Society*, 1962, **84**, 1091-1095.
21. E. S. Lewis and L. G. Spears, *Journal of the American Chemical Society*, 1985, **107**, 3918-3921.
22. F. H. Westheimer, S. Huang and F. Covitz, *Journal of the American Chemical Society*, 1988, **110**, 181-185.
23. R. N. Mehrotra, *European Chemical Bulletin*, 2013, **2**, 758-776.
24. W. P. Jencks and J. Regenstein, in *Handbook of Biochemistry and Molecular Biology, Fourth Edition*, CRC Press, Editon edn., 2010, pp. 595-635.
25. J. P. Guthrie, *Canadian Journal of Chemistry*, 1979, **57**, 236-239.
26. S. C. L. Kamerlin and J. Wilkie, *Organic & Biomolecular Chemistry*, 2007, **5**, 2098-2108.
27. C. A. Bunton, *Journal of Chemical Education*, 1968, **45**, 21.
28. J. Florián and A. Warshel, *The Journal of Physical Chemistry B*, 1998, **102**, 719-734.
29. A. C. Hengge and I. Onyido, *Current Organic Chemistry*, 2005, **9**, 61-74.
30. J. K. Lassila, J. G. Zalatan and D. Herschlag, *Annual Review of Biochemistry*, 2011, **80**, 669-702.
31. A. J. Kirby, M. Medeiros, J. R. Mora, P. S. M. Oliveira, A. Amer, N. H. Williams and F. Nome, *The Journal of Organic Chemistry*, 2013, **78**, 1343-1353.

32. C. A. Bunton, D. R. Llewellyn, K. G. Oldham and C. A. Vernon, *Journal of the Chemical Society (Resumed)*, 1958, 3574-3587.
33. A. J. Kirby and A. G. Varvoglis, *Journal of the American Chemical Society*, 1967, **89**, 415-423.
34. P. W. C. Barnard, C. A. Bunton, D. Kellerman, M. M. Mhala, B. Silver, C. A. Vernon and V. A. Welch, *Journal of the Chemical Society B: Physical Organic*, 1966, 227-235.
35. C. A. Bunton and S. J. Farber, *The Journal of Organic Chemistry*, 1969, **34**, 767-772.
36. C. Bunton, M. Mhala, K. Oldham and C. Vernon, *Journal of the Chemical Society (Resumed)*, 1960, 3293-3301.
37. J. Kumamoto and F. H. Westheimer, *Journal of the American Chemical Society*, 1955, **77**, 2515-2518.
38. N. H. Williams and P. Wyman, *Chemical Communications*, 2001, 1268-1269.
39. A. J. Kirby and M. Younas, *Journal of the Chemical Society B: Physical Organic*, 1970, 510-513.
40. N. Tarrat, *Journal of Molecular Structure: THEOCHEM*, 2010, **941**, 56-60.
41. E. Karl-Kroupa, C. F. Callis and E. Seifter, *Industrial & Engineering Chemistry*, 1957, **49**, 2061-2062.
42. G. A. Abbott, *Journal of the American Chemical Society*, 1909, **31**, 763-770.
43. J. W. Williard, Y. K. Kim and J. M. Sullivan, *Journal of Chemical & Engineering Data*, 1984, **29**, 436-438.
44. R. K. Osterheld, *The Journal of Physical Chemistry*, 1958, **62**, 1133-1135.
45. J. D. McGilvery and J. P. Crowther, *Canadian Journal of Chemistry*, 1954, **32**, 174-185.
46. D. L. Miller and T. Ukena, *Journal of the American Chemical Society*, 1969, **91**, 3050-3053.
47. E. Mayaan, K. Range and D. York, *J Biol Inorg Chem*, 2004, **9**, 807-817.
48. P. J. Briggs, D. P. N. Satchell and G. F. White, *Journal of the Chemical Society B: Physical Organic*, 1970, 1008-1012.
49. N. H. Williams, A.-M. Lebuis and J. Chin, *Journal of the American Chemical Society*, 1999, **121**, 3341-3348.
50. N. H. Williams, *Journal of the American Chemical Society*, 2000, **122**, 12023-12024.
51. S. J. Admiraal and D. Herschlag, *Chemistry & Biology*, 1995, **2**, 729-739.
52. C. H. Oestreich and M. M. Jones, *Biochemistry*, 1967, **6**, 1515-1519.
53. W. P. Taylor and T. S. Widlanski, *Chemistry & Biology*, 1995, **2**, 713-718.
54. T. S. Widlanski and W. Taylor, in *Comprehensive Natural Products Chemistry*, eds. S. D. Barton, K. Nakanishi and O. Meth-Cohn, Pergamon, Oxford, Editon edn., 1999, pp. 139-162.
55. L. Sun, D. C. Martin and E. R. Kantrowitz, *Biochemistry*, 1999, **38**, 2842-2848.
56. J. G. Zalatan, T. D. Fenn, A. T. Brunger and D. Herschlag, *Biochemistry*, 2006, **45**, 9788-9803.
57. M. L. Applebury and J. E. Coleman, *Journal of Biological Chemistry*, 1969, **244**, 308-318.
58. J. A. Reynolds and M. J. Schlesinger, *Biochemistry*, 1967, **6**, 3552-3559.
59. T. Salminen, J. Kaepylae, P. Heikinheimo, J. Kankare, A. Goldman, J. Heinonen, A. A. Baykov, B. S. Cooperman and R. Lahti, *Biochemistry*, 1995, **34**, 782-791.
60. E. H. Harutyunyan, I. P. Kuranova, B. K. Vainshtein, W. E. Höhne, V. S. Lamzin, Z. Dauter, A. V. Teplyakov and K. S. Wilson, *European Journal of Biochemistry*, 1996, **239**, 220-228.
61. S. Avaeva, O. Grigorjeva, V. Mitkevich, V. Sklyankina and S. Varfolomeyev, *FEBS Letters*, 1999, **464**, 169-173.
62. T. Sitnik, J. Vainonen, E. Rodina, T. Nazarova, S. Kurilova, N. Vorobyeva and S. Avaeva, *IUBMB Life*, 2003, **55**, 37-41.
63. T. Hyytiä, P. Halonen, A. Salminen, A. Goldman, R. Lahti and B. S. Cooperman, *Biochemistry*, 2001, **40**, 4645-4653.

64. L. Yang, R.-Z. Liao, J.-G. Yu and R.-Z. Liu, *The Journal of Physical Chemistry B*, 2009, **113**, 6505-6510.
65. T. Kajander, J. Kellosalo and A. Goldman, *FEBS Letters*, 2013, **587**, 1863-1869.
66. S. Muniyan, N. Chaturvedi, J. Dwyer, C. LaGrange, W. Chaney and M.-F. Lin, *International Journal of Molecular Sciences*, 2013, **14**, 10438-10464.
67. T. Klabunde, N. Sträter, R. Fröhlich, H. Witzel and B. Krebs, *Journal of Molecular Biology*, 1996, **259**, 737-748.
68. G. Schenk, N. Mitić, G. R. Hanson and P. Comba, *Coordination Chemistry Reviews*, 2013, **257**, 473-482.
69. D. Barford, A. K. Das and M.-P. Egloff, *Annual Review of Biophysics and Biomolecular Structure*, 1998, **27**, 133-164.
70. D. Barford, in *Handbook of Cell Signaling (Second Edition)*, Academic Press, San Diego, Editon edn., 2010, pp. 677-681.
71. Y. Shi, *Cell*, 2009, **139**, 468-484.
72. J. Sanvoisin and D. Gani, *Bioorganic & Medicinal Chemistry Letters*, 2001, **11**, 471-474.
73. E. van Schaftingen and I. Gerin, *Biochemical Journal*, 2002, **362**, 513-532.
74. A. Burchell, *Kidney International* 1996, **49**, 953-958.
75. A. Ghosh, J.-J. Shieh, C.-J. Pan, M.-S. Sun and J. Y. Chou, *Journal of Biological Chemistry*, 2002, **277**, 32837-32842.
76. J.-J. Shieh, M. Terzioglu, H. Hiraiwa, J. Marsh, C.-J. Pan, L.-Y. Chen and J. Y. Chou, *Journal of Biological Chemistry*, 2002, **277**, 5047-5053.
77. A. Peet, *Marks' Basic Medical Biochemistry*, Fourth Ed. edn., Lippincott Williams & Wilkins, Baltimore, 2012.
78. N. S. Ging and J. M. Sturtevant, *Journal of the American Chemical Society*, 1954, **76**, 2087-2091.
79. P. Ohlmeyer and R. Shatas, *Archives of Biochemistry and Biophysics*, 1952, **36**, 411-420.
80. J. M. Sturtevant, *Journal of the American Chemical Society*, 1955, **77**, 255-258.
81. R. C. Woledge and P. J. Reilly, *Biophysical Journal*, 1988, **54**, 97-104.
82. R. C. Woledge, *Progress in Biophysics and Molecular Biology*, 1971, **22**, 37-74.
83. F. D. Carlson, *The Journal of general physiology*, 1960, **44**, 33-60.
84. R. B. Stockbridge and R. Wolfenden, *Journal of Biological Chemistry*, 2011, **286**, 18538-18546.
85. M. J. Todd and J. Gomez, *Analytical Biochemistry*, 2001, **296**, 179-187.
86. W. D. Kumler and J. J. Eiler, *Journal of the American Chemical Society*, 1943, **65**, 2355-2361.
87. R. L. Carroll and R. E. Mesmer, *Inorganic Chemistry*, 1967, **6**, 1137-1142.
88. R. E. Mesmer and R. L. Carroll, *Journal of the American Chemical Society*, 1966, **88**, 1381-1387.
89. R. P. Mitra, H. C. Malhotra and D. V. S. Jain, *Transactions of the Faraday Society*, 1966, **62**, 167-172.
90. J. P. Crowther and A. E. R. Westman, *Canadian Journal of Chemistry*, 1954, **32**, 42-48.
91. M. Kawabe, O. Ohashi and I. Yamaguchi, *Bulletin of the Chemical Society of Japan*, 1970, **43**, 3705-3710.
92. N. T. Powles, PhD Thesis,University of Huddersfield, 2005.
93. M. Watanabe, S. Sato and H. Saito, *Bulletin of the Chemical Society of Japan*, 1976, **49**, 2474-2478.
94. H. Fukada and K. Takahashi, *Proteins: Structure, Function, and Bioinformatics*, 1998, **33**, 159-166.
95. M. Tetas and J. M. Lowenstein, *Biochemistry*, 1963, **2**, 350-357.
96. S. Ueda and Y. Sasaki, *Bulletin of the Chemical Society of Japan*, 1971, **44**, 1972-1973.

97. I. E. Catrina and A. C. Hengge, *Journal of the American Chemical Society*, 1999, **121**, 2156-2163.
98. D. E. Bryant, D. Greenfield, R. D. Walshaw, B. R. G. Johnson, B. Herschy, C. Smith, M. A. Pasek, R. Telford, I. Scowen, T. Munshi, H. G. M. Edwards, C. R. Cousins, I. A. Crawford and T. P. Kee, *Geochimica et Cosmochimica Acta*, 2013, **109**, 90-112.
99. A. J. Felsenfeld and B. S. Levine, *American Journal of Kidney Diseases : The Official Journal of the National Kidney Foundation*, 2012, **60**, 655-661.
100. M. E. Stroppolo, M. Falconi, A. M. Caccuri and A. Desideri, *Cellular and Molecular Life Sciences* 2001, **58**, 1451-1460.
101. R. N. Goldberg, N. Kishore and R. M. Lennen, *Journal of Physical and Chemical Reference Data*, 2002, **31**, 231-370.
102. K. S. Pitzer, *Journal of the American Chemical Society*, 1937, **59**, 2365-2371.
103. C.-h. Wu, R. J. Witnosky, P. George and R. J. Rutman, *Journal of the American Chemical Society*, 1967, **89**, 1987-1991.
104. J. E. Mills, C. A. Maryanoff, R. M. Cosgrove, L. Scott and D. F. McComsey, *Organic Preparations and Procedures International*, 1984, **16**, 97-114.
105. E. M. Arnett and R. Reich, *Journal of the American Chemical Society*, 1980, **102**, 5892-5902.
106. D. N. Kevill, *Journal of the Chemical Society, Chemical Communications*, 1981, 421-422.
107. W. Chen, S. A. Elfeky, Y. Nonne, L. Male, K. Ahmed, C. Amiable, P. Axe, S. Yamada, T. D. James, S. D. Bull and J. S. Fossey, *Chemical Communications*, 2011, **47**, 253-255.
108. J. Marek, P. Stodulka, J. Cabal, O. Soukup, M. Pohanka, J. Korabecny, K. Musilek and K. Kuca, *Molecules*, 2010, **15**, 1967-1972.
109. E. M. Kosower, *Journal of the American Chemical Society*, 1955, **77**, 3883-3885.
110. P. Madaan and V. K. Tyagi, *Journal of Oleo Science*, 2008, **57**, 197-215.
111. C. D. Vanderwal, *The Journal of Organic Chemistry*, 2011, **76**, 9555-9567.
112. T. M. Nguyen, M. d. R. Sanchez-Salvatori, J.-C. Wypych and C. Marazano, *The Journal of Organic Chemistry*, 2007, **72**, 5916-5919.
113. Y. Okamoto and Y. Shimakawa, *The Journal of Organic Chemistry*, 1970, **35**, 3752-3756.
114. P. C. Kearney and D. D. Kaufman, *Herbicides: Chemistry, Degradation and Mode of Action*, Marcel Dekker, New York, 1967.
115. J. R. Casey, P. E. Morgan, D. Vullo, A. Scozzafava, A. Mastrolorenzo and C. T. Supuran, *Journal of Medicinal Chemistry*, 2004, **47**, 2337-2347.
116. M. Gholizadeh, B. Maleki, M. Pourayoubi, M. Kia and B. Notash, *Acta Crystallographica Section E*, 2011, **67**, o1614-o1615.
117. A. Albert-Kiszely, B. E. Pjetursson, G. E. Salvi, J. Witt, A. Hamilton, G. R. Persson and N. P. Lang, *Journal of Clinical Periodontology*, 2007, **34**, 658-667.
118. M. Diaw, A. Chagnes, B. Carré, P. Willmann and D. Lemordant, *Journal of Power Sources*, 2005, **146**, 682-684.
119. K. Fujimoto, D. Morisaki, M. Yoshida, T. Namba, K. Hye-Sook, Y. Wataya, H. Kourai, H. Kakuta and K. Sasaki, *Bioorganic & Medicinal Chemistry Letters*, 2006, **16**, 2758-2760.
120. J. R. Harjani, R. D. Singer, M. T. Garcia and P. J. Scammells, *Green Chemistry*, 2009, **11**, 83-90.
121. B. Bittner, R. J. Wrobel and E. Milchert, *The Journal of Chemical Thermodynamics*, 2012, **55**, 159-165.
122. R. P. Swatloski, S. K. Spear, J. D. Holbrey and R. D. Rogers, *Journal of the American Chemical Society*, 2002, **124**, 4974-4975.
123. S. Zhu, Y. Wu, Q. Chen, Z. Yu, C. Wang, S. Jin, Y. Ding and G. Wu, *Green Chemistry*, 2006, **8**, 325-327.
124. M. Gericke, P. Fardim and T. Heinze, *Molecules*, 2012, **17**, 7458-7502.

125. S. H. Baer and A. B. Prescott, *Journal of the American Chemical Society*, 1896, **18**, 988-989.
126. B. Almarzoqi, A. V. George and N. S. Isaacs, *Tetrahedron*, 1986, **42**, 601-607.
127. F. Kröhnke, *Chemische Berichte*, 1950, **83**, 50-59.
128. I. Brudgam and H. Hartl, *Acta Crystallographica Section C*, 1986, **42**, 866-868.
129. W.-Z. Fu, W.-J. Wang, Y.-Y. Niu and S. W. Ng, *Acta Crystallographica Section E*, 2010, **66**, o1211.
130. M. Al-Ktaifani and M. Rukiah, *Chem. Pap.*, 2011, **65**, 469-476.
131. M. H. O'Leary and R. W. Stach, *The Journal of Organic Chemistry*, 1972, **37**, 1491-1493.
132. E. M. Kosower and J. W. Patton, *Tetrahedron*, 1966, **22**, 2081-2093.
133. R. A. Olofson and D. M. Zimmerman, *Journal of the American Chemical Society*, 1967, **89**, 5057-5059.
134. C. Fernandez, V. G. Toscano, H. Chaimovich, M. J. Politi and N. Hioka, *Journal of Physical Organic Chemistry*, 1998, **11**, 25-30.
135. A. N. Kost, S. P. Gromov and R. S. Sagitullin, *Tetrahedron*, 1981, **37**, 3423-3454.
136. E. Klingsberg, *The Chemistry of Heterocyclic Compounds, Pyridine and Its Derivatives Part 2*, Interscience Publishers, New York, 1961.
137. J. Kavalek, J. Polanský and V. Štěrba, *Collection of Czechoslovak Chemical Communications*, 1974, **39**, 1049-1060.
138. R. Eisenthal and A. R. Katritzky, *Tetrahedron*, 1965, **21**, 2205-2213.
139. S. L. Johnson and K. A. Rumon, *Tetrahedron Letters*, 1966, **7**, 1721-1726.
140. F. T. Boyle and R. Hull, *Journal of the Chemical Society, Perkin Transactions 1*, 1974, 1541-1546.
141. R. G. Pearson and R. L. Dillon, *Journal of the American Chemical Society*, 1953, **75**, 2439-2443.
142. F. A. Carey and R. J. Sundberg, *Advanced Organic Chemistry: Part A: Structure and Mechanisms*, Springer, 2007.
143. E. V. Anslyn and D. A. Dougherty, *Modern Physical Organic Chemistry*, University Science, 2006.
144. J. P. Richard, G. Williams and J. Gao, *Journal of the American Chemical Society*, 1999, **121**, 715-726.
145. J. Crugeiras, A. Rios, T. L. Amyes and J. P. Richard, *Organic & Biomolecular Chemistry*, 2005, **3**, 2145-2149.
146. J. P. Richard and T. L. Amyes, *Current Opinion in Chemical Biology*, 2001, **5**, 626-633.
147. P. A. Sims, A. L. Menefee, T. M. Larsen, S. O. Mansoorabadi and G. H. Reed, *Journal of Molecular Biology*, 2006, **355**, 422-431.
148. S. W. Benson, *Angewandte Chemie International Edition in English*, 1978, **17**, 812-819.
149. D.H.Williams and I. Fleming, *Spectroscopic methods in organic chemistry*, 5th edn., McGraw-Hill, England, 1996.
150. A. B. Rudine, M. G. Walter and C. C. Wamser, *The Journal of Organic Chemistry*, 2010, **75**, 4292-4295.
151. K. B. Wiberg, *Chemical Reviews*, 1955, **55**, 713-743.
152. H. C. Van der Plas, *Accounts of Chemical Research*, 1978, **11**, 462-468.
153. J. A. Zoltewicz and C. L. Smith, *Journal of the American Chemical Society*, 1967, **89**, 3358-3359.
154. J. A. Zoltewicz and L. S. Helmick, *Journal of the American Chemical Society*, 1970, **92**, 7547-7552.
155. H. F. Koch, W. Tumas and R. Knoll, *Journal of the American Chemical Society*, 1981, **103**, 5423-5429.
156. A. K. Covington, R. A. Robinson and R. G. Bates, *The Journal of Physical Chemistry*, 1966, **70**, 3820-3824.
157. M. Eigen, *Angewandte Chemie International Edition in English*, 1964, **3**, 1-19.

158. J. P. Fox and W. P. Jencks, *Journal of the American Chemical Society*, 1974, **96**, 1436-1449.
159. J. P. Richard, T. L. Amyes and M. M. Toteva, *Accounts of Chemical Research*, 2001, **34**, 981-988.
160. A. Rios, A. C. O'Donoghue, T. L. Amyes and J. P. Richard, *Canadian Journal of Chemistry*, 2005, **83**, 1536-1542.
161. A. Rios, T. L. Amyes and J. P. Richard, *Journal of the American Chemical Society*, 2000, **122**, 9373-9385.
162. A. E. Reed and P. v. R. Schleyer, *Journal of the American Chemical Society*, 1987, **109**, 7362-7373.
163. S. Hati and D. Datta, *The Journal of Organic Chemistry*, 1992, **57**, 6056-6057.
164. R. Lalancette, W. Furey, J. Costanzo, P. Hemmes and F. Jordan, *Acta Crystallographica Section B: Structural Crystallography and Crystal Chemistry*, 1978, **34**, 2950-2953.
165. M. N. Kammer, L. V. Koplitz and J. T. Mague, *Acta Crystallographica Section E*, 2013, **69**, o1281.
166. N. Kebede and J. W. Pavlik, *Journal of Heterocyclic Chemistry*, 1997, **34**, 685-686.
167. F. Li, Q. Chen, C.-C. Liu, Y.-H. Wu, X.-P. Liu and G.-F. Yang, *Appl Magn Reson*, 2012, **42**, 169-177.
168. W. W. Paudler and L. S. Helmick, *Chemical Communications (London)*, 1967, 377-378.
169. R. B. Morin and M. Gorman, *Chemistry and Biology of Beta-Lactam Antibiotics*, Academic Press, 1982.
170. M.I.Page, *The Chemistry of β-Lactams*, 1st Edition edn., Blackie Academic & Professional, Glasgow, 1992.
171. G. Seltmann and O. Holst, *The Bacterial Cell Wall*, Springer, New York, 2002.
172. S. Srivastava, *Understanding Bacteria*, Kluwer Academic Publishers, Dordrecht, Netherlands, 2003.
173. L. P. Kotra and S. Mobashery, *Bulletin de l'Institut Pasteur*, 1998, **96**, 139-150.
174. G. D. Wright, *Chemical Communications*, 2011, **47**, 4055-4061.
175. G. Bushnell, F. Mitrani-Gold and L. M. Mundy, *International Journal of Infectious Diseases*, 2013, e325–e333.
176. W. M. Backer, *The World of the Cell*, 6th edn., Pearson Education, Inc, San Francisco, 2006.
177. E. Y. Furuya and F. D. Lowy, *Nature Reviews Microbiology*, 2006, **4**, 36-45.
178. J. Hatcher, R. Dhillon and B. Azadian, *Journal of the Intensive Care Society*, 2012, **13**, 297-303.
179. C. Walsh, *Nature*, 2000, **406**, 775-781.
180. C. Walsh, *Antibiotics: actions, origins, resistance*, ASM Press, Washington, 2003.
181. B. G. Hall and M. Barlow, *Journal of Antimicrobial Chemotherapy*, 2005, **55**, 1050-1051.
182. K. Bush and G. A. Jacoby, *Antimicrobial Agents and Chemotherapy*, 2010, **54**, 969-976.
183. B. G. Hall and M. Barlow, *Drug Resistance Updates : Reviews and Commentaries in Antimicrobial and Anticancer Chemotherapy*, 2004, **7**, 111-123.
184. S. M. Drawz and R. A. Bonomo, *Clinical Microbiology Reviews*, 2010, **23**, 160-201.
185. A. Matagne, A. Dubus, M. Galleni and J.-M. Frère, *Natural Product Reports*, 1999, **16**, 1-19.
186. C. Fenollar-Ferrer, J. Frau, J. Donoso and F. Muñoz, *Theoretical Chemistry Accounts*, 2008, **121**, 209-218.
187. K. Bush, *Critical Care*, 2010, **14**, 224.
188. G. A. Jacoby, *Clinical Microbiology Reviews*, 2009, **22**, 161-182.
189. P. A. Bradford, *Clinical Microbiology Reviews*, 2001, **14**, 933-951.
190. C. Héritier, L. Poirel, D. Aubert and P. Nordmann, *Antimicrobial Agents and Chemotherapy*, 2003, **47**, 268-273.

191. R. R. Watkins, K. M. Papp-Wallace, S. M. Drawz and R. A. Bonomo, *Frontiers in Microbiology*, 2013, **4**, 1-8.
192. L. D. Sabath and E. P. Abraham, *Biochemical Journal*, 1966, **98**.
193. M. I. Page and A. Badarau, *Bioinorganic chemistry and applications*, 2008, 1-14.
194. J. D. Buynak, *Biochemical Pharmacology*, 2006, **71**, 930-940.
195. L. E. Horsfall, G. Garau, B. M. R. Lienard, O. Dideberg, C. J. Schofield, J. M. Frere and M. Galleni, *Antimicrob. Agents Chemother.*, 2007, **51**, 2136-2142.
196. C. Bebrone, *Antimicrobial agents and chemotherapy*, 2009, **53**, 4464-4471.
197. G. Garau, I. Garcia-Saez, C. Bebrone, C. Anne, P. Mercuri, M. Galleni, J.-M. Frere and O. Dideberg, *Antimicrob. Agents Chemother.*, 2004, **48**, 2347-2349.
198. F. K. Majiduddin, I. C. Materon and T. G. Palzkill, *International Journal of Medical Microbiology*, 2002, **292**, 127-137.
199. C. Bebrone, *Biochemical Pharmacology*, 2007, **74**, 1686-1701.
200. O. Jacquin, D. Balbeur, C. Damblon, P. Marchot, E. De Pauw, G. C. Roberts, J.-M. Frère and A. Matagne, *Journal of Molecular Biology*, 2009, **392**, 1278-1291.
201. A. Carfi, *The EMBO journal*, 1995, **14**, 4914.
202. A. Badarau and M. Page, *Journal of Biological Inorganic Chemistry*, 2008, **13**, 919-928.
203. D. de Seny, C. Prosperi-Meys, C. Bebrone, G. M. Rossolini, M. I. Page, P. Noel, J.-M. Frère and M. Galleni, *Biochem. J.*, 2002, **363**, 687-696.
204. R. M. Breece, L. I. Llarrull, M. F. Tioni, A. J. Vila and D. L. Tierney, *Journal of Inorganic Biochemistry*, 2012, **111**, 182-186.
205. G. Garau, C. Bebrone, C. Anne, M. Galleni, J.-M. Frère and O. Dideberg, *Journal of Molecular Biology*, 2005, **345**, 785-795.
206. B. M. R. Lienard, G. Garau, L. Horsfall, A. I. Karsisiotis, C. Damblon, P. Lassaux, C. Papamicael, G. C. K. Roberts, M. Galleni, O. Dideberg, J.-M. Frere and C. J. Schofield, *Organic & Biomolecular Chemistry*, 2008, **6**, 2282-2294.
207. C. Bebrone, C. Anne, F. Kerff, G. Garau, K. De vriendt, R. Lantin, B. Devreese, J. Van beeumen, O. Dideberg, J.-M. Frère and M. Galleni, *Biochem J*, 2008, **414**, 151-159.
208. K. De Vriendt, G. Van Driessche, B. Devreese, C. Bebrone, C. Anne, J. Frère, M. Galleni and J. Van Beeumen, *Journal of The American Society for Mass Spectrometry*, 2006, **17**, 180-188.
209. A. Tamilselvi and G. Mugesh, *Journal of Biological Inorganic Chemistry*, 2008, **13**, 1039-1053.
210. K. A. McCall, C.-c. Huang and C. A. Fierke, *The Journal of nutrition*, 2000, **130**, 1437S-1446S.
211. S. Bounaga, A. Laws, M. Galleni and M. Page, *Biochemical Journal*, 1998, **331**, 703-711.
212. Z. Xiao and A. G. Wedd, *Natural Product Reports*, 2010, **27**, 768-789.
213. M. Hernandez Valladares, A. Felici, G. Weber, H. W. Adolph, M. Zeppezauer, G. M. Rossolini, G. Amicosante, J.-M. Frère and M. Galleni, *Biochemistry*, 1997, **36**, 11534-11541.
214. J. C. Martinez, J. Murciano-Calles, E. S. Cobos, M. Iglesias-Bexiga, I. Luque and J. Ruiz-Sanz, *Intechopen*, 2013, 73-105.
215. C. A. Hunter and H. L. Anderson, *Angewandte Chemie International Edition*, 2009, **48**, 7488-7499.
216. U. Heinz and H.-W. Adolph, *Cellular and Molecular Life Sciences*, 2004, **61**, 2827-2839.
217. M. W. Freyer and E. A. Lewis, *Methods in Cell Biology*, 2008, **84**, 79-113.
218. J. Tellinghuisen, *The Journal of Physical Chemistry B*, 2005, **109**, 20027-20035.
219. M. M. Pierce, C. Raman and B. T. Nall, *Methods*, 1999, **19**, 213-221.
220. A. L. Feig, *Biopolymers*, 2007, **87**, 293-301.
221. W. B. Turnbull, *MicroCal Application Note*, 2005, 2-3.

222. I. Herrera and M. A. Winnik, *The Journal of Physical Chemistry B*, 2013, **117**, 8659-8672.
223. N. J. Buurma and I. Haq, *Methods*, 2007, **42**, 162-172.
224. J. Tellinghuisen, *Analytical Biochemistry*, 2008, **373**, 395-397.
225. L. S. Mizoue and J. Tellinghuisen, *Biophysical Chemistry*, 2004, **110**, 15-24.